# A comparative study of cosmic ray modulation models

**JL Raath**

**20368879**

Dissertation submitted in partial fulfillment of the requirements for the degree *Magister Scientiae* in Space Physics (specialising in Physics) at the Potchefstroom Campus of the North-West University

Supervisor: Prof MS Potgieter

Co-supervisor: Dr RD Strauss

May 2015

I have seen the dark universe yawning
Where the black planets roll without aim,
Where they roll in their horror unheeded,
Without knowledge, or lustre, or name.
– **H.P. Lovecraft,** ***Nemesis***

To my mother
**Stephanie Suzan Raath** *née* **Graham**
and in loving memory of my father
**Jan Louis Raath**
**(1950 – 2012)**

# Abstract

Until recently, numerical modulation models for the solar modulation of cosmic rays have been based primarily on finite difference approaches; however, models based on the solution of an appropriate set of stochastic differential equations have become increasingly popular. This study utilises such a spatially three-dimensional and time-stationary model, based on that of Strauss et al. (2011b). The remarkable numerical stability and powerful illustrative capabilities of this model are utilised extensively and in a distinctly comparative fashion to enable new insights into the processes of modulation. The model is refined to provide for both the Smith-Bieber (Smith and Bieber, 1991) and Jokipii-Kóta (Jokipii and Kóta, 1989) modifications to the Parker heliospheric magnetic field (Parker, 1958) and the implications for modulation are investigated. During this investigation it is conclusively illustrated that the Parker field is most conducive to drift dominated modulation, while the Jokipii-Kóta and Smith-Bieber modifications are seen to induce successively larger contributions from diffusive processes. A further refinement to the model is the incorporation of a different profile for the heliospheric current sheet. This profile is defined by its latitudinal extent given by Kóta and Jokipii (1983), as opposed to the profile given by Jokipii and Thomas (1981). An extensive investigation into current sheet related matters is launched, illustrating the difference between these current sheet geometries, the associated drift velocity fields and the effect on modulation. At high levels of solar activity, such that the current sheet enters deep enough into the polar regions, the profile of Kóta and Jokipii (1983) is found to significantly reduce the effective inward (outward) drifts of positively (negatively) charged particles during $A > 0$ polarity cycles. The analogous effect is true for $A < 0$ polarity cycles and the overall effect is of such an extent that the $A > 0$ and $A < 0$ solutions are found to coincide at the highest levels of solar activity to form a closed loop. This is a result that has never before been achieved without having to scale down the drift coefficient to zero at solar maximum, as was done by e.g. Ndiitwani et al. (2005). Furthermore, it is found that the drift velocity fields associated with these two current sheet profiles lead to significant differences in modulation even at such low levels of solar activity where no difference in the geometries of these profiles are yet in evidence. The model is finally applied to reproduce four observed galactic proton spectra, selected from PAMELA measurements (Adriani et al., 2013) during the atypical solar minimum of 2006 to 2009; a new proton local interstellar spectrum was employed. The results are found to be in accordance with that found by other authors and in particular Vos (2011), i.e. the diffusion was required to consistently increase from 2006 to 2009 and, in addition, the rigidity dependence below $\sim$ 3 GV was required to change over this time so that the spectra became increasingly softer.

Keywords: solar modulation, cosmic rays, stochastic differential equations; drift coefficient; diffusive processes; heliospheric current sheet; heliospheric magnetic field; solar activity; magnetic polarity cycles; local interstellar proton spectrum.

# Opsomming

Numeriese modelle vir die modulasie van kosmiese strale in die heliosfeer is in die verlede hoofsaaklik gebaseer op eindige verskille metodes; meer onlangs het sulke modelle wat gebaseer is op die oplos van 'n toepaslike stel stochastiese differensiaal-vergelykings meer gewild geraak. Hierdie studie maak gebruik van so 'n ruimtelik drie-dimensionele en tydsonafhanklike model, gebaseer op dié van Strauss et al. (2011b). Die merkwaardige numeriese stabiliteit en kragtige illustrerende vermoëns van die model word ekstensief en in 'n vergelykende manier benut om nuwe insigte in modulasie prosesse te verkry. Die model is uitgebrei om te voorsien vir beide die Smith-Bieber (Smith en Bieber, 1991) en Jokipii-Kóta (Jokipii en Kóta, 1989) modifikasies van die Parker heliosferiese magneetveld (Parker, 1958). Die implikasies van hierdie modifikasies vir modulasie is ondersoek en daar is gevind dat die Parkerveld dryf gedomineerde modulasie sterk aanmoedig, terwyl die Jokipii-Kóta en Smith-Bieber modifikasies opeenvolgend groter bydrae van diffusie bewerkstellig. 'n Verdere uitbreiding van die model is die inkorporasie van 'n ander profiel vir die neutrale heliosferiese vlak. Hierdie profiel is gedefinieer deur die uitdrukking vir die latitudinale omvang, gegee deur Kóta en Jokipii (1983), en word vergelyk met die profiel soos gegee deur Jokipii en Thomas (1981). 'n Omvangryke ondersoek is geloots in sake wat betrekking het op die neutrale vlak en die verskil tussen die geometrieë, die geassosieerde dryfsnelheidvelde en die uiteindelike impak op modulasie is ondersoek. Daar is gevind dat by hoë vlakke van sonaktiwiteit, sodanig dat die neutrale vlak diep genoeg in die poolgebiede indring, die profiel van Kóta en Jokipii (1983) die effektiewe inwaartse (uitwaartse) dryf van positief (negatief) gelaaide deeltjies tydens 'n $A > 0$ polariteit-siklus beduidend inhibeer. Die analoog is waar vir die $A < 0$ siklus en die totale effek is so groot dat die $A > 0$ en $A < 0$ oplossings saamval om 'n geslote lis vorm by die hoogste vlakke van sonaktiwiteit. Hierdie is 'n resultaat wat nog nooit van tevore bereik is sonder om die dryfkoëffisiënt by die hoogste vlakke van sonaktiwiteit af te skaal tot nul nie, soos gedoen deur bv. Ndiitwani et al. (2005). Dit is verder gevind dat die dryfsnelheidvelde ge-assosieer met hierdie twee profiele onderskeidelik lei tot beduidende verskille in modulasie, selfs by vlakke van sonaktiwiteit wat so laag is dat daar nog geen verskil tussen die onderskeie geometrieë sigbaar is nie. Die model is uiteindelik toegepas om vier waargenome galaktiese proton spektra, afgelei uit metings van die PAMELA instrument (Adriani et al., 2013) tydens die ongewone sonminimum van 2006 tot 2009 te herproduseer; 'n nuwe lokale interstellêre proton spektrum is gebruik. Die resultate is in ooreenkoms met die van ander outeurs en, spesifiek, die van Vos (2011). Daar is gevind dat die diffusie deurlopend moes toeneem vanaf 2006 tot 2009 en dat die styfheidsafhanklikheid onder $\sim 3$ GV ook moes verander, sodat die spektra toenemend sagter geword het.

Sleutelwoorde: modulasie, kosmiese strale, stochastiese differensiaal-vergelykings; dryf; diffusie; heliosferiese magneetveld; neutrale heliosferiese vlak; sonaktiwiteit; magnetiese polariteit-siklusse; dryfkoëffisiënt; lokale interstellêre proton spektrum.

# Nomenclature

Listed below are the acronyms and abbreviations used in the text.

| | |
|---|---|
| 1D | One-Dimensional |
| 2D | Two-Dimensional |
| 3D | Three-Dimensional |
| ACR | Anomalous Cosmic Ray |
| ADI | Alternating Direction Implicit |
| AU | Astronomical Unit [1] |
| BS | Bow Shock |
| CR | Cosmic Ray |
| eV | Electron Volt [2] |
| FLS | Fast Latitude Scan |
| GCR | Galactic Cosmic Ray |
| HCS | Heliospheric Current Sheet |
| HMF | Heliospheric Magnetic Field |
| HP | Heliopause |
| IBEX | Interstellar Boundary Explorer |
| ISM | Interstellar Medium |
| JKM | Jokipii-Kóta Modification |
| LIS | Local Interstellar Spectrum |
| LISM | Local Interstellar Medium |
| MFP | Mean Free Path |
| MHD | Magneto-hydrodynamic |
| NLGC | Non-Linear Guiding Center |
| PAMELA | Payload for Antimatter Matter Exploration and Light-nuclei Astrophysics |
| PHMF | Parker Heliospheric Magnetic Field |
| PUs | Program Units |
| SBM | Smith-Bieber Modification |
| SDE | Stochastic Differential Equation |
| SN | Sunspot Number |
| SW | Solar Wind |
| TPE | Transport Equation |
| TS | Termination Shock |

[1] Defined to be the average distance between the Earth and the Sun, 1 AU= $1.49 \times 10^8$ km.
[2] 1 eV = $1.6 \times 10^{-19}$ J ($10^3$ eV = 1 keV, $10^6$ eV = 1 MeV, $10^9$ eV = 1 GeV).

# Contents

# Chapter 1

# Introduction

Cosmic ray (CR) modulation models based on stochastic differential equations (SDEs) have become increasingly popular in recent times; this field of study was once dominated by numerical models based on the finite difference approach of the alternating direction implicit (ADI) method. Models based on the solution of the relevant set of SDEs were first introduced to the Potchefstroom modulation group by Strauss et al. (2011b); a complete description of the mathematical construction of this model was presented by Kopp et al. (2012). This spatially three-dimensional (3D) and time independent SDE-based model is refined and utilised extensively in this study.

Stochastic differential equations are discussed briefly and the stochastic transport model is derived, following Strauss (2013). The numerous advantages of SDE-based models over finite difference models are pointed out and the benchmarking carried out to establish the validity and reliability of the model is summarised. Making use of the powerful illustrative capabilities of the SDE-based model, an extensive investigation is launched into the properties and features of this refined model. One prominent refinement is the incorporation of the Smith-Bieber (Smith and Bieber, 1991) and Jokipii-Kóta (Jokipii and Kóta, 1989) modifications to the heliospheric magnetic field (HMF). These modified HMF profiles and their effects on modulation are investigated and the Smith-Bieber modification is used throughout the rest of this work. A second prominent refinement to the pre-established SDE-based model is the incorporation of a different profile for the neutral heliospheric current sheet (HCS) and the drift velocity field associated with this profile. This HCS profile is defined by its latitudinal extent, for which the expression is given by Kóta and Jokipii (1983), and it is compared to the profile defined by the latitudinal extent as given by Jokipii and Thomas (1981). In particular, the effects that these two HCS profiles have on CR modulation are compared, with the effects on drifts being illustrated and discussed in much detail. The numerical stability of the SDE-based model makes it possible to carry out these comparisons over the entire range of solar activity, i.e. from solar minimum to extreme solar maximum conditions. Because of issues surrounding the inherent numerical stability, such a study is extremely difficult to accomplish with the use of ADI-based models.

The SDE-based model is finally applied to reproduce four observed galactic proton spectra, selected from measurements by PAMELA during the atypical solar minimum of 2006 to 2009. The results thus obtained are compared to the results of the ADI-based study carried out by Vos (2011). This application serves as an independent test of the ADI-based results as well as a demonstration of the ability of this model to reproduce observations.

Throughout this work, it is important to keep in mind that the model makes use of pseudo-particles and that these are not real or actual particles. The focus is, however,

primarily on what these results suggest about the behaviour of actual particles, i.e. what it says about modulation processes in the heliosphere and, as such, the results are most often interpreted from this perspective.

The structuring of this work is as follows:
**Chapter 2** provides the relevant background pertinent to the field of heliospheric physics and the solar modulation of CRs. This includes discussions on the magnetic activity cycle of the Sun, the solar wind and the structuring of the heliosphere. The Parker model for the HMF is discussed together with two prominent modifications to this model; the Fisk HMF model (Fisk, 1996) is briefly described, but not pursued further. The HCS is also discussed and the HCS tilt angle is introduced as a proxy for the solar activity cycle. This is followed by an overview of CRs and their classification according to origin, together with an illustration of the solar cycle dependence of CR counting rate measured by neutron monitors on Earth. The chapter concludes with a brief description of the PAMELA and Voyagers 1 and 2 space missions.

**Chapter 3** presents a mathematical treatment of the relevant theory behind particle transport in the heliosphere. Attention is in particular given to the proton drift and diffusion coefficients and the values assumed for these coefficients in this work. The relevant mathematical expressions are converted to spherical coordinates, to be implemented in a numerical modulation model.

**Chapter 4** is devoted to a discussion of the numerical modulation model utilised in this study. This model is based on the solution of a set of SDEs and, as such, this chapter includes a discussion of the basics of SDEs and illustrates how it is applied to solve physical problems. The SDE-based CR transport model is then derived by arriving at the correct set of SDEs and specifying the appropriate boundary conditions. This chapter also includes an overview of the modulation models developed by the Potchefstroom modulation group and distinguishes between SDE-based models and the more traditional finite difference models based on the ADI-method. The many advantages of SDE-based models over finite difference models are emphasised and the numerical prowess of SDE-based models is motivated. An extensive overview of the benchmarking carried out to establish the validity and reliability of the SDE-based model of this study is also given.

The properties and features of the numerical modulation model are investigated in **Chapter 5**. The main points concerning the benchmarking, implementation and advantages of the model described in Chapter 4 are summarised, whereafter general topics that are of importance in the case of any numerical model are investigated. These topics include the accuracy and convergence of solutions obtained when utilising the model, as well as the effect of implementing different boundary conditions. The modifications to the magnetic field are implemented in the model and these different HMF profiles are compared; the effect on the drift and diffusion coefficients, as well as the modulation resulting from each of these HMF profiles are also compared. The significant part of this chapter consists of an investigation into matters related to the HCS: an extensive investigation is launched into two different expressions for the latitudinal extent of the HCS, i.e. two different HCS profiles, and the implications for modulation. The latitudinal extent for these two profiles are respectively given by Jokipii and Thomas (1981) and by Kóta and Jokipii (1983). The mathematical expressions for the drift fields associated with each of these HCS profiles are compared, a formal derivation being presented for the HCS defined by Kóta and Jokipii (1983). Owing to the numerical stability of the SDE-based model, this investigation is carried out over solar activity levels covering both extremities of solar minimum and maximum; studies during the highest levels of solar activity are extremely difficult to accomplish with the use of ADI-based models. The last section of Chapter 5

stipulates possible future refinements to the model.

**Chapter 6** presents an application of the SDE-based numerical modulation model, reproducing the 2006 to 2009 PAMELA proton spectra. The results obtained from the utilisation of this model is compared with the results obtained by Vos (2011), who employed an ADI-based model. In the light of selecting an appropriate proton local interstellar spectrum (LIS), the crossing of Voyager 1 into the outer heliosheath is also discussed as well as when it will actually start measuring the pristine LIS; some prominent research on this topic is summarised. Also, conditions in the heliosphere during the atypical solar minimum of solar cycle 23/24 are briefly discussed.

**Chapter 7** gives a summary of this work and presents all the significant conclusions drawn during the course of this study. A list of possible future avenues of research or refinements to this model is also presented.

Though a nomenclature defining all the relevant abbreviations is included in this study, it was the aim to present the work in such a fashion as to limit the need for the use of this nomenclature. In each chapter, when a concept is referred to for the first time, it is written out in full and the abbreviation given in brackets. Furthermore, in the summaries and conclusions of each chapter, the words are again written out in full when used for the first time, followed by the abbreviation in brackets. Finally, no new sentence is ever started with an abbreviation as the first word. Regarding the use of acronyms in this work, the full meaning of the word is only written out where most relevant; when not written out in full, however, the context will be clear.

Aspects of this work were presented at the following conferences and workshops:

- The 2011 National Meeting of the Centre for High Performance Computing (CHPC) in Johannesburg, South Africa (December 2011).
- The $57^{\text{th}}$ Annual Conference of the South African Institute of Physics (SAIP) in Pretoria, South Africa (July 2012).
- Workshop entitled 'Cosmic Rays: from the Galaxy to the Heliosphere; a Numerical Modeling Approach' in Potchefstroom, South Africa (March 2014).
- The $40^{\text{th}}$ Biannual General Assembly of the Committee on Space Research (COSPAR) in Moscow, Russia (August 2014).

# Chapter 2

# The Sun, the Heliosphere and Cosmic Rays

## 2.1 Introduction

The Sun and its retinue constituting the solar system, travel through the interstellar medium at a velocity of $\sim 25$ km.s$^{-1}$, heading more or less in the direction of the Scorpio constellation. On its path, the Sun blows a magnetic bubble into the interstellar medium by means of its solar wind. This bubble is called the heliosphere and ensconces all of the solar system, thereby providing protection against bombardment by vast amounts of highly energetic atomic and subatomic particles called cosmic rays (CRs).

This chapter introduces the reader to the relevant terms and concepts needed to understand the basics of heliospheric and cosmic ray studies. The general properties of the heliosphere are discussed, with emphasis on the magnetic nature of the Sun, the solar wind (SW), the heliospheric magnetic field (HMF), and the neutral heliospheric current sheet (HCS). After a physical picture of the sun-heliosphere relation is established, the concept of cosmic rays is introduced together with their classification according to origin, as well as their modulation in the heliosphere over the course of the solar magnetic cycle. Finally, a few spacecraft missions most relevant to this study are discussed. Special attention is reserved for the PAMELA experiment and its realised and potential contributions to the field of cosmic ray modulation studies.

## 2.2 The Magnetically Variable Sun

As our nearest star, the Sun is vital to sustain life on Earth. Not only are we dependent on the Sun for the fact that it provides us with the heat, light, and other forms of energy we need to sustain life, but also for the protection it provides against cosmic radiation, provided by its magnetic properties. Solar magnetism is a highly dynamic property of the Sun, and it therefore serves to give the field of cosmic ray modulation studies a very dynamic character. As such, a good working knowledge of the basic properties of the Sun is essential. Here, only the most essential information will be given. For a detailed discussion, see e.g. Hey (2002).

Hale (1908) made the discovery of magnetic fields in the cooler, darker, planet-sized regions on the Sun known as sunspots. Today it is known that sunspots are the result of solar magnetic flux tubes piercing the photosphere (the visible surface) of the Sun. An effect known as magnetic buoyancy, described by Parker (1955), easily explains how this comes about. Magnetic buoyancy merely implicates that material inside of magnetic flux

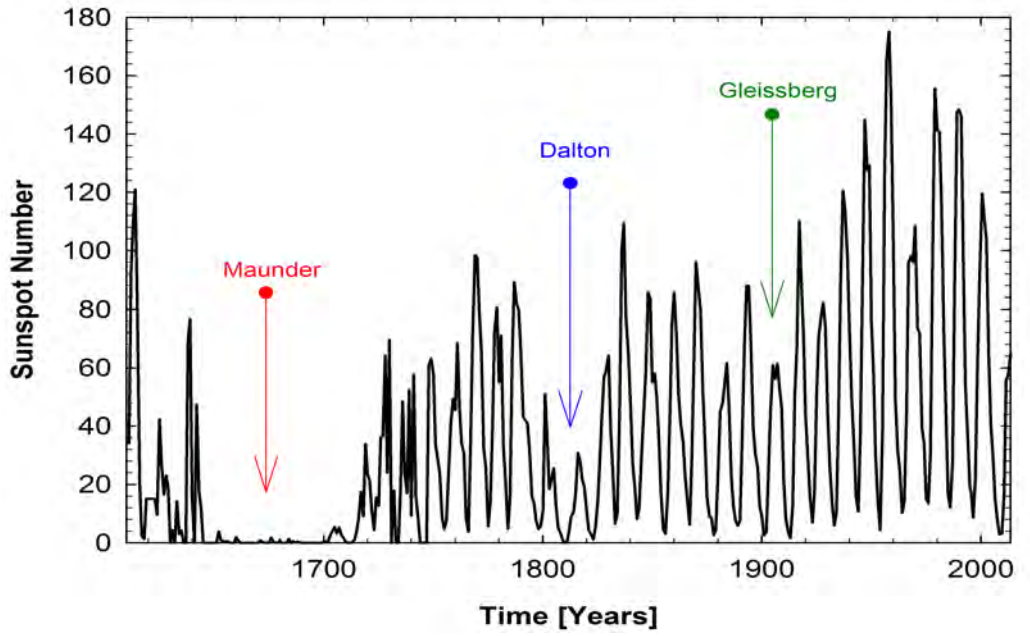


Figure 2.1: *The yearly averaged international SN dating from 1600 up to the present time. Three of the solar 'Grand Minima' are indicated. Data obtained from Solar Influences Data Analysis Center (http://sidc.be/index.php3).*

tubes, being less dense than the surrounding plasma, becomes buoyant and eventually pierces the photosphere, creating a sunspot or a pair of sunspots. By implication, such a pair of spots would have opposite polarity.

Recordings of the sunspot number (SN) have been kept since the 1600s, quantifying the number of sunspots visible on the solar surface at a given time. Figure 2.1 shows the yearly averaged SN as a function of time from 1600 until present. Keeping in mind the above explanation of the origin of sunspots, or the mechanism by which they are created, a correlation between the SN and the magnetic activity of the Sun is not surprising. A clear $\sim$ 11 year cycle in the SN is depicted in Figure 2.1, correlating to the solar cycle: every $\sim$ 11 years the Sun goes through a period of intense magnetic activity, called solar maximum; such a maximum period is marked by an increase in the SN, the magnetic field strength of the Sun and the occurrence of more transient events, e.g. solar flares and coronal mass ejections; solar maximum is followed by a decrease in solar activity towards solar minimum, a period marked by low SNs and magnetically quiet conditions on the Sun. The SN is therefore often employed as a proxy for solar activity. This $\sim$ 11 year solar activity periodicity causes a similar cycle in the properties of the heliosphere, as will be discussed in the rest of this chapter. For a comprehensive review of solar activity over millennia, see Usoskin (2013).

From Figure 2.1 it is also clear that there are epochs in which the overall recorded SN was very low. These periods are often called 'Grand Minima' and may serve as proxy for space climate conditions. As the SN and solar activity are correlated, the Grand Minima seem to correspond with a drop in global temperatures across the Earth (e.g. Calder, 1997; Soon and Yaskell, 2003; Svensmark and Calder, 2007). The Dalton and Gleissberg minima together with the most notable of the Grand minima, the Maunder Minimum extending from $\sim$ 1600 to $\sim$ 1710, are indicated in the figure. For a detailed discussion of the Maunder Minimum and its apparent implications for the Earth's climate, see e.g.

Soon and Yaskell (2003). Comprehensive reviews were also compiled by Scherer et al. (2005, 2006b).

## 2.3 The Solar Wind and Termination Shock

Some 50 years ago the concept of the SW, originally called "solar corpuscular radiation", was introduced to account for observations of comet tails always pointing radially away from the Sun; this fact could not be explained by mere solar radiation pressure (Biermann, 1961; see also Fichtner, 2001 and references therein). The nature of the SW was debated by scientists including Parker (1958), who described it as a supersonic magnetised fluid. Parker (1963) showed that the only way in which the Sun could remain in equilibrium was for the solar corona to expand at supersonic speeds, forming the SW. This can be shown by solving the hydrostatic equations for the Sun (e.g. Choudhuri, 1998). For a review of the early work done on the subject of the SW, the reader is referred to Parker (1961, 2001).

Due to the coronal origin of the SW, its composition is very similar, mainly containing protons, as observed by the Ulysses spacecraft (von Steiger et al., 2000). The coronal connection or coupling also leads to the SW structure largely depending on the coronal structure, which, in turn, is shaped by the magnetic field structure present in the corona. The solar magnetic field, therefore, dominates the original SW outflow.

The Sun's global magnetic field takes on its simplest form during solar minimum conditions. At such times two different types of coronal magnetic field structures can be distinguished: regions containing open magnetic field lines, and regions containing closed magnetic field lines. These structures eventually result in different SW and interplanetary magnetic field properties. When the field lines are closed they form perpendicular loops to the radial SW outflow and so inhibits the outflow. These regions give rise to the so-called slow SW streams and are generally found at low heliographic latitudes where the SW has typical values of $\sim 400$ km.s$^{-1}$ (Schwenn, 1983; Marsch, 1991). On the other hand, regions containing open magnetic field lines are less inhibiting to the radial SW outflow and give rise to the fast SW streams having typical values of $\sim 800$ km.s$^{-1}$. Such regions are found at higher heliographic latitudes, since the source of these open magnetic field lines are found to be the large unipolar coronal holes near the poles (e.g. Krieger et al., 1973).

This latitudinal dependence of the SW speed near solar minimum has been confirmed by measurements taken by Ulysses (e.g. Phillips et al., 1995) and is shown in Figure 2.2. The daily averaged SW speed measured by Ulysses during its three fast latitudinal scans (FLSs) is shown as a function of heliographic latitude. The first and third FLSs took place during times of solar minimum and are shown in the top panel of the figure (blue and green plots respectively); a clear latitudinal dependence in the SW speed profile is observed: the slow SW streams are seen in the equatorial region between $\sim 20°$ S and $\sim 20°$ N, whereas the fast SW streams are found at latitudes $\gtrsim 20°$ in both the Northern and Southern hemispheres. The approximated latitudinal dependence assumed for modeling purposes is also shown in Figure 2.2 (red curve). The remaining FLS occurred during solar maximum conditions and is illustrated in the bottom panel (orange plot). Under these circumstances there appears to be a mixture of fast and slow SW streams so that no well-defined SW speed profile is discernible (e.g. Richardson, 2001).

For the purposes of this study, the radial SW speed dependence is assumed to be relatively simple and corresponds to that found by Sheeley et al. (1997). These authors found that the SW, across all latitudes, accelerates within 0.1 AU from the Sun, after which it becomes a steady flow at 0.3 AU. Figure 2.3 shows the SW as a function

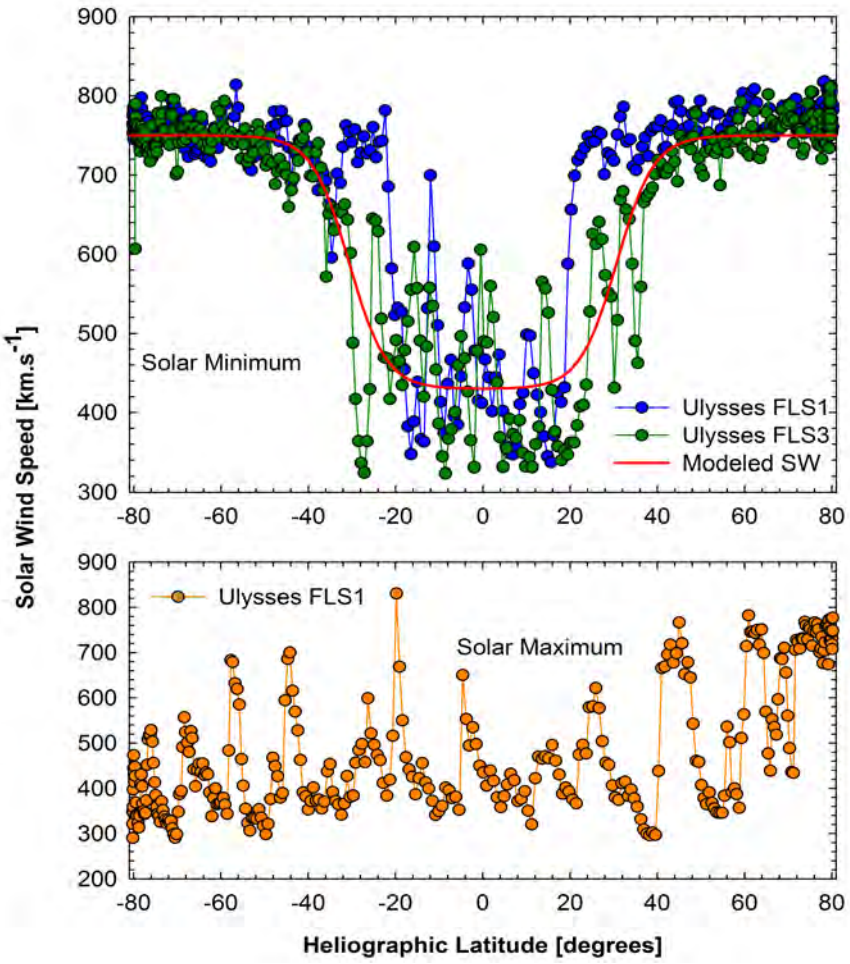


Figure 2.2: *The latitudinal dependence of the SW speed at solar minimum (top panel) and solar maximum (bottom panel). The first and third FLSs by Ulysses, represented by the blue and green plots respectively, show a clear latitudinal dependence for the SW during solar minimum. The second FLS, taken during solar maximum conditions and represented by the orange plot, shows no such latitudinal dependence. The red curve represents the SW model that gives the best approximation to the third FLS profile. Data obtained from http://cohoweb.gsfc.nasa.gov.*

of radial distance as measured by Pioneer 10 (green lines) and Voyager 2 (blue lines); measurements by Voyager 1 are not shown, since these only go up to November 1980 (http://cohoweb.gsfc.nasa.gov) because of a non-functional plasma detector. The relatively steady flow of the SW is clearly illustrated in Figure 2.3. The assumed SW speed profiles, as given below, are once again indicated in the figure, showing two modeled scenarios that correspond to the fast and slow SW profiles respectively (solid and dashed red curves). Note the sudden decrease in speed shown by the Voyager 2 measurements at $\sim$ 84 AU which corresponds to the termination shock (TS) crossing. As discussed in most text books on plasma physics (e.g. Choudhuri, 1998), the supersonic flow cannot steadily decelerate to a subsonic flow and this transition must always be discontinuous, i.e. a shock.

In order to model the SW profile and incorporate these results into a modulation model, the SW velocity $\vec{V}_{\rm sw}(r,\theta)$ is assumed to be directed radially outwards, and that

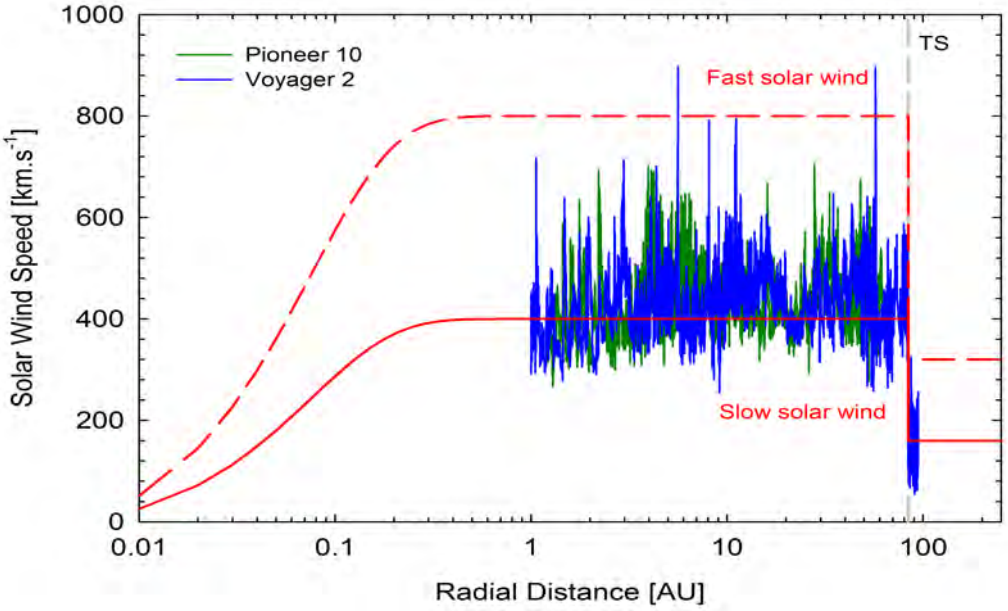


Figure 2.3: *The radial dependence of the SW speed. The green and blue plots show hourly averaged measurements by Pioneer 10 and Voyager 2 respectively. The red curves represent the modeled SW speed profiles, the solid and dashed lines corresponding to the fast and the slow SW respectively. The model includes a TS at 84 AU. Data taken from http://cohoweb.gsfc.nasa.gov.*

the radial and latitudinal dependencies are independent of each other so that

$$\vec{V}_{\rm sw}(r,\theta) \equiv V_{\rm sw}(r,\theta)\vec{\rm e}_r = V_0 V_r(r) V_\theta(\theta)\vec{\rm e}_r, \tag{2.1}$$

where $r$ is the radial distance from the Sun in AUs, $\theta$ is the polar angle (or co-latitude, with $\theta = 90^\circ$ defining the equatorial plane), $\vec{\rm e}_r$ the unit vector in the radial direction and $V_0 = 400$ km.s$^{-1}$. For solar minimum conditions the characteristic SW latitude dependence $V_\theta(\theta)$ (represented by the red curve in Figure 2.2) is given by

$$V_\theta(\theta) = 1.475 \mp 0.4 \tanh\left[6.8\left(\theta - \frac{\pi}{2} \pm \varphi\right)\right], \tag{2.2}$$

where the top and bottom signs correspond to the Northern (for $0 \leq \theta \leq \pi/2$) and Southern (for $\pi/2 \leq \theta \leq \pi$) hemispheres respectively. The purpose of the quantity $\varphi$ is to establish the polar angle at which $V_{\rm sw}$ begins to undergo transition from the slow to the fast SW speed and in this study it is given by $\varphi = \alpha + 15\pi/180$ where $\alpha$ is the HCS tilt angle or the angle between the rotational and magnetic axes of the Sun. As previously mentioned, there is no latitudinal dependence under solar maximum conditions and for such cases it is assumed that

$$V_\theta(\theta) = 1.0. \tag{2.3}$$

A similar approach to modeling the basic features of the SW was followed by e.g. Strauss (2010) and Vos (2011); apart from the numerical values of the parameters being altered, the approaches followed by e.g. Hattingh (1998) and Langner (2004) were also similar.

The radial dependence of the SW speed, $V_r(r)$, inside the TS can be modeled as

$$V_r(r) = 1 - \exp\left[\frac{40}{3}\left(\frac{r_\odot - r}{r_0}\right)\right], \tag{2.4}$$

with $r_\odot = 0.005$ AU the Sun's radius, and $r_0 = 1$ AU. This expression is superposed on the data in Figure 2.3 (solid and dashed red lines). To make provision for a decrease at the TS, the expression for the SW speed must be changed to

$$V_{\rm sw}(r,\theta) = V_{\rm sw}(r_{\rm TS},\theta)\frac{s+1}{2s} - V_{\rm sw}(r_{\rm TS},\theta)\frac{s-1}{2s}\tanh\left(\frac{r-r_{\rm TS}}{L}\right), \tag{2.5}$$

with $r_{\rm TS}$ the radial position of the TS, $L = 1.2$ AU the shock scale length, and $s = 2.5$ the shock compression ratio which is defined by $s = V_1/V_2$, where $V_1$ is the SW speed in the upstream region and $V_2$ is the speed in the downstream region. See e.g. Li et al. (2008) for a discussion about the properties of the TS. See also e.g. Marsch et al. (2003) for a review on the SW.

## 2.4 The Structure of the Heliosphere

In the previous section, the concept of the supersonically expanding SW was introduced. By this mechanism the Sun 'blows a bubble' into interstellar space; this bubble can be described as the sphere of influence of the Sun and is known as the heliosphere or, in astrophysical terms, the local astrosphere. This section discusses the structure and geometry of the heliosphere, albeit only in the most general terms. The reader is referred to e.g. Strauss (2013), Pogorelov et al. (2008, 2009) for detailed studies of global heliospheric properties. See also Fichtner and Scherer (2000) for an overview of the heliosphere.

As the Sun moves through interstellar space, the heliosphere interacts with the interstellar medium (ISM) so that, although still approximated by spherical geometry in most modulation models, the heliosphere is deformed into distinctive nose and tail regions, where the nose region is in the direction in which the heliosphere is moving. Figure 2.4 is a magneto-hydrodynamic (MHD) simulated meridional cut of the heliosphere from Strauss (2013). The assumed trajectories of the Voyager 1 and 2 spacecraft are also indicated, projected onto the same plane. The colour scales in the panels labeled (a) to (d) respectively indicate particle density, plasma speed, magnitude of the heliospheric magnetic field (to be discussed in the next section), and temperature. The ISM flow is from the right and the first notable structure to form is the bow shock (BS) at about 200 AU from the Sun in the nose direction along the equatorial plane (see also Pauls et al., 1995). The existence of the BS, however, is currently under investigation with McComas et al. (2012) indicating that the BS may be replaced with a much more extended bow wave region (see also Pogorelov et al., 2009); this is disputed, on the other hand, by Scherer and Fichtner (2014) in favor of the existence of the BS.

According to this figure, moving radially inward along the equatorial plane from the position of the BS, the heliopause (HP) is encountered at about 100 AU from the Sun. The HP separates solar from interstellar material and serves as the effective boundary between the heliosphere and the ISM. The region between the BS and the HP is known as the outer heliosheath. In Chapter 6 of this work, the HP and observations indicating that Voyager 1 had crossed the HP in August 2012 (see e.g. Webber et al., 2012 and Gurnett et al., 2013) are discussed. At about 75 AU in the equatorial plane, the supersonic SW decreases to subsonic speeds and the termination shock (TS) is formed. The region of the heliosphere between the HP and the TS is known as the inner heliosheath and; here it will most often simply be referred to as the heliosheath, since the outer heliosheath is largely neglected for the rest of this work. The existence of the TS was confirmed when Voyagers 1 and 2 respectively crossed into the heliosheath at distances of 94 AU in 2004 (Stone et al., 2005) and 84 AU in 2007 (Stone et al., 2008).

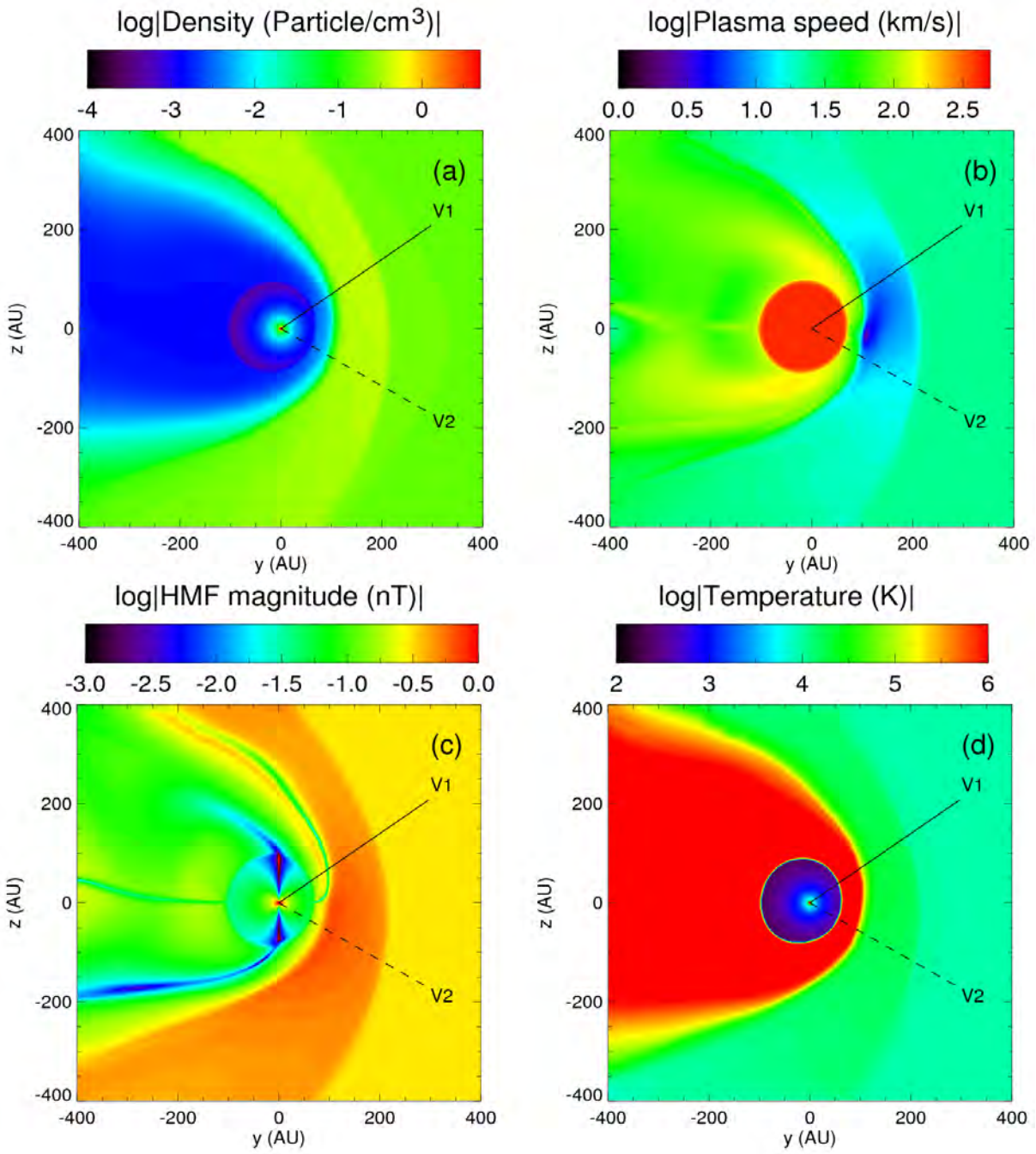


Figure 2.4: *The MHD modeled heliospheric environment in terms of particle density, plasma speed, magnitude of the heliospheric magnetic field, and temperature (panels labeled (a), (b), (c) and (d) respectively) in the meridional plane of the heliosphere. The ISM flow is directed towards the left and the approximate trajectories of the Voyagers 1 and 2 spacecraft (projected in the same plane) are indicated by the solid and dashed lines respectively. This figure was taken from Strauss (2013).*

The presentation of Figure 2.4 was merely to illustrate the structure of heliosphere, without going into the details of MHD modeling; MHD models are not considered in this study and only isolated references to these models will occur, with Chapter 6 featuring some MHD results in connection with the HP and the measurement of the pristine local interstellar spectrum (LIS) by Voyager 1. For a detailed discussion of this figure, see Strauss (2013).

## 2.5 The Heliospheric Magnetic Field

In Section 2.3 it was indicated that the Sun's magnetic field dominates the outflow of the corona near the solar surface. However, at a radial distance of about $2.5r_{\odot}$ (called the solar source surface), where the hydrodynamic pressure becomes greater than the magnetic pressure, the SW flow becomes radial and dominates the magnetic field. Because of the high conductivity of the SW plasma, the Sun's magnetic field gets frozen into or embedded in the SW, and is carried off into interplanetary space, forming the HMF. This process is discussed in detail by e.g. Kallenrode (2001) and Smith (2000, 2008).

Figure 2.5 shows the daily averaged HMF magnitude at Earth (green lines) as function of time from 1973 up to the present time. The yearly averaged SN (orange lines) is also included for comparison with the solar cycle. The HMF displays an $\sim$ 11 year cycle in its magnitude which is in sync with the SN, i.e. with the solar activity cycle. The HMF has an average magnitude of $\sim$ 5 nT at Earth during solar minimum conditions, and increases to $\sim$ 10 - 12 nT during solar maximum conditions. The so-called Hale cycle (epochs of opposite magnetic polarity) is also indicated in Figure 2.5: the HMF points outward from the northern hemisphere of the Sun during periods of $A > 0$ magnetic polarity, e.g. during the periods $\sim$ 1971 - $\sim$ 1982 and $\sim$ 1992 - $\sim$ 2003; during periods of $A < 0$ magnetic polarity however, the magnetic polarity reverses to point inwards in the northern hemisphere of the Sun as observed during e.g. $\sim$ 1982 - $\sim$ 1992 and $\sim$ 2003 - $\sim$ 2013. The HMF therefore exhibits both an $\sim$ 11 and $\sim$ 22 year cycle, i.e. its magnitude varies according to the $\sim$ 11 year solar cycle, whereas its polarity varies according to the $\sim$ 22 year Hale cycle. For a review on early developments relating to the HMF (previously called the interplanetary magnetic field), see Parker (2001).

### 2.5.1 Parker Heliospheric Magnetic Field

Since the Sun rotates about an axis perpendicular to the equatorial plane, the HMF should exhibit a spiral structure, called the Parker spiral (Parker, 1963). This spiral structure is illustrated in Figure 2.6. Parker's approach to describe the HMF followed MHD theory, thereby avoiding electric fields and currents. The Parker model is basically a SW hydrodynamic model in which the magnetic field is ignored as long as the acceleration of the coronal plasma is unaffected. The magnetic field is simply added to serve as a 'tracer' in the SW flow (e.g. Smith, 2008).

Parker (1958) first derived an analytical model to describe the HMF, summarised by the expression

$$\vec{B} = B_0 \left[\frac{r_0}{r}\right]^2 \left(\vec{\mathrm{e}}_r - \frac{\Omega(r - r_{\odot})\sin\theta}{V_{\mathrm{sw}}}\vec{\mathrm{e}}_{\phi}\right), \tag{2.6}$$

describing the Parker spiral, and is valid for $r > r_{\odot}$. More compactly, Eq. (2.6) can be written as

$$\vec{B} = B_0 \left[\frac{r_0}{r}\right]^2 (\vec{\mathrm{e}}_r - \tan\psi\vec{\mathrm{e}}_{\phi}), \tag{2.7}$$

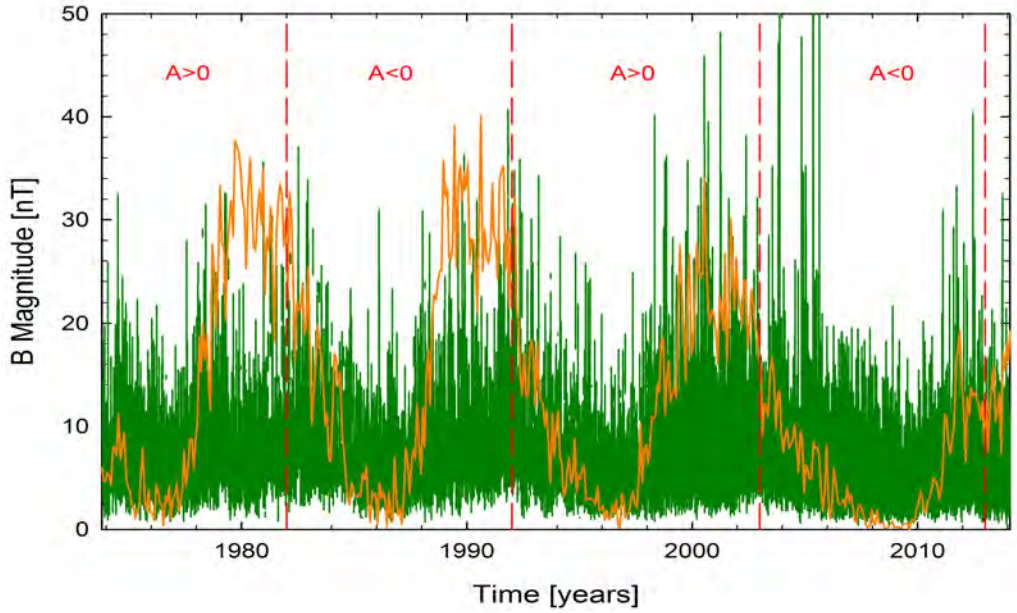


Figure 2.5: *The daily averaged magnitude of the HMF at Earth, showing the dependence of the HMF magnitude on the solar cycle (green lines). The monthly averaged SN is also shown (orange lines) for comparison with the solar cycle. Epochs of opposite magnetic polarity are indicated by the vertical dashed red lines. HMF data taken from NSSDC COHOWeb: http://cohoweb.gsfc.nasa.gov.*

where $\vec{e}_r$ and $\vec{e}_\phi$ are unit vectors in the radial and azimuthal directions respectively. $B_0$ is the HMF magnitude at $r_0 = 1$ AU (i.e. at Earth), $\Omega = 2.66 \times 10^{-6}$ rad.s$^{-1}$ is the average angular rotation speed of the Sun, and $V_{\rm sw}$ is the SW speed, with $\psi$ the Parker spiral angle or "garden hose" angle, defined as the angle between the radial direction and the direction of the average HMF at any given position. This angle can be expressed as

$$\tan\psi = \frac{\Omega(r - r_\odot)}{V_{\rm sw}} \sin\theta. \tag{2.8}$$

These expressions are consistent for an HMF structure of Archimedean spirals lying on cones of constant heliographic latitude, as shown in Figure 2.6. In the equatorial plane, the spiral angle $\psi$ at Earth is typically 45°, after which it increases with distance to 90° at $r \gtrsim 10$ AU.

Much can be gleaned from simplified expressions describing only the magnitude of the HMF. The HMF magnitude follows directly from Eq. (2.7), and is given by

$$B = B_0 \left[\frac{r_0}{r}\right]^2 \sqrt{1 + \tan^2\psi}. \tag{2.9}$$

From Eq. (2.9) it is evident that $B$ decreases as $r^{-2}$ in the polar regions. However, this causes drift effects (to be discussed in Chapter 3) to be grossly over-estimated in the these regions, as in the modeling by Jokipii and Kopriva (1979). Therefore, as explained in the following sections, the Parker field (PHMF) is modified in the polar regions, changing the $B \propto r^{-2}$ dependence to $B \propto r^{-1}$ instead. This effectively remedies the situation. From a physics point of view, these modifications are backed up by the known fact that, since the solar surface near the poles are granular and turbulent regions that constantly change with time, the radial magnetic field lines in these regions are in a state of unstable

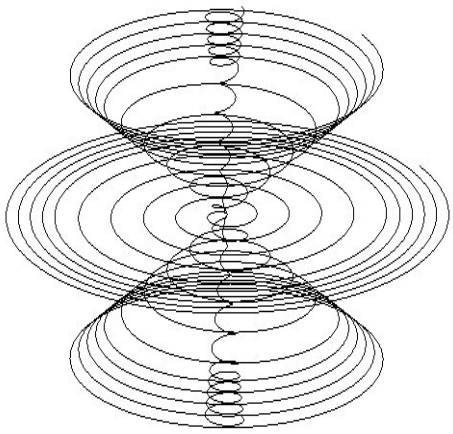

Figure 2.6: *A representation of the Parker magnetic field's spiral form at polar angles of* $\theta = 5°$ *and* $\theta = 175°$, $\theta = 45°$ *and* $\theta = 135°$, *and* $\theta = 90°$ *respectively. The Sun is in the middle of the figure. At the radial distance where the TS in encountered, the HMF lines are compressed upon entering the heliosheath due to the slow down of the SW flow.*

equilibrium; this turbulence then results in transverse magnetic field components which regularly lead to deviations from the smooth Parker field geometry in the polar regions (Jokipii and Kóta, 1989; Forsyth et al., 1996). The net effect is an average magnetic field magnitude that is larger in the polar regions than in regions further away from the poles.

### 2.5.2 Jokipii-Kóta Modified Field

Jokipii and Kóta (1989) showed that the effect of small perpendicular magnetic field components near the solar surface leads to a larger magnetic field at greater radial distances in the polar regions. These authors argued that the average direction of these small components would cancel out so that only the magnitude of the magnetic field is modified. They put forward the following modified expression for the Parker spiral field

$$B = B_0 \left[\frac{r_0}{r}\right]^2 \sqrt{1 + \left(\frac{\Omega(r - r_\odot)\sin\theta}{V_{\rm sw}}\right)^2 + \left(\frac{r\delta}{r_\odot}\right)^2}, \tag{2.10}$$

introducing the quantity $\delta$ to signify the magnitude of the extra, superimposed, transverse magnetic field. The Jokipii-Kóta modification is henceforth referred to as the JKM, while the term containing $\delta$ will be referred to as the JKM modification term. However, upon this modification, the requirement that the magnetic field remains divergence free, i.e. $\nabla \cdot \vec{B} = 0$, is no longer complied with and therefore the JKM is technically incorrect. Steenberg (1998) stated that the magnetic field will remain divergence free if $\delta = \delta(\theta) \propto (\sin\theta)^{-1}$, so that

$$\delta(\theta) = \frac{\delta_{\rm m}}{\sin\theta}, \tag{2.11}$$

with $\delta_{\rm m} = 8.7 \times 10^{-5}$ (see also Langner, 2004). This value for $\delta_{\rm m}$ implies $\delta(\theta) = 0.002$ near the poles and $\delta(\theta) \approx 0$ in the ecliptic plane. The effect of this modification, therefore, is

to bring about the changes required in the polar regions, without noticeably altering the field in the equatorial plane. Geometrically speaking, a cone centered around the polar regions is induced in which the HMF is increased so as to decrease as $r^{-1}$ instead of $r^{-2}$.

Comparisons of the JKM, as given in Eq. (2.10), with the PHMF are carried out in Chapter 5. For applications where $\delta(\theta) = 0.002$ throughout all heliolatitudes, see e.g. Haasbroek and Potgieter (1995), Jokipii et al. (1995), Hattingh (1998), Potgieter and Ferreira (1999), Potgieter (2000) and Moeketsi (2004). See also Moraal (1990) for a modification that incorporates the same compensating physical effects as the JKM.

### 2.5.3 Smith-Bieber Modified HMF

Smith and Bieber (1991) analyzed data collected by various satellites and found magnetic field spirals at Earth more tightly wound than that predicted by the Parker theory. Consequently, they suggested a modification to the Parker spiral by reasoning that the difference in rotational speed of the equatorial and polar regions of the Sun would cause small azimuthal magnetic field components to develop. This would lead to larger spiral angles at larger radial distances, and would provide an explanation for the larger spiral angles at Earth. At the same time, this modification would have a significant effect on the HMF structure at the high latitude regions.

These authors modified the expression for the spiral angle, arriving at

$$\tan\psi = \frac{\Omega(r-b)\sin\theta}{V_{\rm sw}(r,\theta)} - \frac{r}{b}\frac{V_{\rm sw}(b,\theta)}{V_{\rm sw}(r,\theta)}\left(\frac{B_{\rm T}(b)}{B_{\rm R}(b)}\right), \tag{2.12}$$

where $B_{\rm T}(b)/B_{\rm R}(b)$ is the ratio of the azimuthal to the radial magnetic field components at a position $b$ near the solar surface, here taken as $b = 20r_{\odot}$. Smith and Bieber (1991) showed that the value of $B_{\rm T}(b)/B_{\rm R}(b)$ is approximately -0.02 and although the value of $b$ assumed here is larger than the original $b = 5r_{\odot}$ assumed by these authors, the value of -0.02 is retained for the purposes of this study.

According to Eq. (2.12), the Smith-Bieber modification (SBM) alters the direction of the PHMF by winding up the magnetic field spirals more tightly; as a consequence, in contrast to the straight line case of Eq. (2.8), the HMF still has an azimuthal component in the polar regions, even at $\theta = 0^{\circ}$.

This modification will be compared with the JKM and PHMF in Chapter 5. The SBM in particular is further illustrated and implemented in Chapter 5; it is also implemented in Chapter 6 where the numerical model of this study is applied in the reproduction of PAMELA proton data. For other implementations of the SBM, see Haasbroek (1993), Haasbroek et al. (1995), and Minnie (2002).

### 2.5.4 Fisk type magnetic fields

Models for the HMF yielding Archimedean Parker spirals are set up under the assumption that the Sun rotates rigidly about its axis. However, e.g. Snodgrass (1983) asserted that the Sun actually undergoes differential rotation where the solar poles rotate $\sim 20\%$ slower than the solar equator (the former and latter of which have rotation periods of $\sim 25$ days and $\sim 32$ days respectively). If it is assumed that the HMF footpoints are connected to the photosphere, they too will undergo differential rotation. Fisk (1996) pointed out that a correction must be made to the Parker spiral model in order to account for this, and put forward a model aptly called the Fisk HMF. In the Fisk model the HMF footpoints undergo a double precession: the rigid rotation of the HMF about the solar magnetic axis (at rate $\Omega$), and the latitude dependent differential rotation $\omega$ about a virtual axis inclined

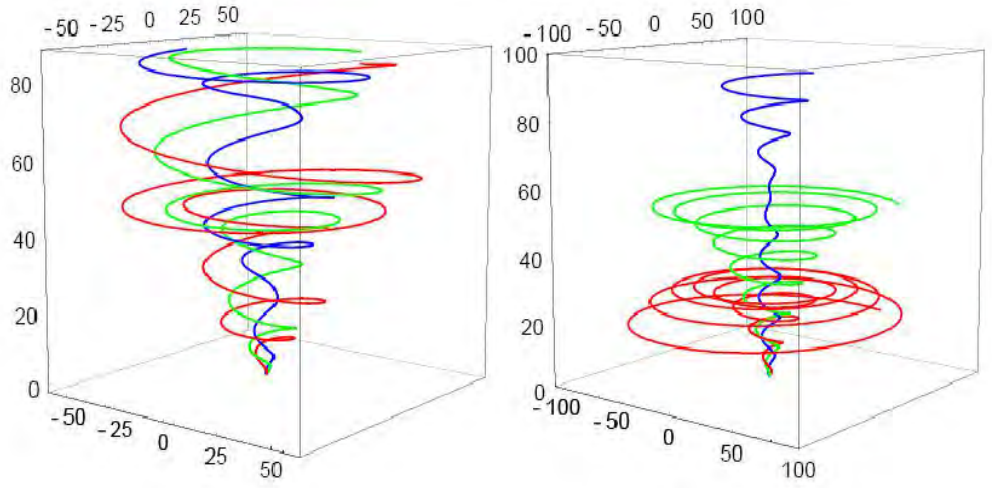


Figure 2.7: *A representation of the Fisk HMF. The left panel shows a Fisk type I field, while the right panel shows a type II field. All the HMF field lines originate at a co-latitude of 30°, but at different longitudes. This figure was taken from Burger and Hattingh (2001).*

at an angle $\beta$ with respect to the solar rotational axis. See e.g. Burger and Hattingh (2001), Burger (2005), Krüger (2005), and Engelbrecht (2008) for detailed discussions on the Fisk field.

The components of the Fisk field are (Zurbuchen et al., 1997)

$$\begin{aligned} B_r &= B_0 \left[\frac{r_0}{r}\right]^2 \\ B_\theta &= B_r \frac{r - r_{ss}}{V_{sw}} \sin\beta_F \sin\left(\phi + \frac{\Omega(r - r_{ss})}{V_{sw}}\right) \\ B_\phi &= B_r \frac{r - r_{ss}}{V_{sw}} \left[\omega \sin\beta_F \cos\theta \cos\left(\phi + \frac{\Omega(r - r_{ss})}{V_{sw}}\right) + \sin\theta(\omega\cos\beta_F - \Omega)\right], \end{aligned} \quad (2.13)$$

where $r_{ss}$ is the radius of the solar source surface. This set of equations describes what is known as the type I Fisk field (see Burger and Hattingh, 2001; Burger, 2005). The type I Fisk field simplifies to the type II Fisk field when $\beta_F = 90°$. A schematic representation of the Fisk HMF is shown in Figure 2.7, where the HMF field lines all originate at co-latitude 30° but at different latitudes. Both Fisk type I and Fisk type II HMF configurations are shown.

Burger and Hitge (2004) proposed a modification to the Fisk field that is known as the Fisk-Parker hybrid field. This modification models the HMF part Parker HMF (being purely Parker in the equatorial regions) and part Fisk HMF (being purely Fisk near the polar regions. In between the equatorial and polar regions the HMF is a combination of the two models. See e.g. Burger and Hatting (2001) and Burger et al. (2008) for a detailed discussion on this HMF model.

The existence of the Fisk HMF might be supported by a tilt angle varying in time, causing regular meridional HMF components (Kóta, 1997, and Kóta, 1999). However, no direct observational evidence has been found to indicate that the HMF indeed has this complex configuration (Roberts et al., 2007). Today, the existence of the Fisk HMF model is still a controversial matter (e.g. Sternal et al., 2011). Furthermore, the Fisk field is inherently three dimensional and time dependent and the accompanying increase in complexity upon incorporating such an HMF configuration is beyond the scope of study for this work.

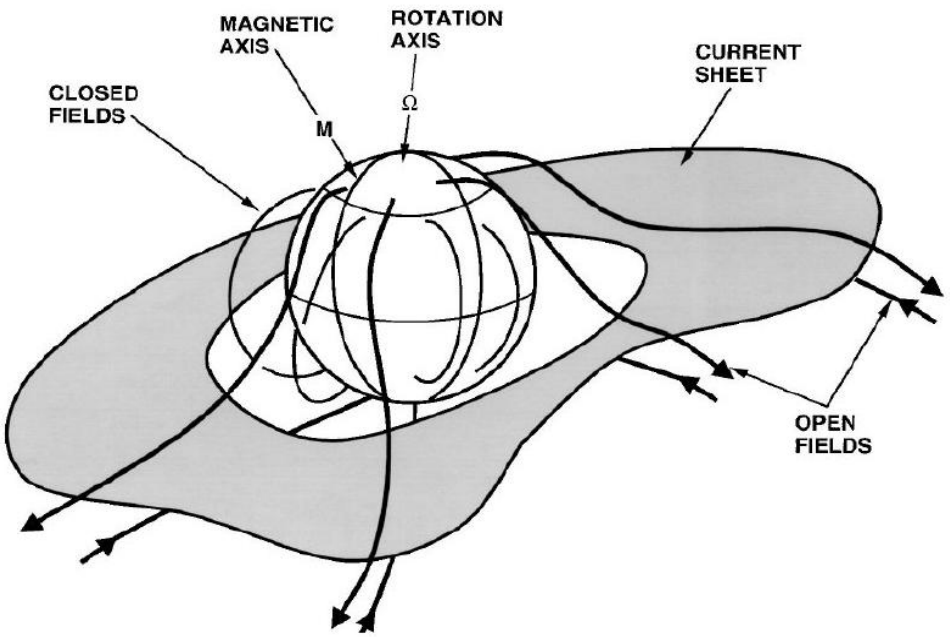


Figure 2.8: *A schematic representation of the HCS. The sheet separates opposingly directed open magnetic field lines originating from the Sun. The HMF below and above the HCS still develops the Parker spiral form. Taken from Smith (2001).*

## 2.6 The Heliospheric Current Sheet

The HCS is an important co-rotating structure in the heliosphere, acting as the heliospheric magnetic equator, i.e. it divides the HMF into hemispheres of opposite polarity. Its formation is the consequence of oppositely directed open magnetic field lines originating in the higher latitudinal regions from both the Northern and the Southern hemispheres; these open magnetic field lines then meet to form the HCS, after having been dragged towards the ecliptic plane. This is illustrated in Figure 2.8. In such a situation, Maxwell's equations require the existence of a neutral sheet to separate the two regions of oppositely directed field lines (Smith, 2001). This implies a jump in polarity when crossing the HCS and these effects were first observed from the early Pioneer missions (Smith, 1989). Furthermore, observations from e.g. Burlaga and Ness (1993) suggest that the HCS can cover the entire extent of the heliosphere during the course of the solar activity cycle. For a detailed review on the HCS, see Smith (2001).

As mentioned earlier, the rotational and magnetic axes of the Sun are misaligned by the tilt angle $\alpha$ (e.g. Hoeksema, 1992), so that the HCS is not flat, but warped into the form of a "ballerina skirt". The tilt angle is computed by applying models to solar field maps, such as the synoptic charts shown in Figure 2.9. Such synoptic charts of the magnetic field strength and polarity are also probably the best type of observational evidence to illustrate the existence of the HCS. The charts in Figure 2.9 are for the solar source surface at about $r = 2.5r_{\odot}$ and are obtained from the Wilcox Solar Observatory (http://wso.stanford.edu). These charts depict measurements for both the Northern and Southern hemispheres during a period of low solar activity (top panel), in December 1995, and a period of high solar activity (bottom panel), in April 1998. The HCS is indicated by the bold black contour and separates the regions of opposite polarity indicated by the different shades of grey. From these charts, the wavy structure of the HCS is clearly illustrated and this waviness is evidently more pronounced at high levels of solar activity.

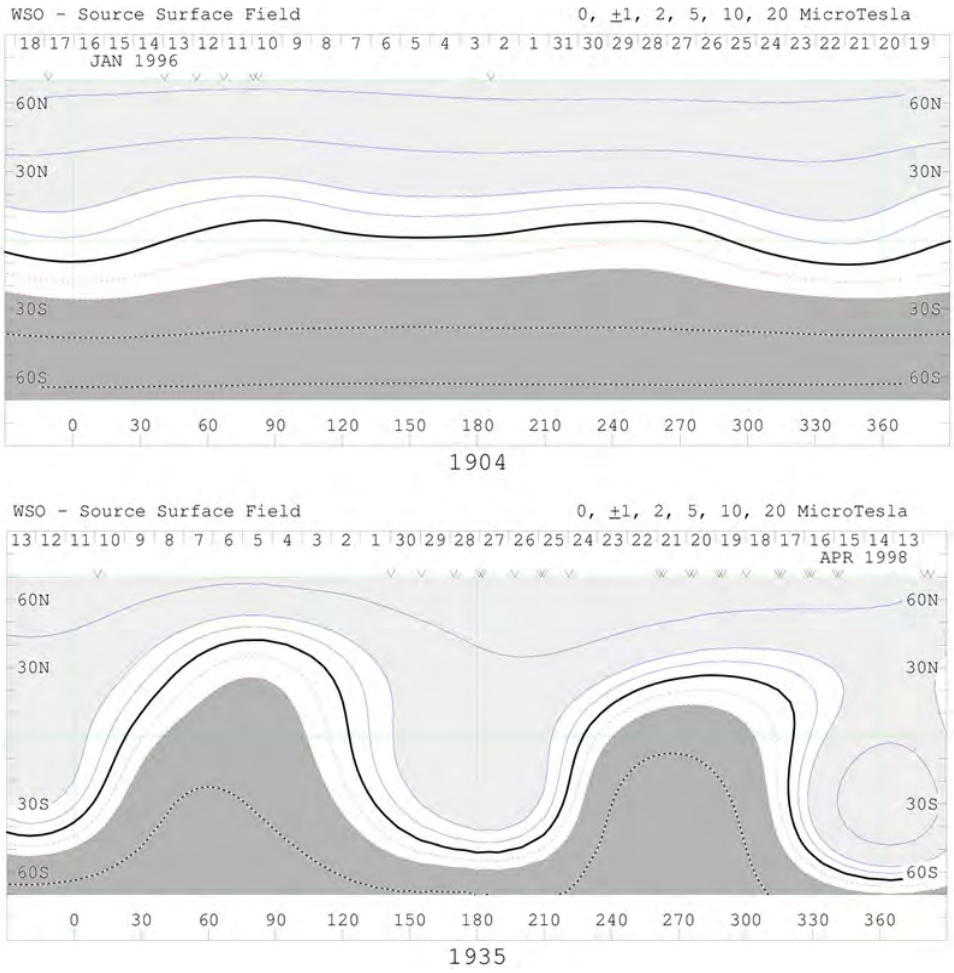


Figure 2.9: *Contour maps of the solar source surface (assumed to be at a radial distance of $r = 2.5r_{\odot}$, showing the magnetic polarity. The top panel corresponds to solar minimum conditions (December 1995 or Carrington rotation 1904), while the bottom panel corresponds to solar maximum conditions (April 1998 or Carrington rotation 1935). The HCS is represented by the thick black line, while the different shades of grey is indicative of the different polarities. This figure was obtained from the Wilcox Solar Observatory at http://wso.stanford.edu, courtesy of J.T. Hoeksema.*

The waviness of the HCS, as represented by $\alpha$, varies with solar activity. This time dependence of $\alpha$ is shown in Figure 2.10, computed from surface field maps by two different tilt angle models. The $\sim 11$ year solar activity cycle is distinguished clearly, with $\alpha \sim 10^{\circ}$ during solar minimum conditions, but increasing to $\alpha \gtrsim 70^{\circ}$ during periods of solar maximum. The HCS tilt angle is most often used as a proxy for solar activity in modulation models and, in this work, also features prominently in this capacity (see Chapter 5).

An expression for the HCS was derived by Jokipii and Thomas (1981), given by

$$\theta^{'} = \frac{\pi}{2} + \sin^{-1}\left[\sin\alpha \sin\left(\phi + \frac{\Omega(r - r_{\odot})}{V_{\rm sw}}\right)\right], \tag{2.14}$$

with $\theta^{'}$ the polar extent of the HCS and $\phi$ the azimuthal angle. This expression, was used by e.g. Hattingh (1998) for cases where $\alpha \leq 25^{\circ}$. Another expression is given by Kóta and Jokipii (1983)

$$\theta^{'} = \frac{\pi}{2} - \tan^{-1}\left[\tan\alpha \sin\left(\phi + \frac{\Omega(r - r_{\odot})}{V_{\rm sw}}\right)\right], \tag{2.15}$$

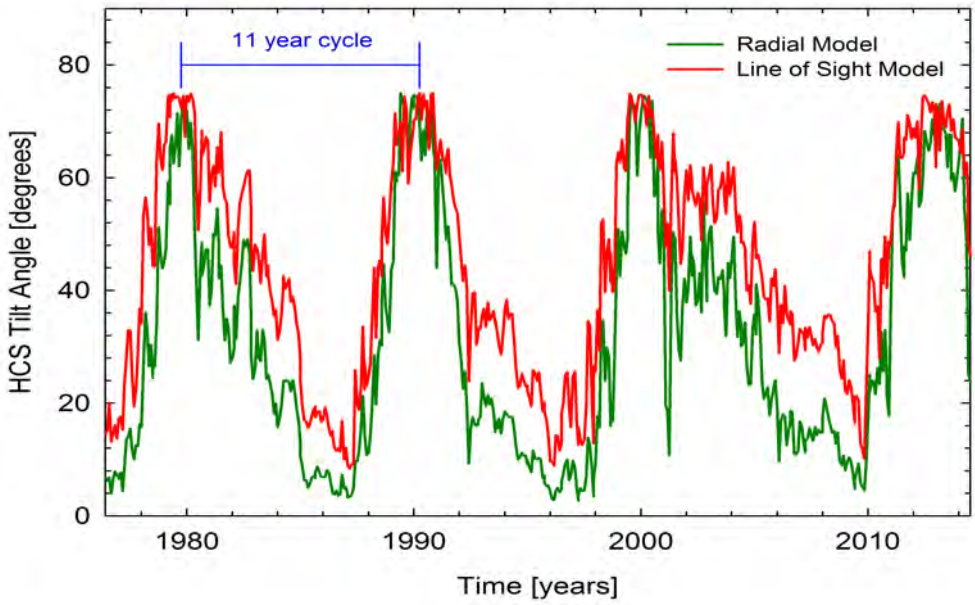


Figure 2.10: *The computed tilt angle $\alpha$ as a function of time from 1976 until present. Tilt angle values calculated by the so-called radial model are represented by the green lines, whereas the red lines show the tilt angle calculated from the line-of-sight model. Data obtained from the Wilcox Solar Observatory at http://wso.stanford.edu.*

and was used by e.g. Langner (2004), who showed that this expression was generally valid up to tilt angles as large as 75°. These two different expressions for the latitudinal extent of the HCS are compared and studied in Chapter 5.

Figure 2.11 shows simulations of the HCS, according to Eq. (2.14), at four different values of the tilt angle $\alpha$ over the first 10 AU of the heliosphere. The three-dimensional (3D) wavy structure of the HCS is clearly illustrated and the waviness is seen to increase as the tilt angle is increased.

In order to incorporate the HCS into the HMF, Eq. (2.7) must be modified to

$$\vec{B} = qA_{\rm c}B_0 \left[\frac{r_0}{r}\right]^2 (\vec{e}_r - \tan\psi\vec{e}_\phi)\left[1 - 2H(\theta - \theta')\right], \tag{2.16}$$

with $q$ the particle charge and $A_{\rm c}$ indicating the magnetic polarity cycle, i.e. $A_{\rm c} \equiv +1$ and $A_{\rm c} \equiv -1$ for the $A > 0$ and $A < 0$ cycles respectively. The function $H(\theta - \theta')$ is the Heaviside step function, given by

$$H(\theta - \theta') \equiv \begin{cases} 0 & \text{when} \quad \theta < \theta' \\ \\ 1 & \text{when} \quad \theta > \theta', \end{cases} \tag{2.17}$$

and causes the HMF polarity to change across the HCS.

## 2.7 Cosmic Rays and Solar Modulation

Cosmic rays are energetic particles which, after being accelerated to very high velocities, propagate throughout the Galaxy. During the historic balloon flights of Viktor Hess in 1911 and 1912 (Hess, 1912), it came to light that the origin of these particles was

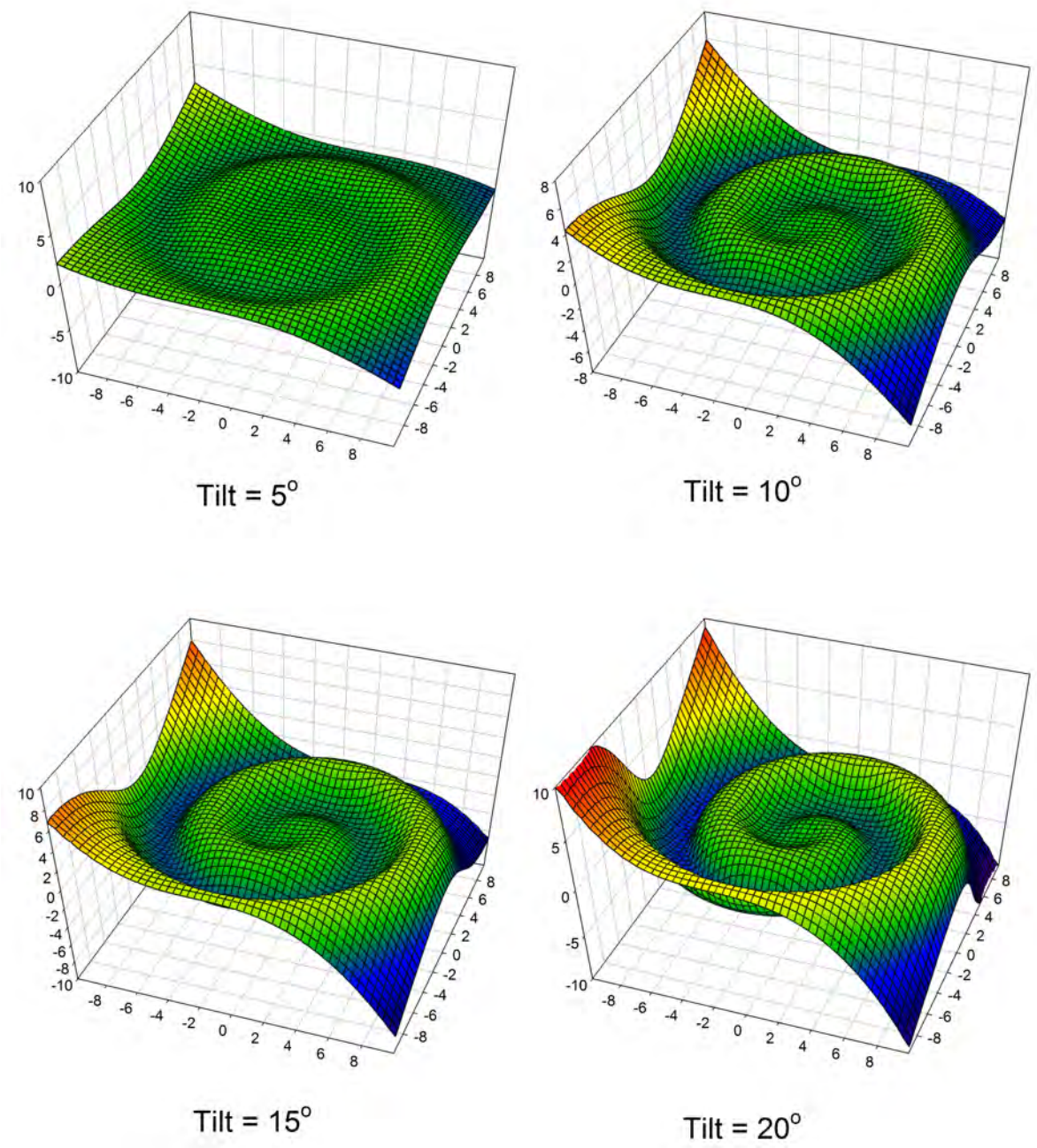


Figure 2.11: *Simulations of the HCS for different tilt angles using Eq. (2.14). The simulations are carried out for the first 10 AU of the heliosphere, with the Sun at the center and for tilt angles of* $\alpha = 5^\circ$ *(top left panel),* $\alpha = 10^\circ$ *(top right panel),* $\alpha = 15^\circ$ *(bottom left panel) and* $\alpha = 20^\circ$ *(bottom right panel).*

extraterrestrial. In 1925 Millikan coined the name "cosmic rays" for these particles and by 1930 Compton and Clay had shown that CRs were electrically charged (for a review see e.g. Simpson, 1998 and Carlson, 2012).

Those CRs that reach Earth are mainly composed of $\sim$ 98 % atomic nuclei (most of which are protons) and $\sim$ 2 % electrons, positrons, and anti-protons, along with small abundances of heavier nuclei (e.g. Longair, 1990; Simpson, 1992).

### 2.7.1 Classification of Cosmic Rays

CRs are generally classified in four major populations, according to their origin. The first of these groups under discussion here, and also the group of importance for this study, is galactic cosmic rays (GCRs). These particles originate from far outside the solar system where they are accelerated by supernovae explosions and consequently distributed over energies from a few hundred keV to as high as $3 \times 10^{21}$ eV (e.g. Koyama et al., 1995, and Tanimori et al., 1998). Ginzburg and Syrovatskii (1969) suggested that GCRs probably originate not only from such explosions, but also from supernovae remnants which may include neutron stars. Direct evidence of particle acceleration in supernovae remnants is obtained from non-thermal radio, X-ray, and gamma-ray radiation (e.g. Ptuskin, 2005). The energy spectrum of GCRs takes on the form of a power law $j \propto E^{-\gamma}$; here, $\gamma \approx 2.6$ is the spectral index, $E$ the kinetic energy in MeV.nucleon$^{-1}$, and $j$ is the differential intensity, usually measured in units of particles.MeV$^{-1}$.m$^{-2}$.s$^{-1}$.sr$^{-1}$. At energies below $\sim$ 30 GeV (e.g. Strauss and Potgieter, 2014a) solar modulation effects become increasingly important so that GCRs measured at Earth no longer have a spectral index of $\gamma \approx 2.6$.

A second group of cosmic rays is known as solar energetic particles (SEPs). These originate from either the solar corona or regions close to the Sun and are related to solar flares (e.g. Forbush, 1946) and coronal mass ejections (CMEs). Shocks in the interplanetary medium can also produce these energetic particles (see e.g. Cliver, 2000; Reames, 2013). Solar energetic particles have energies at the lower end of the spectrum up to several hundred MeV. These particles are not important for the purposes of this study and are consequently ignored.

The third population of CRs is known as the anomalous component of cosmic rays (ACRs). Since these particles enter the heliosphere as neutral interstellar atoms, they are initially unaffected by the HMF. Close to the Sun, however, they become singly ionised through photo-ionisation (Pesses et al., 1981) or through charge-exchange occurring mainly in the heliosheath (Fahr et al., 2000). The resulting ions are then "picked up" by the HMF and transported to the solar wind TS; they are now aptly called pick-up ions. At the TS they are accelerated up to energies of $\sim$ 100 MeV through a process of first order Fermi acceleration, gaining energy by multiple crossings of the TS. (See e.g. Fichtner, 2001 for a review; see also Strauss, 2010). This group of CRs does not feature prominently in this work and is only mentioned where applicable.

A group of CRs called Jovian electrons is the fourth and final population of CRs. Jovian electrons originate from the magnetosphere of Jupiter and were discovered in 1973 by Pioneer 10 during the Jupiter fly-by. It is well known that the magnetosphere of Jupiter is a relatively strong source of electrons at energies $\sim$ 30 MeV (e.g. Simpson et al., 1974, and Chenette et al., 1974). When released into the interplanetary medium, Jovian electrons dominate these low energy electron intensities within the first $\sim$ 10 AU from the Sun. For a detailed study of the transport of Jovian electrons in the heliosphere, see Ferreira (2002). These particles are not a topic of this work and only a few references will occur where needed.

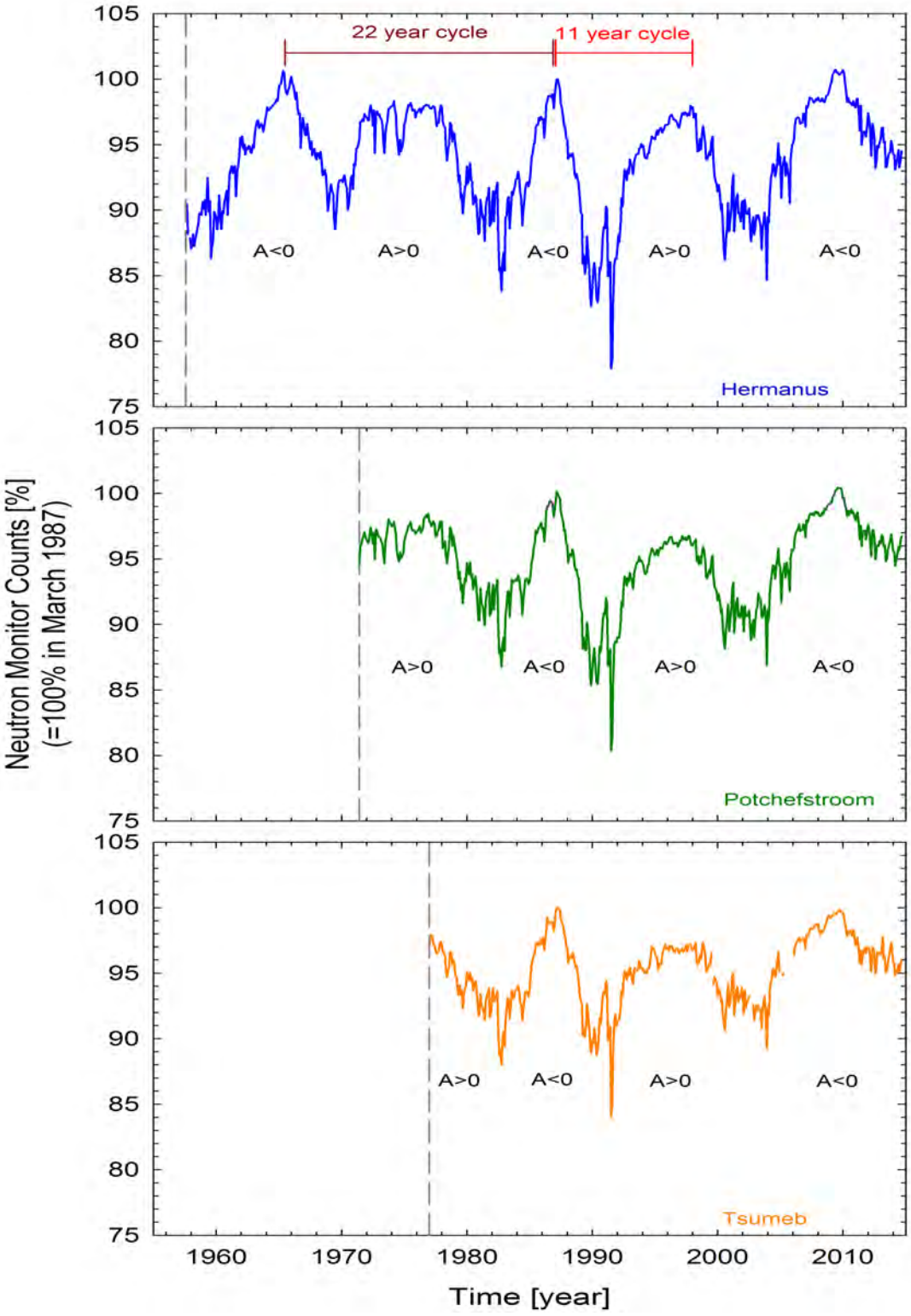


Figure 2.12: *Cosmic ray count rate as a function of time (normalised to 100% in March 1987). Measurements from neutron monitors in Hermanus, Potchefstroom and Tsumeb are shown in the top, middle and bottom panels respectively. The ∼ 11 year and ∼ 22 year cycles are indicated in the top panel. The vertical dashed lines indicate the beginning of data in each case. Data obtained from http://www.nwu.ac.za/neutron-monitor-data.*

### 2.7.2 Solar Modulation of Cosmic Rays

Cosmic rays are observed at Earth after traveling through the heliosphere and being modulated by all the physical processes to be explained in Chapter 3. When a CR enters the atmosphere of the Earth, it can collide with an atmospheric molecule to subsequently produce a shower of multiple particles. Neutron monitors on Earth then detect these secondary particles to give an indication of the CR flux at Earth.

Figure 2.12 shows an example of a long term record of neutron monitor count rates at ground or sea level. The top panel shows the count rate of the Hermanus neutron monitor from 1957 up to present, while the middle and bottom panels show measurements by the neutron monitors in Potchefstroom and Tsumeb respectively; the cutoff rigidities of these neutron monitors are $\sim 4.58$ GV, $\sim 6.94$ GV and $\sim 9.15$ GV respectively. The count rate in each case has been normalised to 100% in March 1987 and two long term cycles are evident in this figure: an $\sim 11$ year cycle which is anti-correlated with solar activity, i.e. high CR counts at Earth during solar minimum conditions, as well as an $\sim 22$ year cycle, related to the Hale cycle through the HMF polarity; these are indicated in the top panel.

Large, steplike decreases and increases in the intensity are also in evidence; these decreases are believed to be related to transient solar events through propagating diffusion barriers forming co-rotating interaction regions and larger structures known as global merged interaction regions. These large transients are not studied in this work. For more details, see e.g. Fujii and McDonald (1995), le Roux and Potgieter (1991, 1995), and Potgieter and Ferreira (2001). See also reviews by Potgieter (1993, 1997), Potgieter et al. (2001), and Heber and Potgieter (2006).

## 2.8 Selected Spacecraft Missions

This section gives a brief description of the spacecraft missions that are most relevant for this study.

### 2.8.1 PAMELA – Payload for Antimatter Matter Exploration and Light-nuclei Astrophysics

Though the primary scientific goal for PAMELA (Payload for Antimatter Matter Exploration and Light-nuclei Astrophysics) is to study the antimatter component of the cosmic radiation at Earth (Picozza et al., 2007), the PAMELA detector is of particular interest in this study for its measurement of the GCR proton spectra at Earth, specifically for the time interval 2006 to 2009. See e.g. Vos (2011), Adriani et al. (2013, 2014), Ndiitwani et al. (2013), Potgieter et al. (2014) and Zhao et al. (2014).

The PAMELA detector has been orbiting the Earth since June 15th, 2006. It is housed inside a pressurised container attached to a Russian Resurs-DK1 Earth-observation satellite that was launched into space by a Soyuz-U rocket from the Baikonur cosmodrome in Kazakhstan. The satellite is orbiting the Earth in an elliptical quasi-polar orbit at altitudes varying between 350 km and 600 km and with an inclination of 70° (Picozza et al., 2007). The instrument is built around a 0.43 nT permanent magnet spectrometer and is comprised of a number of sub-detectors capable of detecting CR particles and to provide accurate information about particle charge, mass, momentum and rigidity over a wide energy range (see e.g. Casolino et al., 2008 and references therein).

Except for the study of the antimatter and galactic components of CRs, PAMELA is also well equipped for other studies relating to the solar modulation of CRs. The detection of SEPs also forms a key field of interest to be studied during the duration of the PAMELA

mission. For an extensive review of the PAMELA mission and its accomplishments up to the present time, see Adriani et al. (2014).

### 2.8.2 Voyager 1 and 2

The NASA (National Aeronautics and Space Administration) twin spacecraft, Voyager 1 and Voyager 2, were launched in September and August of 1977 respectively. The Voyager 2 spacecraft encountered the planets Jupiter, Saturn, Uranus and Neptune on its way out of the solar system. Voyager 1 encountered Jupiter and Saturn. Completing their primary mission of planetary exploration, the Voyager 1 and 2 spacecraft are currently − and have been for some time − the most distant human made objects in space, respectively at $\sim$ 130 AU and $\sim$ 106 AU away from the Sun, roughly in the nose direction of the heliosphere, and traveling at a speed of $\sim 3.6$ AU.year$^{-1}$ (current positions obtained from http://voyager.jpl.nasa.gov/where). Voyager 1 is situated at 34.4° above the equatorial plane, while Voyager 2 is situated at 28.8° below the equatorial plane of the Sun.

Equipped with e.g. magnetic field, plasma, CR and low energy CR instruments on board, the Voyager spacecraft started with the second part of their mission, the 'Voyager interstellar mission', in 1989, with the goal of exploring the local interstellar medium (LISM). These spacecraft have in the meantime encountered the TS in December of 2004 and August of 2007 respectively (Stone at al., 2005; Burlaga et al., 2008). Recently, in August of 2012, Voyager 1 crossed the HP and has started its sampling of the LISM. This is discussed in more detail in Chapter 6, since the HP crossing is of particular interest for the determination of the local interstellar spectrum (LIS) that was used in this work.

## 2.9 Summary

This chapter introduced the relevant terms and concepts needed to understand the basics of the heliospheric modulation of cosmic rays (CRs). Section 2.2 explained the magnetic nature of the Sun and introduced the sunspot number (SN) as a proxy for solar magnetic activity. The SN since 1600 up to the present time was shown in Figure 2.1, thereby illustrating the $\sim$ 11 year magnetic activity cycle of the Sun.

The concept of the solar wind (SW) was introduced in Section 2.3, where it was explained that, in order for the Sun to remain in equilibrium, the solar corona must expand from the Sun to form the SW. The latitudinal profile of the SW speed was illustrated in Figure 2.2, shown together with data from fast latitude scans by Ulysses. The radial profile was illustrated in Figure 2.3, together with data from Pioneer 10 and Voyager 2; the SW termination shock (TS) was also illustrated in this figure. Having motivated the expansion of the SW to create the heliosphere, the resulting structure of the heliosphere was discussed in Section 2.4. This was done with the help of a magneto-hydrodynamic (MHD) simulation of the heliosphere in Figure 2.4, illustrating all relevant structures such as the TS, the heliopause (HP) and the bow shock (BS); this figure also made it possible to illustrate the region of the heliosphere known as the heliosheath, located between the TS and the HP.

In Section 2.5 it was explained that the solar magnetic field gets frozen into the SW and carried out into the heliosphere to form the heliospheric magnetic field (HMF). Figure 2.6 showed the time development of the HMF magnitude at Earth, together with its correlation with the SN, i.e. solar activity. In Figure 2.6 it was illustrated how the unmodified Parker heliospheric magnetic field (PHMF) field lines form a spiral structure. However, since the PHMF causes drift effects in the polar regions to be considerably over estimated, two modifications to this structure were considered. These modifications are

the Jokipii-Kóta (JKM) and Smith-Bieber (SBM) modifications. It was argued that the JKM was technically not correct and that, instead, the SBM will be extensively utilised in this work.

The next section was devoted to a description of the major three-dimensional (3D) co-rotating heliospheric structure known as the neutral heliospheric current sheet (HCS). The principle behind the formation of this structure was illustrated in Figure 2.8, with observational evidence for the existence of the HCS provided by means of synoptic charts in Figure 2.9. Furthermore, the HCS tilt angle $\alpha$ was introduced as proxy for the solar cycle; Figure 2.10 presented a plot of $\alpha$ vs time according to two tilt angle models, i.e. the radial and line of sight models. Simulations of the HCS for various values of $\alpha$ were shown in Figure 2.11.

Cosmic rays and CR modulation were discussed in Section 2.7. These particles were first classified according to origin, after which it was illustrated how the count rates of these particles at Earth, as measured by neutron monitors, vary with solar activity; Figure 2.12 showed the cosmic ray count rate at Earth as function of time, the $\sim 11$ year and $\sim 22$ year cycles again being clearly in evidence.

The final section of this chapter had a look at the spacecraft missions most relevant to this study. The most prominent of these was the PAMELA experiment, since Chapter 6 will make use of galactic proton data from PAMELA in an application of the numerical modulation model of this work. The Voyager 1 and 2 spacecraft were also discussed, as Voyager 1 will be important when it comes to selecting the local interstellar proton spectrum to be used in this work.

# Chapter 3

# Particle Transport in the Heliosphere

## 3.1 Introduction

The modulation of galactic cosmic rays (GCRs) in the heliosphere is determined by a number of physical modulation processes. These processes alter the differential intensity and distribution of cosmic rays (CRs) as a function of energy, position in the heliosphere, and time. It is therefore essential in CR modulation studies to take into account these processes in the most effective and realistic way, and hence they must be understood as fully as possible.

This chapter is devoted to a discussion of the Parker transport equation (TPE), an equation that takes into account most of the physical modulation processes in the heliosphere. The processes of drift and diffusion are discussed in the necessary detail and the relevant expressions are presented. The TPE is finally converted to spherical coordinates so that it can be implemented in a mathematical modulation model that approximates the geometry of the heliosphere as spherical.

## 3.2 The Transport Equation

The relevant transport equation (TPE), originally derived by Parker (1965) and re-derived by Gleeson and Axford (1967), is given by

$$\frac{\partial f}{\partial t} = -\left(\vec{V}_{\rm sw} + \langle \vec{v}_{\rm d} \rangle\right) \cdot \nabla f + \nabla \cdot (\mathbf{K}_{\rm s} \cdot \nabla f) + \frac{1}{3}\left(\nabla \cdot \vec{V}_{\rm sw}\right) \frac{\partial f}{\partial \ln p} + Q, \tag{3.1}$$

in terms of the omni-directional CR distribution function $f(\vec{r}, p, t)$, where $\vec{r}$ is the position, $p$ the particle momentum, and $t$ is the time. This equation contains the relevant transport phenomena and the terms are, from left to right: time dependent changes, outward convection by the bulk solar wind (SW) flow $\vec{V}_{\rm sw}$, CR drifts in terms of the pitch angle averaged guiding centre drift velocity $\langle \vec{v}_{\rm d} \rangle$, spatial diffusion through the symmetric diffusion tensor $\mathbf{K}_{\rm s}$, adiabatic energy losses and gains through the solar wind divergence $\nabla \cdot \vec{V}_{\rm sw}$, and any possible sources of CRs inside the heliosphere (Jovian electrons, for example), $Q(\vec{r}, p, t)$. See e.g. Fisk (1999) and Potgieter (1998, 2011, 2013) for overviews of all the heliospheric transport processes.

Though this work does provide for a heliosheath and a termination shock (TS) as heliospheric entities, it does not incorporate diffusive shock acceleration, also known as Fermi I acceleration. The TS employed in this work is therefore rather described as a 'simulated' TS, since it is established entirely through Eq. (2.5), by which $\vec{V}_{\rm sw}$ drops to lower values over the TS at $r = r_{\rm TS}$. This is sufficient for the purposes of this study, since

the focus here is on the modulation of GCRs and these effects would become important when, for example, the anomalous component of cosmic rays (ACRs) is considered. For a TPE that includes an additional term for the inclusion of Fermi II acceleration (stochastic acceleration), derived from a more general Fokker-Planck equation, see e.g. Schlickeiser (2002) and Strauss (2010). For details on the further refinement of the TPE, see Gleeson and Axford (1968), Jokipii and Parker (1970) and Schlickeiser (2002).

Although the TPE is written in terms of momentum, it is usually solved in terms of rigidity, defined as

$$\begin{aligned} P &\equiv \frac{pc}{q} \\ &= \frac{mvc}{Ze}, \end{aligned} \tag{3.2}$$

with $p = mv$ the particle's momentum, $q = Ze$ its charge, and $c$ the speed of light.

The total energy of a relativistic particle can be written as

$$\begin{aligned} E_{\mathrm{p}}^2 &= p^2c^2 + m_0^2c^4 \\ &= \left(T_{\mathrm{p}} + E_{0,\mathrm{p}}\right)^2, \end{aligned} \tag{3.3}$$

where $m_0$ is the particle rest-mass and $T_{\mathrm{p}}$ and $E_{0,\mathrm{p}}$ are the total kinetic energy and total rest energy of the particle respectively. Then, in terms of rigidity, the total energy is

$$E_{\mathrm{p}}^2 = P^2(Ze)^2 + E_{0,\mathrm{p}}^2. \tag{3.4}$$

For data comparison purposes, these quantities are rewritten in terms of the total energy per nucleon $E_{\mathrm{n}}$ and the total kinetic energy per nucleon $T_{\mathrm{n}}$, as

$$\begin{aligned} A^2E_{\mathrm{n}}^2 &= P^2(Ze)^2 + A^2E_0^2 \\ &= (AT_{\mathrm{n}} + AE_0)^2, \end{aligned} \tag{3.5}$$

where $A$ is the mass number and $E_0$ the rest-energy of a single nucleon. The total kinetic energy per nucleon can be written in terms of particle rigidity as

$$T_{\mathrm{n}} = \sqrt{P^2\left(\frac{Ze}{A}\right)^2 + E_0^2} - E_0, \tag{3.6}$$

or, conversely, the rigidity can be written in terms of the kinetic energy per nucleon

$$\begin{aligned} P &= \left(\frac{A}{Ze}\right)\sqrt{\left(T_{\mathrm{n}} + E_0\right)^2 - E_0^2} \\ &= \left(\frac{A}{Ze}\right)\sqrt{T_{\mathrm{n}}\left(T_{\mathrm{n}} + 2E_0\right)}. \end{aligned} \tag{3.7}$$

From these expressions, another useful quantity is defined, namely the ratio of the particle

speed to the speed of light, $\beta_c$, given by

$$\begin{aligned}\beta_c &= \frac{v}{c} \\ &= \frac{pc}{mc^2} \\ &= \frac{\sqrt{T_{\rm n}(T_{\rm n}+2E_0)}}{T_{\rm n}+E_0} \\ &= \frac{P}{\sqrt{P^2+\left(\frac{A}{Ze}\right)^2 E_0^2}}.\end{aligned} \tag{3.8}$$

From this equation, the relation between rigidity, kinetic energy, and $\beta_c$ is

$$\begin{aligned}P &= \frac{A}{Z}\sqrt{T_{\rm n}(T_{\rm n}+2E_0)} \\ &= \left(\frac{A}{Z}\right)\beta_c(T_{\rm n}+E_0).\end{aligned} \tag{3.9}$$

Furthermore, the density of particles within a region $d^3r$ with a momentum between $\vec{p}$ and $\vec{p}+d\vec{p}$ is related to the full CR distribution function by

$$\begin{aligned}n &= \int F\left(\vec{r},\vec{p},t\right) d^3p \\ &= \int_p p^2 \left[\int_\Omega F\left(\vec{r},\vec{p},t\right) d\Omega\right] dp,\end{aligned} \tag{3.10}$$

where the relation $d^3p = p^2 dp d\Omega$ was used. Also, the differential particle density $U_p$ is related to $n$ by

$$n \equiv \int U_p\left(\vec{r},p,t\right) dp, \tag{3.11}$$

resulting in

$$U_p\left(\vec{r},p,t\right) = \int_\Omega p^2 F\left(\vec{r},\vec{p},t\right) d\Omega. \tag{3.12}$$

The omni-directional (or pitch angle) average of $F\left(\vec{r},\vec{p},t\right)$, as used in this study, can be calculated as

$$\begin{aligned}f\left(\vec{r},p,t\right) &\equiv \frac{\int_\Omega F\left(\vec{r},\vec{p},t\right) d\Omega}{\int_\Omega d\Omega} \\ &= \frac{1}{4\pi}\int_\Omega F\left(\vec{r},\vec{p},t\right) d\Omega,\end{aligned} \tag{3.13}$$

leading to the relation

$$U_p\left(\vec{r},p,t\right) = 4\pi p^2 f\left(\vec{r},p,t\right). \tag{3.14}$$

The differential intensity, in units of particles/unit area/unit time/unit momentum/unit solid angle, is defined as

$$\begin{aligned}j_p\left(\vec{r},p,t\right) &= \frac{vU_p\left(\vec{r},p,t\right)}{\int_\Omega d\Omega} \\ &= \frac{vU_p\left(\vec{r},p,t\right)}{4\pi} \\ &= vp^2 f\left(\vec{r},p,t\right).\end{aligned} \tag{3.15}$$

The particle speed can be eliminated from this equation by noting that

$$\frac{\partial p}{\partial E} = \frac{1}{v}, \tag{3.16}$$

and by using the relation $jdE = j_p dp$, it follows that

$$\begin{aligned} j\left(\vec{r}, p, t\right) &= \frac{v}{4\pi} U_p \frac{dp}{dE} \\ &= \frac{1}{4\pi} U_p \\ &= p^2 f\left(\vec{r}, p, t\right), \end{aligned} \tag{3.17}$$

in units of particles/unit area/unit time/unit kinetic energy per nucleus/unit solid angle. See also Potgieter (1984) and Strauss (2010).

## 3.3 Particle Drifts

Due to the large scale HMF, CRs will undergo a combination of gradient, curvature, and current sheet drifts. The current sheet drifts are due to the switch in magnetic polarity across the neutral heliospheric current sheet (HCS) (e.g. Burger and Potgieter, 1989). The original derivation of the TPE (Parker, 1965) did include drifts, but these effects were neglected in modulation models until Jokipii et al. (1977) pointed out that drifts may indeed play a significant role in CR modulation and, furthermore, can explain the observed HMF polarity dependent CR observations (e.g. Jokipii and Kopriva, 1979; Potgieter and Moraal, 1985).

In the most general case the pitch angle averaged guiding center drift velocity is given by

$$\langle \vec{v}_{\rm d} \rangle = \frac{pv}{3q} \frac{(\omega \tau_{\rm d})^2}{1 + (\omega \tau_{\rm d})^2} \nabla \times \frac{\vec{B}}{B^2}, \tag{3.18}$$

where the suppression of drifts by turbulence (scattering) is included (see Minnie et al., 2007 and references therin). Here, $\omega$ is the particle gyro-frequency and $\tau_{\rm d}$ is a time scale defined by scattering. The quantities $\vec{B}$ and $B$ are the magnetic field vector and magnitude respectively, as defined in Chapter 2. Eq. (3.18) can be written as

$$\begin{aligned} \langle \vec{v}_{\rm d} \rangle &= \nabla \times \frac{pc}{q} \frac{v}{c} \frac{1}{3B} \frac{(\omega \tau_{\rm d})^2}{1 + (\omega \tau_{\rm d})^2} \frac{\vec{B}}{B} \\ &= \nabla \times \frac{P \beta_c}{3B} \frac{(\omega \tau_{\rm d})^2}{1 + (\omega \tau_{\rm d})^2} \frac{\vec{B}}{B} \\ &= \nabla \times \frac{v}{3} r_{\rm L} \frac{(\omega \tau_{\rm d})^2}{1 + (\omega \tau_{\rm d})^2} \vec{\rm e}_B, \end{aligned} \tag{3.19}$$

in terms of the maximal Larmor radius

$$\begin{aligned} r_{\rm L} &= \frac{mv}{qB} \\ &= \frac{P}{Bc}, \end{aligned} \tag{3.20}$$

and where $\vec{\rm e}_B = \vec{B}/B$ is a unit vector directed along $\vec{B}$.

The assumption of weak scattering, i.e. assuming that a particle undergoes a large number of gyrations before being scattered, leads to a drift velocity taking on its maximal weak scattering value and therefore

$$(\omega\tau_{\rm d})^{\rm ws} >> 1. \tag{3.21}$$

With this assumption, Eq. (3.19) reduces to

$$\begin{aligned} \langle\vec{v}_{\rm d}\rangle^{\rm ws} &= \nabla\times\frac{v}{3}r_{\rm L}\vec{\rm e}_B \\ &= \nabla\times\kappa_{\rm D}\vec{\rm e}_B, \end{aligned} \tag{3.22}$$

with the weak scattering drift coefficient given by

$$\kappa_{\rm D}^{\rm ws} = \frac{v}{3}r_{\rm L}. \tag{3.23}$$

Note that for very strong scattering $(\omega\tau_{\rm d})^{\rm ss}\to 0$, and it follows that $\kappa_{\rm D}^{\rm ss}\to 0$ so that no particle drift is present.

The drift coefficient is related to the so-called drift scale through

$$\lambda_{\rm D} = \kappa_{\rm D}\frac{3}{v}, \tag{3.24}$$

which, in this work, is presented in astronomical units (AU), i.e. in units of length. For the weak scattering scenario, the drift scale becomes $\lambda_{\rm D}^{\rm ws} = r_{\rm L}$.

The exact form of the suppression factor on $\kappa_{\rm D}$ is not yet known, and continues to be studied (Minnie et al., 2007; Visser, 2009). As in Strauss (2010), in this study the approach of Burger et al. (2000, 2008) is followed, where it is assumed that $(\omega\tau_{\rm d})\sim P$, resulting in

$$\kappa_{\rm D} = \kappa_{\rm D,0}\frac{v}{3}r_{\rm L}\frac{(P/P_0)^2}{1+(P/P_0)^2}, \tag{3.25}$$

with $P_0 = 1$ GV added on dimensional grounds; in this study, $P_0\in\{1/\sqrt{10}, 1/\sqrt{40}\}$ GV, in accordance with Vos (2011). The parameter $\kappa_{\rm D,0}\in[0,1]$ and is a parameter used to scale the drift from zero ($\kappa_{\rm D,0}=0$) to one hundred ($\kappa_{\rm D,0}=1$) percent. The need to introduce this parameter follows from Potgieter et al. (1989), who showed that full drifts at all energies were not plausible and that $\kappa_{\rm D,0}$ needed to be reduced in order to reproduce CR observations (Webber et al., 1990). Furthermore, Ferreira and Potgieter (2004) showed that $\kappa_{\rm D,0}\in[0.0, 0.1]$ was needed to reproduce solar maximum observations; see also Ndiitwani et al. (2005). However, in this work $\kappa_{\rm D,0} = 1.0$ is used throughout.

Figure 3.1 shows the rigidity and radial dependencies of the drift scale $\lambda_{\rm D}$, employing a Smith-Bieber modified magnetic field (SBM) as explained in Chapter 2; see Eq. (2.12). Comparisons with the cases of the unmodified Parker field (PHMF), i.e. Eq. (2.9), and Jokipii-Kóta modified field (JKM), i.e. Eq. (2.10), are carried out in Chapter 5. The top panel of Figure 3.1 depicts the rigidity dependence of the drift scale $\lambda_{\rm D}$ at Earth. The solid red and blue lines show the cases where drifts have been modified according to Eq. (3.25), below $P_0 = 1/\sqrt{10}$ GV and $P_0 = 1/\sqrt{40}$ GV respectively. These two values for $P_0$ are indicated by the red and blue vertical lines respectively. The vertical displacement in $\lambda_{\rm D}$ for these two cases is attributed to different values being assumed for the magnetic field; this is discussed in Chapter 6. The weak scattering limit for $\lambda_{\rm D}$ is also shown for both these cases. It is clear from this figure that, for the modified form of $\kappa_{\rm D}$, $\lambda_{\rm D}$ is significantly reduced when $P < P_0$, and drifts at these low energies can therefore be neglected, i.e. at rigidities $P << P_0$.

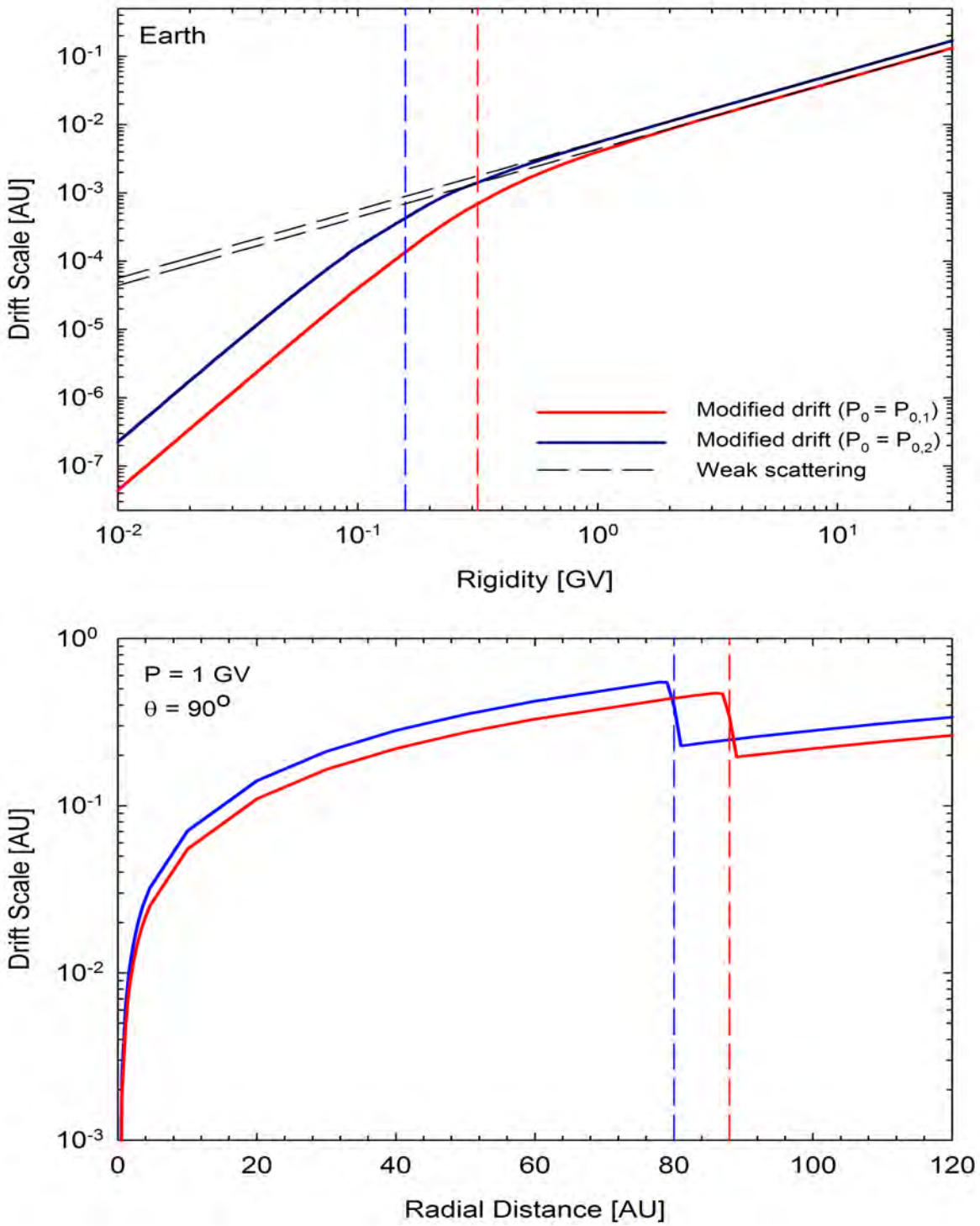


Figure 3.1: *The top panel shows the drift scale $\lambda_D$ as a function of rigidity at the position of the Earth for the weak scattering case (dashed lines), i.e. Eq. (3.23), and for the scattering modified approximation, i.e. Eq. (3.25), for the cases of $P_0 = P_{0,1} = 1/\sqrt{10}$ (solid red line) and $P_0 = P_{0,2} = 1/\sqrt{40}$ (solid blue line). The vertical lines indicate these values of $P_0$ for each of the two cases respectively. The bottom panel shows the radial dependence of $\lambda_D$, again in each of the two cases. In the first case, the position of the TS was at $r_{TS} = 80$ AU (dashed blue line), while in the second case it was at $r_{TS} = 88$ AU (dashed red line). The SBM is selected for the HMF profile.*

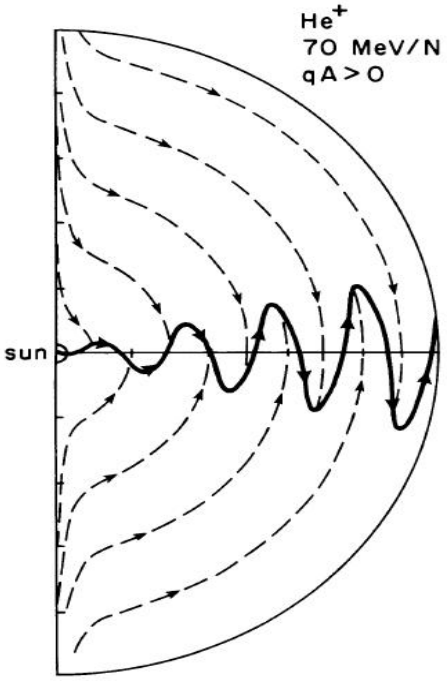


Figure 3.2: *Average drift velocity streamlines in the meridional plane of the heliosphere for positive particles in the $A > 0$ magnetic polarity cycle. The drift directions will reverse for negatively charged particles, as well as for the $A < 0$ polarity cycle. The figure is taken from Pesses et al. (1981).*

The radial dependence of $\lambda_{\rm D}$ at 1 GV is depicted in the bottom panel of Figure 3.1, again for each of the cases where $P_0 = 1/\sqrt{10}$ GV and $P_0 = 1/\sqrt{40}$ GV. The vertical dashed blue and red lines now indicate the position of the TS, being set to $r_{\rm TS} = 80$ AU in the former and $r_{\rm TS} = 88$ AU in the latter cases respectively; this will be discussed further in Chapter 6. From the top panel of Figure 3.1, it is clear that the modified and weak scattering values of $\kappa_{\rm D}$ are comparable at this rigidity and, as such, this panel also shows $r_{\rm L}$ indirectly. From the expressions presented earlier, the radial dependence of $\lambda_{\rm D}$ is seen to be essentially governed by $B$ which, in turn, is dependent on the magnitude of $V_{\rm sw}$ through Eqs. (2.8) and (2.9). The drift scale is therefore seen to decrease sharply over the TS and then to resume the same radial dependence that it had just before the TS was encountered. This profile beyond the TS is sufficient for the purposes of this study; for a discussion of $\lambda_{\rm D}$ profiles in the heliosheath, see e.g. Strauss (2010).

Figure 3.2 depicts a meridional cut of the heliosphere and shows the global drift directions. Solving for $d\vec{l} \times \langle \vec{v}_{\rm D} \rangle = 0$, streamlines of the drift velocity can be obtained and the arrowed lines show these streamlines for positively charged particles during the $A > 0$ magnetic polarity cycle (Pesses et al., 1981). It is clear that, during such a polarity cycle, positive particles drift primarily from the polar regions down towards the equatorial plane, and outwards along the HCS. For negatively charged particles, this behaviour will be reversed. The drift directions during the $A < 0$ polarity cycle are reversed again. See also Potgieter (1984), Burger (1987) and Hattingh (1998).

The TPE is solved in spherical coordinates (see Section 3.5), and for this purpose the drift velocity and drift coefficient are rewritten in terms of the asymmetrical drift tensor $\mathbf{K}_{\rm D}$. This follows from the fact that the rotation of a vector may be rewritten as the divergence of a second rank tensor (e.g. Minnie et al., 2007), leading to

$$\nabla \times \kappa_{\rm D} \vec{\rm e}_B = -\nabla \cdot \mathbf{K}_{\rm D}, \tag{3.26}$$

with

$$\mathbf{K}_{\mathrm{D}} = \begin{bmatrix} 0 & 0 & 0 \\ 0 & 0 & \kappa_{\mathrm{D}} \\ 0 & -\kappa_{\mathrm{D}} & 0 \end{bmatrix}, \tag{3.27}$$

called the asymmetrical drift tensor. In later sections the reason for choosing this form will become clear.

For HCS drifts, the basic approach followed is that of Strauss et al. (2012). The specifics of this topic, including the relevant expressions, are discussed in more detail in Chapter 5.

## 3.4 Particle Diffusion

Cosmic rays undergo diffusive propagation or "random walk" in the heliosphere as a result of fluctuations in the HMF. The process by which this happens is called pitch angle scattering and can be described by weak turbulence quasi-linear theory (QLT), first introduced by Jokipii (1966). This diffusive propagation of CRs is generally interpreted as waves (e.g. Schlickeiser, 1988) or as dynamical turbulence (e.g. Bieber and Matthaeus, 1991) and it is described through the elements of the symmetric diffusion tensor $\mathbf{K}_{\mathrm{s}}$ in Eq. (3.1), which can be written in HMF-aligned coordinates as

$$\mathbf{K}_{\mathrm{s}} = \begin{bmatrix} \kappa_{||} & 0 & 0 \\ 0 & \kappa_{\perp\theta} & 0 \\ 0 & 0 & \kappa_{\perp r} \end{bmatrix}, \tag{3.28}$$

with $\kappa_{||}$ the component parallel to the mean HMF and the other two components $\kappa_{\perp\theta}$ and $\kappa_{\perp r}$ perpendicular to the HMF and in the $\vec{e}_\theta$ and $\vec{e}_r$ directions respectively. Each element of this tensor is called a diffusion coefficient, and Figure 3.3 gives a schematic illustration of the directions in which each of these diffusion coefficients operate with respect to the HMF.

Each diffusion coefficient is related to the corresponding mean free path (MFP) through

$$\kappa = \frac{v}{3}\lambda, \tag{3.29}$$

where, in this work, $\lambda$ is in astronomical units (AU), i.e. in units of length, producing a more tangible and intuitively predictable variable. A comprehensive study of these transport parameters as well as the underlying turbulence theory is beyond the scope of this study. See e.g. Hattingh (1998), Minnie (2006), Shalchi (2009) and Engelbrecht (2008, 2012) for in-depth studies pertaining to these matters.

### 3.4.1 Parallel Diffusion

An expression for the pitch angle averaged parallel diffusion coefficient can be derived from the Fokker-Planck equation using the method of Earl (1974). From this it follows that

$$\kappa_{||} = \frac{v^2}{8}\int_{-1}^{1} \frac{(1-\mu^2)^2}{\Phi(\mu)} d\mu, \tag{3.30}$$

where $\Phi(\mu)$ is the pitch angle diffusion coefficient and is essentially the rate of particle scattering; this parameter depends on the turbulence model considered and hence the dependence on $\mu$. The calculation of $\Phi(\mu)$ requires a power spectrum of the magnetic field fluctuations. An example of such a spectrum is shown in Figure 3.4 and it is clearly

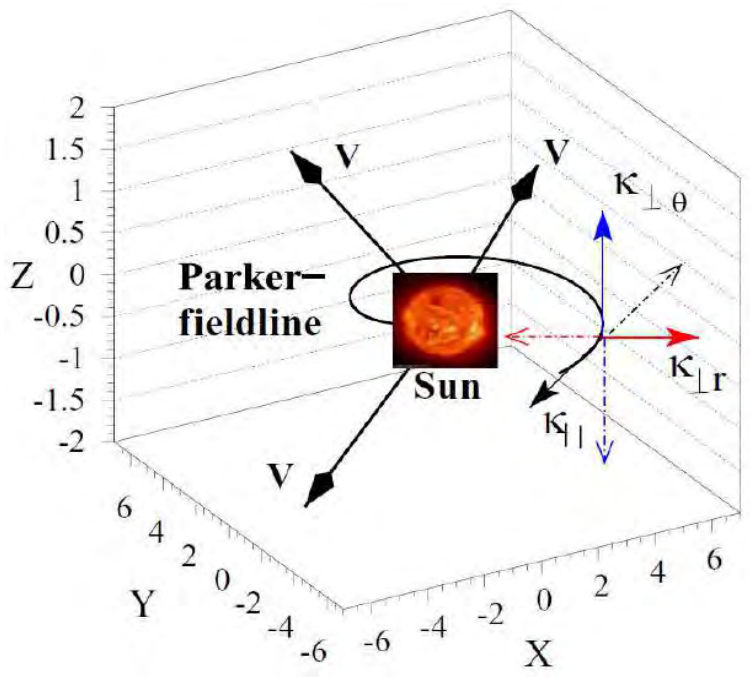


Figure 3.3: *The directions of the parallel and perpendicular diffusion coefficient components of the symmetrical tensor, with respect to a magnetic field line in the equatorial plane. The radially expanding SW is indicated by the arrows emanating from the Sun. This figure was taken from Heber and Potgieter (2006).*

divisible into three distinct ranges: the energy range at low wavenumbers, where the power spectrum variation is independent of the wavenumber $k$; the inertial range at intermediate wavenumbers, where the variation is proportional to $k^{-5/3}$; the dissipation range at high wave numbers, where the variation is proportional to $k^{-3}$ (e.g. Bieber et al., 1994). See Teufel and Schlickeiser (2003) for a derivation of piecewise continuous expressions for the parallel MFPs from QLT for a full turbulence spectrum for two models of dynamical turbulence, namely the damping model and the random sweeping model (Bieber et al., 1994). See also Shalchi and Schlickeiser (2004).

In this study, however, a simplified approach for the rigidity dependence of the diffusion coefficients is followed; see Vos (2011), Strauss (2010), Langner (2004), and Ferreira et al. (2001b), for similar approaches. As in Vos (2011), it is assumed that the spatial dependence of the parallel diffusion coefficient is inversely proportional to the magnitude of the magnetic field and this study uses the same expression for the parallel diffusion of protons, given by

$$\kappa_{||} = \kappa_{||,0}\beta_c \frac{B_0}{B}\left[\frac{\left(\frac{P}{P_0'}\right)^c + \left(\frac{P_\mathrm{k}}{P_0'}\right)^c}{1+\left(\frac{P_\mathrm{k}}{P_0'}\right)^c}\right]^{\frac{b-a}{c}}\left(\frac{P}{P_0'}\right)^a, \tag{3.31}$$

where $\kappa_{||,0}$ is a constant in units of $6 \times 10^{20}$ cm$^2$.s$^{-1}$, with $P_0' = 1$ GV and $B_0 = 1$ nT added to obtain the correct dimensions. Here $a$ and $b$ are dimensionless constants and determine the slope of the rigidity dependence below and above a rigidity $P_\mathrm{k}$ respectively. The quantity $c$ is another dimensionless constant (with a value between 3 and 4) and determines the smoothness of the transition between the two slopes $P^a$ and $P^b$ at $P_\mathrm{k}$.

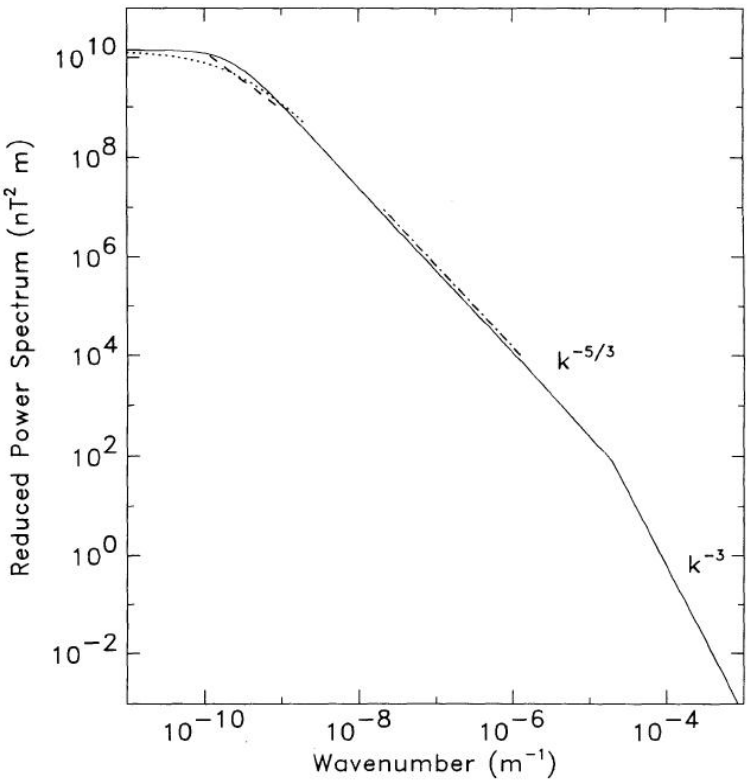


Figure 3.4: *A typical slab turbulence power spectrum model (solid line) for the heliosphere at Earth compared to observations (dashed and dotted lines). Figure taken from Bieber et al. (1994).*

The rigidity dependence is therefore essentially a double power-law. In this work, $P_{\mathrm{k}} \in \{4.0, 4.2\}$ GV; this will be discussed in Chapter 6.

Figure 3.5 shows the rigidity and radial dependencies of the parallel mean free path $\lambda_{||}$, employing the SBM; once again, a comparison with the cases for the PHMF and JKM is carried out in Chapter 5. The top panel shows the rigidity dependence of $\lambda_{||}$ for protons at Earth (solid lines), as given by Eq. (3.31). The observational Palmer consensus values (Palmer, 1982) are indicated by the green block. From this figure it follows that the rigidity dependence above $\sim 5$ GV is fixed at $P^{1.95}$, while below $\sim 3$ GV it varies between $P^{0.73}$ (solid red line) and $P^{0.85}$ (solid blue line); this difference as well as the vertical displacement are due to time dependent changes in quantities such as the averaged HCS tilt angle $\alpha$ and HMF values which are required for changing solar activity, as discussed in Chapter 6. Between $\sim 3$ GV and $\sim 5$ GV the rigidity dependence in each case is seen to transition from the weaker dependence to $P^{1.95}$.

The bottom panel of Figure 3.5 gives the radial dependence of $\lambda_{||}$ for 1 GV protons in the equatorial plane, as used in this study (solid lines). The difference between the solid red and blue lines is as explained for the top panel. As a result of the $B^{-1}$ dependence of $\kappa_{||}$ in Eq. (3.31), the radial dependence of $\lambda_{||}$ is proportional to $r$, following from Eq. (2.9). This is equivalent to the radial profile used by Vos (2011), the only difference being that the HMF employed here is the SBM instead of the JKM; since these profiles are drawn in the equatorial plane, however, this difference should be negligible. As illustrated in Vos (2011), the radial profile is also similar to that of Strauss (2010). Across the TS $\lambda_{||}$ drops by approximately a factor of $s^2$ (with $s$ the TS compression ratio) and then continue with the same radial dependence it had upstream of the TS. As in the case for the drift scale

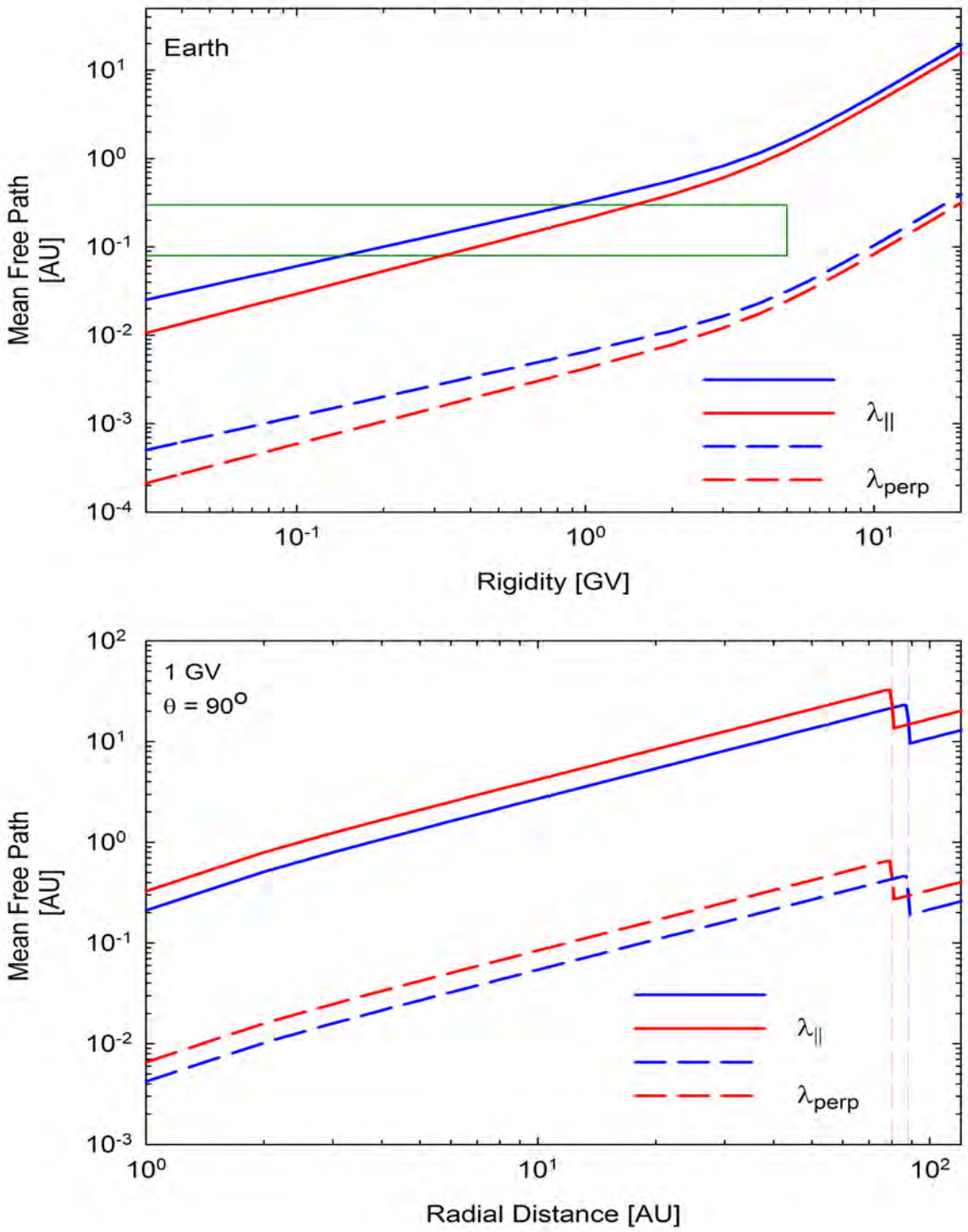


Figure 3.5: *The top panel shows the parallel (solid lines) and perpendicular (dashed lines) MFPs for protons at Earth, as used in this study, as a function of rigidity in the equatorial plane. The difference between the two sets of MFPs (red and blue lines) corresponds to a time dependent change as a result of changing solar activity, as proxied by the HCS tilt angle $\alpha$. The observational Palmer consensus values are indicated by the green block. Similarly, the bottom panel shows the radial dependence for both the parallel and perpendicular MFPs of 1 GV protons as used in this study in the equatorial plane. The different positions of the TS are indicated by the vertical dashed red and blue lines. The SBM is selected for the HMF profile.*

$\lambda_D$, this profile beyond the TS is sufficient for the purposes of this study and the reader is referred to e.g. Strauss (2010) for a discussion of $\lambda_{||}$ profiles in the heliosheath.

### 3.4.2 Perpendicular Diffusion

Cosmic ray particles are also scattered perpendicular to the magnetic field. This can be the result of the particles' gyrocentres that are displaced transverse to the mean HMF through scattering, or due to the random walk of the magnetic field lines themselves. In numerical models, these processes are taken into account collectively via the perpendicular diffusion coefficient $\kappa_\perp$. As previously mentioned, $\kappa_\perp$ can be subdivided into two possibly independent coefficients describing the perpendicular diffusion in the radial ($\kappa_{\perp r}$) and the polar ($\kappa_{\perp\theta}$) directions. It has also been established that $\kappa_\perp$ plays a significant role in the modulation of CRs (e.g. Potgieter, 1996, 2000; Ferreira et al., 2000). See also e.g. Jokipii (2001) for earlier theoretical work related to perpendicular diffusion.

In the presence of parallel diffusion, however, a pure field line random walk scenario gives an insufficient description of perpendicular diffusion, since particles sometimes retrace their paths after they backscatter; this process has not been taken into account until the proposed non-linear guiding center (NLGC) theory of particle diffusion by Matthaeus et al. (2003). According to NLGC theory, the process of perpendicular diffusion is a combination of field line random walk, backscattering from parallel diffusion, and the transfer of particles across the field lines due to the perpendicular complexity of the magnetic field. See Bieber et al. (2004) for a discussion of the general properties of the NLGC theory and comparison with observations. See also Shalchi (2009) for recent efforts, emphasising that the theory is not yet fully developed and that several issues still remain unresolved so that it should be seen as a work in progress.

In this work, $\kappa_\perp$ is scaled as $\kappa_{||}$. This has become standard practice and has been confirmed by Giacalone and Jokipii (1999), who found that the ratio $\kappa_\perp/\kappa_{||}$ has a value between 0.02 and 0.04. In addition, observations from the Ulysses spacecraft have revealed that the latitude dependence of CR protons is significantly less than predicted by classical drift models (Potgieter and Haasbroek, 1993), which led Kóta and Jokipii (1995) to propose the concept of an anisotropic $\kappa_\perp$, where $\kappa_{\perp\theta} > \kappa_{\perp r}$ in the off-equatorial regions (e.g. Potgieter, 1996; Burger et al., 2000). The effect of such anisotropic perpendicular diffusion on CR modulation has been studied in detail by e.g. Ferreira et al. (2000). This anisotropy of $\kappa_\perp$ has been accounted for in this work, as was done by e.g. Langner (2000) and Vos (2011), so that

$$\kappa_{\perp r} = \kappa^0_{\perp r}\kappa_{||} \tag{3.32}$$

and

$$\kappa_{\perp\theta} = f(\theta)\kappa^0_{\perp\theta}\kappa_{||}, \tag{3.33}$$

where $\kappa^0_{\perp r} = \kappa^0_{\perp\theta} = 0.02$ are dimensionless constants, and

$$f(\theta) = A^+ + A^- \tanh\left[\frac{1}{\Delta\theta}\left(\widetilde{\theta} - \frac{\pi}{2} + \theta_F\right)\right]. \tag{3.34}$$

Here $A^\pm = \dfrac{d \pm 1}{2}$, $\Delta\theta = 1/8$, with

$$\widetilde{\theta} = \begin{cases} \theta & \text{for} \quad \theta \geq \dfrac{\pi}{2} \\ \\ \pi - \theta & \text{for} \quad \theta < \dfrac{\pi}{2}, \end{cases} \tag{3.35}$$

and

$$\theta_{\mathrm{F}} = \begin{cases} \dfrac{-35^{\circ}\pi}{180^{\circ}} & \text{for} \quad \theta \geq \dfrac{\pi}{2} \\ \dfrac{35^{\circ}\pi}{180^{\circ}} & \text{for} \quad \theta < \dfrac{\pi}{2}, \end{cases} \tag{3.36}$$

where $d$ is a dimensionless constant that determines the enhancement factor of $\kappa_{\perp\theta}$ from its value in the equatorial plane towards the poles, with respect to $\kappa_{||}$.

The top panel of Figure 3.5 also depicts the rigidity dependence of $\kappa_{\perp}$ for protons at Earth in the equatorial plane (dashed lines), where it has been assumed that both $\kappa_{\perp r}$ and $\kappa_{\perp\theta}$ have the same rigidity dependence, and is scaled with $\kappa_{||}$. The radial dependence of $\lambda_{\perp}$ for protons in the equatorial plane, given by the dashed lines in the bottom panel of Figure 3.5, is once again similar to that of Vos (2011) who also indicated that it was comparable to the MFP of Burger et al. (2000), also used by Strauss (2010).

## 3.5 The Transport Equation in Spherical Coordinates

An HMF-aligned coordinate system, as described earlier, has one axis parallel to the mean HMF ($\vec{B} = B_0\vec{\mathrm{e}}_z$) in the $r\phi-$plane ($\vec{\mathrm{e}}_{||}$), and another perpendicular to the first in the $\vec{\mathrm{e}}_{\theta}$ direction ($\vec{\mathrm{e}}_1$), and a third axis in the $r\theta-$plane perpendicular to the first two ($\vec{\mathrm{e}}_2$), forming a right-handed coordinate system. Within such system, an asymmetrical tensor $\mathbf{K}$, consisting of a symmetrical diffusion tensor $\mathbf{K}_{\mathrm{s}}$ − as in Eq. (3.1) − and an asymmetrical drift tensor $\mathbf{K}_{\mathrm{D}}$ − as in Eq. (3.27) − can be set up. This tensor then contains the necessary diffusion and drift coefficients that determine the extent of particle modulation in the heliosphere and is given by

$$\begin{aligned} \mathbf{K} &= \mathbf{K}_{\mathrm{s}} + \mathbf{K}_{\mathrm{D}} \\ &= \begin{bmatrix} \kappa_{||} & 0 & 0 \\ 0 & \kappa_{\perp\theta} & 0 \\ 0 & 0 & \kappa_{\perp r} \end{bmatrix} + \begin{bmatrix} 0 & 0 & 0 \\ 0 & 0 & \kappa_{\mathrm{D}} \\ 0 & -\kappa_{\mathrm{D}} & 0 \end{bmatrix} \\ &= \begin{bmatrix} \kappa_{||} & 0 & 0 \\ 0 & \kappa_{\perp\theta} & \kappa_{\mathrm{D}} \\ 0 & -\kappa_{\mathrm{D}} & \kappa_{\perp r} \end{bmatrix}, \end{aligned} \tag{3.37}$$

in HMF-aligned coordinates. By combining these tensors in this way, it is possible to rewrite the TPE of Eq. (3.1) in a more compact form as

$$\frac{\partial f}{\partial t} = -\vec{V}_{\mathrm{sw}} \cdot \nabla f + \nabla \cdot (\mathbf{K} \cdot \nabla f) + \frac{1}{3}(\nabla \cdot \vec{V}_{\mathrm{sw}}) \frac{\partial f}{\partial \ln p}, \tag{3.38}$$

where the average guiding center drift velocity $\langle \vec{v}_{\mathrm{d}} \rangle$ is now included in the tensor $\mathbf{K}$ and the source term $Q$ has has now been set to zero.

Since the geometry of the heliosphere is best approximated as spherical, the TPE is rewritten in terms of spherical coordinates. The HMF-aligned coordinate system is related to the spherical coordinate system by

$$\begin{aligned} \vec{\mathrm{e}}_{||} &= \cos\psi\vec{\mathrm{e}}_r - \sin\psi\vec{\mathrm{e}}_{\phi} \\ \vec{\mathrm{e}}_1 &= \vec{\mathrm{e}}_{\theta} \\ \vec{\mathrm{e}}_2 &= \vec{\mathrm{e}}_{||} \times \vec{\mathrm{e}}_1 = \sin\psi\vec{\mathrm{e}}_r + \cos\psi\vec{\mathrm{e}}_{\phi}, \end{aligned} \tag{3.39}$$

where $\psi$ is the spiral angle, defined as the angle between the parallel component of the magnetic field (in the $\vec{e}_{||}$ direction) and the radial direction $\vec{e}_r$. The tensor $\mathbf{K}$ can therefore be written in terms of heliocentric spherical coordinates by specifying an appropriate transformation matrix $\mathbf{T}$, for which it is required that $\det(\mathbf{T}) = 1$. This matrix is given by

$$\mathbf{T} = \begin{bmatrix} \cos\psi & 0 & \sin\psi \\ 0 & 1 & 0 \\ -\sin\psi & 0 & \cos\psi \end{bmatrix}, \tag{3.40}$$

so that the tensor $\mathbf{K}$ in spherical coordinates is

$$\begin{aligned} \mathbf{K} &= \mathbf{T}\mathbf{K}\mathbf{T}^T \\ &= \begin{bmatrix} \cos\psi & 0 & \sin\psi \\ 0 & 1 & 0 \\ -\sin\psi & 0 & \cos\psi \end{bmatrix} \begin{bmatrix} \kappa_{||} & 0 & 0 \\ 0 & \kappa_{\perp\theta} & \kappa_{\mathrm{D}} \\ 0 & -\kappa_{\mathrm{D}} & \kappa_{\perp r} \end{bmatrix} \begin{bmatrix} \cos\psi & 0 & -\sin\psi \\ 0 & 1 & 0 \\ \sin\psi & 0 & \cos\psi \end{bmatrix} \\ &= \begin{bmatrix} \kappa_{||}\cos^2\psi + \kappa_{\perp r}\sin^2\psi & -\kappa_{\mathrm{D}}\sin\psi & (\kappa_{\perp r} - \kappa_{||})\cos\psi\sin\psi \\ \kappa_{\mathrm{D}}\sin\psi & \kappa_{\perp\theta} & \kappa_{\mathrm{D}}\cos\psi \\ (\kappa_{\perp r} - \kappa_{||})\cos\psi\sin\psi & -\kappa_{\mathrm{D}}\cos\psi & \kappa_{||}\sin^2\psi + \kappa_{\perp r}\cos^2\psi \end{bmatrix} \\ &= \begin{bmatrix} \kappa_{rr} & \kappa_{r\theta} & \kappa_{r\phi} \\ \kappa_{\theta r} & \kappa_{\theta\theta} & \kappa_{\theta\phi} \\ \kappa_{\phi r} & \kappa_{\phi\theta} & \kappa_{\phi\phi} \end{bmatrix}. \end{aligned} \tag{3.41}$$

The TPE in Eq. (3.38) can now be written in terms of spherical coordinates as

$$\begin{aligned} \frac{\partial f}{\partial t} &= \left[\frac{1}{r^2}\frac{\partial}{\partial r}\left(r^2\kappa_{rr}\right) + \frac{1}{r\sin\theta}\frac{\partial}{\partial\theta}\left(\kappa_{\theta r}\sin\theta\right) + \frac{1}{r\sin\theta}\frac{\partial\kappa_{\phi r}}{\partial\phi} - V_{\mathrm{sw}}\right]\frac{\partial f}{\partial r} \\ &+ \left[\frac{1}{r^2}\frac{\partial}{\partial r}\left(r\kappa_{r\theta}\right) + \frac{1}{r^2\sin\theta}\frac{\partial}{\partial\theta}\left(\kappa_{\theta\theta}\sin\theta\right) + \frac{1}{r^2\sin\theta}\frac{\partial\kappa_{\phi\theta}}{\partial\phi}\right]\frac{\partial f}{\partial\theta} \\ &+ \left[\frac{1}{r^2\sin\theta}\frac{\partial}{\partial r}\left(r\kappa_{r\phi}\right) + \frac{1}{r^2\sin\theta}\frac{\partial\kappa_{\theta\phi}}{\partial\theta} + \frac{1}{r^2\sin^2\theta}\frac{\partial\kappa_{\phi\phi}}{\partial\phi}\right]\frac{\partial f}{\partial\phi} \\ &+ \kappa_{rr}\frac{\partial^2 f}{\partial r^2} + \frac{\kappa_{\theta\theta}}{r^2}\frac{\partial^2 f}{\partial\theta^2} + \frac{\kappa_{\phi\phi}}{r^2\sin^2\theta}\frac{\partial^2 f}{\partial\phi^2} + \frac{2\kappa_{r\phi}}{r\sin\theta}\frac{\partial^2 f}{\partial r\partial\phi} \\ &+ \frac{1}{3r^2}\frac{\partial}{\partial r}(r^2 V_{\mathrm{sw}})\frac{\partial f}{\partial\ln p}, \end{aligned} \tag{3.42}$$

where it is assumed that the SW is axis-symmetrical and purely radial, i.e. $\vec{V}_{\mathrm{sw}} = V_{\mathrm{sw}}\vec{e}_r$. This version of the TPE is now rearranged in order to isolate the various terms that respectively constitute the modulation processes of diffusion, drift, convection, and adiabatic

energy losses, so that Eq. (3.42) becomes

$$\begin{aligned}
\frac{\partial f}{\partial t} &= \overbrace{\left[\frac{1}{r^2}\frac{\partial}{\partial r}(r^2\kappa_{rr}) + \frac{1}{r\sin\theta}\frac{\partial \kappa_{\phi r}}{\partial \phi}\right]\frac{\partial f}{\partial r} + \left[\frac{1}{r^2\sin\theta}\frac{\partial}{\partial\theta}(\kappa_{\theta\theta}\sin\theta)\right]\frac{\partial f}{\partial\theta}}^{\text{diffusion}} \\
&+ \overbrace{\left[\frac{1}{r^2\sin\theta}\frac{\partial}{\partial r}(r\kappa_{r\phi}) + \frac{1}{r^2\sin^2\theta}\frac{\partial\kappa_{\phi\phi}}{\partial\phi}\right]\frac{\partial f}{\partial\phi}}^{\text{diffusion}} \\
&+ \overbrace{\kappa_{rr}\frac{\partial^2 f}{\partial r^2} + \frac{\kappa_{\theta\theta}}{r^2}\frac{\partial f^2}{\partial\theta^2} + \frac{\kappa_{\phi\phi}}{r^2\sin^2\theta}\frac{\partial^2 f}{\partial\phi^2} + \frac{2\kappa_{r\phi}}{r\sin\theta}\frac{\partial^2 f}{\partial r\partial\phi}}^{\text{diffusion}} \\
&+ \overbrace{\left[-\langle\vec{v}_{\mathrm{d}}\rangle_r\right]\frac{\partial f}{\partial r} + \left[-\frac{1}{r}\langle\vec{v}_{\mathrm{d}}\rangle_\theta\right]\frac{\partial f}{\partial\theta} + \left[-\frac{1}{r\sin\theta}\langle\vec{v}_{\mathrm{d}}\rangle_\phi\right]\frac{\partial f}{\partial\phi}}^{\text{drift}} \\
&- \overbrace{V_{\mathrm{sw}}\frac{\partial f}{\partial r}}^{\text{convection}} \\
&+ \overbrace{\frac{1}{3r^2}\frac{\partial}{\partial r}(r^2 V_{\mathrm{sw}})\frac{\partial f}{\partial\ln p}}^{\text{adiabatic energy losses}},
\end{aligned} \tag{3.43}$$

where the first three lines contain the terms that describe the inward diffusion, the fourth line contains the terms that describe particle drift motions, and the terms of the fifth and sixth lines represent convection and adiabatic energy losses respectively; see also e.g. Hattingh (1998), Ferreira (2002), Vos (2011) and Strauss (2013).

## 3.6 Summary

After the importance of a suitable transport equation, i.e. an equation that provides for most of the physical modulation processes in the heliosphere, was indicated in the introduction to this chapter, Section 3.2 introduced the Parker transport equation (TPE) in Eq. (3.1). All the relations needed for an implementation of the TPE were explained, including relations between particle energy and rigidity, and between the omnidirectional distribution function and particle density.

As one of the major physical modulation processes in the heliosphere, the basic theory behind particle drifts was presented in the next section, arriving at the expression for the drift coefficient used in this study, namely Eq. (3.25). The drift scale $\lambda_{\mathrm{D}}$, as used in this study, was illustrated in Figure 3.1; the drift patterns for positive and negatively charged particles during both $A > 0$ and $A < 0$ polarity cycles were explained with the help of Figure 3.2.

Section 3.4 presented a discussion of particle diffusion and was subdivided into two sections to treat the parallel and perpendicular diffusion separately. Expressions were given for the parallel diffusion coefficient $\kappa_{||}$, i.e. Eq. (3.31), as well as for the perpendicular diffusion coefficients $\kappa_{\perp r}$ and $\kappa_{\perp\theta}$, i.e. Eqs. (3.32) and (3.33). The rigidity and radial dependencies of these coefficients were illustrated in Figure 3.5.

The last section presented a conversion of the TPE from a field-aligned coordinate system to spherical coordinates to arrive at Eq. (3.43); the physical role of each of the terms in this equation was clearly indicated.

# Chapter 4

# The Numerical Model

## 4.1 Introduction

Chapter 4 commences with a discussion of the relevant background concerning the most prominent numerical models in the field of cosmic ray (CR) modulation studies. It is then motivated why the specific model, based on stochastic differential equations (SDEs), was favored for application in this study, pointing out its various advantages over other models such as the more traditional finite difference models. The relevant theory of SDEs is presented and its implementation is illustrated by means of the simple example of one-dimensional (1D) Brownian motion. The theory of SDEs is then finally implemented in the case of the Parker transport equation (TPE), leading to the SDE-based CR modulation model. The chapter ends with a description of previous benchmarks and applications of this model, clearly establishing its validity and reliability.

## 4.2 Numerical Models for Cosmic Ray Modulation

This section sheds light on the current state of CR modulation studies and sketches a picture of the history and development of this subject. The discussion on specific numerical models is kept brief and for detailed discussions of previous numerical models and of the applicable numerical methods to obtain solutions for the TPE, the reader is referred to Potgieter (1984), le Roux (1990), Steenkamp (1995), Hattingh (1998), Ferreira (2002), Langner (2004), and Strauss (2010, 2013).

The numerical models used in CR modulation studies were traditionally based on the finite difference scheme known as the alternating direction implicit (ADI) method. More recently, models based on the solution of sets of stochastic differential equations (SDEs) have become popular. The next two subsections are devoted to discussing context establishing background information concerning these two prominent numerical approaches. Section 4.2.3 points out the advantages of the SDE-based model, favoring it for application in this study.

### 4.2.1 ADI-based Models

This discussion roughly groups the ADI-based models into three basic categories, namely steady-state models, time-dependent models, and termination shock (TS) models; magneto-hydrodynamic (MHD) models are not considered for the purpose of this study. In this work, numerical models are described as 1D, 2D, or 3D; this, however, only refers to the spatial dimensions − these models are also dependent on energy, constituting an extra dimension, as well as time in the case of time dependent models. Each of the groups

listed above is discussed briefly, with only the research performed by the Potchefstroom modulation group over the last decade being discussed in more detail.

The first numerical solution of the TPE was developed by Fisk (1971). This solution assumed a steady state as well as spherical symmetry, i.e. a 1D model with the radial distance as the only spatial variable. Later, the polar angle was included to form an axisymmetric (2D) steady-state model without drifts (Fisk, 1973). Moraal and Gleeson (1975) improved on this and a few years later gradient and curvature drifts for a flat heliospheric current sheet (HCS) were included in separately developed steady-state 2D models by Moraal et al. (1979) and Jokipii and Kopriva (1979). The waviness of the HCS was first emulated in 2D models by Potgieter (1984) and Burger (1987). See also Potgieter and Moraal (1985) and Potgieter and Burger (1990). After this, an improved 2D wavy current sheet model was developed by Hattingh (1993). See also Hattingh and Burger (1995a).

Kóta and Jokipii (1983) developed the first fully 3D, steady-state model including drifts and a wavy HCS. Further work was later done on this subject by Hatting (1998) (see also Williams, 1990; Hattingh and Burger, 1995b) and by Gil and Alania (2001). Three-dimensional models obviously use more computer time and memory and the claim to fame of the Potchefstroom modulation group has been that modulation in the heliosphere can in many cases be described just as well when using a 2D model as with the use of a 3D model. Such a comparison between 2D and 3D steady-state models was performed by Hattingh (1998) and Ferreira (1998) who found the agreement to be excellent, concluding that 2D models could be used with great confidence. Fichtner et al. (2000) and Ferreira et al. (2001a) independently developed 3D steady-state models including the Jovian magnetosphere as a source of low-energy electrons. This model was improved and extensively utilised by Ferreira (2002).

The "standard" ADI-based model in three dimensions (i.e. three spatial dimensions and energy) has been applied to several different studies. Moeketsi (2004) applied the model in the study of galactic and Jovian electrons in the heliosphere (see also Moeketsi et al., 2005). Nkosi (2006) used the 3D steady-state model of Ferreira (2002) in the study of heliospheric anisotropies in these particles (see also Nkosi et al., 2008, 2011). Vos (2011) comprehensively applied an improved version of the model to the modulation of GCR protons and electrons at Earth, as observed by the PAMELA spacecraft from 2006 to 2009 (see also Potgieter et al., 2014 and Vos et al., 2013a, b). Nndanganeni (2012) also used the 3D steady-state model to study the modulation of GCR electrons from the inner to the outer heliosphere (see also Potgieter and Nndanganeni, 2013).

The first spherically symmetric and time-dependent model was developed by Perko and Fisk (1983), and later extended to two and three dimensions (le Roux, 1990; Fichtner et al., 2001). The extension to two dimensions enabled the study of long-term CR modulation effects and the effects of outward propagating global merged interaction regions (GMIRs) at large radial distances (Potgieter and le Roux, 1994; le Roux and Potgieter, 1995). The extension to three dimensions (Fichtner et al., 2000) was limited to the case for electrons and neglected adiabatic cooling of electrons at lower energies by performing a momentum averaging of the Parker TPE.

In order to calculate CR intensities realistically over consecutive solar cycles, Ferreira and Potgieter (2004) introduced a compound approach where the transport parameters were scaled time-dependently with a function that depends on the observed magnetic field at Earth and the observed HCS tilt angle $\alpha$. This approach has its origin in the work of Ferreira (2002) and effectively simulates the modulation effects of propagating barriers as they move outward in a spatially 2D heliosphere. Ndiitwani (2005) used an improved compound approach to study the time-dependent modulation of CRs in the

heliosphere (see also Ndiitwani et al., 2005). This work was continued by Magidimisha (2010). Time-dependent modulation of CR protons in the inner heliosphere during the solar minimum of 2009 has been studied by Ndiitwani et al. (2013), making use of data provided by PAMELA. Manuel (2013) improved the compound approach by implementing recent theoretical advances in the model and used the model in the study of time-dependent modulation of GCRs in the heliosphere (see also Manuel et al., 2011a, 2014). The model was also used to study signatures of a heliospheric asymmetry and to produce model predictions along the Voyager 1 and Voyager 2 trajectories (Manuel et al., 2013). See also Manuel et al. (2011b) in this regard.

Jokipii (1986) developed the first axisymmetric time-dependent diffusion shock acceleration model to include the heliospheric TS, which gave a natural explanation of several observed features of the anomalous component. Potgieter and Moraal (1988) evinced the possibility to include shock acceleration in a steady-state spherically symmetric model by specifying the appropriate boundary conditions with regard to the CR streaming and spectra at the TS. This model was later expanded to 2D by Potgieter (1989). Still later, Steenkamp (1995) independently developed a 2D shock acceleration model with a discontinuous transition of the solar wind velocity $V_{\rm sw}$ across the TS to study the anomalous component (see also Steenkamp and Moraal, 1993); le Roux et al. (1996) developed a similar model, but with a continuous transition of $V_{\rm sw}$ across the TS. This model was only applied in 1D, although originally developed in 2D; it was expanded by Haasbroek (1997) to include drifts. The Steenkamp (1995) model was improved by Steenberg (1998) and applied extensively to ACRs (see also Steenberg and Moraal, 1996). Ferreira (2002) extensively applied an improved version of the Haasbroek (1997) model to study the TS effects on low-energy galactic and Jovian electrons.

The model was significantly improved by Langner (2004), enabling the simulation of CR modulation at not only solar minimum conditions, but also at moderate solar maximum conditions, i.e. the model was adapted to successfully simulate situations where larger tilt angles up to $\sim 75^\circ$ are concerned. The model was then applied to study the effects of TS acceleration on CRs in the heliosphere (Langner, 2004); a flurry of publications followed on this work, looking specifically at various CR species, e.g. protons and anti-protons, galactic and anomalous Helium, positrons and electrons, and also Carbon and Boron (Langner and Potgieter, 2004a, b; Potgieter and Langner, 2004a, b). The model was also adapted to describe an asymmetric heliosphere and applied in numerous studies (see e.g. Langner and Potgieter, 2005). The model was then improved by Ngobeni (2006), for the first time including the effect of a latitude dependent TS shock, based on the hydrodynamic modeling results of Scherer et al. (2006a). See also Langner and Potgieter (2006) and Ngobeni and Potgieter (2010) in this regard. Utilising this model, work on CR anisotropies in the outer heliosphere was carried out by Ngobeni and Potgieter (2008) and the effects of an asymmetrical heliosphere were investigated by Ngobeni and Potgieter (2011, 2012). Recently, Strauss (2010) improved the model by incorporating stochastic acceleration or momentum diffusion and applying it in the study of the anomalous component of CRs; see also Strauss et al. (2010) and Strauss et al. (2011a) for the case of anomalous Oxygen.

### 4.2.2 SDE-based Models

The use of SDE-based models by the Potchefstroom modulation group started with the model introduced by Strauss et al. (2011b). This is a 3D and time stationary model and, like the models discussed above, includes energy as an extra dimension; the model has since been benchmarked and implemented extensively (see Section 4.6). It is this model

that is improved upon and applied in Chapter 5 and Chapter 6 of this study.

After Zhang (1999) successfully applied SDEs to study CR modulation in the heliosphere, the use of such models has become highly popular. SDE-based models have been used to study the transport of pickup ions (Fichtner et al., 1996), solar energetic particles (Dröge et al., 2010), and other aspects of CR modulation (Florinski and Pogorelov, 2009; Pei et al., 2010). Some historical and contemporary models are discussed by e.g. Krülls and Achterberg (1994), Yamada et al. (1998), Alanko-Huotari et al. (2007), Kopp et al. (2012), Bobik et al. (2012) and Luo et al. (2013a). Kopp et al. (2012) also discussed the mathematical and practical implementation of SDEs for a variety of general transport equations.

### 4.2.3 Favoring the SDE-based Model

The reasons for favoring the SDE-based model are legion. Its advantages range from purely technical considerations to aspects of direct significance to the physics of CR modulation in the heliosphere.

On the technical side, the SDE-approach leads to a numerical model that is ideal for implementation on multiple processors. As will become clear in Section 4.5, the equations at the heart of this model, i.e. Eq. (4.22), form a set of independent Markov chains, i.e. in each of these independent chains the next solution is also independent of the previous solution. This allows for parts of the numerical code to be executed simultaneously and independently, saving a great deal of computation time. ADI-based models, on the other hand, only allow for a linear execution of the numerical code in which each next solution is also dependent on the previous solution.

When it comes to the physics of CR modulation, the advantages of the SDE-approach were illustrated in much detail by Strauss et al. (2011b, c, 2012) as well as Strauss (2013). The model is especially powerful in its ability to visualise the modulation process and, as such, is able to calculate pseudo-particle trajectories or − equivalently stated − follow the evolution of individual density elements; this leads to the possibility of calculating other modulation features which were previously not possible. The concept of a pseudo-particle and also that of pseudo-particle trajectories/traces feature in much of the text to follow and have been discussed in detail by Strauss (2013). For the purpose of this study, it is only important to take notice that a pseudo-particle does not represent an actual, physical particle, but is rather defined as an ensemble of real CR particles, where the ensemble is constructed in such a way that it results in a gyro- and isotropic collection of particles; a more accurate term for a pseudo-particle is that of a "phase space density element". The concept of a pseudo-particle trajectory will become clear in the following sections.

Two especially useful quantities of which the calculation is enabled by this ability to construct pseudo-particle trajectories, are the *propagation times* ($\tau$) and *energy losses* ($\Delta E$) of particles in the heliosphere. The propagation time $\tau$ is defined as the amount of time (on average) that a CR particle spends traveling from the HP to Earth, while $\Delta E$ is defined as the associated loss in energy of that particle, being subjected to modulation in the heliosphere. Notice that this paragraph is written from the perspective of a time forward evolution. In terms of time backward evolution, the values of $\tau$ and $\Delta E$ remain the same, though the definitions would change accordingly, i.e. $\Delta E$ now being a gain in energy. Calculations of $\tau$ and $\Delta E$ and the significant new insight it brings into the modulation process were illustrated by Strauss et al. (2011b, c, 2012) and Strauss (2013). Some of these aspects are discussed in more detail in Section 4.6 of this work.

Another major advantage of the SDE-approach is the remarkable numerical stability of the model as well as the independence of a spatial grid. This makes it possible to

incorporate into the model detailed (realistic) descriptions of the heliosphere and heliospheric structures. Examples of such implementations include the works of Strauss et al. (2011b), including the relative motion of Jupiter, and Strauss et al. (2012), implementing a fully 3D wavy HCS. ADI-based models, on the other hand, are notoriously unstable when solving differential equations in higher dimensions.

The statistical nature of the SDE-based model has yet another advantage as a consequence: it enables an interpretation of the obtained results within the framework of *accuracy*, i.e. valid comment on the accuracy of these solutions is possible. This matter is discussed in more detail in Chapter 5.

There are really not many disadvantages to the implementation of the SDE-based model, the only "real" disadvantage being the inherent difficulty to calculate global CR intensities. The model only calculates the CR intensity at a single point in phase space and must therefore be repeated for each other position in phase space where the intensity is required. This issue, however, can be overcome by implementing multiple instances of the model on different computational nodes of a computer cluster.

Except for this one "real" disadvantage, there are some factors that should be kept in mind when working with the SDE-based model. Because of its basically unconditional numerical stability, the model will allow a user to calculate solutions for unrealistic and even unphysical situations without running into trouble in the process of calculation. Any user of such code, therefore, would have to possess a good working knowledge of the particular model; only then can reliable conclusions from such obtained results be drawn. Much of this problem can be solved, however, by building statements into the code that are designed to test conditions for validity. The problem may also be alleviated by including a user's manual with the code.

Overall, the advantages of SDE-based models are plenty and by far outweigh the few disadvantages. The valuable new insight and intuitively confirming results provided by its powerful visualisation capabilities cannot be ignored in the study of CR modulation in the heliosphere. Furthermore, this type of model may allow much advancement in this field because of its numerically stable nature.

## 4.3 Stochastic Differential Equations

Stochastic calculus is a well developed field and, in this work, only the most essential principles are discussed, borrowing directly from the work of Strauss (2013) to construct the following three sections of this chapter. For any further reading on this topic, the reader is referred to several standard texts on SDEs (e.g. Gardiner, 1983; Kloeden et al., 1994; Kloeden and Platen, 1999; Øksendal, 2003).

For the purpose of this work, it is sufficient to define an SDE as any equation that can be cast into the general form

$$\frac{\partial x(t)}{\partial t} = \mu(x,t) + \sigma(x,t)\zeta(t), \tag{4.1}$$

for the 1D case where $\mu(x,t)$ and $\sigma(x,t)$ are continuous functions, while $\zeta(t)$ represents a rapidly varying stochastic function, also referred to as the noise term. The first and second terms on the right hand side of Eq. (4.1) are referred to as the *drift* and *diffusion* terms respectively. These terms are not to be confused with the physical drift and diffusive terms present in the TPE. Moreover, only SDEs of the Itō type are considered, where Eq. (4.1) can be rewritten as

$$dx(t) = \mu(x,t)dt + \sigma(x,t)dW(t), \tag{4.2}$$

where $dW(t)$ represents the Wiener process. This is a time stationary stochastic Levy process where the time increments have a Normal distribution with a mean of zero (i.e. a Gaussian distribution) and a variance of $dt$; $dW(t) = W(t) - W(t - dt) \sim \mathcal{N}(0, dt)$.

Eq. (4.1) can be integrated as

$$x(t) = x_0 + \int_0^t \mu(x, t^{'})dt^{'} + \int_0^t \sigma(x, t^{'})dW(t^{'}), \tag{4.3}$$

where the first integral is a normal (Riemann or Lebesgue) integral, while the second is an Itō type stochastic integral. Since analytical solutions for SDEs are only available for a limited few scenarios, Eq. (4.3) is usually integrated numerically. In this work, the SDEs are integrated by using the Euler-Maruyama numerical scheme (Maruyama, 1955), where a finite time step $\Delta t$ is chosen and Eq. (4.2) is solved iteratively

$$x^{t+\Delta t} = x^t + \mu(x, t)\Delta t + \sigma(x, t)\Delta W(\Delta t), \tag{4.4}$$

from an initial position $x = x_0$ at time $t = 0$ and continued until the boundary is reached at $x = x_\mathrm{e}$ at $t = t_\mathrm{e}$, or until a temporal integration limit is reached at $t = t^\mathrm{N}$; in this work, $\Delta t = 0.001$ PUs, i.e. program units. The Wiener process is discretised as

$$\Delta W(\Delta t) = \sqrt{\Delta t} \cdot \Lambda(t), \tag{4.5}$$

where $\Lambda(t)$ is a simulated Gaussian distributed pseudo-random number. The temporal evolution of $x$ forms a trajectory through phase space, which is generally referred to as the trajectory of a pseudo-particle. Integrating Eq. (4.4) for a single pseudo-particle has no significance, as integration must be carried out over all possible trajectories, so that Eq. (4.4) is usually integrated $N \gg 1$ times; this is also referred to as tracing $N$ pseudo-particles.

Figure 4.1 shows the integration trajectories of $N = 1 \times 10^4$ pseudo-particles using Eq. (4.4) with $\mu(x, t) = 0$ and $\sigma(x, t) = \sqrt{2}$ (top panel) and for $\mu(x, t) = 1$ and $\sigma(x, t) = \sqrt{2}$ (bottom panel). All trajectories start at $x = x_0$ and are continued until $t^\mathrm{N} = 1000$. The trajectory of the last pseudo-particle is coloured red to illustrate the behaviour of a single pseudo-particle. It is important to note that the pseudo-particles all start out at the same position, while, on average, moving to larger values of $|x|$ with time.

A normalised (conditional) probability density $\rho^{'}(x, t)$ can be calculated from the pseudo-particle trajectories, such that

$$\int_\Omega \rho^{'}(x, t)d\Omega = 1, \tag{4.6}$$

where $\Omega$ denotes the entire integration space. Numerically this is done by dividing e.g. $x$ into a series of bins, e.g. $N^{'}$ intervals, and calculating the number of pseudo-particles ending up in each bin, i.e. bin $i$ has $N_i$ particles, and dividing by $N$. The discretised version of Eq. (4.6) thus reads

$$\sum_{i=1}^{N^{'}} \rho_i^{'}(x, t) = \sum_{i=1}^{N^{'}} \frac{N_i}{N} = 1. \tag{4.7}$$

The results of the top panel of Figure 4.1 were binned at different times and the results presented in Figure 4.2. The different pseudo-particle trajectories are again shown in the $xt$-plane, while the numerically calculated $\rho^{'}(x, t)$ is shown in red at $t = 200, 400, 600, 800, 1000$. Note that at $t = 0$, $\rho^{'}(x, t) = \delta(x - 0, t - 0)$, where $\delta$ presents a Dirac-delta function, while at later times, the distribution becomes Gaussian. The next section discusses the results of this figure.

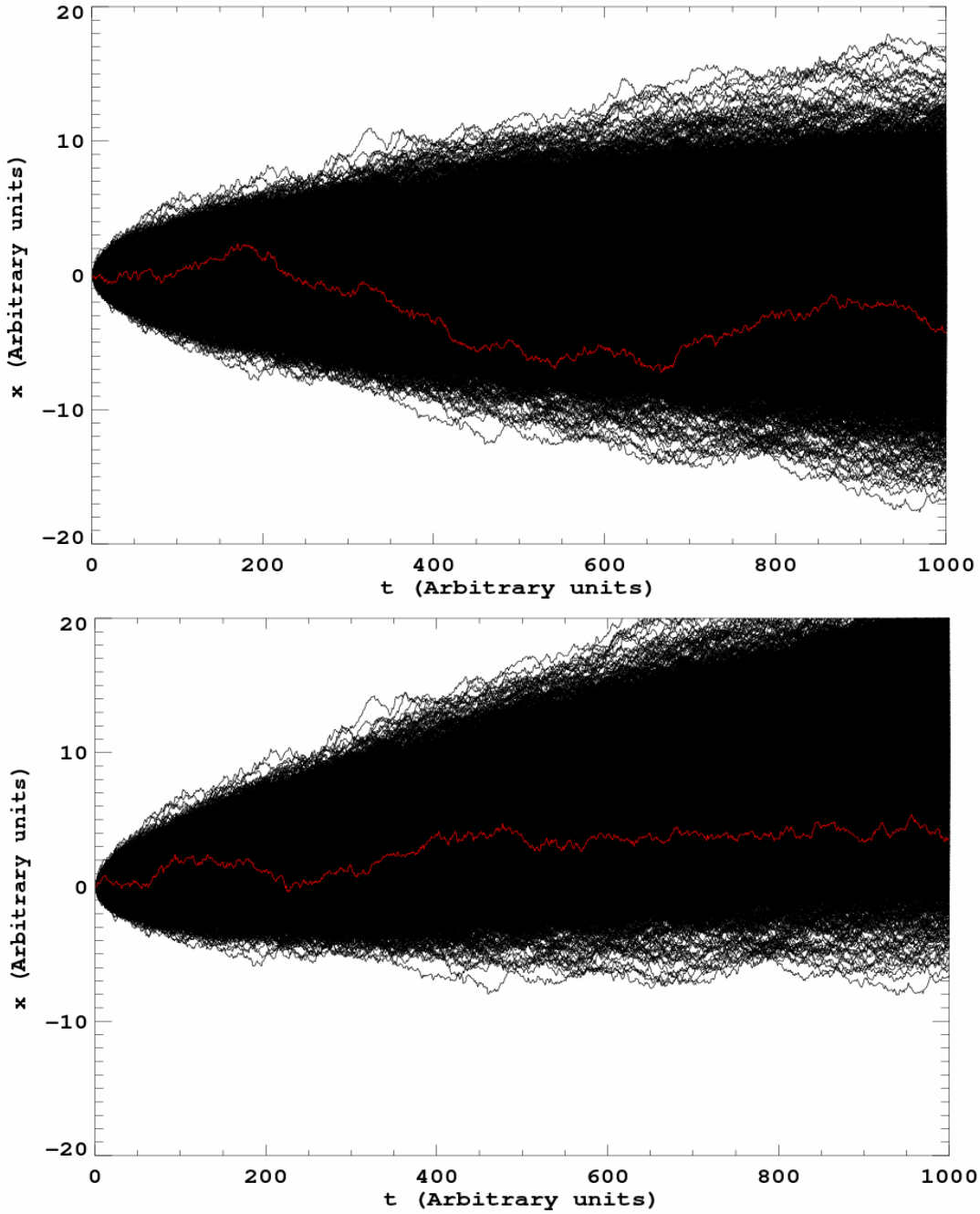


Figure 4.1: *Solutions of Eq. (4.4) using* $\mu(x,t) = 0$ *and* $\sigma(x,t) = \sqrt{2}$ *(top panel) and using* $\mu(x,t) = 1$ *and* $\sigma(x,t) = \sqrt{2}$ *(bottom panel). The integration process is repeated for* $N = 1 \times 10^4$ *pseudo-particles, with the trajectory of the last pseudo-particle coloured red. This figure was taken from Strauss (2013).*

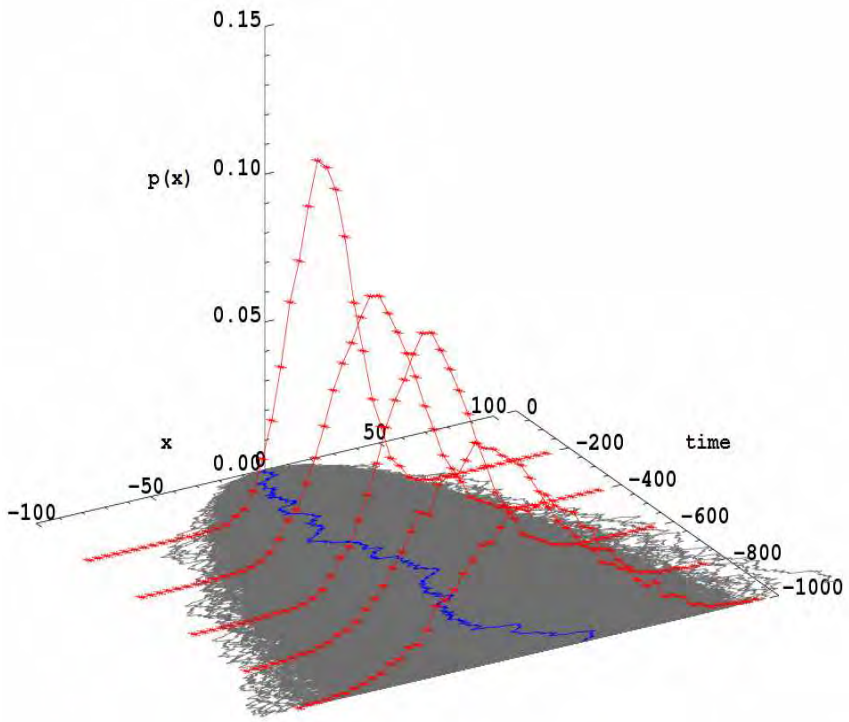


Figure 4.2: *The xt-plane again shows the pseudo-particle traces originally shown in the top panel of Figure 4.1, while the calculated $\rho^{'}(x,t)$ is shown in red at different times. The trajectory of the last pseudo-particle is coloured blue. This figure was taken from Strauss (2013).*

## 4.4 Brownian Motion

Using Itō's lemma, it can be shown that every SDE (or set of SDEs) has an equivalent Fokker-Planck formulation. This is summarised by the so-called Kolmogorov equations, where the 1D time forward Kolmogorov equation, given by

$$\frac{\partial \rho^{'}(x,t)}{\partial t} = \frac{\partial}{\partial x}\left[\mu(x,t)\rho^{'}(x,t)\right] + \frac{1}{2}\frac{\partial^2}{\partial x^2}\left[c(x,t)\rho^{'}(x,t)\right], \tag{4.8}$$

with $c(x,t) = \sigma^2(x,t)$, is equivalent to Eq. (4.2). Any partial differential equation can thus be transformed into an SDE (or set thereof) and vice versa. Using the case of 1D Brownian motion (the apparent irregular motion of particles in a medium), this section illustrates this equivalence.

Assuming Brownian motion due to collisions between e.g. pollen grains and water molecules, Einstein used thermodynamic principles to prove that the evolution of the pollen grains' probability distribution is given by Fick's law

$$\frac{\partial \rho^{'}(x,t)}{\partial t} = -V\frac{\partial \rho^{'}(x,t)}{\partial x} + \kappa\frac{\partial^2 \rho^{'}(x,t)}{\partial x^2}, \tag{4.9}$$

for constant values of $V$ (the convective speed of the medium) and $\kappa$ (the diffusion coefficient). Using the initial condition $\rho^{'}(x,t) = \delta(x-0, t-0)$ and absorbing boundaries, $\rho^{'}(x \longrightarrow \infty, t) = 0$, this equation can be solved analytically to give

$$\rho^{'}(x,t) = \frac{1}{\sqrt{4\pi\kappa t}}\exp\left[\frac{-(x-Vt)^2}{4\kappa t}\right]. \tag{4.10}$$

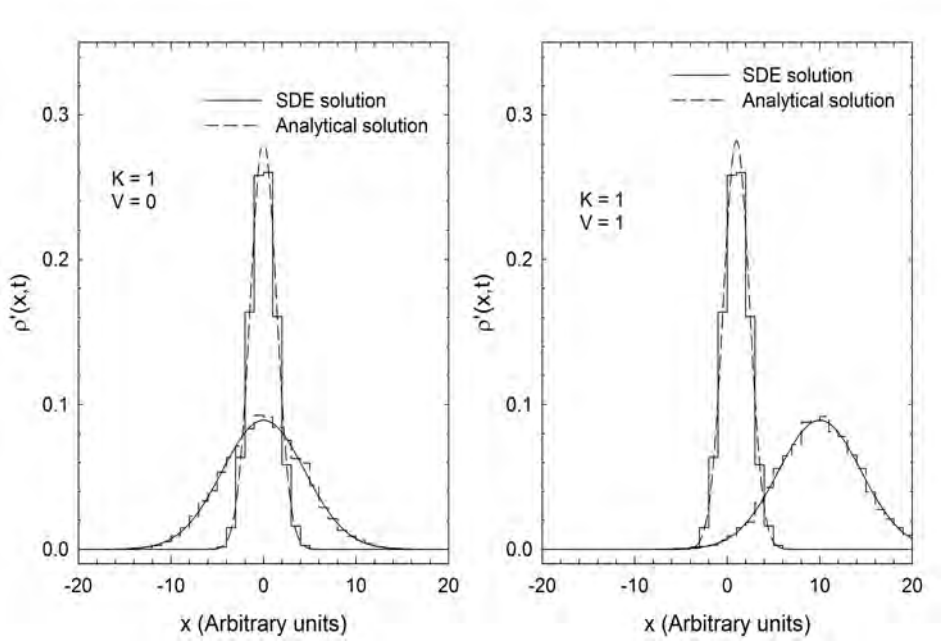


Figure 4.3: *Solutions of Eq. (4.10) for the parameters $\kappa = 1$, $V = 0$ (left panel) and $\kappa = 1$, $V = 1$ (right panel) for $t = 10500$, shown as the dashed lines. The solid lines show the calculated $\rho^{'}(x,t)$ from the SDE-approach in the previous section. In the left panel $\rho^{'}(x,t)$ is calculated from the results shown in the top panel of Figure 4.1, while the results from the bottom panel of that figure are shown in the right panel of this figure. This figure was taken from Strauss (2013).*

This analytical solution is shown in Figure 4.3 for the parameters $\kappa = 1$, $V = 0$ (left panel) and $\kappa = 1$, $V = 1$ (right panel) at $t = 10500$ as the dashed lines. Starting from a delta function, $\rho^{'}(x,t)$ becomes Gaussian, and with time, becomes increasingly broader. This is a well known characteristic of normal diffusion (also referred to as Brownian diffusion). When convection is included in the diffusion process, the Gaussian distribution remains, while $\rho^{'}(x,t)$ is simply convected along $x$.

Using Eq. (4.8), it is clear that Eq. (4.9) and Eq. (4.2) describe the same process, and therefore have the same $\rho^{'}(x,t)$ when

$$\begin{aligned} \mu(x,t) &= V \\ \sigma(x,t) &= \sqrt{2\kappa}. \end{aligned} \tag{4.11}$$

The SDE corresponding to Eq. (4.9) is generally referred to as the Langevin equation and gives an equivalent formulation of Brownian motion. The results from the SDE integration process discussed in the previous section are included in Figure 4.3 and shown as the solid lines. It is clear that both approaches, the SDE- and the more traditional partial differential equation (PDE-) approach, yield the same $\rho^{'}(x,t)$ when the boundary conditions and coefficients used in both approaches are equivalent. Moreover, making the connection between the results of the previous section and Brownian motion, the results of Figure 4.1 can now be interpreted from a physics point-of-view. The integration trajectories can be interpreted, for this specific case, as a possible trajectory of a neutral particle undergoing diffusion and convection in a medium, e.g. at $t = 0$ pollen grains are released at $x = 0$ in a standing pond (top panel) and in a moving stream (bottom panel). In the top panel they undergo diffusion, which leads to $\langle \Delta x^2 \rangle \propto \langle \Delta t \rangle$, so that the particles generally move away from one another (i.e. the particle density gradient becomes smaller

with time). In the bottom panel, where the pollen grains also undergo convection, the medium simply convects the particle density toward larger values of $x$.

## 4.5 The SDE-based Cosmic Ray Transport Model

This section establishes the SDE-based CR transport model by deriving the general SDE-formulation of the TPE and explaining how it can be solved numerically to model GCR transport in the heliosphere. The boundary conditions applicable in the model are also discussed.

### 4.5.1 SDE-formulation for the TPE

The TPE is solved by means of SDEs in a so-called *time backward* fashion. The time backward and time forward approaches are equivalent, but for CR modulation, the latter approach is numerically easier to handle and also computationally much faster. An *observational point* is chosen $(\vec{x}^0, s^0)$, i.e. the phase space position where the CR intensity will be calculated, and the trajectory of a pseudo-particle is then integrated time backwards until a modulation boundary is reached at $(\vec{x}^{\mathrm{e}}, s^{\mathrm{N}})$. Here, $s$ is the time backward parameter, related to $t$ by

$$s = t^{\mathrm{N}} - t, \tag{4.12}$$

i.e. in the normal time forward scenario, integration is performed in the time domain $t = 0 \longrightarrow t = t^{\mathrm{N}}$, while in the time backward case, this becomes $s = 0(t = t^{\mathrm{N}}) \longrightarrow s = s^{\mathrm{N}}(t = 0)$. In both cases, however, the temporal integration domain remains constant, i.e. $t^{\mathrm{N}} = s^{\mathrm{N}}$. Furthermore, $\vec{x}$ represents any set of phase space coordinates. From Eq. (4.12) it follows that

$$\frac{\partial}{\partial t} = -\frac{\partial}{\partial s}. \tag{4.13}$$

For an $n$ dimensional set of SDEs, the general formulation becomes

$$dx_i = \mu_i(x_i, s)ds + \sum_{j=1}^{n} \sigma_{ij}(x_i, s) \cdot dW_i(s), \tag{4.14}$$

where $\vec{\mu}$ is an $n$-dimensional vector and $\boldsymbol{\sigma}$ is an $n \times n$ matrix. When time backward integration is performed, Eq. (4.14) is equivalent to the following Fokker-Planck equation (also referred to as the time backward Kolmogorov equation)

$$-\frac{\partial \rho'(x_i, s)}{\partial s} = \sum_{i=1}^{n} \mu_i(x_i, s)\frac{\partial \rho'(x_i, s)}{\partial x_i} + \frac{1}{2}\sum_{i=1}^{n}\sum_{j=1}^{n} C_{ij}(x_i, s)\frac{\partial^2 \rho'(x_i, s)}{\partial x_i \partial x_j}. \tag{4.15}$$

Note that this equation is similar to Eq. (4.8), although the latter is in a conservative form. See Kopp et al. (2012) for a detailed discussion on how the time forward and backward SDE-formulation is related to different Fokker-Planck equations. Here,

$$C_{ij}(x_i, s) \equiv \left(\sigma_{ij}(x_i, s) \cdot \sigma_{ij}(x_i, s)^T\right). \tag{4.16}$$

The TPE can therefore be cast into the form of Eq. (4.15), the quantities $\vec{\mu}$ and $\boldsymbol{\sigma}$ obtained, and the equivalent SDE-formulation for CR transport emerges naturally. The $n$-dimensional TPE is therefore transformed into a set of $n - 1$, 2D SDEs, with the latter being much easier to handle numerically.

Equivalent to Eq. (3.42), the TPE in spherical coordinates can be written as

$$\begin{aligned}
\frac{\partial f}{\partial t} &= \left[\frac{1}{r^2}\frac{\partial}{\partial r}\left(r^2\kappa_{rr}\right) + \frac{1}{r\sin\theta}\frac{\partial}{\partial\theta}\left(\kappa_{\theta r}\sin\theta\right) + \frac{1}{r\sin\theta}\frac{\partial\kappa_{\phi r}}{\partial\phi} - V_r\right]\frac{\partial f}{\partial r} \\
&+ \left[\frac{1}{r^2}\frac{\partial}{\partial r}\left(r\kappa_{r\theta}\right) + \frac{1}{r^2\sin\theta}\frac{\partial}{\partial\theta}\left(\kappa_{\theta\theta}\sin\theta\right) + \frac{1}{r^2\sin\theta}\frac{\partial\kappa_{\phi\theta}}{\partial\phi} - \frac{1}{r}V_\theta\right]\frac{\partial f}{\partial\theta} \\
&+ \left[\frac{1}{r^2\sin\theta}\frac{\partial}{\partial r}\left(r\kappa_{r\phi}\right) + \frac{1}{r^2\sin\theta}\frac{\partial\kappa_{\theta\phi}}{\partial\theta} + \frac{1}{r^2\sin^2\theta}\frac{\partial\kappa_{\phi\phi}}{\partial\phi} - \frac{1}{r\sin\theta}V_\phi\right]\frac{\partial f}{\partial\phi} \\
&+ \kappa_{rr}\frac{\partial^2 f}{\partial r^2} + \frac{\kappa_{\theta\theta}}{r^2}\frac{\partial^2 f}{\partial\theta^2} + \frac{\kappa_{\phi\phi}}{r^2\sin^2\theta}\frac{\partial^2 f}{\partial\phi^2} + \frac{2\kappa_{r\phi}}{r\sin\theta}\frac{\partial^2 f}{\partial r\partial\phi} + \frac{2\kappa_{r\theta}}{r}\frac{\partial^2 f}{\partial r\partial\theta} \\
&+ \frac{2\kappa_{\theta\phi}}{r^2\sin\theta}\frac{\partial^2 j}{\partial\phi\partial\theta} + \frac{p}{3}\left(\nabla\cdot\vec{V}_{\rm sw}\right)\frac{\partial f}{\partial p},
\end{aligned} \tag{4.17}$$

where $\vec{V} = \vec{V}_{\rm sw} + \vec{v}_{\rm d}$ was introduced. Assuming that $f(\vec{x},t) \propto \rho'(\vec{x},t)$ and using Eq. (4.13), it follows that

$$\begin{aligned}
\mu_r &= \frac{1}{r^2}\frac{\partial}{\partial r}\left(r^2\kappa_{rr}\right) + \frac{1}{r\sin\theta}\frac{\partial}{\partial\theta}\left(\kappa_{\theta r}\sin\theta\right) + \frac{1}{r\sin\theta}\frac{\partial\kappa_{\phi r}}{\partial\phi} - V_r \\
\mu_\theta &= \frac{1}{r^2}\frac{\partial}{\partial r}\left(r\kappa_{r\theta}\right) + \frac{1}{r^2\sin\theta}\frac{\partial}{\partial\theta}\left(\kappa_{\theta\theta}\sin\theta\right) + \frac{1}{r^2\sin\theta}\frac{\partial\kappa_{\phi\theta}}{\partial\phi} - \frac{1}{r}V_\theta \\
\mu_\phi &= \frac{1}{r^2\sin\theta}\frac{\partial}{\partial r}\left(r\kappa_{r\phi}\right) + \frac{1}{r^2\sin\theta}\frac{\partial\kappa_{\theta\phi}}{\partial\theta} + \frac{1}{r^2\sin^2\theta}\frac{\partial\kappa_{\phi\phi}}{\partial\phi} - \frac{1}{r\sin\theta}V_\phi \\
\mu_p &= \frac{p}{3}\left(\nabla\cdot\vec{V}_{\rm sw}\right),
\end{aligned} \tag{4.18}$$

and

$$\mathbf{C} = \begin{bmatrix} \kappa_{rr} & \frac{\kappa_{r\theta}}{r} & \frac{\kappa_{r\phi}}{r\sin\theta} \\ \frac{\kappa_{r\theta}}{r} & \frac{\kappa_{\theta\theta}}{r^2} & \frac{\kappa_{\theta\phi}}{r^2\sin\theta} \\ \frac{\kappa_{r\phi}}{r\sin\theta} & \frac{\kappa_{\theta\phi}}{r^2\sin\theta} & \frac{\kappa_{\phi\phi}}{r^2\sin\theta} \end{bmatrix}, \tag{4.19}$$

and the multi-dimensional Wiener process

$$d\vec{W} = \left[dW_r, dW_\theta, dW_\phi\right]. \tag{4.20}$$

Note that because only spatial diffusion is taken into account, $\boldsymbol{\sigma}$ can be reduced from a $4 \times 4$ matrix to a $3 \times 3$ matrix (see also the discussion by Kopp et al., 2012). To calculate $\boldsymbol{\sigma}$, the square root of $\mathbf{C}$ must be calculated. As discussed by e.g. Johnson et al. (2002), the magnitude and form of $\boldsymbol{\sigma}$ may not be unique, but all of these $\boldsymbol{\sigma}$'s will be mathematically equivalent. Here, $\sigma_{\theta r} = \sigma_{\phi r} = \sigma_{\phi\theta} = 0$, while the other elements of $\boldsymbol{\sigma}$ are

given by

$$\begin{aligned}
\sigma_{rr} &= \sqrt{\frac{\kappa_{\phi\phi}\kappa_{r\theta}^2 - 2\kappa_{r\phi}\kappa_{r\theta}\kappa_{\theta\phi} + \kappa_{rr}\kappa_{\theta\phi}^2 + \kappa_{\theta\theta}\kappa_{r\phi}^2 - \kappa_{rr}\kappa_{\theta\theta}\kappa_{\phi\phi}}{\kappa_{\theta\phi}^2 - \kappa_{\theta\theta}\kappa_{\phi\phi}}} \\
\sigma_{r\theta} &= \frac{\kappa_{r\phi}\kappa_{\theta\phi} - \kappa_{r\theta}\kappa_{\phi\phi}}{\kappa_{\theta\phi}^2 - \kappa_{\theta\theta}\kappa_{\phi\phi}}\sqrt{\kappa_{\theta\theta} - \frac{\kappa_{\theta\phi}^2}{\kappa_{\phi\phi}}} \\
\sigma_{r\phi} &= \frac{\kappa_{r\phi}}{\sqrt{\kappa_{\phi\phi}}} \\
\sigma_{\theta\theta} &= \frac{1}{r}\sqrt{\kappa_{\theta\theta} - \frac{\kappa_{\theta\phi}^2}{\kappa_{\phi\phi}}} \\
\sigma_{\theta\phi} &= \frac{\kappa_{\theta\phi}}{r\sqrt{\kappa_{\phi\phi}}} \\
\sigma_{\phi\phi} &= \frac{\sqrt{\kappa_{\phi\phi}}}{r\sin\theta}.
\end{aligned} \tag{4.21}$$

The set of SDEs governing CR transport therefore becomes

$$\begin{aligned}
dr &= \mu_r \cdot ds + \sigma_{rr} \cdot dW_r + \sigma_{r\theta} \cdot dW_\theta + \sigma_{r\phi} \cdot dW_\phi \\
d\theta &= \mu_\theta \cdot ds + \sigma_{\theta\theta} \cdot dW_\theta + \sigma_{\theta\phi} \cdot dW_\phi \\
d\phi &= \mu_\phi \cdot ds + \sigma_{\phi\phi} \cdot dW_\phi \\
dp &= \mu_p \cdot ds,
\end{aligned} \tag{4.22}$$

which can be integrated relatively easily by means of the Euler-Maruyama scheme mentioned earlier. Note that the momentum SDE can also be rewritten in terms of kinetic energy as

$$dE = \frac{1}{3}\left(\nabla \cdot \vec{V}_{\rm sw}\right)\Gamma E \cdot ds, \tag{4.23}$$

with

$$\Gamma \equiv \frac{E + 2E_0}{E + E_0}, \tag{4.24}$$

where $E_0$ is the rest mass energy.

### 4.5.2 Boundary Conditions

#### The Outer Modulation Boundary

A Dirichlet boundary condition is specified at the HP for GCRs as the local interstellar spectrum (LIS). In general it can be handled by using the Green's function interpretation of the conditional probability density $\rho'(\vec{x}, t)$ (e.g. Webb and Gleeson, 1977),

$$f(\vec{x}^0, t^0) = \int_0^{t^0} \int_{\vec{x}\in\Omega_{\rm b}} f_{\rm b}(\vec{x}, t)\rho'(\vec{x}, t)d\Omega dt + \int_\Omega f_{\rm a}(\vec{x}, 0)\rho'(\vec{x}, 0)d\Omega, \tag{4.25}$$

where $f_{\rm b}(\vec{x}, t)$ represents the boundary condition (i.e. the LIS), $f(\vec{x}^0, t^0)$ the phase space position where the intensity is calculated, i.e. the observational point. In the last term on the right hand side, $f_{\rm a}(\vec{x}, 0)$ represents the initial condition, which for CR modulation is

usually set to zero; this corresponds to a heliosphere initially empty of CRs. The boundary of the integration domain is represented by $\Omega_\mathrm{b}$ and $\vec{x} = \{r, \theta, \phi, p\}$. For the purposes of this work, only steady state solutions of the TPE are considered, where $t \longrightarrow \infty$ (no temporal restriction on the time), reducing Eq. (4.25) to

$$f(\vec{x}^0) = \int_{\vec{x}\in\Omega_\mathrm{b}} f_\mathrm{b}(\vec{x})\rho^{'}(\vec{x})d\Omega. \tag{4.26}$$

For CRs, the boundary values are only momentum dependent so that only integration over momentum space is performed, i.e. $d\Omega \longrightarrow dp$,

$$f(\vec{x}^0) = \int_0^p f_\mathrm{b}(p^{'})\rho(\vec{x})dp^{'}\Big|_{\vec{x}\in\Omega_\mathrm{b}}, \tag{4.27}$$

which is essentially a convolution of the boundary condition and the probability distributions.

An approach that is numerically easy is used to incorporate this boundary condition. The weighted value of $f(\vec{x}^0)$ is calculated for each pseudo-particle individually, whereupon it is normalised to the correct magnitude at the end of the integration process. For a single pseudo-particle, reaching a momentum dependent boundary with $p_i = p_i^\mathrm{e}$ (where $i$ labels the pseudo-particles),

$$\rho_i^{'}(\vec{x}) = \delta(p_i - p_i^\mathrm{e})|_{\vec{x}\in\Omega_\mathrm{b}}, \tag{4.28}$$

because of the normalisation condition. This implies that

$$f_i(\vec{x}^0) = f_\mathrm{b}(p_i^\mathrm{e}), \tag{4.29}$$

so that each pseudo-particle traced to the boundary makes some weighted contribution to the total solution. Repeating for $N \gg 1$ pseudo-particles, the numerical solution of the TPE can be calculated as

$$f(\vec{x}^0) = \frac{1}{N}\sum_{i=1}^{N} f_\mathrm{b}(p_i^\mathrm{e}), \tag{4.30}$$

which follows from Eqs. (4.7) and (4.27).

### The Inner Modulation Boundary

The inner modulation boundary is a Neumann boundary condition. Generally, all models assume a boundary condition at small values of $r$. This is mainly done because some of the heliospheric parameters, e.g. the HMF, is undefined at $r = 0$. Here, a reflecting inner boundary condition is assumed at $r_\mathrm{in} = 0.1$ AU,

$$\frac{\partial f(\vec{x})}{\partial r}\Big|_{r=r_\mathrm{in}} = 0. \tag{4.31}$$

For SDEs, this means that a pseudo-particle penetrating this boundary is again placed into the computational domain by reflection at the boundary

$$r < r_\mathrm{in} : r \longrightarrow 2r_\mathrm{in} - r. \tag{4.32}$$

In Chapter 5, the use of the reflective as well as an absorbing boundary is discussed, illustrating their respective effects on modulation.

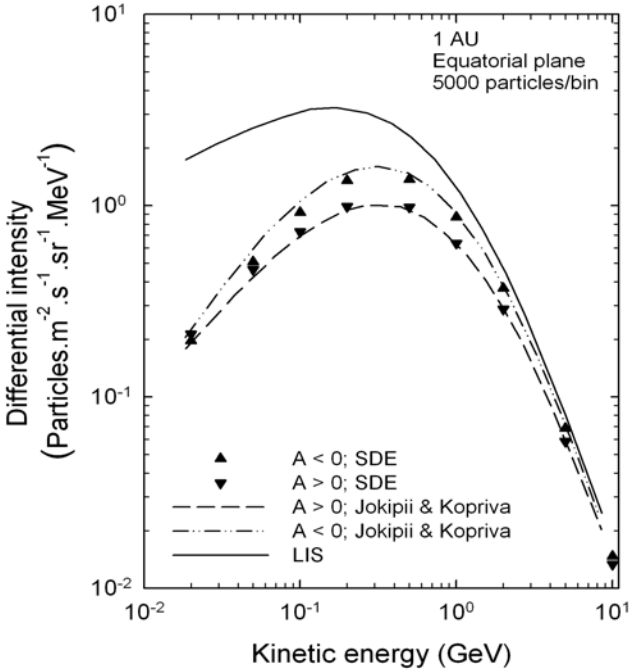


Figure 4.4: *Benchmarking of the 3D SDE-based model with the earlier 2D finite difference model of Jokipii and Kopriva (1979) for the modulation of GCR protons at Earth. The results from these authors are shown by the lines, while the SDE-results are represented by the scatter plots. The solid line represents the LIS. Here, $N = 5 \times 10^3$ pseudo-particles were traced for each phase-space position in the SDE-based model. This figure was taken from Strauss et al. (2011b).*

### Other Boundary Related Conditions

Although the SDE-approach does not have to prescribe boundary conditions at the computational domains of the angular coordinates, the angular position of the pseudo-particles needs to be renormalised so that $\theta \in [0, \pi]$ and $\phi \in [0, 2\pi]$. This is done by specifying the following conditions:

$$\begin{array}{lll} \phi < 0 & : & \phi \longrightarrow \phi + 2\pi \\ \phi > 2\pi & : & \phi \longrightarrow \phi - 2\pi \\ \theta < 0 & : & \theta \longrightarrow |\theta|; \phi \longrightarrow \phi \pm \pi \\ \theta > \pi & : & \theta \longrightarrow 2\pi - \theta; \phi \longrightarrow \phi \pm \pi, \end{array} \tag{4.33}$$

which occur when the pseudo-particle either propagates around the ecliptic plane or crosses the solar poles.

## 4.6 Previous Benchmarks and Implementations of the SDE-based Model

The validity and reliability of the SDE-based numerical model have been established in the past by extensive benchmarking and this section gives an overview of this process (Strauss et al., 2011b, c, 2012) as well as key implementations of the model in its various stages of development. Section 4.2.3 pointed out the reasons for favoring an SDE-based modulation model over the more traditional ADI-based models, and in this section some

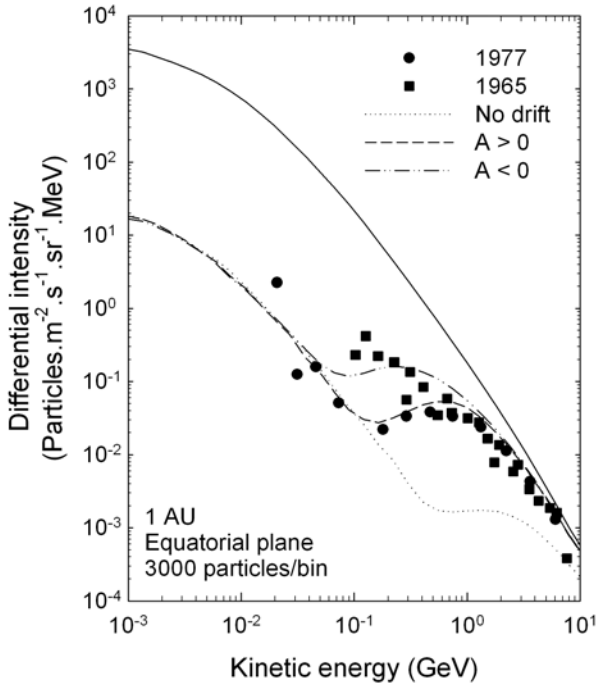


Figure 4.5: *Computed GCR electron energy spectra at Earth with respect to the LIS at 140 AU for three cases: neglecting drifts in the model (dotted line), and for the $A > 0$ (dashed line) and $A < 0$ (dash-dotted line) HMF polarity cycles. Electron observations at Earth for both HMF cycles ($A < 0$ in 1965 and $A > 0$ in 1977), taken from a compilation by Potgieter and Moraal (1985), are shown for qualitative comparison. This figure was taken from Strauss et al. (2011b).*

of those topics are illustrated. A summary of this quite lengthy section can be found in Chapter 5.2.

In the benchmarking of Strauss et al. (2011b), the SDE-based model was utilised to model the modulation of galactic and Jovian electrons. At that time, the model was still employing a flat HCS and, for this reason, the results of Jokipii and Kopriva (1979) were selected for the benchmark. Jokipii and Kopriva (1979) used a finite difference numerical scheme in two spatial dimensions $(r, \theta)$.

Figure 4.4 shows the results for galactic protons in the two HMF polarity cycles, with all modulation parameters chosen to be the same as that of Jokipii and Kopriva (1979), but with the HCS drift approximated by an expression by Burger et al. (1985). The scatter plots show the SDE-based results, while the dashed and dash-dotted lines represent the results by Jokipii and Kopriva (1979). The solid line shows the unmodulated spectrum (LIS). These results clearly compare excellently. Zhang (1999) also benchmarked an SDE-based model, developed in Cartesian coordinates, with the results of Jokipii and Kopriva (1979) and found similar good agreement. This good comparison between the three models proved the SDE-approach of Strauss et al. (2011b), using spherical coordinates, to be equally valid and reliable.

Furthermore, except for the benchmarking, the modulation results of Strauss et al. (2011b) also served as confirmation of the model. In Figure 4.5, energy spectra for GCR electrons are shown for three cases: a non-drift solution (dotted line), a solution for the $A > 0$ polarity cycle (dashed line), and a solution for the $A < 0$ cycle (dash-dotted line). The solid line shows the assumed LIS at the HP. Also included are electron observations at Earth from 1977 ($A > 0$ cycle) and 1965 ($A < 0$ cycle) taken from Potgieter and Moraal

(1985). This qualitative comparison between the modeled and observed spectra showed that the SDE-approach was able to reproduce HMF-polarity-dependent modulation at Earth. Note that below $\sim$ 30 MeV all computed solutions converge to the non-drift solution; this effect was due to a drift suppression factor in the expression for the drift coefficient at low energies. These results are in excellent agreement with ADI-based modeling of galactic electrons (Potgieter, 1996). The work of Strauss et al. (2011b) also considered the modulation of Jovian electrons. Results of energy spectra, as well as radial intensity profiles, with the inclusion of both galactic and Jovian electrons into the model, showed the same qualitative behaviour as noted in previous modulation studies (e.g. Potgieter and Ferreira, 2002). The model was also able to reproduce the well-known $\sim$ 13 month periodicity in Jovian electron intensities as observed at Earth over longer timescales, in accordance with observations from e.g. Moses (1987), and the ADI-based modeling of Ferreira et al. (2004).

As mentioned earlier, the SDE-based model allows for the calculation of pseudo-particle trajectories, from which valuable insight into the modulation process can be gleaned. Figure 4.6 presents such a spatially 3D representation of GCR electron trajectories. The configuration on the left is for the $A > 0$ cycle, while the right hand side depicts the situation for the $A < 0$ cycle, the axes being labeled in units of AU. This illustration, which is impossible to produce with non-SDE-models, illustrates results which are in qualitative agreement with results from ADI-based models: it confirms that electrons observed at Earth during the $A > 0$ cycle drift to the inner heliosphere via the equatorial regions and stay close to the HCS until they reach Earth; for the $A < 0$ cycle, exactly the opposite is predicted, where electrons drift inward from the polar regions to reach the equatorial regions and the Earth.

Strauss et al. (2011b) also allotted some time to discuss the two quantities (first mentioned in Section 4.2.3) that specifically cannot be calculated using ADI-based models, namely propagation times and energy losses of particles (electrons) in the heliosphere. It was found that the propagation time in the $A > 0$ cycle was a factor $\sim 2$ greater than that during the $A < 0$ cycle. This is as expected, since electrons drifting inward from the poles must reach Earth in a lesser amount of time than electrons drifting inwards along the HCS. The propagation time in the case of the non-drift scenario was the greatest; again, as expected, since in this case the electrons had no help from drifts in reaching the Earth. Furthermore, Strauss et al. (2011b) made the connection between the propagation times and energy losses of particles and confirmed it to be correctly described by the model.

The benchmarking of Strauss et al. (2011c) was done focusing specifically on the propagation times and energy losses of CRs in the heliosphere. First, this was done for a spatially 1D scenario so that comparisons with analytical solutions were possible. The first of these 1D cases was a diffusion dominated scenario. Figure 4.7 shows the expectation value of the propagation time $\langle\tau\rangle$ (in units of days) as a function of the diffusion coefficient $\kappa$ (in PUs), as calculated for this scenario. The solid line represents the analytical solution obtained via the probability model of Parker (1965), while the scatter plot represents the solution obtained when utilising the SDE-based model for the same scenario. Excellent agreement between the two solutions was obtained, validating the SDE-approach in calculating $\langle\tau\rangle$.

A second 1D scenario included the effect of convection in the modulation. In this case, analytical solutions of the equation from the probability model are only possible for very limited cases (Parker, 1965; O'Gallagher, 1975). Therefore, for purposes of the benchmarking, the probability wave equation was solved numerically and done so by means of a finite difference scheme. Figure 4.8 shows these propagation times, again as a function of $\kappa$. The scatter points show the results from the SDE-based model, while the

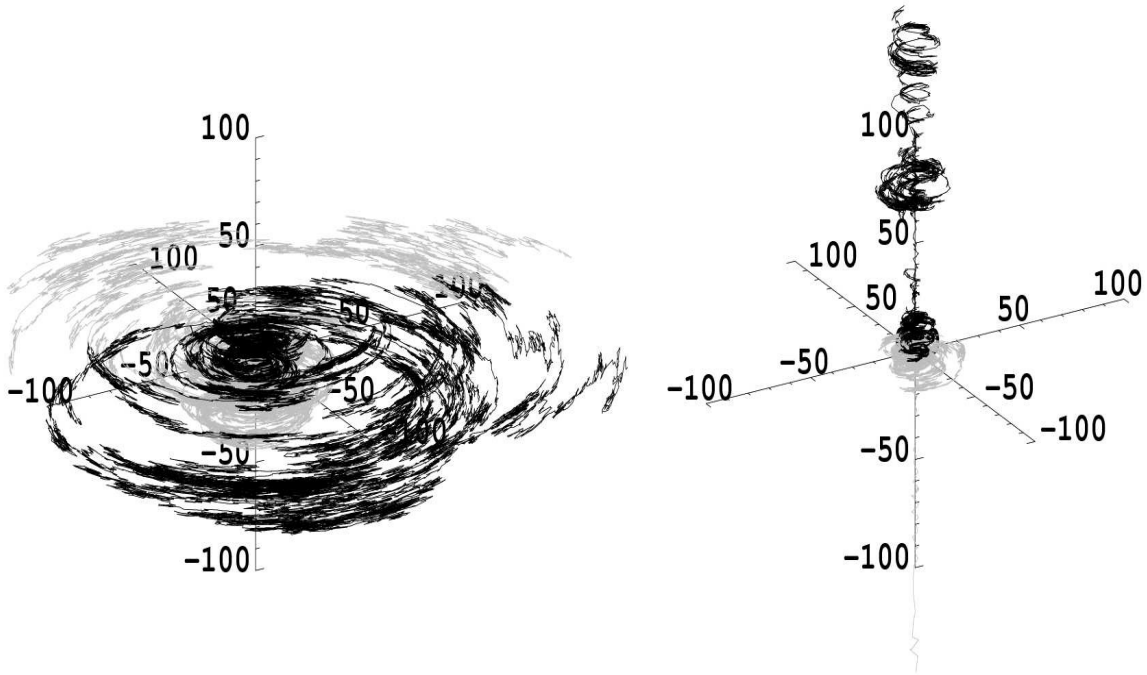


Figure 4.6: *3D spatial representation of trajectories for pseudo-particles (GCR electrons). Two representative particle trajectories (black and grey lines) are shown for the $A > 0$ (left panel) and $A < 0$ (right panel) HMF polarity cycles. In the $A < 0$ cycle, the pseudo-particles are transported mainly toward higher latitudes, while in the $A > 0$ cycle, the particles remain confined to low latitudes and drift inward mainly along the HCS. This figure was taken from Strauss et al. (2011b).*

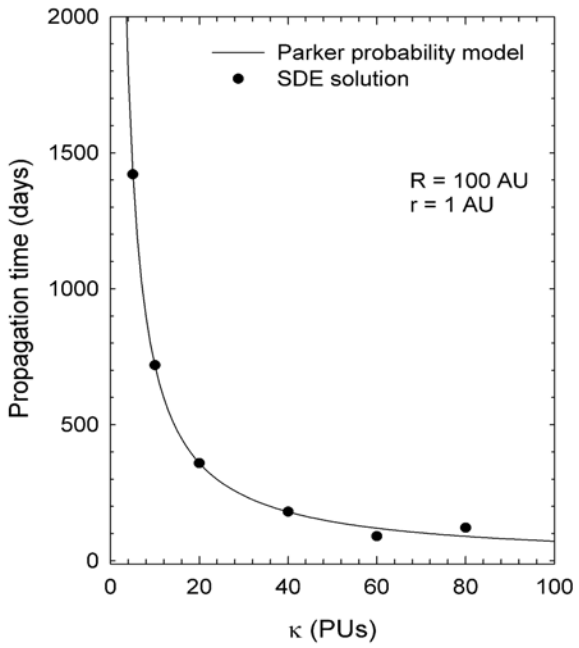


Figure 4.7: *Plot of propagation time $\langle\tau\rangle$ as a function of $\kappa$, as calculated according to the probability model (solid line) and as calculated by the SDE-based model (scatter points) for a diffusion dominated scenario. From a time forwards perspective, the value of $R$ indicates the assumed starting point of the particle (at the HP), while $r$ indicates the end position (Earth). This figure was taken from Strauss et al. (2011c).*

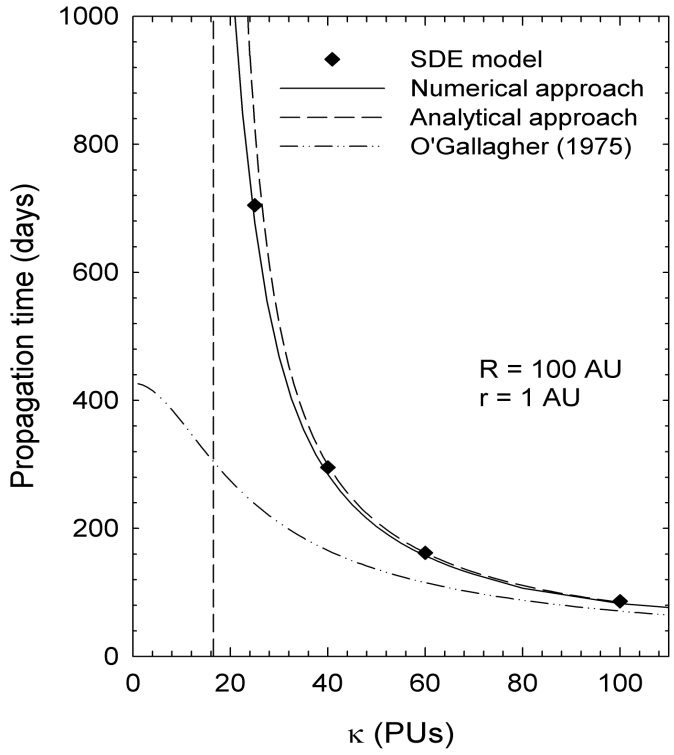


Figure 4.8: *The propagation time $\langle\tau\rangle$ as a function of $\kappa$ for the convection-diffusion model. Scatter points show results of the SDE-model, the solid line of the numerical probability wave approach, the dashed line the analytical solution derived by Strauss et al. (2011c), and the dash-dotted line the analytical solution of O'Gallagher (1975). This figure was taken from Strauss et al. (2011c).*

solid line shows $\langle\tau\rangle$ as calculated numerically according to the wave probability approach. The dashed line shows $\langle\tau\rangle$ as calculated analytically by Strauss et al. (2011c), while the dash-dotted line does so for the solution calculated by O'Gallagher (1975). The vertical dashed line shows the value of $\kappa$ where $\langle\tau\rangle$ as calculated analytically by Strauss et al. (2011c) goes to infinity. For larger values of $\kappa$ the results from the SDE-based model are in good comparison with the analytical solution of Strauss et al. (2011c), while being in good comparison with the numerical wave probability results over all values of $\kappa$. The analytical solution of O'Gallagher (1975), however, deviates completely from the SDE-results; this solution predicts a finite $\langle\tau\rangle$ when $\kappa \longrightarrow 0$, which is clearly not a physical situation for CRs in the heliosphere. This very good agreement between models once again validates the SDE-approach in the calculation of $\langle\tau\rangle$.

As stated earlier, this work of Strauss et al. (2011c) also afforded a more in-depth look at the energy losses experienced by CRs in the heliosphere. If $E^0$ is the energy with which a pseudo-particle ends up at the observational point Earth (speaking from a time forward perspective) and $E^{\mathrm{e}}$ is the energy of that pseudo-particle when it enters the modulation volume at the HP, then the expectation value of the fractional energy loss can be expressed as $\langle E^{\mathrm{e}}/E^0\rangle$. Figure 4.9 shows such values as a function of $\kappa$, with the scatter points representing the SDE-based results. The solid line shows the analytical approximation for relativistic CRs, while the dashed line does so for the case of non-relativistic CRs. The horizontal dotted line shows the limiting case of $\langle E^{\mathrm{e}}/E^0\rangle = 1$. The SDE-based electron solutions agree quite well with the analytically calculated relativistic

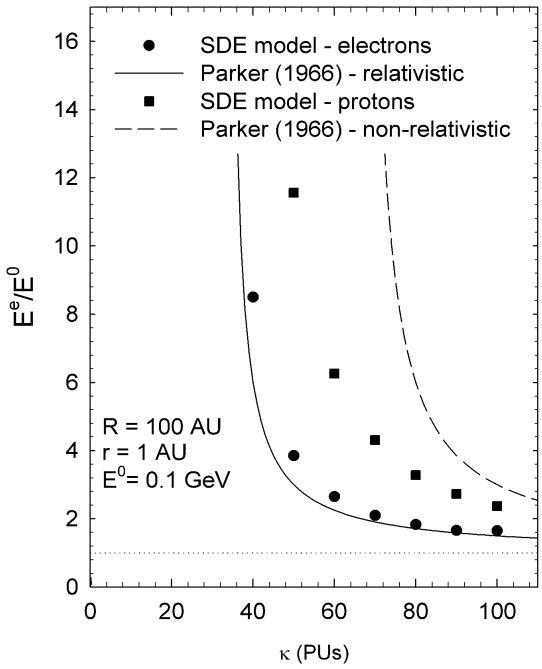


Figure 4.9: *The scatter plots show $\langle E^{\mathrm{e}}/E^0\rangle$ as a function of $\kappa$, as calculated by the SDE-based model. The solid line is the analytical approximation for relativistic CRs, the dashed line for non-relativistic CRs and the horizontal dotted line shows the limiting case of $\langle E^{\mathrm{e}}/E^0\rangle = 1$. This figure was taken from Strauss et al. (2011c).*

case. For protons, the fractional energy loss is expected to be somewhere in between the relativistic and non-relativistic approximations and this is exactly what the SDE-solutions yield. These good comparisons between the results indicate the validity of the SDE-approach in calculating the energy losses experienced by CRs in the heliosphere.

After this thorough benchmarking of Strauss et al. (2011c), the authors applied the model to calculate propagation times and energy losses for GCR protons and electrons in the case of a spatially 3D configuration. The effects of drifts were included and it was illustrated that the model handled these appropriately, according to the assumptions relevant to the modulation parameters.

The work of Strauss et al. (2012) took the 3D SDE-based model another step further by implementing a wavy HCS. The model was benchmarked against two other models, namely that of Pei et al. (2012) and that discussed by Burger (2012). These authors used different numerical schemes, with Pei et al. (2012) using SDEs and Burger (2012) making use of a finite difference scheme. In addition, different approaches to the implementation of the HCS were followed by these authors, with the approach of Strauss et al. (2012) being similar to that of Pei et al. (2012).

Figure 4.10 shows a comparison between the results of these three models. All simulations represent GCR proton energy spectra at Earth in the $A < 0$ drift cycle and using modulation parameters identical to those used by Kóta and Jokipii (1983). Two model scenarios are shown, namely the case for a flat ($\alpha = 0°$) and a warped ($\alpha = 30°$) HCS respectively. It is clear that the results from all three these models agree well, vindicating the approach of Strauss et al. (2012) both in the sense of the numerical scheme and in the sense of the implementation of the drift field. The small discrepancy between the results for the $\alpha = 30°$ case is due to a different expression being used for the extent of the HCS

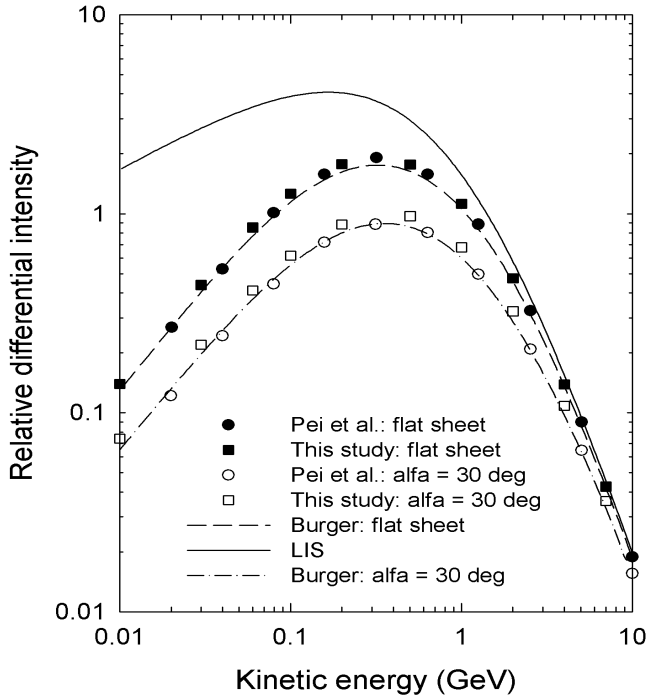


Figure 4.10: *A comparison between proton energy spectra as computed by various spatially 3D drift models. The squares, circles and broken lines respectively represent results from Strauss et al. (2012), Pei et al. (2012) and Burger (2012). Two modeled scenarios are shown: the case for a flat HCS with* $\alpha = 0°$ *and an azimuthaly varying HCS with* $\alpha = 30°$*. This figure was taken from Strauss et al. (2012).*

in the different models, disappearing as $\alpha \longrightarrow 0°$.

The modeling results of Strauss et al. (2012) included computed CR intensities for the different drift cycles and values of $\alpha$. These showed behaviour similar to what is known to be predicted by first generation modulation models and are, as such, in accordance with general drift considerations. The effectiveness of HCS drifts in the $A < 0$ cycle was investigated by calculating propagation times for different values of $\alpha$ and comparing these values to the total path length of the HCS. These results were once again in accord with general drift considerations so that the ability of the SDE-based model to accurately calculate propagation times and incorporate drift effects for a scenario including a fully 3D wavy HCS was validated.

From this discussion it is clear that the SDE-based numerical modulation model has been benchmarked extensively and proven to be valid and reliable. For further discussion of benchmarks and implementations of the model, see Strauss (2013).

## 4.7 Summary and Conclusions

After the introduction in Section 4.1, the reader was introduced to the different numerical models utilised for the purpose of CR modulation studies. These entailed numerical models based on the finite difference approach of the alternating direction implicit (ADI) method and numerical models based on the solution of the appropriate set of stochastic differential equations (SDEs). Numerical models of various degrees of complexity and in various states of development were discussed. The advantages and disadvantages of these

models were considered and it was concluded that, in addition to its numerical prowess, SDE-based models also allow for significant new insights into the physical processes of cosmic ray (CR) modulation in the heliosphere.

In the next section the most essential and relevant theory behind SDEs was discussed; the required definitions and terminology were laid down and the grounds for implementing the theory were established. Section 4.4 illustrated such an implementation in the form of one-dimensional (1D) Brownian motion.

Section 4.5 comprised the core of this chapter, introducing the 3D SDE-based CR modulation model extensively utilised in this work. In the first of two subsections, the SDE-formulation was implemented in the case of the TPE, i.e. the set of SDEs corresponding to the Parker transport equation (TPE) was derived. The second of the two subsections was devoted to establishing the boundary conditions assumed by the model.

The last section was reserved for an overview of previous benchmarks and implementations of the SDE-based model, illustrating its validity and reliability. Some of the advantages discussed in Section 4.2.3 were also revisited in the short discussions on modulation results. This section came to the clear conclusion that the SDE-based numerical model was able to accurately and reliably describe CR modulation in the heliosphere.

# Chapter 5

# Properties and Features of the Numerical Model

## 5.1 Introduction

Chapter 5 familiarises the reader with the specifics of the numerical modulation model used in this study, which is based on the solution of the set of stochastic differential equations (SDEs) that corresponds to the Parker transport equation (TPE). It sketches a background in terms of the established SDE-based model prior to this work and gives an overview of the benchmarking processes that have established its credibility. The basic considerations with all numerical models, namely those of the accuracy and convergence of numerical solutions, as well as the choice of boundary conditions, are discussed. The advancements brought to the pre-established model by this study are introduced and discussed in detail, establishing the model which forms the basis of this work. In this regard, much emphasis is placed on the treatment of the heliospheric neutral current sheet (HCS) and its implications for modulation. The chapter ends with a discussion of further possible improvements to this model that could be developed in future.

## 5.2 Overview of Benchmarking, Implementations and Advantages

The SDE-based modulation model used in this study is based on a numerical model that has been developed and extensively benchmarked by Strauss et al. (2011b, c, 2012). This section shortly revisits Chapter 4 by giving an overview of the benchmarking process during the development of this model; the reader is also reminded of the main advantages of the SDE-based model.

Strauss et al. (2011b) benchmarked the modulation model established at that time with galactic proton energy spectra from Jokipii and Kopriva (1979). Zhang (1999) also benched a three-dimensional (3D) SDE-model, using Cartesian coordinates, with these results. After Strauss et al. (2011b) had found very good comparison with both these models, it was taken as a vindication of the SDE-modeling approach, where the TPE is solved directly in spherical coordinates. As further vindication, a qualitative comparison with observations showed that the model could reproduce electron transport in successive drift cycles. The model was also shown to produce the same qualitative behaviour as noted in previous modulation studies when it comes to electron modulation, including both galactic and Jovian electrons. With regard to Jovian electrons, the model was also shown to be able to reproduce the $\sim 13$ month periodicity in the intensities as observed at

Earth over longer timescales. To summarise, it was shown that the SDE-type modulation model at that time could successfully reproduce the modulation of both galactic and Jovian electrons, as studied previously by models based on the finite difference approach of the alternating direction implicit (ADI) method.

Strauss et al. (2011c) benchmarked their numerical model with known analytical solutions. Since analytical solutions to the TPE are only possible for a few simplified scenarios, this was restricted to a spatially 1D case. Their comparison was successful and thus served as further vindication of their modeling approach. They also compared the energy losses that cosmic rays (CRs) experienced inside the heliosphere, as calculated with their SDE-model which included CR drifts, with previous modeling results (e.g. Potgieter and Moraal, 1985) and found remarkable good agreement for both magnetic polarity cycles.

The model was then improved to implement a wavy neutral current sheet and benchmarked again (Strauss et al., 2012). The benchmarking was done against two other models, namely those discussed by Burger (2012) and Pei et al. (2012) respectively. These models used different numerical schemes with Pei et al. (2012) using an SDE-based numerical model and Burger (2012) using a more traditional finite difference numerical method. The drift field was handled differently in these models, with the approach of Strauss et al. (2012) being similar to that adopted by Pei et al. (2012). Two scenarios were benchmarked: one for a flat neutral current sheet (HCS), i.e. tilt angle $\alpha = 0°$, and one for a warped HCS using $\alpha = 30°$. Strauss et al. (2012) established that the results from all three these models agreed well, once again vindicating their modeling approach − this time with regard to both the numerical scheme and the implementation of the drift field.

In addition to the benchmarking that was carried out, the advantages of using an SDE-based model were also emphasised (Strauss et al., 2011b, c, 2012). It was pointed out that this method allowed for the computation of modulation features which were not possible with the use of previous modulation models. These features included the propagation times that CRs spend in the heliosphere and the quantification of their energy losses during this period by tracing pseudo-particle trajectories. Such trajectories also afford vivid physical illustrations of particle drift and diffusion processes in the heliosphere. Furthermore, because of the numerical stability of the model, more detailed and realistic descriptions of the heliospheric environment can be implemented. The reader is referred to Strauss et al. (2011b, c, 2012) and Strauss (2013) for further details on this subject.

## 5.3 Accuracy and Convergence of Numerical Solutions

Both the questions of accuracy and convergence are important ones in the case of any numerical model. In cases where analytical solutions are obtainable, *accuracy* can be defined as the degree to which the numerically produced solutions deviate from those obtained by analytical means. In other words, the analytical solution is seen as the 'true' solution. *Convergence* can be defined as the tendency of the numerically produced solutions to converge on (or more closely reproduce) the 'true' solution as more and more accurate solutions are obtained.

However, as already mentioned and explained in Chapters 3 and 4, the TPE does not allow for sufficiently inclusive analytical solutions. This has as a consequence that the accuracy and convergence of a numerical model are difficult terms to define, because there simply is no 'true' solution available. In the case of the ADI-based modulation models this

is certainly the case. This complicates modulation studies, since the margin of error on such numerically produced spectra is consequently not easily determined; this fact adds to the difficulties surrounding uncertainties in observation and limitations in theoretical approaches.

In utilising the SDE-based model, however, the concept of the margin of error in any one numerical solution may be much clearer. If $N$ is the number of pseudo-particles used in a simulation, then the statistical groundwork of the model indicates that the solution will be uncertain to within about $1/\sqrt{N} \times 100\%$ of some 'true' solution, defined as a solution in which an infinite number of pseudo-particles is used. The term accuracy is thus defined in this context. However, care has to be taken when assigning such limits to uncertainties for the case of any specific result obtained by using the model, since the calculations performed in obtaining such a result may have led to alterations in these limits. For instance, a result obtained by taking the ratio of two spectra solutions, each with an uncertainty of $1/\sqrt{N} \times 100\%$, will naturally have an uncertainty larger than this value. In addition to this statistical margin of error, there is also a truncation error $\Delta f$ which is of $\mathcal{O}\Delta t$, where $\Delta t$ was defined in Chapter 4. This truncation error is a consequence of the integration of the set of SDEs via the Euler-Maruyama scheme (Maruyama, 1955); however, in this study, $\Delta t$ is kept sufficiently small so that this error is negligible.

In the case of the SDE-based model, the question of convergence has been touched on in the paragraph on accuracy: the greater the number of pseudo-particles $N$ used to obtain the numerical solution, the closer this solution gets to some 'true' solution; there is thus convergence to this solution as $N$ is increased. Figure 5.1 illustrates this convergence, showing galactic cosmic ray (GCR) proton energy spectra at Earth, produced using an increasing number of pseudo-particles, ranging from $N = 10$ (solid red line) to $N = 1\times10^4$ (dashed light blue line). For the sake of the argument it is assumed that the solution using $N = 1\times10^4$ is the 'true' (or at least most accurate) solution. Deviations from this solution start out large, in the case of $N = 10$, and then gradually decrease to the levels displayed by the spectrum using $N = 1\times10^3$ (solid black line). The differences between the spectra using $N = 1\times10^4$ and $N = 1\times10^3$ are hardly significant on the scale of the solutions and led to the decision of employing $N = 1 \times 10^3$ pseudo-particles for simulations of spectra solutions carried out in this work. This implies an uncertainty of about 3% on the numerically produced spectra; to decrease this value to about 1%, using $N = 1 \times 10^4$ is not economical when the amount of extra computation time is considered. Figure 5.1 only goes up to 5 GeV so as to better illustrate the convergence; at higher energies the deviations become even smaller due to decreased modulation.

## 5.4 Boundary Conditions

This section explains and motivates the nature of the boundary conditions chosen to be implemented in the model for the purposes of this study. It also illustrates the degree of sensitivity that the model exhibits to alterations in these conditions and ultimately shows that the behaviour of the model is logical and coherent in this regard.

Throughout this work a reflective inner boundary is assumed, as described in Chapter 4. This inner boundary is situated at $r = r_{\text{in}} = 0.1$ AU; this value is chosen so as to be of the order of the solar source surface, i.e. the radial distance at which the solar wind (SW) flow becomes radial. Figure 5.2 shows proton spectra at Earth and illustrates the effect of changing the value of $r_{\text{in}}$ to, respectively, the assumed minimum value of 0.005 AU (surface of the Sun), 0.5 AU (an intermediate value), and to a value of 0.9 AU which is close to the maximum of 1.0 AU (since the spectra solutions are calculated at $r = 1.0$ AU, an $r_{\text{in}} > 1.0$ AU would not make any physical sense). From this figure, it is immediately

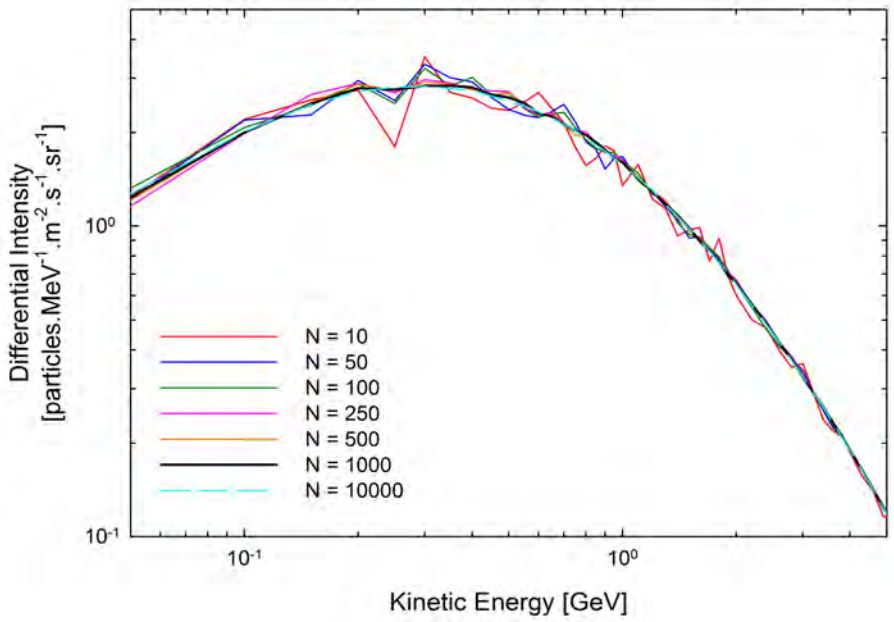


Figure 5.1: *Solutions of GCR proton spectra at Earth produced using an increasing number of pseudo-particles $N$. The convergence to the assumed 'true' solution using $N = 1 \times 10^4$ (dashed light blue line) is illustrated. The solid red line represents the solution for $N = 10$, displaying large deviations from the 'true' solution. As $N$ is increased, these deviations get smaller and smaller until, finally, for $N = 1 \times 10^3$ (solid black line) the deviations are insignificant on the scale of the figure.*

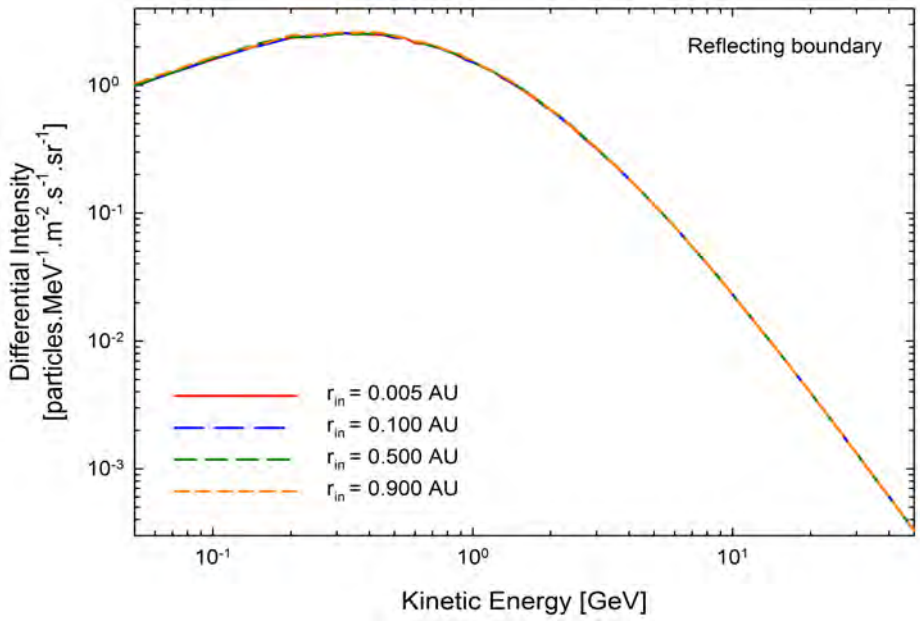


Figure 5.2: *Computed proton spectra at Earth for different values of a reflective inner modulation boundary $r_{\mathrm{in}}$. The spectra are not all clearly discernible due to the close similarity to one another. Spectra are shown using $r_{\mathrm{in}} = 0.005$ AU (solid red line), 0.1 AU (dashed blue line), 0.5 AU (dashed green line), and 0.9 AU (dashed orange line).*

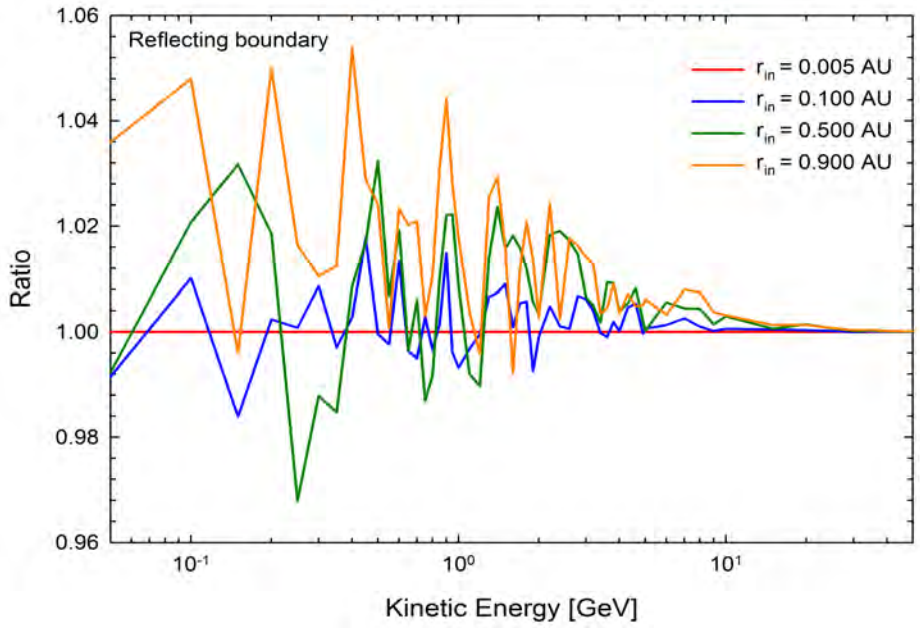


Figure 5.3: *Ratios of each of the proton spectra in Figure 5.2 to the spectrum obtained when the reflective inner boundary is set to* $r_{\text{in}} = 0.005$ *AU. The red, blue, green, and orange lines represent the ratios for the spectra with* $r_{\text{in}}$ *set to 0.005 AU, 0.1 AU, 0.5 AU, and 0.9 AU respectively.*

evident that, for a reflecting inner boundary, any realistic change in the value of $r_{\text{in}}$ does not result in any significant change in the energy spectra at Earth. The solutions are very close together and overlay each other to such an extent that some are barely visible.

Having a closer look at these results, Figure 5.3 confirms the closeness of these solutions by plotting the ratios of each of the spectra to the spectrum using $r_{\text{in}} = 0.005$ AU. The difference between the spectrum using the minimum value $r_{\text{in}} = 0.005$ AU and the spectrum using the maximum value $r_{\text{in}} = 0.9$ AU amounts to no more than $\sim 5.6\%$. From this, it is clear that no significant changes occur in the energy spectra when altering the value of the inner modulation boundary.

Upon consideration of the processes involved in calculating these spectra, the results portrayed in Figures 5.2 and 5.3 are expected and predictable. Changing the value of the inner modulation boundary merely implies a change $\delta V_{\text{m}}$ in the total modulation volume $V_{\text{m}}$. When $\delta V_{\text{m}} << V_{\text{m}}$, the effect on the computed results are expected to be negligible, provided that the time $T_{\text{m}}$ spent by CRs in the modulation volume does not change significantly either, i.e. $\delta T_{\text{m}} \approx 0$. In the case of a reflecting boundary, intuition dictates that $\delta T_{\text{m}} \propto \delta V_{\text{m}}$ and a sufficiently small $\delta V_{\text{m}}$ should leave $T_{\text{m}}$ unchanged, resulting in insignificant to no changes at all in spectra solutions. The relation between $\delta V_{\text{m}}$ and $\delta T_{\text{m}}$, combined with the type of modulation boundary used, is a subject that can be explored in much more detail; in this study, however, only the basics are needed.

Though this work assumes a reflective inner boundary throughout, a brief discussion of the effects upon implementation of an absorbing inner boundary is in order. Figure 5.4 is similar to Figure 5.2, but makes use of an inner absorbing boundary. This time the effects of altering the value of $r_{\text{in}}$ are more pronounced. Especially for the case where $r_{\text{in}} = 0.5$ AU (dashed green line) and for the case where $r_{\text{in}} = 0.9$ AU (dashed orange line). The lower energy ends of these spectra are seen to have increased with successive increases in

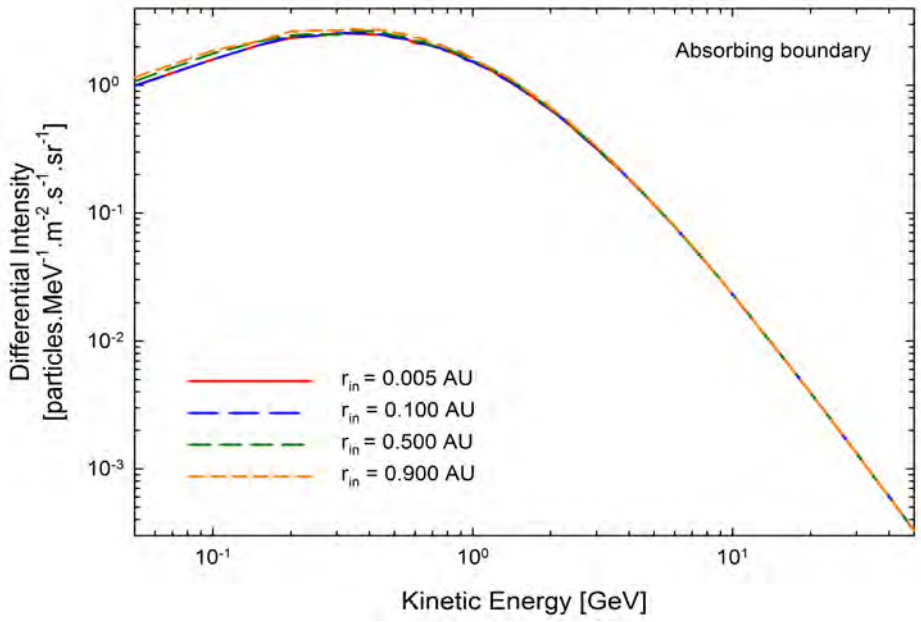


Figure 5.4: *Similar to Figure 5.2, but using an absorbing inner boundary. The spectra for the different values of $r_{\mathrm{in}}$ are easier to distinguish here. The coloured lines represent the spectra as indicated in Figure 5.2.*

$r_{\mathrm{in}}$. Figure 5.5 is similar to Figure 5.3 and indicates that in the cases where $r_{\mathrm{in}} = 0.5$ (green line) and $r_{\mathrm{in}} = 0.9$ AU (orange line), the spectra differed from the spectrum using $r_{\mathrm{in}} = 0.005$ AU by $\sim 11$ % and $\sim 17$ % respectively. These are differences of a magnitude that, according to the assumptions of this work, cannot be solely ascribed to the statistical nature of the calculation process. Note that the spectrum using $r_{\mathrm{in}} = 0.1$ AU still only differs by up to $\sim 2$ %; hence these differences are attributed to statistical considerations.

Again, considering how the SDE-based model obtains solutions of the kind using an inner absorbing boundary, these results are in accordance with what one would expect. Shifting the inner boundary to values closer to 1.0 AU does indeed decrease $V_{\mathrm{m}}$, but not any more so than in the case of the reflecting inner boundary and the effect must still be negligible. The nature of the absorbing boundary, however, provides for significant changes in $T_{\mathrm{m}}$. In the case of the reflecting inner boundary, the pseudo-particle could be reflected many times before reaching the outer boundary; in the case of the absorbing boundary, once a pseudo-particle reaches the inner boundary, it gets canceled and a new pseudo-particle is traced; when this pseudo-particle reaches the outer modulation boundary, it has not undergone reflection anywhere, and hence its $T_{\mathrm{m}}$ is decreased relative to that for a reflected pseudo-particle. This decrease in $T_{\mathrm{m}}$ accosts for the higher intensities. The effect is prominent at lower energies, since this is the area most sensitive to modulation.

Figure 5.6 shows the ratios of the spectra solutions obtained using a reflective inner boundary to those obtained using an absorbing inner boundary. The ratios are shown for each of the cases $r_{\mathrm{in}} = 0.005$ AU (red line), 0.1 AU (blue line), 0.5 AU (green line), and 0.9 AU (orange line). The most important result from this figure is that the differences in the spectra when using $r_{\mathrm{in}} = 0.1$ AU reach no more than $\sim 2\%$ and are thus neglected. This implies that, for the value of $r_{\mathrm{in}} = 0.1$ AU as used in this study, there is no significant difference in the energy spectra produced at Earth using a reflective inner boundary and

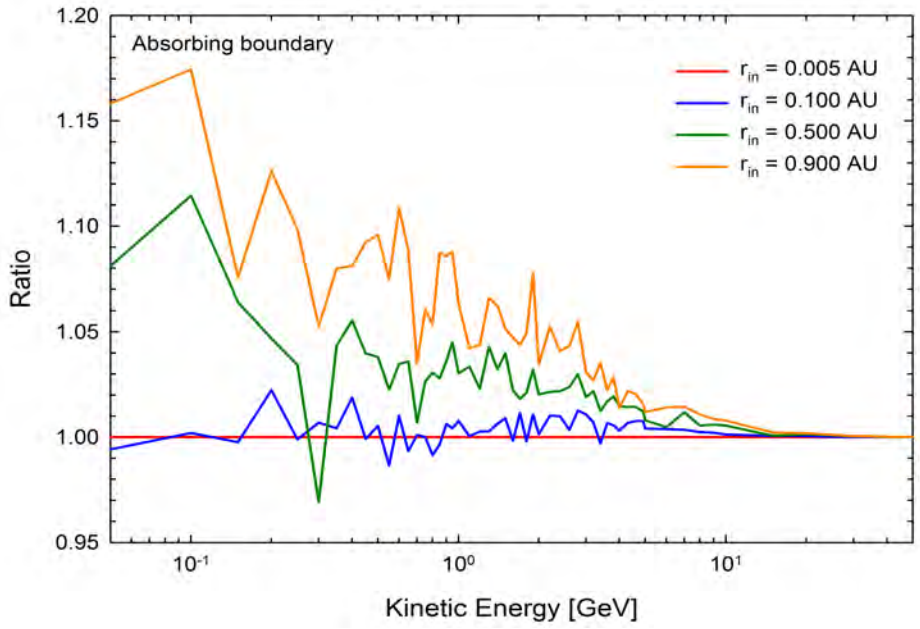


Figure 5.5: *Ratios of each of the proton spectra in Figure 5.4 to the spectrum obtained when the absorbing inner boundary is set to* $r_{\text{in}} = 0.005$ *AU. The red, blue, green, and orange lines represent the ratios for the spectra with* $r_{\text{in}}$ *set to 0.005 AU, 0.1 AU, 0.5 AU, and 0.9 AU respectively.*

those produced using an absorbing inner boundary. The effect of using an absorbing inner boundary instead of a reflective one does, however, gain in prominence as the value of $r_{\text{in}}$ is increased and the spectra reach differences of $\sim 11\%$ at the lowest energies; the reasons for this increased effect at greater $r_{\text{in}}$ are as discussed in the previous paragraph.

Considering these results, the effect of changing the value of the outer modulation boundary $r_{\text{out}}$ is readily anticipated. Figure 5.7 shows proton spectra at a heliocentric distance of 50.0 AU in the equatorial plane, using different values for $r_{\text{out}}$. The red line shows the spectrum using $r_{\text{out}} = 120$ AU, while the blue, green and orange lines represent the cases for $r_{\text{out}} = 100$ AU, 80 AU and 60 AU respectively. These spectra (in this order) are subsequently higher, reflecting the fact that a decreased $r_{\text{out}}$ leads to a smaller $V_{\text{m}}$ and $T_{\text{m}}$ which, in turn, implies less modulation and higher intensities. Once again, the effect is greatest at the lower energy ends of the spectra, since these ranges of energy are most sensitive to modulation.

## 5.5 Modification of the Heliospheric Magnetic Field

One of the most significant advancements this work brings to the pre-established model discussed in Chapter 4 and in Section 5.2, is the modification of the Parker field (PHMF) by incorporating both the Smith-Bieber (Smith and Bieber, 1991) and Jokipii-Kóta (Jokipii and Kóta, 1989) modifications. As mentioned in Chapter 2, this work primarily employs the Smith-Bieber modified field (SBM) and, as such, much of the work in this chapter is centered around this modification.

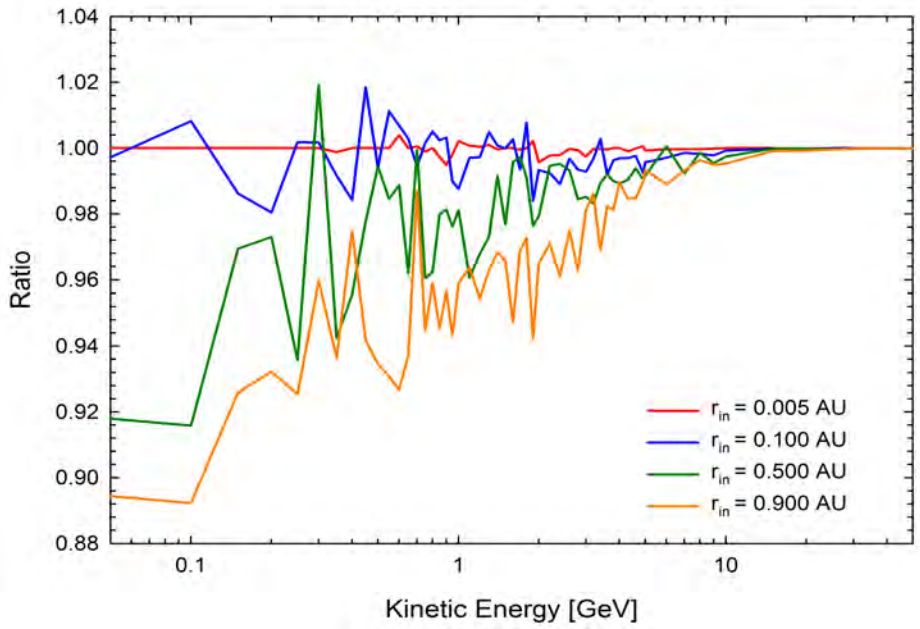


Figure 5.6: *Ratios of spectra using a reflective inner boundary to the corresponding spectra using an absorbing inner boundary. The ratios for $r_{\text{in}} = 0.005$ AU, 0.1 AU, 0.5 AU, and 0.9 AU are represented by the red, blue, green, and orange lines respectively.*

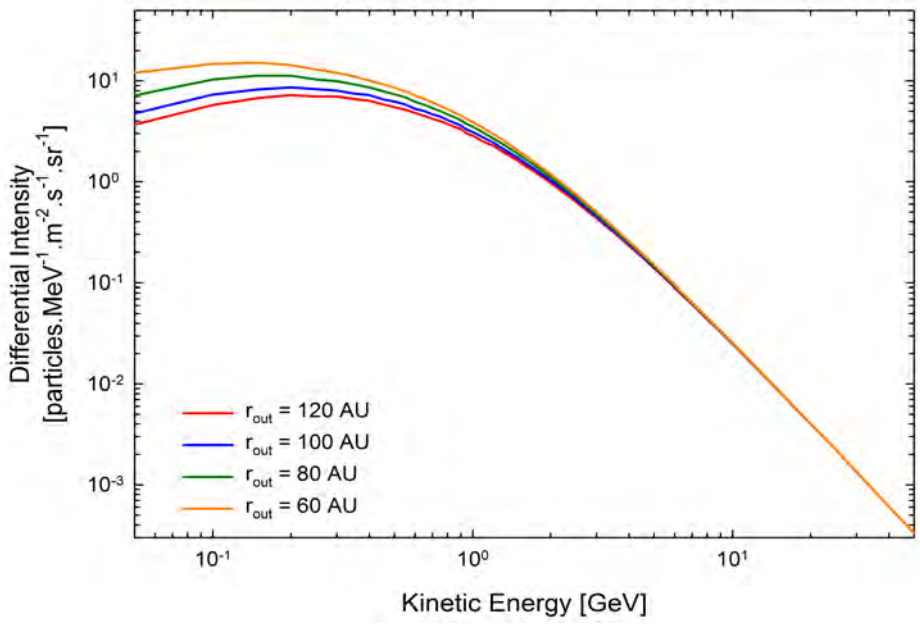


Figure 5.7: *Proton spectra in the equatorial plane at 50 AU, illustrating the effect of changing the distance to the outer modulation boundary. The red line shows the spectrum calculated with an outer boundary $r_{\text{out}} = 120$ AU, while the blue, green and orange lines do so for $r_{\text{out}} = 100$ AU, 80 AU, and 60 AU respectively.*

### 5.5.1 Modified Magnetic Field Profiles

As was explained in Chapter 2, both the SBM and the Jokipii-Kóta modification (JKM) modify the PHMF in such a way as to change its radial dependence in the polar regions from $B \propto 1/r^2$ to $B \propto 1/r$, reducing the extremely high drift velocities otherwise found in these regions. Each of these modifications, however, does so in its own way.

The top panel of Figure 5.8 compares the radial profiles of the PHMF, SBM, and JKM in the equatorial regions, assuming a magnetic field magnitude of 5.05 nT at Earth. All three of these HMF profiles start out with an $r^{-1.95}$ dependence at the smallest radial distances and end with an $r^{-1.00}$ dependence just before the TS at $r = r_{\mathrm{TS}}$, where the SW velocity $V_{\mathrm{sw}}$ drops by a factor of 2.5 and brings about a step-like increase; after the TS, the $r^{-1.00}$ dependent decrease is continued. In the case of the PHMF, the $r^{-1.95}$ dependence continues up to a radial distance of about 0.5 AU, where it begins to transition into a weaker dependence to eventually reach $r^{-1.00}$ at $\sim$ 3.0 AU. Although not clearly discernible on the scale of this graph, the SBM and JKM were determined to enter the $r^{-1.00}$ dependence by a distance of up to 1 AU earlier than the PHMF.

The bottom panel of Figure 5.8 compares the radial profiles of the PHMF, SBM, and JKM in the polar regions and illustrates the effects of the modifications more clearly, since it is − by design − in the polar regions that the differences between the three HMF profiles are most pronounced. The PHMF and both the SBM and the JKM start out with an $r^{-1.96}$ dependence at the smallest radial distances. At a radial distance between 6 AU and 7 AU the PHMF starts transitioning into a weaker radial dependence and keeps up this transition to reach its weakest dependence of $r^{-1.10}$ at a radial distance of between 40 AU and 50 AU; this is then maintained up to the TS. The SBM begins its transition into the weaker radial dependence at a smaller radial distance between 1 AU and 2 AU and reaches $r^{-1.00}$ at about 20 AU, continuing up to the TS. The JKM begins the transition into the weaker radial dependence even earlier than the SBM at $\sim$ 1 AU and reaches $r^{-1.00}$ between 8 and 9 AU, once again continuing up to the TS. In all three cases, the dependence before the TS is regained after the TS.

Notice that, in the polar regions, the JKM profile does not undergo the upward step at the TS to the extent shown by the PHMF and SBM; in fact, the JKM profile barely shows any increase at all. This suppression of the TS in the polar regions is not an intended effect and is a consequence of the fact that the TS is simulated entirely by the drop in $V_{\mathrm{sw}}$ at $r_{\mathrm{TS}}$. In the instance of the JKM, the modification term in Eq. (2.10) is much larger than the term containing $V_{\mathrm{sw}}$ and hence the effect of the drop in $V_{\mathrm{sw}}$ at $r_{\mathrm{TS}}$ is markedly less pronounced. The implication for numerical modeling is a mere technical issue though, that can readily be addressed by appropriate boundary conditions in the polar regions. However, this is not a problem that needs to be considered any further for the purposes of this work, since it is the SBM that is assigned the primary role.

It is clear from Figure 5.8 that both the SBM and JKM have the desired effect of drastically reducing the radial dependence of the HMF in the polar regions: the transition into the weaker radial dependence is initiated at much smaller $r$ than in the case of the PHMF, ensuring significantly larger magnetic field magnitudes $B$. It is also noted that because the SBM starts its transition into the weaker radial dependence at larger radial distances than does the JKM, its effect on $B$ is less pronounced than that of the JKM. Although not illustrated in Figure 5.8, it is of decisive importance to note that this less effectual status of the SBM when compared to the JKM is only *locally* true, i.e. it is only valid *at* or *very close* to the poles as in this case $\theta = 5°$. Figure 5.9 will indicate that the SBM is effected over a larger part of the modulation space so that its overall effect may indeed be greater than that of the JKM.

The four panels of Figure 5.9 show the unfolding of the PHMF, SBM, and JKM

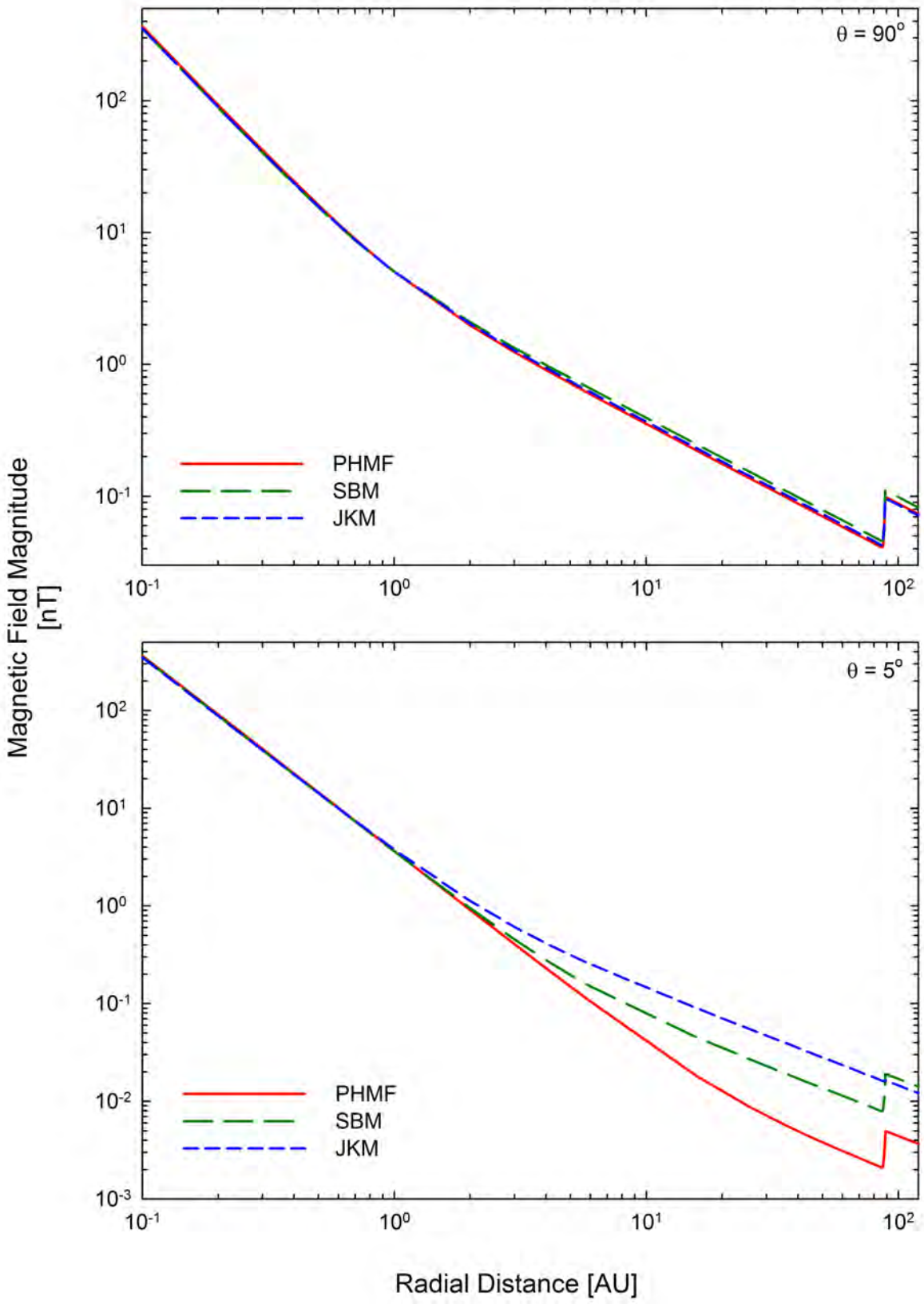


Figure 5.8: *Magnetic field magnitude radial profiles in the equatorial regions (top panel) and in the polar regions (bottom panel). The PHMF is indicated by the solid red line while the SBM and JKM are represented by the dashed green and blue lines respectively.*

latitudinal profiles over successive radial distances of 1 AU, 10 AU, 50 AU, and 100 AU. From the first panel it is clear that, at 1 AU, the effects of both the SBM and JKM are negligible in the equatorial regions, but become more pronounced towards the poles. Taking the equator $\theta = 90°$ as reference and moving towards the poles, the deviation of the SBM from the PHMF is seen to start at about $\theta \in \{68°, 112°\}$, continuing towards the respective poles. The SBM is greater than the PHMF up to about $\theta \in \{14°, 166°\}$, where it drops below and eventually reaches a maximum deviation from the PHMF of $\sim 0.08$ nT at the poles. The difference between the PHMF and JKM is seen to consistently increase towards the polar regions $\theta \in \{0°, 180°\}$, where the JKM eventually reaches levels of $\sim$ 0.12 nT higher than the PHMF.

The picture at a radial distance of 10 AU has unfolded to be significantly different from the profiles at 1 AU. The SBM is seen to have already modified the PHMF in the equatorial regions, amounting to a value of about 0.04 nT higher than the PHMF at $\theta = 90°$. Towards the poles the difference between the SBM and PHMF increases to about 0.06 nT at intermediate latitudes, declining again to about 0.03 nT at $\theta \in \{0°, 180°\}$. The SBM, at the equator, is initially higher than the JKM, but drops below it at about $\theta \in \{48°, 132°\}$, and continues to do so up to the polar regions. Small deviations from the PHMF in the equatorial regions are also seen to be induced by the JKM, amounting to no more than 0.02 nT at $\theta = 90°$. As was the case at 1 AU, the effect of the JKM increases towards the poles where it reaches levels of about 0.10 nT higher than the PHMF. The picture at 50 AU looks qualitatively the same as that at 10 AU, only the magnitude of the HMF being smaller. Comparing with Figure 5.8, it is clear that this qualitative picture is continued up to the TS.

The fourth panel of Figure 5.9 shows the latitudinal profiles at 100 AU, a distance comfortably beyond the TS. The SBM is still higher than the PHMF at all latitudes, now being higher than the PHMF by about 0.01 nT in the equatorial regions and by about 0.02 nT in the polar regions. The JKM is, curiously enough, at more or less the same level as the SBM in the polar regions; it lies just below the PHMF at $\theta = 90°$, but climbs above it at $\sim \theta \in \{45°, 135°\}$, eventually reaching the level of the SBM at the poles.

### 5.5.2 Impact on Modulation

From Eq. (3.25), defining the drift coefficient and from Eqs. (3.31) to (3.33), defining the diffusion coefficients used in this study, it is clear that the choice of HMF profile directly influences the spatial dependence of these coefficients.

Figure 5.10 shows the radial profiles of the parallel mean free paths $\lambda_{||}$ of 1 GV protons for each of the PHMF (solid red lines), the SBM (dashed green lines), and the JKM (dashed blue lines). The upper three lines represent the values of $\lambda_{||}$ in the polar ($\theta = 5°$) regions, while the lower three lines do so in the equatorial regions at $\theta = 90°$. As expected, the effects of the modifications are minimal in the equatorial regions, while being far more significant in the polar regions. In the equatorial regions, the $\lambda_{||}$s for each of the PHMF, SBM and JKM are identical at small $r$ and then start diverging from one another at about 1 AU. This divergence is not significant however, and both the $\lambda_{||}$s for the SBM and JKM end up being only marginally below the PHMF, the SBM being the lowest. In the polar regions, the $\lambda_{||}$s for each of the PHMF, SBM and JKM are again seen to start out together at small $r$ and then to diverge at greater $r$. As should be the case, the $\lambda_{||}$s for the SBM and JKM are observed to start diverging from the PHMF at more or less the same radial distances at which the HMF profiles in Figure 5.8 started diverging from one another. In the polar regions the $\lambda_{||}$s for both the SBM and JKM then keep significantly lower than that for the PHMF, the JKM being the lowest up to $r_{\mathrm{TS}}$ where the SBM drops

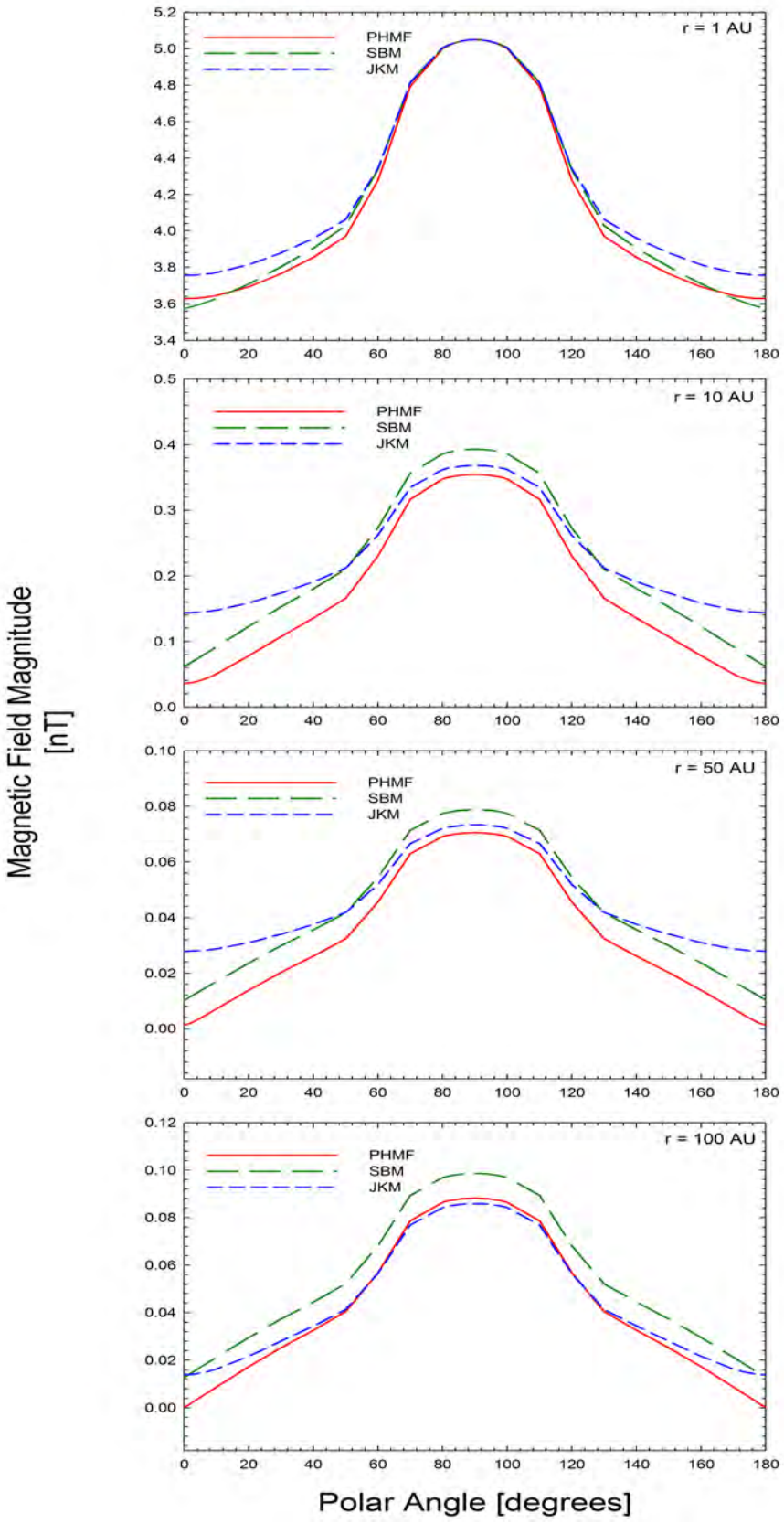


Figure 5.9: *Magnetic field latitudinal profiles at four selected radial distances $r = 1$ AU (first panel), 10 AU (second panel), 50 AU (third panel), and 100 AU (fourth panel). The PHMF is indicated by the solid red line while the SBM and JKM are represented by the dashed green and blue lines respectively.*

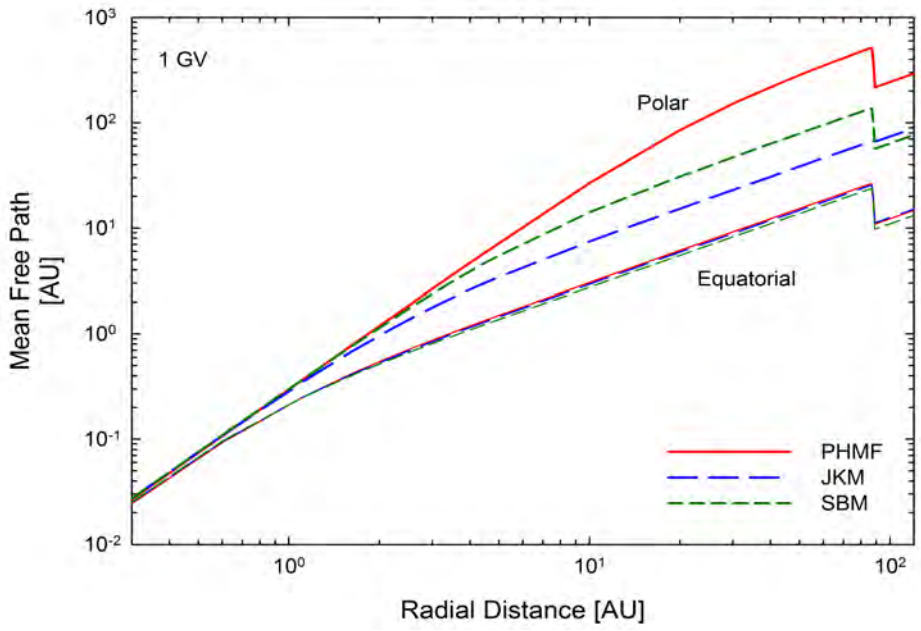


Figure 5.10: *Radial profiles for the parallel mean free paths $\lambda_{||}$ of a 1 GV proton for each of the PHMF (red lines), the SBM (green lines), and the JKM (blue lines). The upper three lines depict the $\lambda_{||}$s in the polar regions, while the lower three lines do so in the equatorial regions.*

below it due to the failure of the JKM to decrease over the TS.

Figure 5.11 is similar to Figure 5.10, but depicts the radial profiles of the drift scale $\lambda_D$ instead of that of the parallel mean free path. Once again, it is clear that the effects are most pronounced in the polar regions and the situation is similar to that of the parallel mean free path. This must be so, since the radial (spatial) dependencies of both the diffusion coefficients (mean free paths) and the drift coefficient (drift scale) are determined and fixed by their $1/B$ dependence.

The effects of the HMF modifications on proton energy spectra at Earth are illustrated in Figure 5.12. The top panel shows the zero-drift solutions and the middle and bottom panels show the $A > 0$ and $A < 0$ solutions respectively. In each of the three panels the PHMF, SBM and JKM solutions are presented by the solid red, green and blue lines, while the local interstellar spectrum (LIS) is indicated by the solid black lines. In the middle and bottom panels, the zero-drift solutions are included for reference, indicated by the dashed lines. For the two drift cases the JKM is not included, since it is expected to be approximately intermediate between the cases for the PHMF and SBM and since the focus of this study is really on cases employing the SBM.

The results from the first panel are as expected: the weaker diffusion induced by both the SBM and the JKM causes these spectra to be lower than the one for the PHMF. The spectrum in the case of the JKM is higher than that for the SBM, confirming that the less effectual status of the SBM referred to earlier is indeed only locally true; the SBM extends its influence over a greater fraction of the modulation volume so that its associated diffusion, integrated over this volume, is weaker than that of the JKM − even though the JKM may display diffusion coefficients which are locally weaker than that of the SBM. This is necessarily also true for the drift coefficient, since it shares the $1/B$ dependence. The results from the middle panel indicate a rise in the intensities in both the cases employing the PHMF and SBM, the rise in the case of the SBM not only greater

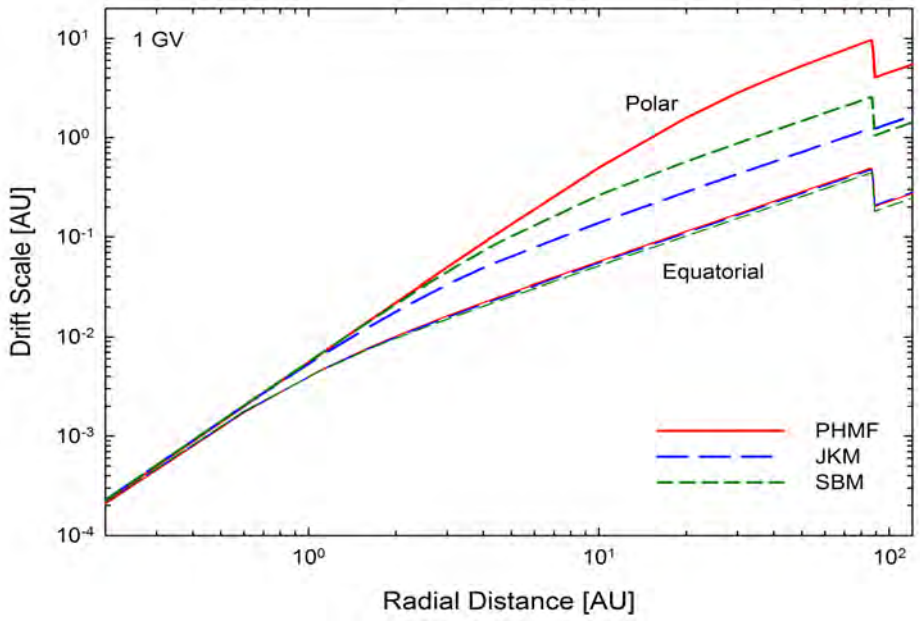


Figure 5.11: *Radial profiles of the drift scale $\lambda_D$ of a 1 GV proton for each of the PHMF (red lines), the SBM (green lines), and the JKM (blue lines). The upper three lines show $\lambda_D$ in the polar regions, while the lower three lines do so in the equatorial regions.*

but also effected up to slightly higher energies, i.e. about 5 GeV instead of 3 GeV in the case for the PHMF. The bottom panel indicates a decrease in intensity for both the PHMF and the SBM with the decrease in the SBM spectrum much smaller and effective up to much lower energies, already leveling with its zero-drift solution at about 400 MeV; the PHMF drift spectrum continues to be lower than its zero-drift solution up to about 1.5 GeV.

It was stated earlier that the main object of both the modifications to the HMF considered here was to reduce drifts in the polar regions. The extent to which these modifications do so can be illustrated very effectively by employing the ability of the SDE-based model to produce pseudo-particle trajectories. To this end a scenario in which drifts play the dominant modulative role is considered; it will be illustrated elaborately in later sections that looking more closely at extreme cases such as this can prove not only insightful, but may also provide the means to explain the results of more general cases. Figure 5.13 is for such a scenario and shows the pseudo-particle trajectories for 1.5 GeV protons in an $A > 0$ drift cycle, reflected in the meridional plane where $Y$ is in the equatorial direction; the neutral current sheet (HCS) with its tilt angle set to $\alpha = 10°$ is also shown (solid black line); the two vertical red lines indicate the position of the termination shock (TS) at $Y = \pm r_{TS}$. The HCS is compressed in the heliosheath, as will be explained in Section 5.6.2. The energy 1.5 GeV was chosen for no other reason than the fact that its behaviour could be described as sufficiently drift dominated given the rest of the specifications for this particular scenario.

At this point, before continuing the discussion of Figure 5.13, it is deemed important to establish the context in which figures of this kind should be interpreted. Differentiation is established between two distinctly different ways of interpreting these results, i.e. interpretations from two distinctly different *perspectives* are established. From a *modeling perspective* such figures are described in terms of pseudo-particles and in a time backwards

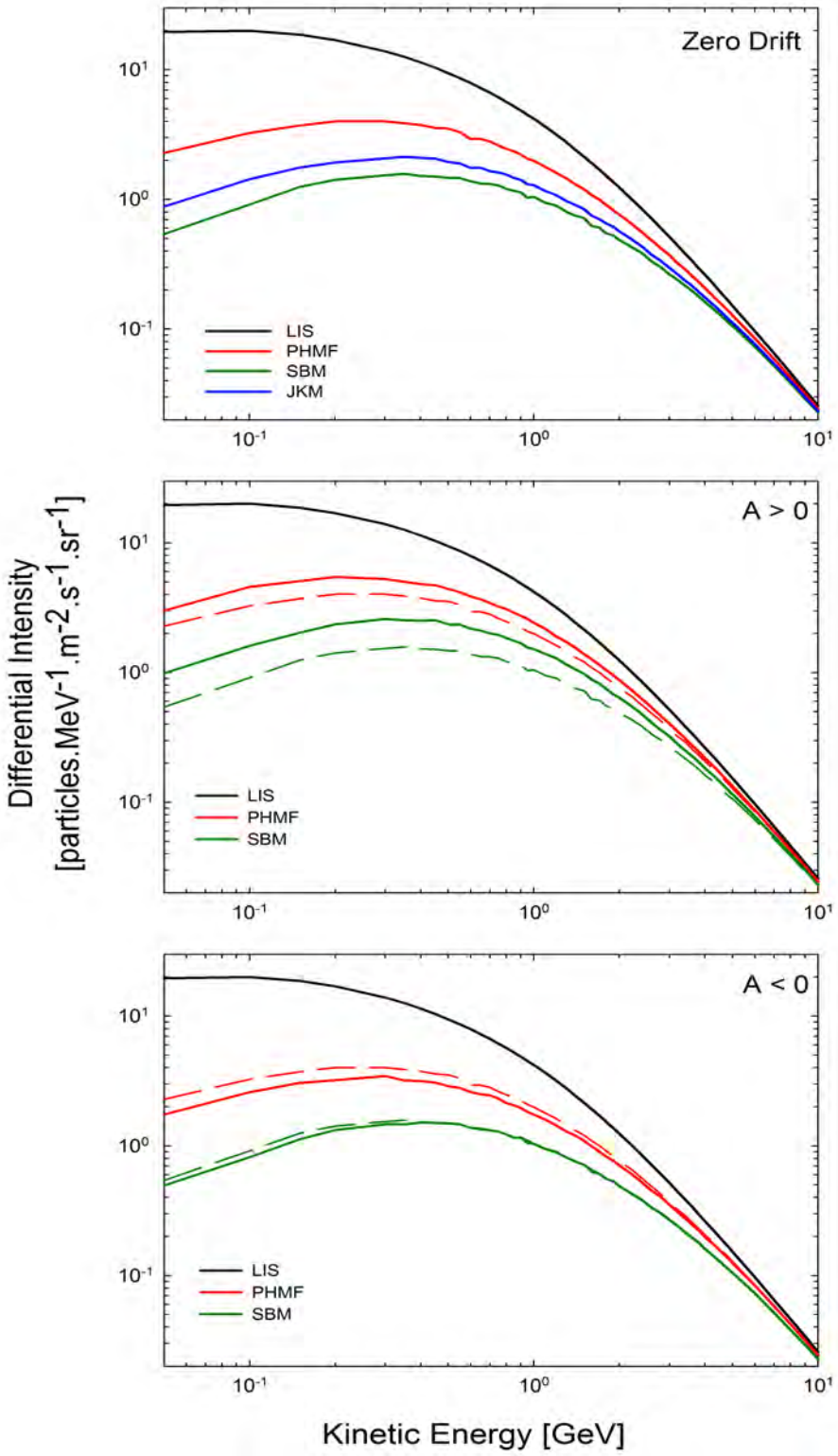


Figure 5.12: *Calculated proton spectra at Earth with respect to the LIS (solid black line) at 120 AU. The top panel presents the results for the zero-drift scenario and shows the PHMF, SBM, and JKM solutions as the red, green, and blue lines respectively. The middle panel depicts the PHMF (solid red line) and SBM (solid green line) results for the case of $A > 0$ drift and includes the zero-drift PHMF and SBM solutions of the top panel (red and green dashed lines) for reference. The bottom panel is similar to the middle one, representing the $A < 0$ results, with the zero-drift solutions once again indicated by the dashed lines.*

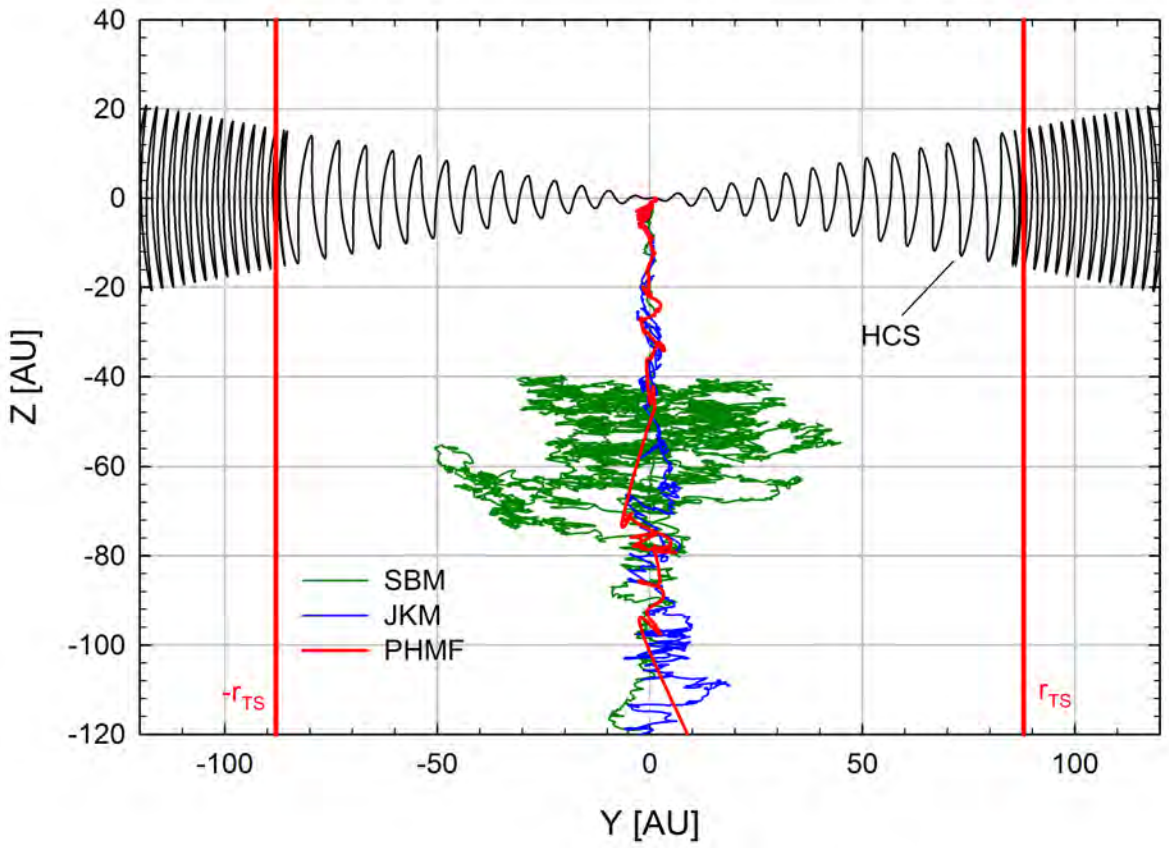


Figure 5.13: *Pseudo-particle trajectories reflected in the meridional plane of the heliosphere for 1.5 GeV protons undergoing drift and diffusion during an $A > 0$ drift cycle where $\alpha = 10°$. The black line depicts the wavy HCS, while the red, green and blue lines respectively show the pseudo-particle trajectories through the polar regions in each of the cases for the PHMF, the SBM, and the JKM. The vertical red lines are drawn at the position of the TS, $Y = \pm r_{\mathrm{TS}}$, which is set at 88.0 AU. The Sun is located at (0,0) with Y the equatorial direction.*

frame while, from a *modulation perspective*, they are described in a time forwards frame and in terms of what it suggests about the movement or behaviour of actual particles (protons) or the actual modulation processes. Therefore, in the text to follow, whenever discussing results of this kind from a modulation perspective, 'pseudo-particles' are merely referred to as 'particles' or 'protons'. The reader is, however, reminded of the fact that pseudo-particles are not actual particles and that pseudo-particle trajectories are by no means the trajectories of real particles − these concepts are as explained in detail in Chapter 4.

From a modulation perspective, therefore, the situation portrayed in Figure 5.13 is described as follows. The red line represents the trajectory of a proton in the case of a PHMF. Drift velocities in this case are seen to be exceedingly high by the fact that the proton undergoes a minimum of random walk movement (diffusion) before reaching the Earth, drifting quickly and efficiently down the pole to reach Earth. This situation is typical of what is called drift dominated modulation (see Potgieter et al., 1989) and why the PHMF must be modified over the poles of the heliosphere. Furthermore, notice that on several occasions the trajectory takes on the form of a straight line, indicating physically impossible high values for the drift speed $v_{\mathrm{d}} > c$. Looking at the cases of the SBM and the JKM (green and blue lines respectively), this problem is seen to be largely

remedied with far fewer − if any − such instances occurring in the respective trajectories. As intended, the SBM is seen to very effectively reduce the dominance of drift in the polar regions: much more random walk diffusion is effected and the proton does not merely drift in along the pole to reach Earth. From this figure it is also clear that the SBM is more effective in its goal of reducing drift over the poles than is the JKM; the JKM also shows a trajectory indicating far less instances of $v_{\mathrm{d}} > c$ and a larger role of diffusion relative to drift, but not to the extent of the SBM.

## 5.6 Matters Related to the Neutral Current Sheet

This section constitutes the core of Chapter 5 and illustrates extensively how the SDE-based model can be utilised to obtain insights into modulation not possible with the use of ADI-based models. Specifically, the subjects of the HCS and HCS drifts − first featured in Chapters 2 and 3 − are treated in more detail. Before seriously embarking on this course, however, the use of the HCS tilt angle as a proxy for solar activity is discussed and some subtleties regarding this matter are pointed out. After this, the two different expressions for the HCS tilt angle, namely Eq. (2.14) and Eq. (2.15), are investigated by first looking at the differences in the respective geometries; then the expressions for the HCS drift velocities associated with each case are presented, with a formal derivation for the case of Eq. (2.15). Finally, the differences in modulation arising with the implementation of each of these HCS profiles are illustrated and discussed.

### 5.6.1 The HCS Tilt Angle as Proxy for Solar Activity

The HCS tilt angle $\alpha$ is usually employed as a parameter to gauge the effects of HCS drifts so that, when $\alpha$ changes from minimum to maximum values, only these drift effects are concerned, i.e. a change in $\alpha$ does not simulate a change in the overall level of solar activity in that it does not bring about the accompanying changes in the diffusion coefficients (e.g. Strauss et al., 2012). The SDE-based model of this work, however, employs the HCS tilt angle as a proxy for solar activity in its totality, i.e. a change in $\alpha$ not only implies a change in the HCS drift effects, but a change in the overall level of solar activity. This fact is owed to the $\alpha$-dependence of the SW profile $V_{\mathrm{sw}}$ presented by Eq. (2.2). As explained in Chapter 2, this effectively establishes a SW profile that changes from solar minimum to solar maximum conditions, proxied by $\alpha$. These changes are then consistently followed through, changing also the magnitude of the magnetic field by Eq. (2.6), and subsequently also the values of the drift coefficient by Eq. (3.25), as well as the diffusion coefficients by Eqs. (3.31) to (3.33).

This matter will be of importance in the rest of Section 5.6 and, as such, some final clarifications are in order. Figure 5.14 shows the zero-drift intensity vs solar activity profile for 1 GeV protons, where solar activity is proxied by $\alpha$ as explained above. The dashed line shows the solution where a change in $\alpha$ corresponds to a change in the HCS drift effects only, i.e. the $\alpha$ in the expression for the SW velocity was kept constant. Meaning that the change in solar activity has been ignored, such solutions are henceforth referred to as *tilt angle only* solutions and when the tilt angle is used in this restricted capacity it is simply indicated by $\alpha$. As must be the case for a zero-drift scenario, the profile shows no dependence on a change in $\alpha$; the profile does show some variation, but this is due to the statistical nature of the SDE-based model. The solid line, on the other hand, illustrates the case where a change in the tilt angle also affects the SW profile to change and from this point onwards, when the tilt angle is used in this capacity, it is referred to as $\alpha_{\mathrm{s}}$. In this case the intensity shows a clear dependence on solar activity, and

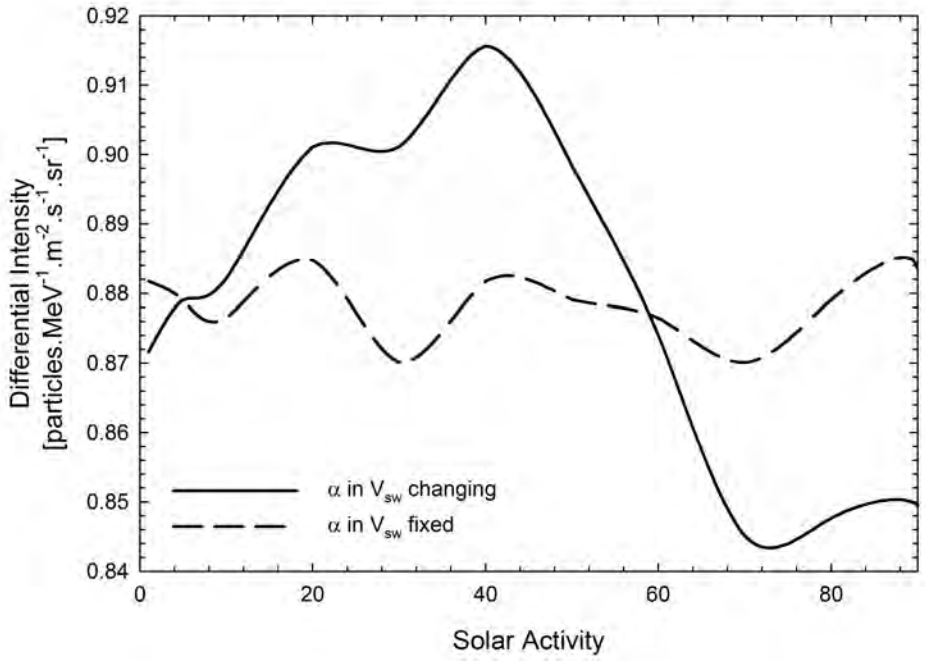


Figure 5.14: *Zero-drift intensity vs solar activity profiles for 1 GeV protons at Earth. The dashed line shows the solution where the $\alpha$ occurring in the expression for $V_{sw}$ was kept fixed, i.e. the tilt angle only solution. The solid line shows the solution for the case where this $\alpha$ naturally changed with increasing solar activity, i.e. the full solution. The latter solution clearly exhibits a solar activity dependence, while the former solution on average does not.*

to distinguish it from the tilt angle only solutions, such solutions are henceforth referred to as *full* solutions.

### 5.6.2 Expressions for the HCS Tilt Angle and its Associated Drift Velocities

#### Two Different Geometries for the HCS

In Chapter 2 it was indicated that either Eq. (2.14) or Eq. (2.15) could be employed to simulate the physical extent of the HCS tilt angle $\alpha$. It was pointed out that these two expressions were equivalent at small values of $\alpha$ and also that Eq. (2.15) was applied up to larger values of $\alpha$ than was Eq. (2.14). However, the differences between these two expressions and their implications for the associated drift velocities along the HCS were not then addressed and will now be discussed in much detail.

Figure 5.15 shows sections in the meridional plane and illustrates the difference in the geometry of the HCS upon employing Eq. (2.14) and Eq. (2.15) respectively. These two cases are henceforth referred to as the cases for $HCS_{arcsin}$ and $HCS_{arctan}$ respectively. In each of the four panels the solid line represents the case for $HCS_{arctan}$, while the dashed line does so for the case of $HCS_{arcsin}$. The top left and right panels show the geometries at tilt angles of $\alpha = 5°$ and $\alpha = 35°$ respectively, while the bottom left and right panels do so for $\alpha = 65°$ and $\alpha = 85°$. At the two lower values of $\alpha$, there is no clear geometrical difference discernible between the two profiles, except for the obvious fact that they are exactly out of phase. At $\alpha = 65°$, however, a discrepancy between the two profiles becomes discernible and at $\alpha = 85°$ this is clearly evident: the peaks − from now on more

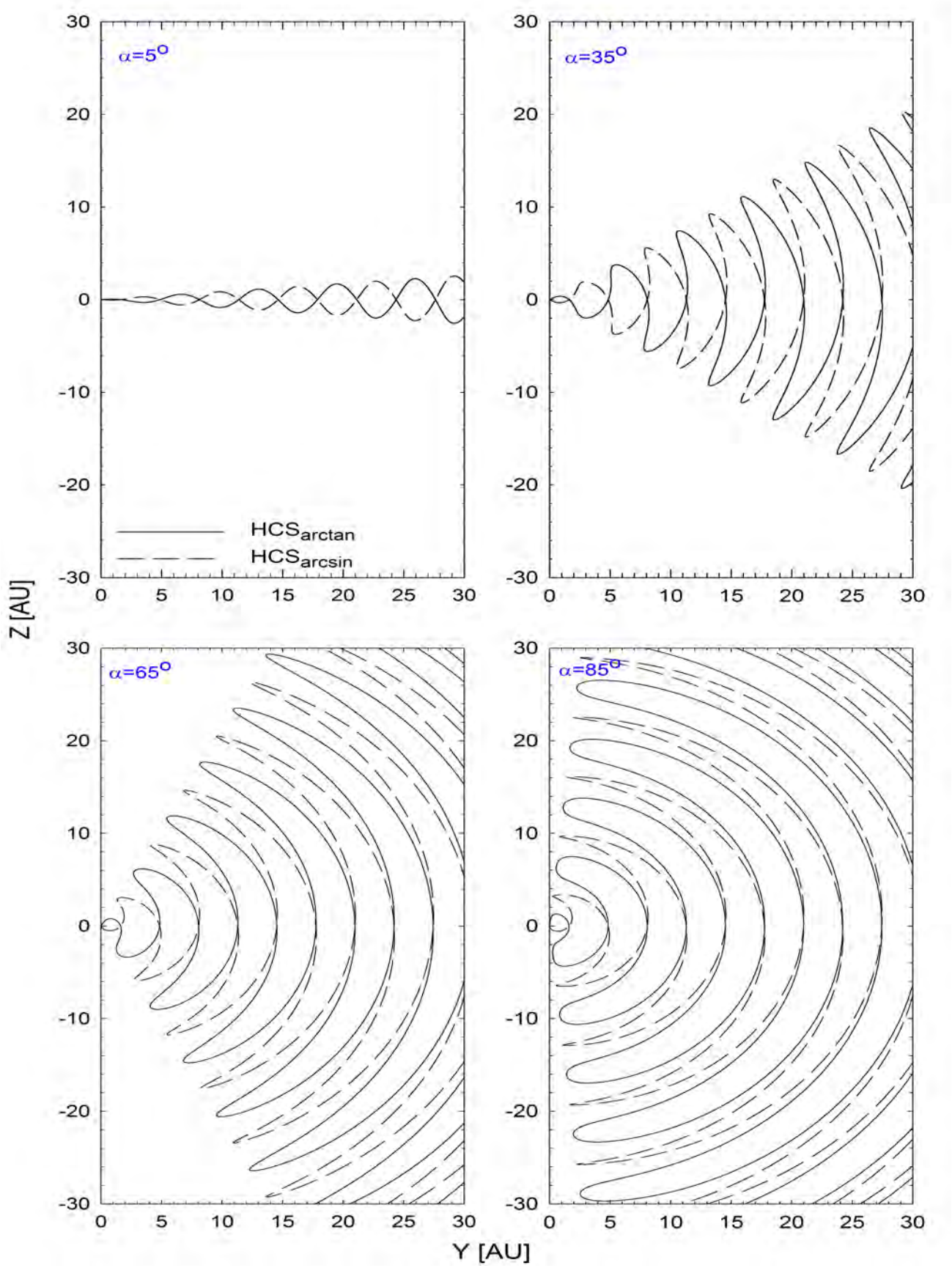


Figure 5.15: *Meridional cuts depicting the* $HCS_{\mathrm{arctan}}$ *(solid lines) and* $HCS_{\mathrm{arcsin}}$ *(dashed lines). The top left panel shows the case for a small tilt angle* $\alpha = 5°$*, the top right panel does so for an increased tilt angle of* $\alpha = 35°$*, and the bottom left and right panels show the two profiles for* $\alpha = 65°$ *and* $\alpha = 85°$ *respectively.*

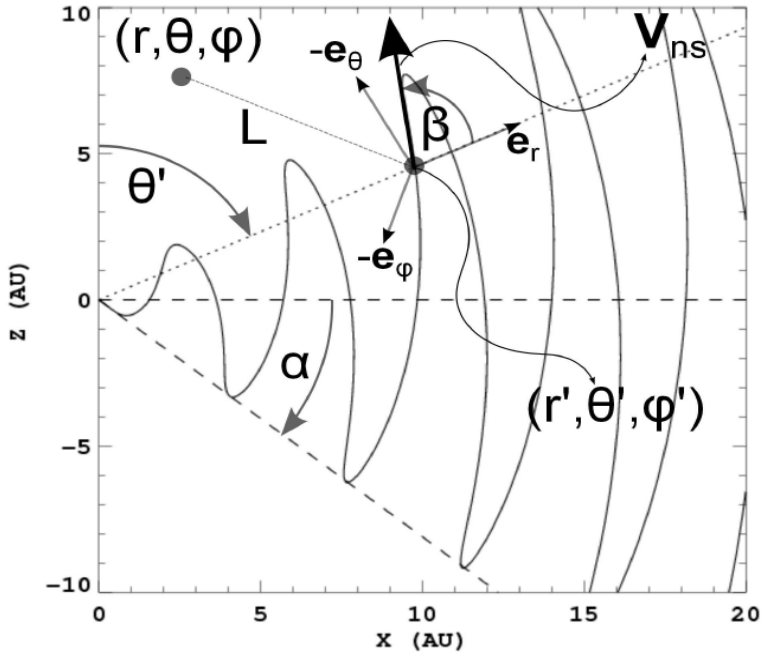


Figure 5.16: *The geometry of the HCS, projected in the meridional plane. All labels refer to the notation used in this work. This figure was taken from Strauss et al. (2012).*

aptly called the *arms* − of the $\mathrm{HCS}_{\mathrm{arctan}}$ profile are notably broader or thicker than in the case for the $\mathrm{HCS}_{\mathrm{arcsin}}$ profile; in the former case the arms end with rounded points, while in the latter case the points are sharp − to such an extent that the $\mathrm{HCS}_{\mathrm{arcsin}}$ may even be less clearly defined at large $\alpha$.

### HCS Drift Velocities

This section derives the HCS drift velocity using Eq. (2.15), i.e. assuming $\mathrm{HCS}_{\mathrm{arctan}}$. For comparison with this case, the analogous expression on assumption of the $\mathrm{HCS}_{\mathrm{arcsin}}$ profile is only shown at the end of this section; it has been derived in detail before (Steenkamp, 1995; Strauss et al., 2012). All quantities and symbols used in the derivation are as defined previously or in this section.

Drifts along the HCS can be evaluated through the same expression as gradient and curvature drifts, the expression given in the form

$$\begin{aligned} \vec{v}_{\mathrm{d}} &= \frac{qv}{3}\nabla \times r_{\mathrm{L}}\frac{\vec{B}}{B} \\ &= \vec{v}_{\mathrm{gc}} + \vec{v}_{\mathrm{ns}}, \end{aligned} \tag{5.1}$$

where $\vec{v}_{\mathrm{d}}$ is the drift velocity, constituted of the gradient and curvature drift component $\vec{v}_{\mathrm{gc}}$ and the neutral sheet drift component $\vec{v}_{\mathrm{ns}}$. An expression for $\vec{v}_{\mathrm{ns}}$ is derived in what follows.

The HCS drift velocity is directed parallel to the HCS and perpendicular to the HMF (e.g. Burger and Potgieter, 1989; Burger et al., 1985). In order to construct an expression for it, a vector directed parallel to the HCS is defined

$$\vec{h} = \cos(\pm\beta)\vec{e}_r + \sin(\pm\beta)\vec{e}_\theta + \cos(\pm\beta)\vec{e}_\phi, \tag{5.2}$$

given in terms of the angle $\beta(r, \theta, \phi, \alpha) \in (-180°, 180°)$. The geometry of this setup is shown in Figure 5.16, taken from Strauss et al. (2012). A projection (at a constant value of $\phi$) of the HCS is shown as the solid wavy line. Assume now a CR particle located at a point $(r, \theta, \phi)$. This CR will 'sense' the effect of the HCS at a point $(r^{'}, \theta^{'}, \phi^{'})$, with $(r^{'}, \theta^{'}, \phi^{'})$ being the point on the HCS that is closest to $(r, \theta, \phi)$. For the $A > 0$ drift cycle, this positively charged CR will drift *upwards* (i.e. towards the northern heliospheric pole) with a velocity $\vec{v}_{\rm ns}$ as indicated in the figure. The angle $\beta$ is defined as the angle between $\vec{h}$ (which will be directed parallel to $\vec{v}_{\rm ns}$) and the radial direction. This angle is calculated as

$$\tan\beta = r\frac{\partial\theta^{'}}{\partial r}, \tag{5.3}$$

(see also the discussion by Burger, 2012) which reduces, for a Parker HMF geometry, to

$$\tan(\pm\beta) = \pm\left[1 - R\frac{\partial V_{\rm sw}}{\partial r}\right] R\frac{\sqrt{\tan^2\alpha - \cot^2\theta^{'}}}{\cot^2\theta^{'} + 1}, \tag{5.4}$$

where, for simplicity, $R$ has been defined as

$$R = \frac{\Omega(r - r_{\odot})}{V_{\rm sw}}. \tag{5.5}$$

In this work, Eq. (5.4) does not assume a constant SW speed as in e.g. Strauss et al. (2012). Instead it is assumed to take on its full radially dependent form, i.e. according to Eqs. (2.4) and (2.5). Similar expressions are given by Caballero-Lopez and Moraal (2003), Burger (2012), and Strauss et al. (2012), but derived by using different expressions for the HCS angular extent $\theta^{'}$. All of these approaches become identical when $\alpha$ is very small, such that $\sin\alpha \approx \tan\alpha \approx \alpha$.

The correct sign of $\beta$ is determined through the relationship

$$\begin{aligned} \frac{\partial\theta^{'}}{\partial r} < 0 \quad &\Rightarrow \quad \beta < 0 \\ \frac{\partial\theta^{'}}{\partial r} > 0 \quad &\Rightarrow \quad \beta > 0. \end{aligned} \tag{5.6}$$

Note that $\cos\beta$ is always positive, while $\sin\beta$ changes sign with the waviness of the HCS.

When all of these results above are combined, the HCS drift velocity is given by

$$\vec{v}_{\rm ns} = v_{\rm ns}\{\cos(\pm\beta)\sin\psi\vec{\rm e}_r + \sin(\pm\beta)\vec{\rm e}_\theta + \cos(\pm\beta)\cos\psi\vec{\rm e}_\phi\} \cdot qA, \tag{5.7}$$

with $\psi$ the HMF spiral angle and $A$ indicating the magnetic polarity cycle (here combined with particle charge $q$); $v_{\rm ns}$ is the magnitude of $\vec{v}_{\rm ns}$, given by the approximation of Burger et al. (1985)

$$v_{\rm ns} = \left\{0.457 - 0.412\frac{|L|}{r_{\rm L}} + 0.0915\frac{|L|^2}{r_{\rm L}^2}\right\} v, \tag{5.8}$$

where $L$ is the smallest distance from the CR's current position to the HCS (Figure 5.16). This expression was derived for a locally flat HCS, meaning that CRs are assumed to interact with only a single fold of the HCS at a given time. The validity of this assumption has been challenged by the simulations of Florinski (2011). This previously unexplored process (that can be called *drift short circuiting*) is, however, not yet understood and is as such not included in the model featured in this work.

Eq. (5.8) is only applied when

$$|L| \leq 2r_{\mathrm{L}}. \tag{5.9}$$

The HCS is thus not added as a true discontinuity, but has an effective *thickness* of $4r_{\mathrm{L}}$. The method in which $L$, i.e. the minimum distance between $(r, \theta, \phi)$ and $(r', \theta', \phi')$ is calculated as explained by Strauss et al. (2012). It was, furthermore, proved that the condition $\nabla \cdot \vec{v}_{\mathrm{d}} = 0$ is automatically satisfied.

For the case of $\mathrm{HCS}_{\mathrm{arcsin}}$, Eq. (5.4) merely changes to

$$\tan(\pm\beta) = \pm \left[1 - R\frac{\partial V_{\mathrm{sw}}}{\partial r}\right] R\frac{\sqrt{\sin^2\alpha - \cos^2\theta'}}{\sin\theta'}, \tag{5.10}$$

where all symbols retain their defined meanings (see also Steenkamp, 1995).

### 5.6.3 Modulation Results

Figure 5.17 shows proton spectra at Earth, the top panel illustrating the situation for a small tilt angle $\alpha = 5°$, while the bottom panel does so for a very large tilt angle $\alpha = 85°$. In both panels the $A > 0$ and $A < 0$ solutions for the case of $\mathrm{HCS}_{\mathrm{arctan}}$ are represented by the dashed orange and blue lines respectively, while in the case for $\mathrm{HCS}_{\mathrm{arcsin}}$ it is presented by the solid green and red lines respectively. In the case of the small tilt angle, the $\mathrm{HCS}_{\mathrm{arctan}}$ and $\mathrm{HCS}_{\mathrm{arcsin}}$ solutions are seen to be identical for all practical purposes. This is expected, since at sufficiently small $\alpha$, the situation approaches $\sin\alpha \approx \tan\alpha \approx \alpha$. For the instance of the large tilt angle, however, the solutions for the two respective HCS geometries differ more significantly with the $A > 0$ solution of the $\mathrm{HCS}_{\mathrm{arctan}}$ case being lower than that of the case for $\mathrm{HCS}_{\mathrm{arcsin}}$ and the $A < 0$ solution being slightly higher. Going from the $\mathrm{HCS}_{\mathrm{arcsin}}$ to the $\mathrm{HCS}_{\mathrm{arctan}}$ geometries, therefore, has the effect of shifting the solutions for the two drift cycles closer towards each other, and from this it may be concluded that, in the case of $\mathrm{HCS}_{\mathrm{arctan}}$ and specifically at the large $\alpha_{\mathrm{s}} = 85°$, the drift effects were suppressed relative to the case of $\mathrm{HCS}_{\mathrm{arcsin}}$.

However insightful, these results present a very limited illustration of the differences in the modulation associated with each of the cases for $\mathrm{HCS}_{\mathrm{arctan}}$ and $\mathrm{HCS}_{\mathrm{arcsin}}$. A much more detailed investigation is afforded by profiles of intensity versus solar activity and this section is primarily devoted to the description and interpretation of such results.

#### Detour: A Drift Dominated Scenario

Before considering modulation under realistic conditions, this section provides a detour examining a case for which the diffusion coefficients were set to such small values that the situation became properly dominated by drift effects, boosted to this dominant status by the large gradients in CR intensities $\nabla j$, brought about by mentioned small diffusion coefficients. The study of this special and extreme case provides insights that will prove vital for a proper understanding of modulation in the more general case of realistically low diffusion to be considered later.

Note that the presentation of this extreme scenario does not start from the assumption that it is dominated by drift effects. Rather, it is presented from the viewpoint of asking what happens to modulation when diffusion coefficients are set to values smaller than what may be considered realistic. It is only then concluded that these low values lead to modulation effects which could only be explained if the scenario were in fact drift dominated and, more specifically, if the role of $\nabla j$ is given due credence.

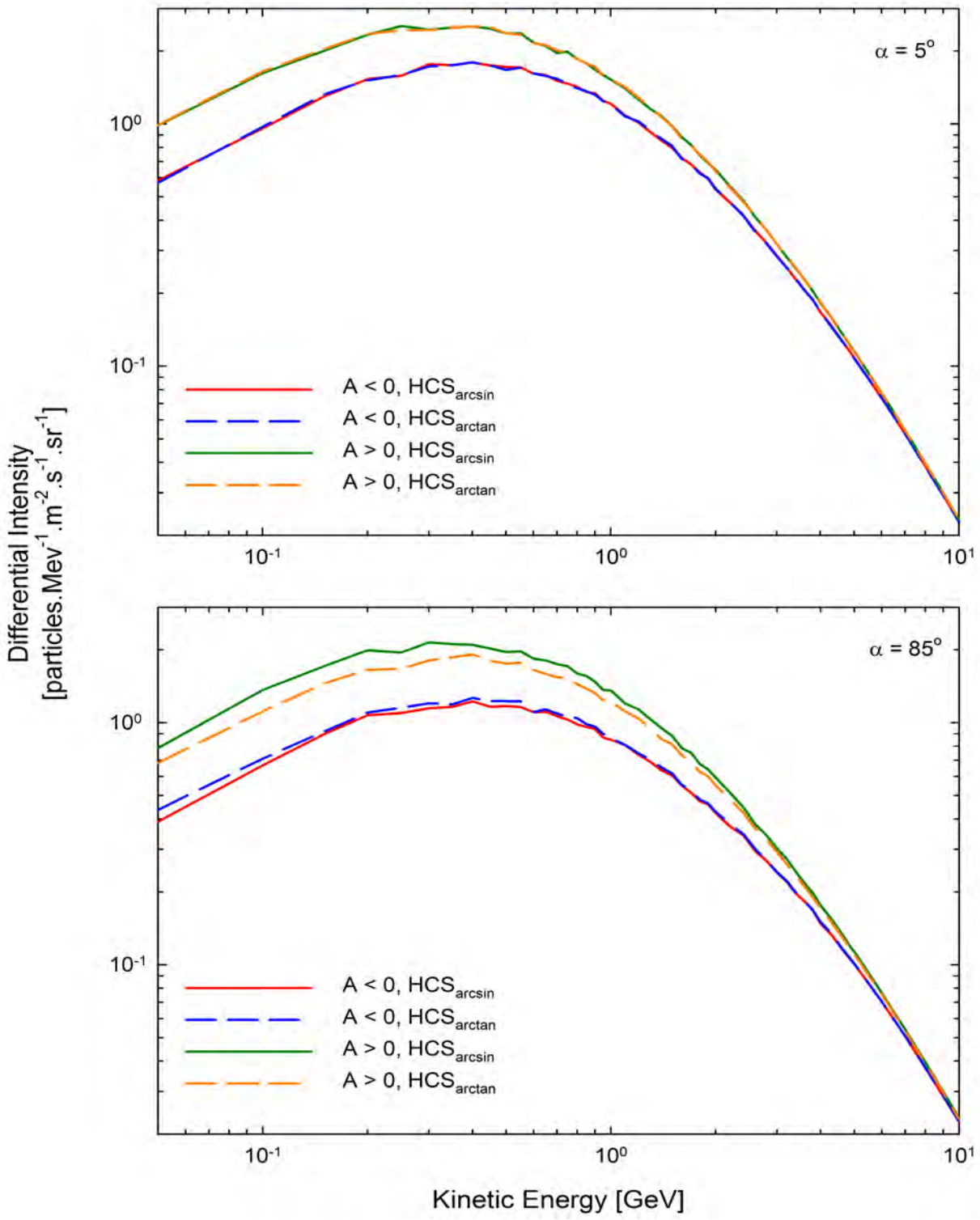


Figure 5.17: *Computed proton spectra at Earth using the SBM for both the $A > 0$ and $A < 0$ drift cycles and for both the cases of $HCS_{\arctan}$ and $HCS_{\arcsin}$. The top panel shows the results in the instance of a small tilt angle $\alpha = 5°$, while the bottom panel does so for a large tilt angle $\alpha = 85°$, close to the theoretical maximum of 90°. The solid red and green lines respectively show the $A < 0$ and $A > 0$ solutions for the case of $HCS_{\arcsin}$, whereas the dashed blue and orange lines respectively show the $A < 0$ and $A > 0$ solutions in the case of $HCS_{\arctan}$.*

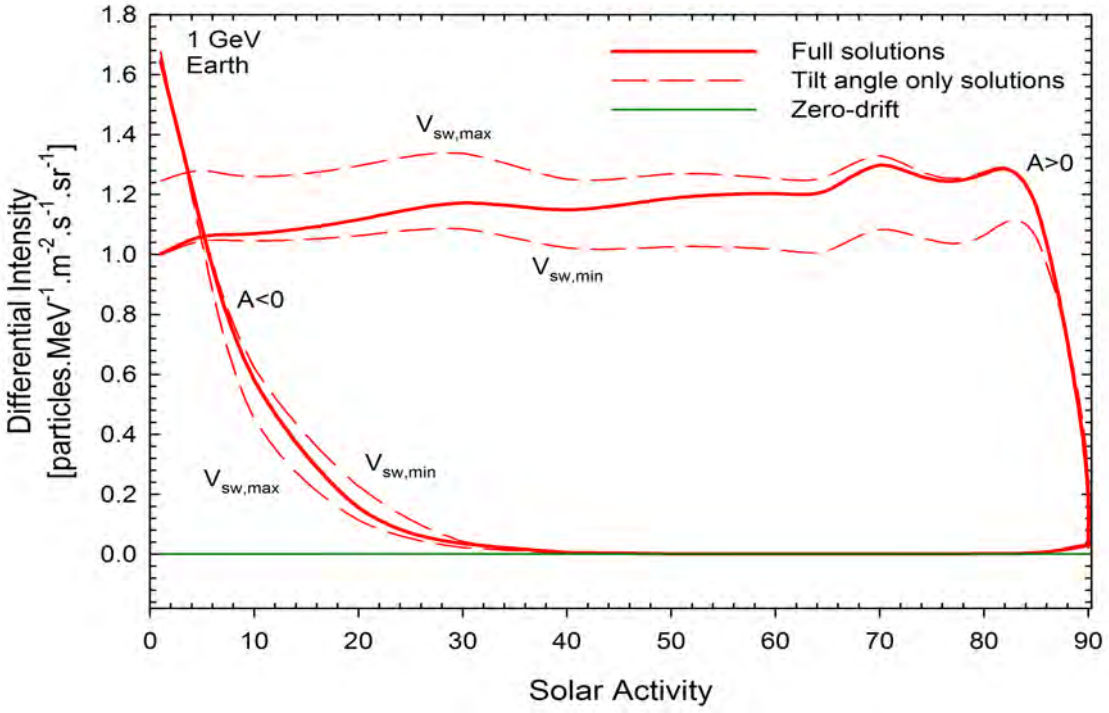


Figure 5.18: *The intensity versus solar activity profiles at Earth for 1 GeV protons for the case of HCS*$_{\rm arctan}$ *and under conditions using a very small* $\kappa_{||,0} = 1.0$. *The full solutions for both the* $A > 0$ *and* $A < 0$ *polarity cycles are indicated (solid thick red lines). The dashed red lines accompanying both of these full solutions represent the tilt angle only solutions and are labelled with* $V_{\rm sw,min}$ *and* $V_{\rm sw,max}$ *indicating that they are solutions for which the* $V_{\rm sw}$ *profile had been fixed to its minimum and maximum solar activity profiles respectively. The solid green line represents the zero-drift solution.*

Figure 5.18 shows the $A > 0$ and $A < 0$ intensity versus solar activity profiles for 1 GeV protons at Earth in the case of HCS$_{\rm arctan}$. The diffusion coefficients were set to low values with $\kappa_{||,0}$ in Eq. (3.31) set to $\kappa_{||,0} = 1.0$ in units of $6 \times 10^{20}$ cm$^2$.s$^{-1}$; henceforth all references to $\kappa_{||,0}$ imply these units. The reader is reminded that, according to Eqs. (3.32) and (3.33), all the diffusion coefficients are scaled with the parallel diffusion coefficient $\kappa_{||}$ so that a change in $\kappa_{||,0}$ affects corresponding changes in all of the diffusion coefficients. A value of $\kappa_{||,0} = 1.0$ corresponds to a parallel mean free path of $\lambda_{||} = 1.95 \times 10^{-2}$AU for a 1 GeV proton at Earth and, from the top panel of Figure 3.5, this value may evidently be considered unrealistically low. An SBM magnetic field with a magnitude at Earth of $B_{\rm e} = 5.05$ nT was assumed and the simulated TS was situated at $r_{\rm TS} = 88.0$ AU. For the sake of completeness and reproducibility, the rest of the parameters in Eq.(3.31) were set to $a = 0.81$, $b = 1.95$, and $c = d = 3.0$, while the settings for drift in Eq. (3.25) were set to $P_{\rm k} = 4.0$ GV, $P_{\rm A,0} = 1/\sqrt{2}$. The inner and outer modulation boundaries were treated as indicated in Chapter 4 and in Section 5.4, with $r_{\rm in} = 0.1$ AU and $r_{\rm out} = 120$ AU. The number of pseudo-particles used was increased from $N = 1 \times 10^3$ for spectra solutions to $N = 1 \times 10^4$ for solutions of this kind, since, for these solutions significant convergence was found to occur when $N$ was increased beyond $N = 1 \times 10^3$ (these results not shown); this implies a margin of error of $\sim 1\%$.

In Figure 5.18, the solid red lines represent the full solutions for both the $A > 0$ and $A < 0$ polarity cycles, while the green line shows the zero-drift solution. Four tilt angle

only solutions are also indicated by the dashed red lines, two for each of the polarity cycles. These tilt angle only solutions are for cases where the SW velocity profile $V_{\rm sw}$ was fixed to solar minimum and solar maximum conditions respectively and are as such labelled with $V_{\rm sw,min}$ and $V_{\rm sw,max}$. For the solar minimum conditions the tilt angle in the expression for $V_{\rm sw}$ was fixed to $\alpha = 1^\circ$ and for the solar maximum case to $\alpha = 89^\circ$. These four tilt angle only solutions are employed to help explain the behaviour of the full solutions

It is immediately clear that the $A > 0$ solution exhibits a peculiar behaviour: intensities are seen to actually increase with an increase in solar activity. This behaviour is in need of explanation. As $\alpha_{\rm s}$ increases, intensities are expected to exclusively decrease according to mechanisms that can be roughly divided into two separate but connected processes: (1) the physical extent (waviness) of the HCS increases, i.e. the operational volume of $\vec{v}_{\rm ns}$ is increased, preventing more protons from reaching Earth; the *operational volume* of $\vec{v}_{\rm ns}$ is defined as the volume over which this drift velocity field exerts itself and is necessarily associated with the area of the HCS ; at large $\alpha_{\rm s}$ the HCS enters the polar regions and significantly impairs inward drift from these regions to dramatically reduce intensities; (2) the fact that the $V_{\rm sw}$ profile changes as a function of the tilt angle through Eq. (2.2) in effect leads to lower SW velocities over larger parts of the heliosphere during solar maximum conditions; by Eq. (2.6), this leads to smaller values, at a given position, for the magnetic field $B$ and by Eqs. (3.25) and (3.31) to (3.33) causes a drop in both the drift and diffusion coefficients. Hence, apparently none of these processes will lead to any increase of intensities as function of $\alpha_{\rm s}$. In the text to follow, whenever reference is made to *the first* or *the second process*, these two processes are implied.

It is hard to think of any way by which the first process could be responsible for the evident increase with $\alpha_{\rm s}$, and the second process is immediately suspected. Consider the two $A > 0$ tilt angle only solutions where the upper and lower of these dashed lines are respectively identified with $V_{\rm sw,max}$ and $V_{\rm sw,min}$. These two solutions are seen to remain at approximately constant values of intensity as $\alpha_{\rm s}$ increases from minimum to maximum values, only dropping off at a very high $\alpha_{\rm s} \approx 82^\circ$. Furthermore, the full solution roughly coincides with the $V_{\rm sw,min}$ solution at the smallest $\alpha_{\rm s}$ and then meets up with the $V_{\rm sw,max}$ solution at $\alpha_{\rm s} \approx 78^\circ$. It is therefore clear that the conjecture that the increase with $\alpha_{\rm s}$ could be contributed entirely to the second effect was indeed correct. Its ability to produce any increase becomes ineffective at $\alpha_{\rm s} \approx 78^\circ$ as the first process takes hold: the HCS now starts to penetrate the polar regions deep enough to significantly obstruct protons from drifting inwards and thus counter the increase. At $\alpha_{\rm s} \gtrsim 82^\circ$ its effect in the polar regions is of such strength that the intensity can only decrease, and it does so rapidly.

However, since the second effect was indicated earlier to also exclusively affect a decrease in intensities with $\alpha_{\rm s}$, it still remains to be explained just how the peculiar increase is brought about. The fact that no such increase in evident in the zero-drift solution, may provide an important clue to arrive at an explanation: the increase must be a drift effect and is not caused, for example, by convection decreasing as $V_{\rm sw}$ gets reduced over the largest part of the heliosphere. Given this, there exists only one explanation: for such small diffusion coefficients, extremely large gradients $\nabla j$ in CR intensities are created and these boost the effectiveness of drift effects to such unprecedented heights as to actually lead to an increase in intensities as function of $\alpha_{\rm s}$. For a scenario in which the diffusion coefficients are this low, any increase in $\alpha_{\rm s}$ that reduces the diffusion coefficients only serves to promote this effect by boosting $\nabla j$ and drift effects even further so that intensities increase as function of $\alpha_{\rm s}$. Modulation at these low levels of diffusion can thus be described as drift dominated. In fact, this is now taken as the defining condition for scenarios thus classified: if the $A > 0$ solution shows any significant increase with $\alpha_{\rm s}$ (an increase greater than the $\sim 1\%$ allowed in this case by the statistical nature of the model),

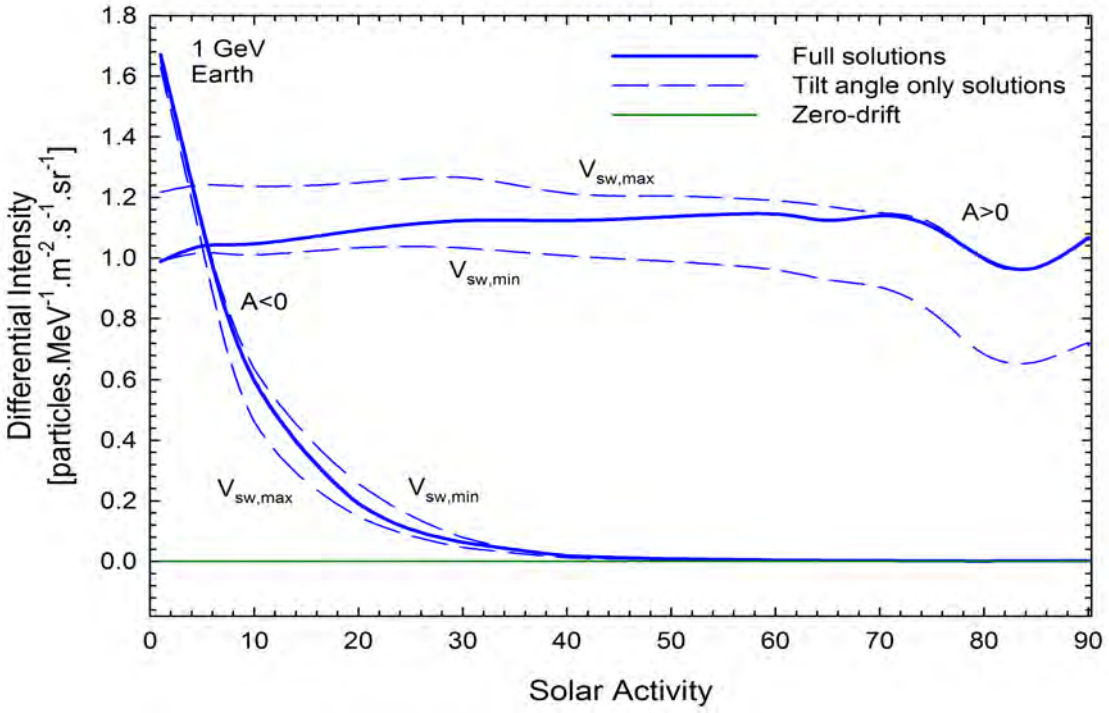


Figure 5.19: *This figure is analogous to Figure 5.18, but for the case of* $HCS_{\mathrm{arcsin}}$.

then such a scenario is defined as *drift dominated*. Finally, the effect of large gradients described here is henceforth referred to as *the effect of large* $\nabla j$ and, since it is brought about by the second process defined above, it may be described as a partner effect of this process.

Though the $A < 0$ polarity cycle profiles show no behaviour that can be called peculiar, it is well worth having a closer look at. According to the first and second processes, these profiles are expected to behave as follows: (1) as $\alpha_{\mathrm{s}}$ is increased, the operative volume of $\vec{v}_{\mathrm{ns}}$ is increased, i.e. the path length of protons drifting inwards along the HCS in the equatorial regions is increased so that it leads to intensities initially dropping off sharply with an increase in $\alpha_{\mathrm{s}}$; such an extended operative volume gives a proton a greater chance of leaving the HCS and to drift out at the poles to even further lower intensities; when the HCS enters the near polar regions it may significantly impair the outward drifts at the poles and increase intensities; (2) by the same means as for the $A > 0$ polarity cycle, the solar activity dependence of $V_{\mathrm{sw}}$ will affect intensities to decrease as function of $\alpha_{\mathrm{s}}$; however, in this case, the effect of large $\nabla j$ will now serve to aid outward drift at the poles and thus contribute to a decrease in intensities so that the solutions labelled by $V_{\mathrm{sw,min}}$ and $V_{\mathrm{sw,max}}$ are actually affected to decrease by both the second effect and its partner effect of large gradients $\nabla j$. Therefore, it is not clear how large a role the effect of large $\nabla j$ plays in this case.

Nonetheless, it is evident from Figure 5.18 that the $A < 0$ profiles react as expected: the $V_{\mathrm{sw,min}}$ solution now lies above the $V_{\mathrm{sw,max}}$ solution, indicative of the decreased drift effects in the latter case. At $\alpha_{\mathrm{s}} \approx 40°$ intensities have reached very small values in the order of $10^{-4}$ particles.$\mathrm{MeV}^{-1}$.$\mathrm{m}^{-2}$.$\mathrm{s}^{-1}$.$\mathrm{sr}^{-1}$, so that the effects of both the first and second processes are no longer discernible and the profiles are seen to flatten off. At $\alpha_{\mathrm{s}} \approx 85°$, however, the increase that can be expected when the HCS enters deep enough into the polar regions is in evidence.

Figure 5.19 is analogous to Figure 5.18, but for the case of $\mathrm{HCS}_{\mathrm{arcsin}}$. Again, the effect of large $\nabla j$ on the $A > 0$ solutions is clearly evident. For solar activity levels $\alpha_{\mathrm{s}} \lesssim 70°$, the difference between the tilt angle only solutions $V_{\mathrm{sw,min}}$ and $V_{\mathrm{sw,max}}$ is seen to be more or less of the same magnitude than in the case for $\mathrm{HCS}_{\mathrm{arctan}}$. Since the second process must be the same for both the cases of $\mathrm{HCS}_{\mathrm{arctan}}$ and $\mathrm{HCS}_{\mathrm{arcsin}}$, this implies that the role of $\nabla j$ in each case is of about the same scale. However, the effectiveness of the first process is seen to differ for the cases of $\mathrm{HCS}_{\mathrm{arctan}}$ and $\mathrm{HCS}_{\mathrm{arcsin}}$: where the $V_{\mathrm{sw,min}}$ and $V_{\mathrm{sw,max}}$ tilt angle only solutions in the case for $\mathrm{HCS}_{\mathrm{arctan}}$ had stayed approximately constant at $\alpha_{\mathrm{s}} \leq 70°$, both solutions are here seen to decrease from the onset. This indicates that in the case of $\mathrm{HCS}_{\mathrm{arcsin}}$ the first process is more effective in decreasing intensities over these ranges of $\alpha_{\mathrm{s}}$, thereby countering the increase brought about by the effect of large $\nabla j$ *in the full solution*. An important conclusion follows from noticing that this is far before any geometrical differences in the two HCS profiles become remotely visible. It must be concluded that $\vec{v}_{\mathrm{ns}}$ for the cases of $\mathrm{HCS}_{\mathrm{arctan}}$ and $\mathrm{HCS}_{\mathrm{arcsin}}$ is already significantly different at even at these low levels of solar activity, i.e. significantly different in the sense that it results in significantly different modulation. This difference in $\vec{v}_{\mathrm{ns}}$ may be as simple as $v_{\mathrm{ns}}$ being larger in the case of $\mathrm{HCS}_{\mathrm{arcsin}}$ or it may be a more involved matter such as the distribution of $\vec{v}_{\mathrm{ns}}$ over its three spatial components being more conducive to effective outward drift along the HCS in the case for $\mathrm{HCS}_{\mathrm{arcsin}}$.

However, at large $\alpha_{\mathrm{s}}$ where $\vec{v}_{\mathrm{ns}}$ enters the polar regions, this more effective status of the first process in the case for $\mathrm{HCS}_{\mathrm{arcsin}}$ is lost. Figure 5.18 has indicated that, in the case for $\mathrm{HCS}_{\mathrm{arctan}}$, the first process firmly takes hold of intensities at $\alpha_{\mathrm{s}} \gtrsim 82°$ to eventually lower it down to levels comparable to that of the zero-drift solution at $\alpha_{\mathrm{s}} = 90°$. Contrary to this, Figure 5.19 now indicates that intensities in the case of $\mathrm{HCS}_{\mathrm{arcsin}}$ only initially show an enhanced decrease at $\alpha_{\mathrm{s}} \approx 72°$; the first process then seems to fail altogether in reducing intensities any further, flattening off at $\alpha_{\mathrm{s}} \approx 83°$ and even increasing after this point. Considering the respective geometries of the $\mathrm{HCS}_{\mathrm{arctan}}$ and $\mathrm{HCS}_{\mathrm{arcsin}}$ shown in Figure 5.15, it is not surprising that the thin HCS arms in the latter case are not able to decrease intensities; this is considered and discussed in more detail later.

While the flattening of the full solution at these high levels of solar activity is thus quite understandable, the actual increase that occurs after $\alpha_{\mathrm{s}} \approx 83°$ is harder to explain and this work restricts itself to some speculation in this regard. The fact that the two tilt angle only solutions differ from each other to a clearly larger extent at these large $\alpha_{\mathrm{s}}$ suggests that the effect of large $\nabla j$ has increased its contribution to modulation at these high levels of solar activity. However, this effect gaining in influence cannot be the cause of the increase in the intensity of the full solution, since the said increase in intensity is also observed in the tilt angle only solutions themselves. Further evidence against this possibility is the fact that at drastically reduced proton energies (not shown), where the situation becomes dominated by diffusion, this increase in intensity at large $\alpha_{\mathrm{s}}$ still features distinctively. Therefore, the increase of the full $A > 0$ solution is an effect of the first process, i.e. a consequence of the interaction of a proton with the $\vec{v}_{\mathrm{ns}}$ field. The question now arises whether it is in any way possible that the net effect on a proton when it crosses the thin arms of the $\mathrm{HCS}_{\mathrm{arcsin}}$, at these large $\alpha_{\mathrm{s}}$, can be to promote its effective inward propagation to subsequently raise intensities at Earth.

Concerning the difference between the $A < 0$ profiles for the cases of $\mathrm{HCS}_{\mathrm{arctan}}$ and $\mathrm{HCS}_{\mathrm{arcsin}}$, there seems to be only one difference worth pointing out. Given that for the $A > 0$ polarity cycle, and over at least $\alpha_{\mathrm{s}} \in (0°, 82°)$, the $\vec{v}_{\mathrm{ns}}$ associated with the case for $\mathrm{HCS}_{\mathrm{arcsin}}$ is more effective in transporting protons outward, it should also be more effective in transporting protons inward during $A < 0$ polarity cycles − at least over the range of $\alpha_{\mathrm{s}}$ in which the $A < 0$ intensities decrease as function of $\alpha_{\mathrm{s}}$. This is seen to

Table 5.1: Values of $\kappa^{c}_{||,0}$, i.e. the value of $\kappa_{||,0}$ in Eq. (3.31) at which a modulation situation becomes drift dominated according to the definition in the text. These values are case specific and are indicated for both the cases of $\text{HCS}_{\text{arctan}}$ and $\text{HCS}_{\text{arcsin}}$ and for the three proton energies 1 GeV, 500 MeV, and 250 MeV.

| **Energy** | **HCS**$_{\text{arctan}}$ | **HCS**$_{\text{arcsin}}$ |
|---|---|---|
| 1 GeV | 5.2 | 2.6 |
| 500 MeV | 6.9 | 2.9 |
| 250 MeV | 7.5 | 3.1 |

be true, noting from Figures 5.18 and 5.19 that, in the case of $\text{HCS}_{\text{arctan}}$, decreases in intensity are discernible up to $\alpha_{\text{s}} \approx 40°$, while for the case of $\text{HCS}_{\text{arcsin}}$ it is visible up to $\alpha_{\text{s}} \approx 46°$; at $\alpha_{\text{s}} \approx 40°$ and $\alpha_{\text{s}} \approx 46°$ respectively, the intensities become so low that no further decreases with $\alpha_{\text{s}}$ are discernible. Furthermore, though not evident from Figures 5.18 and 5.19, the intensity levels after $\alpha_{\text{s}} \approx 40°$ and $\alpha_{\text{s}} \approx 46°$ respectively, indicated that the decrease in the intensity of the case for $\text{HCS}_{\text{arcsin}}$ was indeed smaller than in the case of $\text{HCS}_{\text{arctan}}$.

From the comparative discussion of Figures 5.18 and 5.19 it is clear that the role of the effect of large $\nabla j$ is more dominant in the case of $\text{HCS}_{\text{arctan}}$ than in the case of $\text{HCS}_{\text{arcsin}}$, even though $\nabla j$ has been concluded to be of about the same magnitude. Specifically as defined in this work, a drift dominated situation entails that − over at least some interval of $\alpha_{\text{s}}$ − the effect of large $\nabla j$ plays the dominant role in determining the intensity versus solar activity profile, i.e. it overpowers both the first and the second processes. As stated earlier, over at least $\alpha_{\text{s}} \in (0°, 82°)$, the first process is exerted more strongly in the case for $\text{HCS}_{\text{arcsin}}$ than in the case for $\text{HCS}_{\text{arctan}}$ and, therefore, in order for the effect of large $\nabla j$ to dominate this process to the same extent as in the case for $\text{HCS}_{\text{arctan}}$, smaller diffusion coefficients are needed. Put differently, in the case for $\text{HCS}_{\text{arcsin}}$, $\kappa_{||,0}$ will have to be reduced to smaller values before the situation will become drift dominated according to definition. The value of $\kappa_{||,0}$ at which a situation comes to satisfy this definition is henceforth referred to as the critical value $\kappa^{c}_{||,0}$; all values below this critical value by implication imply a drift dominated scenario. The second and third columns of the first row of Table 5.1 show the values of $\kappa^{c}_{||,0}$ for 1 GeV protons for the cases of $\text{HCS}_{\text{arctan}}$ and $\text{HCS}_{\text{arcsin}}$ respectively and confirms that the value of $\kappa^{c}_{||,0}$ is smaller in the case for $\text{HCS}_{\text{arcsin}}$ than in the case for $\text{HCS}_{\text{arctan}}$: $\kappa^{c}_{||,0} = 2.6$ in the former case, while in the latter case $\kappa^{c}_{||,0} = 5.2$.

Since diffusion is a function of particle energy by Eqs. (3.31), the value of $\kappa^{c}_{||,0}$ is naturally also dependent on particle energy. Since the effect of large $\nabla j$ is what defines a drift dominated scenario, the particular energy dependence of $\kappa^{c}_{||,0}$ can be motivated to sufficient means by explaining it via a simple consideration of the way in which $\nabla j$ is expected to react to changes in particle energy. Particles of lower energy will have smaller diffusion coefficients according to Eq. (3.31), which implies larger $\nabla j$ at the same value of $\kappa_{||,0}$. Thus, at lower energies the value of $\kappa^{c}_{||,0}$ is expected to be larger. The second and third rows of Table 5.1 clearly indicate this to be true: in the case for $\text{HCS}_{\text{arctan}}$, $\kappa^{c}_{||,0}$ increases from 5.2 to 6.9 to 7.5 as proton energies drop from 1 GeV to 500 MeV to 250 MeV; in the case for $\text{HCS}_{\text{arcsin}}$ the energy dependence of $\kappa^{c}_{||,0}$ is seemingly weaker with values increasing from 2.6 to 2.9 to 3.1 for the same decrease in energy. It is notable that the energy dependence in both the cases for $\text{HCS}_{\text{arctan}}$ and $\text{HCS}_{\text{arcsin}}$ becomes weaker as energy gets lower.

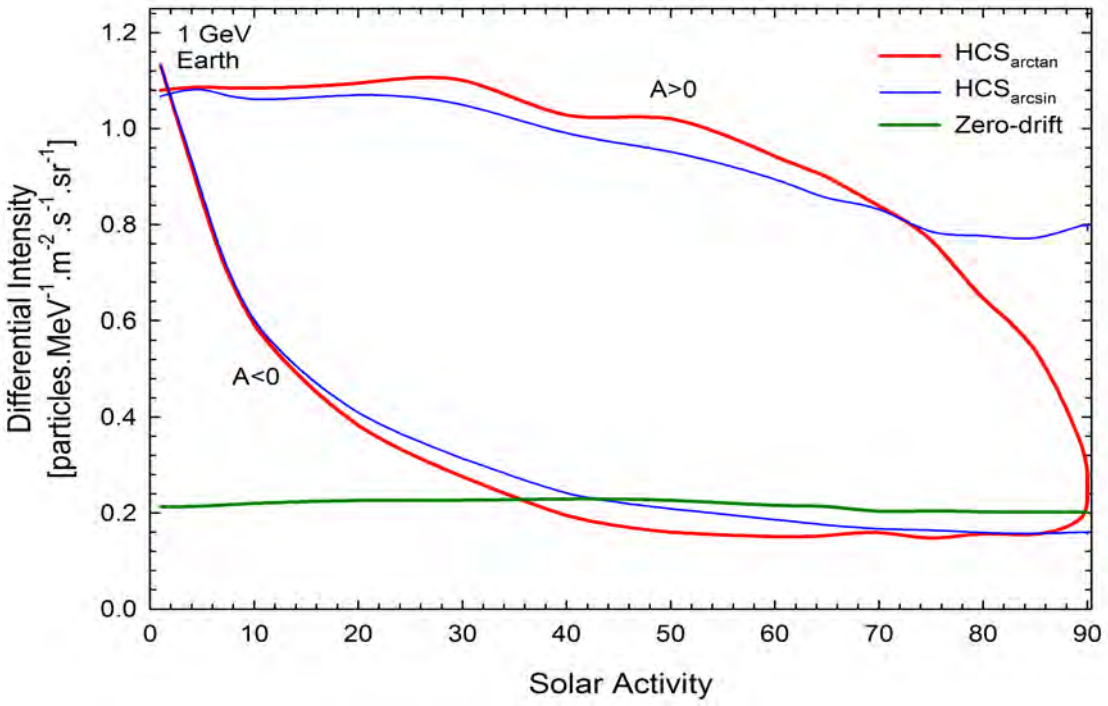


Figure 5.20: *The intensity versus solar activity profiles at Earth for a 1 GeV proton for both polarity cycles and for both the geometries of HCS*$_{\text{arctan}}$ *(red lines) and HCS*$_{\text{arcsin}}$ *(blue lines). The zero-drift solution is indicated by the green line.*

### A Scenario for Realistically Low Diffusion

Equipped with the insight provided by the investigation of the drift dominated scenario, this section looks at a more general scenario in which diffusion was fixed to a more realistic level. It was, however, still kept relatively low so as to not overly suppress the drift effects which form the central subject of this investigation.

Figure 5.20 shows the intensity versus solar activity profiles for 1 GeV protons in both the $A > 0$ and $A < 0$ polarity cycles and for both the cases of HCS$_{\text{arctan}}$ (red lines) and HCS$_{\text{arcsin}}$ (blue lines). The green line shows the zero-drift solution. All of these solutions are calculated at Earth and using settings identical to those for Figures 5.18 and 5.19, but with the exception of the diffusion coefficients now being increased by setting $\kappa_{||,0} = 7.0$. This value for $\kappa_{||,0}$ corresponds to a parallel mean free path $\lambda_{||} = 1.36 \times 10^{-1}$ AU for a 1 GeV proton at Earth and from the top panel of Figure 3.5 this is evidently a value which can be considered realistically low.

It is seen that the $A > 0$ solutions for the HCS$_{\text{arctan}}$ and HCS$_{\text{arcsin}}$ cases start out at more or less identical levels of intensity, but almost immediately at $\alpha_s \approx 6°$ begin to diverge systematically from each other with any further increase in $\alpha_s$. Both cases show a decrease with an increase in $\alpha_s$, the case for HCS$_{\text{arctan}}$ initially more moderately, hence remaining at higher levels than the profile for the case of HCS$_{\text{arcsin}}$ for some time. As $\alpha_s$ increases though, the HCS$_{\text{arctan}}$ profile starts dropping off more sharply than that of the case for HCS$_{\text{arcsin}}$ so that, at $\alpha_s \approx 72°$, it drops below the HCS$_{\text{arcsin}}$ profile. It continues its decrease to reach levels of intensity in the order of the zero-drift solution at $\alpha_s \approx 90°$. The HCS$_{\text{arcsin}}$ profile, on the other hand, seizes its decrease as a function of $\alpha_s$ and is seen to flatten off at $\alpha_s \approx 75°$; at $\alpha_s \gtrsim 85°$ it shows a slight increase.

Looking at the $A < 0$ solutions, the $\text{HCS}_{\text{arctan}}$ and $\text{HCS}_{\text{arcsin}}$ cases yield identical levels of intensity up to about $\alpha_s \approx 10°$ and then start to diverge, with the former case dropping below the latter. The solution in the case for $\text{HCS}_{\text{arctan}}$ reaches the level of the zero-drift solution at $\alpha_s = \alpha_s^* \approx 36°$, while that in the case for $\text{HCS}_{\text{arcsin}}$ does so only at $\alpha_s^* \approx 42°$. The values of $\alpha_s^*$ for the two cases are thus still separated by the same $\sim 6°$ that was found for the drift dominated scenario where $\alpha_s^* \approx 40°$ and $\alpha_s^* \approx 46°$ for $\text{HCS}_{\text{arctan}}$ and $\text{HCS}_{\text{arcsin}}$ respectively. In contrast to the drift dominated scenario however, intensity levels now never decrease to such low values that changes in intensity with $\alpha_s$ become indiscernible; intensities never decrease below $\sim 1.5 \times 10^{-1}$ particles.$\text{MeV}^{-1}.\text{m}^{-2}.\text{s}^{-1}.\text{sr}^{-1}$. Both the solutions for $\text{HCS}_{\text{arctan}}$ and $\text{HCS}_{\text{arcsin}}$ is now seen to continue to decrease beyond $\alpha_s = \alpha_s^*$ to levels below that of the zero-drift solution. Although the solution in the case for $\text{HCS}_{\text{arctan}}$ levels off at $\alpha_s \approx 52°$ while in the case for $\text{HCS}_{\text{arcsin}}$ it continues to decrease up to $\alpha_s \approx 80°$, the solution of the former case is seen to remain below that of the latter case until, at $\alpha_s \approx 62°$, it shows signs of increasing to return to the levels of the latter case at $\alpha_s \approx 70°$. At $\alpha_s \approx 85°$ the $\text{HCS}_{\text{arctan}}$ solution is seen to sharply increase with any further increase in solar activity, and at $\alpha_s \approx 90°$ it reaches intensities in the order of the zero-drift solution, neatly closing the loop with the $A > 0$ solution. The solution in the case of $\text{HCS}_{\text{arcsin}}$, on the other hand, does not show this increase but remains approximately constant. Note that the $\alpha_s$ dependence of the zero-drift solution as indicated in Figure 5.14 is indeed still present, but of such an insignificant scale in relation to that of the drift solutions that it is not even discernible in Figure 5.20.

The groundwork needed to interpret these results was established extensively during the treatment of the drift dominated scenario and it is therefore at some risk of duplication that the results described above are explained. As this scenario is not drift dominated, the effect of large $\nabla j$ is rendered less effective and modulation is dominated by the first and second processes which both cause intensities to decrease as function of $\alpha_s$. Hence, the $A > 0$ solutions in both the cases for $\text{HCS}_{\text{arctan}}$ and $\text{HCS}_{\text{arcsin}}$ now exclusively decrease as function of $\alpha_s$; the exception being the slight increase of the solution for the case of $\text{HCS}_{\text{arcsin}}$ at the largest values of $\alpha_s$. The fact that the intensity profile in the case for $\text{HCS}_{\text{arctan}}$ is initially higher than that for the case of $\text{HCS}_{\text{arcsin}}$ is due to the first process which has been identified as being more effective in the latter of these cases; this again illustrates that the $\vec{v}_{\text{ns}}$ fields associated with these two cases are different even at such small $\alpha_s$ where no differences are as yet evident in the geometries of the two cases. At some value of $\alpha_s$ the situation is turned around so that the effect is stronger in the case for $\text{HCS}_{\text{arctan}}$; this occurs soon after the value of $\alpha_s$ at which the solution for $\text{HCS}_{\text{arctan}}$ begins to decrease more rapidly than that in the case of $\text{HCS}_{\text{arcsin}}$.

The fact that the $A < 0$ solution for the case of $\text{HCS}_{\text{arctan}}$ is lower than that in the case of $\text{HCS}_{\text{arcsin}}$ is to be expected if the first process is, in the latter case, more effective over these levels of solar activity: the solution for $\text{HCS}_{\text{arcsin}}$ will be higher due to the more effective inward drift along the HCS. The downwards migration of $\alpha_s^*$ when diffusion is increased is in accord with what is expected. Larger diffusion must imply a profile that flattens off at lower values of $\alpha_s$ since larger diffusion will provide means of countering a decrease due to expansion of the HCS: short circuiting of the HCS will become effective at smaller $\alpha_s$, causing any further expansion of the HCS to be ineffective in decreasing intensities. This must, in turn, be reflected in the values for $\alpha_s^*$.

The focus is now turned to the difference between the profiles specifically for the respective cases of $\text{HCS}_{\text{arctan}}$ and $\text{HCS}_{\text{arcsin}}$ for the current scenario of realistically low diffusion and at larger values of $\alpha_s$. The result of the $A > 0$ and $A < 0$ solutions in the case of $\text{HCS}_{\text{arctan}}$ nearing the intensity levels of the zero-drift solution at the highest levels of solar activity and, in doing so, neatly closing up at $\alpha_s \approx 90°$ has not been achieved

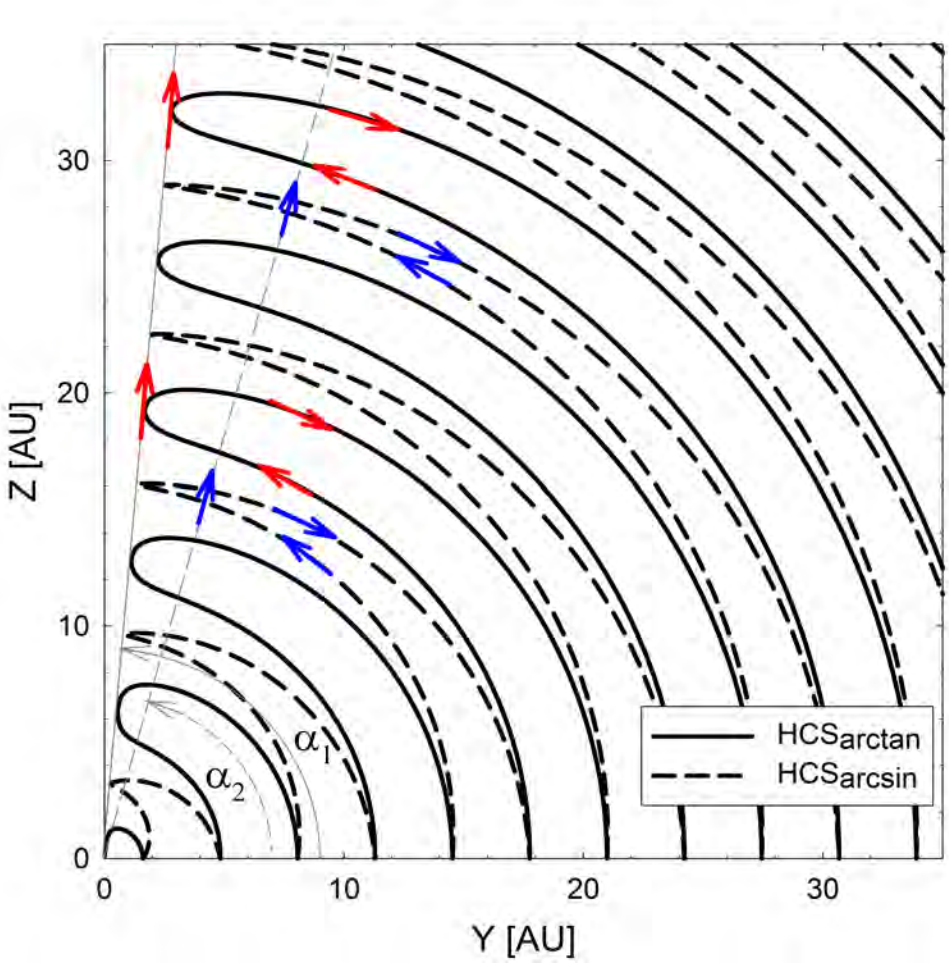


Figure 5.21: *An illustration of the concept of an effective tilt angle* $\alpha_e$ *in the meridional plane, with* $Y$ *the equatorial direction. Using* $\alpha = 85°$*, the solid black line shows the* $HCS_{\text{arctan}}$ *geometrical profile, while the dashed black line shows the* $HCS_{\text{arcsin}}$ *profile. The red and blue arrows show the supposed current sheet drifts of a proton for these two cases respectively. The angles* $\alpha_1$ *and* $\alpha_2$ *represent the respective effective tilt angles.*

before. Since the first process was indicated to take over in determining the intensity profiles at these high levels of $\alpha_s$ for both $A > 0$ and $A < 0$ polarity cycles, this difference in the behaviour of the $\text{HCS}_{\text{arctan}}$ and $\text{HCS}_{\text{arcsin}}$ intensity profiles is necessarily still an effect of the drift velocity fields associated with each of these current sheets respectively. Drift effects in the case for $\text{HCS}_{\text{arctan}}$ are suppressed relative to that of the case for $\text{HCS}_{\text{arcsin}}$. This was also illustrated by the results of Figure 5.17.

The more detailed explanation of what happens at these high levels of solar activity that was postponed during the discussion of the drift dominated scenario, is now presented. At these high levels of solar activity the geometries of the cases for $\text{HCS}_{\text{arctan}}$ and $\text{HCS}_{\text{arcsin}}$ are significantly different and this affords an explanation of these results from a geometrical perspective, i.e. by considering the differences in the geometries of these two cases. However, it is important to keep in mind that the entire HCS drift velocity field $\vec{v}_{\text{ns}}$ is indiscriminately connected to the geometry of the HCS. In fact, the geometry of the HCS is nothing else than the spatial distribution of $\vec{v}_{\text{ns}}$ in the heliosphere.

From a geometrical perspective then, for the $A > 0$ polarity cycle, the question to be considered is how a proton drifting inwards from the polar regions will be affected upon encountering the geometries of the cases for $\text{HCS}_{\text{arctan}}$ and $\text{HCS}_{\text{arcsin}}$ respectively. It is

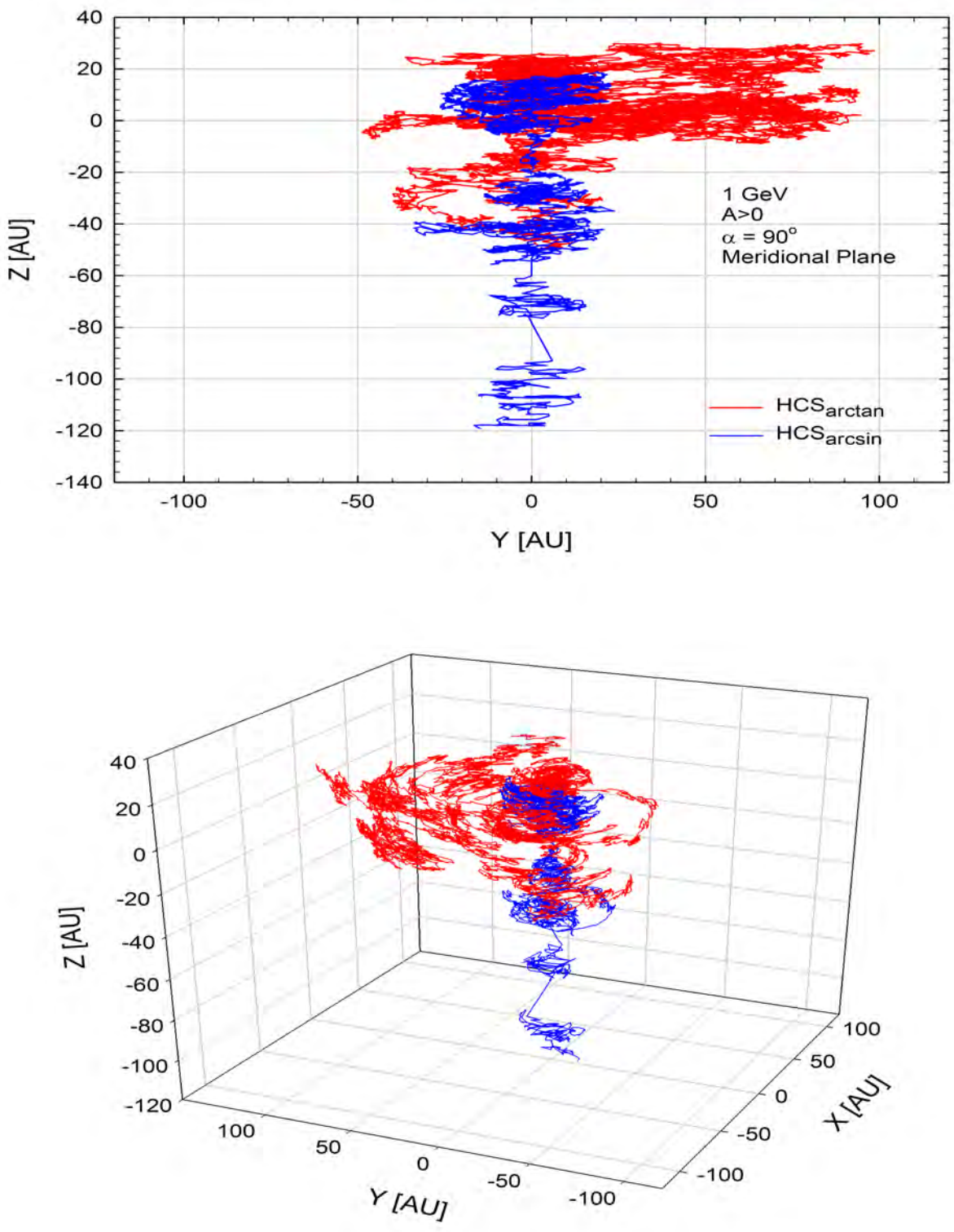


Figure 5.22: *Pseudo-particle trajectories for 1 GeV protons during an $A > 0$ polarity cycle. The top panel shows the trajectories projected in the meridional plane, while the bottom panel shows the 3D version. In both these panels the trajectory in the case of $HCS_{\text{arctan}}$ is represented by the red lines, while the blue lines represent the case for $HCS_{\text{arcsin}}$.*

quite conceivable, and even to be expected, that a proton encountering the thin arms of the $HCS_{arcsin}$ geometry will experience significantly less 'resistance' in reaching Earth than should a proton that encounters the the thicker arms of the $HCS_{arctan}$ geometry. Protons will thus be diverted from reaching Earth more effectively in the latter case and the result will be lower intensities at Earth. Similarly, during the $A < 0$ polarity cycle, the $HCS_{arctan}$ geometry will prevent protons from drifting out at the poles and will result in higher intensities, while the geometry of the case for $HCS_{arcsin}$ will not be able to effect any increase. The question whether the thin arms of the $HCS_{arcsin}$ can actually assist these protons in reaching Earth at very high $\alpha_s$ remains.

At this stage, and in this context, it is convenient to define an *effective tilt angle* $\alpha_e$, which is the tilt angle 'experienced' by a proton of a given energy, i.e. the tilt angle to which it effectively reacts. At a fixed tilt angle $\alpha$ which is large enough so that the geometric differences between the cases for $HCS_{arctan}$ and $HCS_{arcsin}$ have set in, a proton encountering the latter geometry will in effect react to a tilt angle $\alpha_e < \alpha$, while in the case of the $HCS_{arctan}$ geometry $\alpha_e$ is expected to be closer to or even equal to the actual tilt angle $\alpha$, i.e. $\alpha_e$ in the case of $HCS_{arctan}$ will be larger than in the case of $HCS_{arcsin}$. This is illustrated by Figure 5.21 and in this instance from the perspective of a proton drifting outwards along the HCS during an $A < 0$ polarity cycle. The red arrows show the expected realisation of HCS drifts in the case for $HCS_{arctan}$, while the blue arrows do so for the $HCS_{arcsin}$ case. The angles $\alpha_1$ and $\alpha_2$ serve to illustrate the effective tilt angles in the cases for $HCS_{arctan}$ and $HCS_{arcsin}$ respectively. It is reasonable to expect that a proton that would in the former case closely follow the physical geometry of the HCS and neatly reverse its drift direction on the HCS at $\alpha_e = \alpha_1 \lesssim \alpha$, would in the latter case reverse its drift direction at a value of $\alpha_e = \alpha_2 < \alpha$ via short circuiting of the HCS. Thus the concept of an effective tilt angle $\alpha_e$ is clearly illustrated (see also le Roux and Potgieter, 1992).

Making use of some of the powerful visualisation techniques enabled by the SDE-based model, the discussion surrounding Figure 5.21 is reinforced. Figure 5.22 shows pseudo-particle trajectories for a 1 GeV proton in the $A > 0$ polarity cycle, the tilt angle set to $\alpha = 90°$ and under the same conditions as was specified for Figure 5.20. The red lines represent the case for $HCS_{arctan}$, while the blue lines do so for the case of $HCS_{arcsin}$. The top panel of Figure 5.22 shows the trajectories as projected in the meridional plane, while the bottom panel presents the 3D version of these trajectories. From a modeling perspective, this figure is interpreted as follows: a pseudo-particle is released at Earth and traced to the boundary of the heliosphere; in the case for $HCS_{arcsin}$ it easily travels outwards to exit the heliosphere in the polar regions while, for the case of $HCS_{arctan}$, it is to such an extent impeded by the HCS that it is diverted from exiting at the poles to exit at some lower latitudinal position.

From a modulation perspective, this means that a proton drifting inwards from the polar regions will indeed more easily cross the thin arms of the case for $HCS_{arcsin}$ and be able to reach Earth. In the case for $HCS_{arctan}$, on the other hand, a proton that has entered the heliosphere in the polar regions will be diverted by the HCS to such a degree that it will not be able to reach the Earth at all, in the process also getting scattered off the HCS by diffusion; rather, protons that do reach Earth will have done so by entering the heliosphere at lower latitudes. This naturally implies lower intensities at Earth for the $HCS_{arctan}$ case since, in such a case, the protons are not able to quickly and efficiently drift in along the poles to contribute to intensities at Earth; rather, a proton may have to enter at a position where it will not be aided by the inward drift from the poles to make its way to Earth. In addition to lacking this aid, such a proton will now also more likely have to compete against magnetic field configurations not as supportive to helping

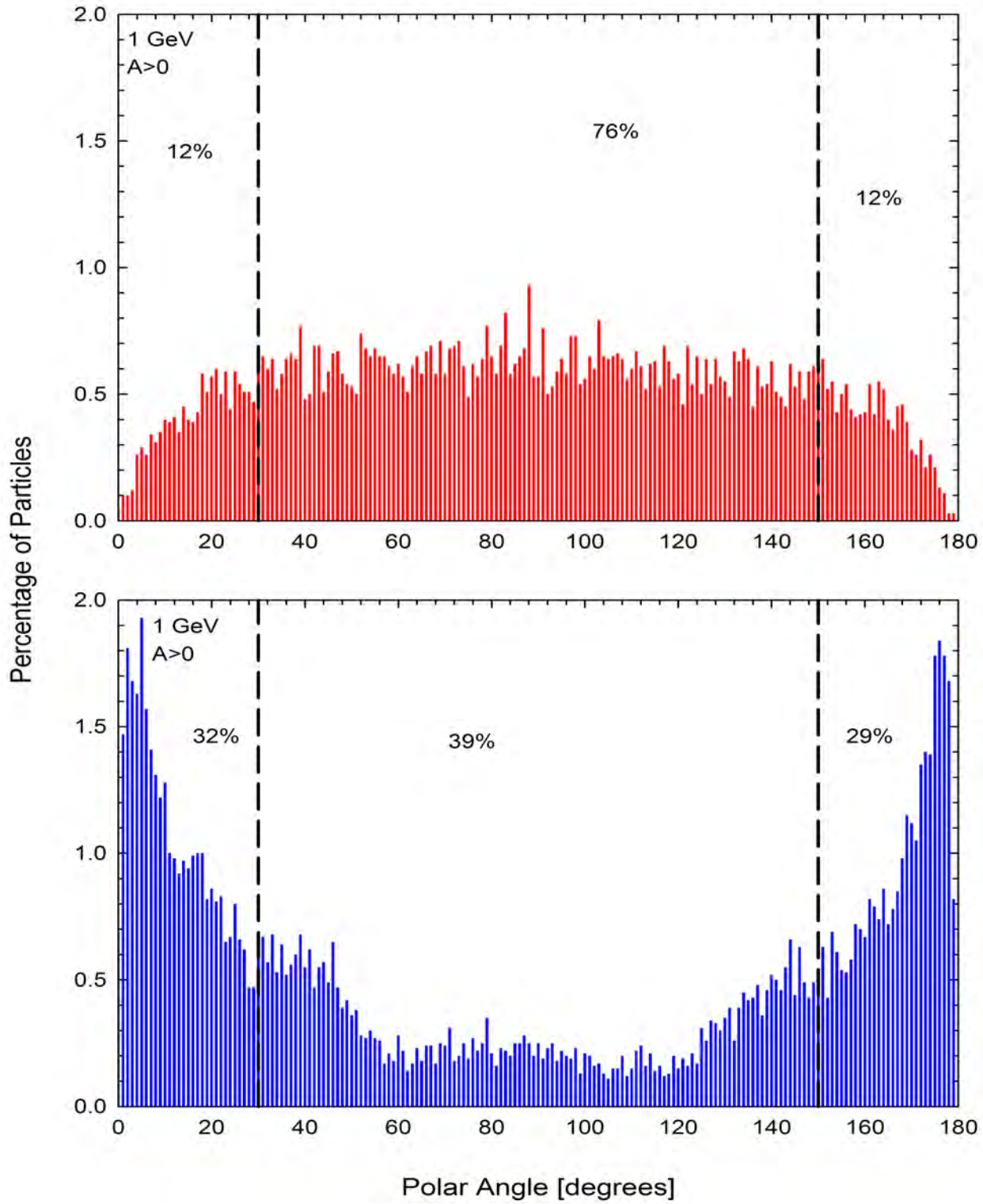


Figure 5.23: *The polar angle distribution of the exit positions of $N = 1 \times 10^4$ pseudo-particles traced from Earth during an $A > 0$ polarity cycle and with $\alpha = 90°$. This is interpreted as the polar angle distribution of the entering positions for this number of 1 GeV protons to have arrived at Earth. The top panel shows the case for $HCS_{\arctan}$, while the bottom panel does so for $HCS_{\arcsin}$. The vertical black dashed lines in both panels are drawn at $\theta = 30°$ and $\theta = 150°$, defining the near polar regions.*

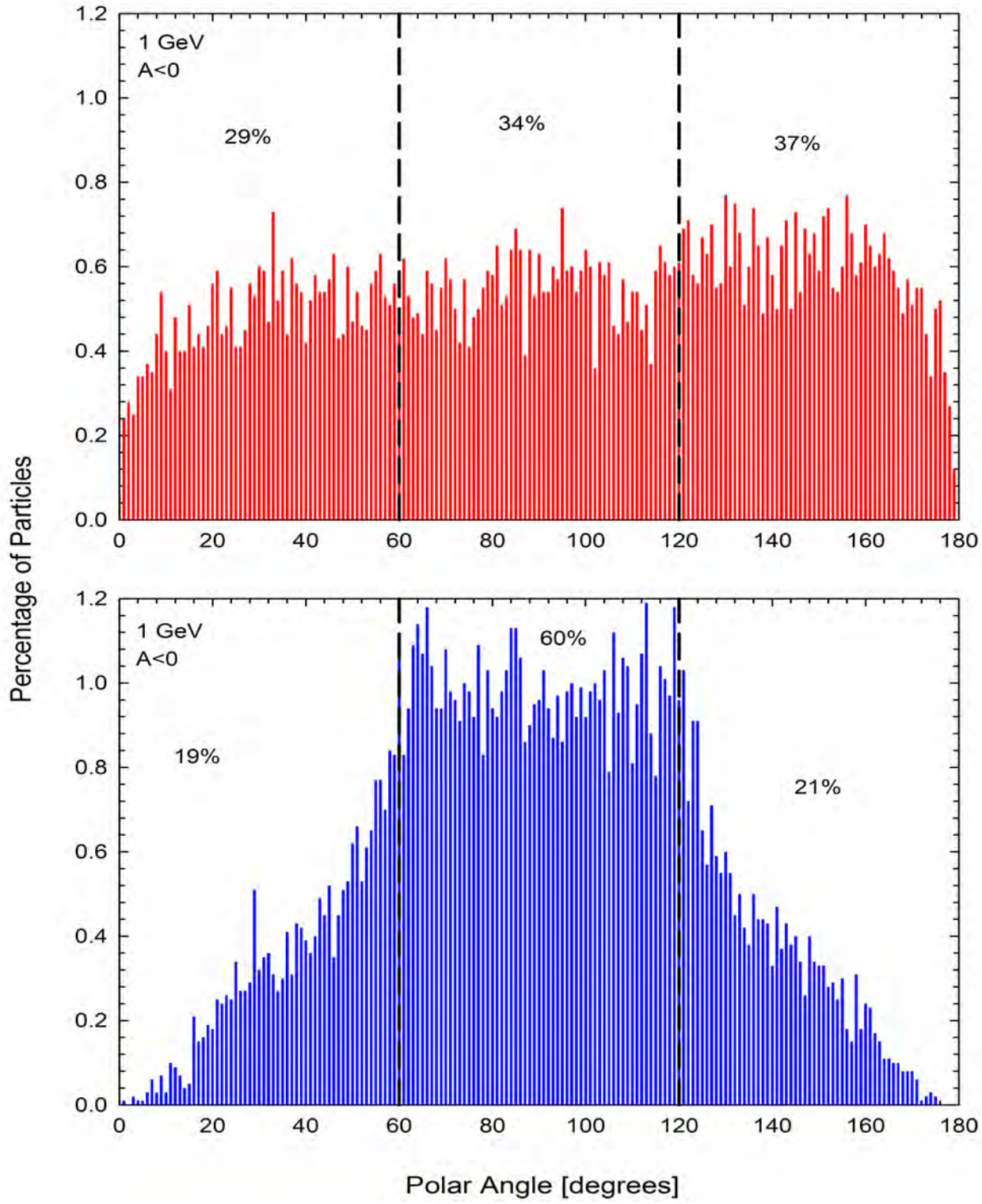


Figure 5.24: *Analogous to Figure 5.23, but for the $A < 0$ polarity cycle. The vertical black dashed lines are drawn at $\theta = 60°$ and $\theta = 120°$.*

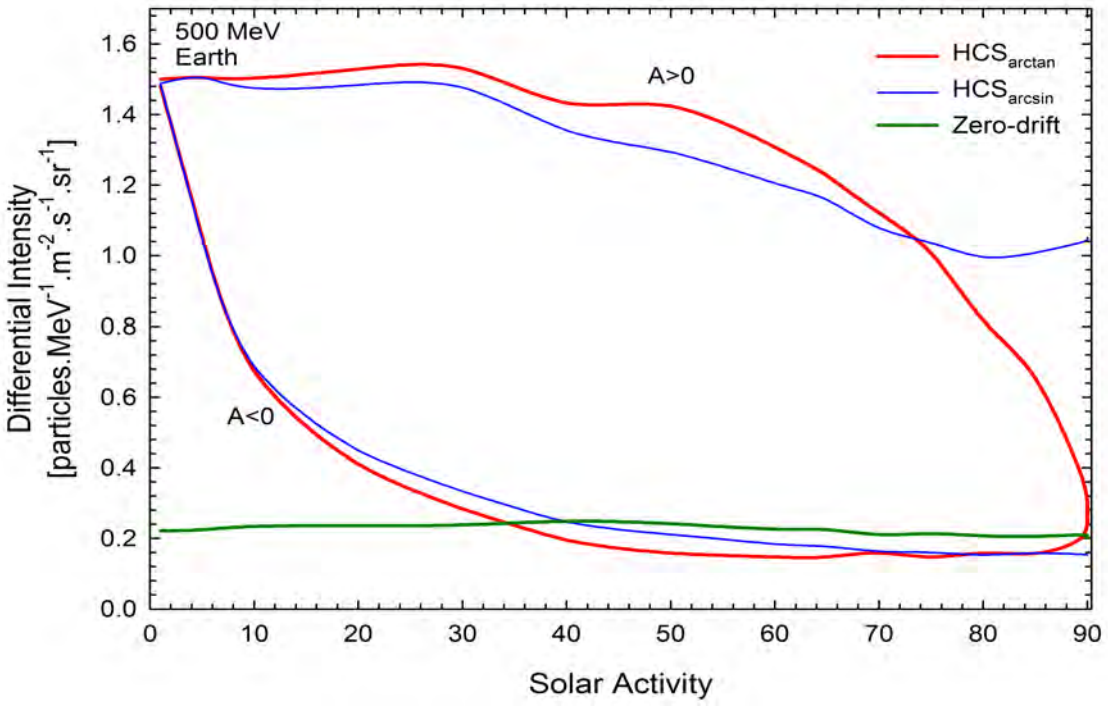


Figure 5.25: *Similar to Figure 5.20, but now for 500 MeV.*

it on its way to Earth, i.e. the closed magnetic field lines of the equatorial regions are substituted for the open magnetic field lines of the polar regions. The overall effect is that the protons are less likely to complete such an encumbered route to Earth, implying that out of a fixed number of protons entering the heliosphere at these lower latitudes, a smaller number of these protons will eventually reach Earth.

Though such trajectories of a single pseudo-particle may in this way shed light on the modulation process, it is more statistically sound to show that these same deductions are also reflected in the overall behaviour of a larger number of pseudo-particles. Since it would be wholly impractical to plot the trajectories of, say $N = 1 \times 10^4$ pseudo-particles, a different approach is followed: for each of the $\text{HCS}_{\text{arctan}}$ and $\text{HCS}_{\text{arcsin}}$ cases this number of pseudo-particles are traced from Earth outwards and the percentage of these pseudo-particles to have exited at each value of the polar angle is calculated and plotted as bar graphs in Figure 5.23 ($A > 0$ polarity cycle) and Figure 5.24 ($A < 0$ polarity cycle). The polar angle is plotted on the horizontal axis so that, for example, the bar at $\theta = 0°$ indicates the percentage of pseudo-particles to have exited the heliosphere at polar angles between 0° and 1°; the bar at $\theta = 179°$ then finally does so for polar angles between 179° and 180°. Again, the tilt angle is set to $\alpha = 90°$.

The top panel of Figure 5.23 presents the case for $\text{HCS}_{\text{arctan}}$ during the $A > 0$ polarity cycle and, from a modulation perspective, shows that the majority of protons to arrive at Earth have entered the heliosphere at intermediate to low latitudes, the number sharply decreasing towards the poles. The two vertical black dashed lines are drawn at polar angles of $\theta = 30°$ and $\theta = 150°$ so that the percentages indicated in the three blocks thus divided indicate that about $\sim 12\%$ of protons have entered between $\theta \in [0°, 30°]$, $\sim 76\%$ between $\theta \in [30°, 150°]$, and the other $\sim 12\%$ between $\theta \in [150°, 180°]$. If the regions within 30° of the poles are now defined as the *near polar regions*, then it is seen that about $\sim 24\%$ of protons have entered the heliosphere in these regions, while the

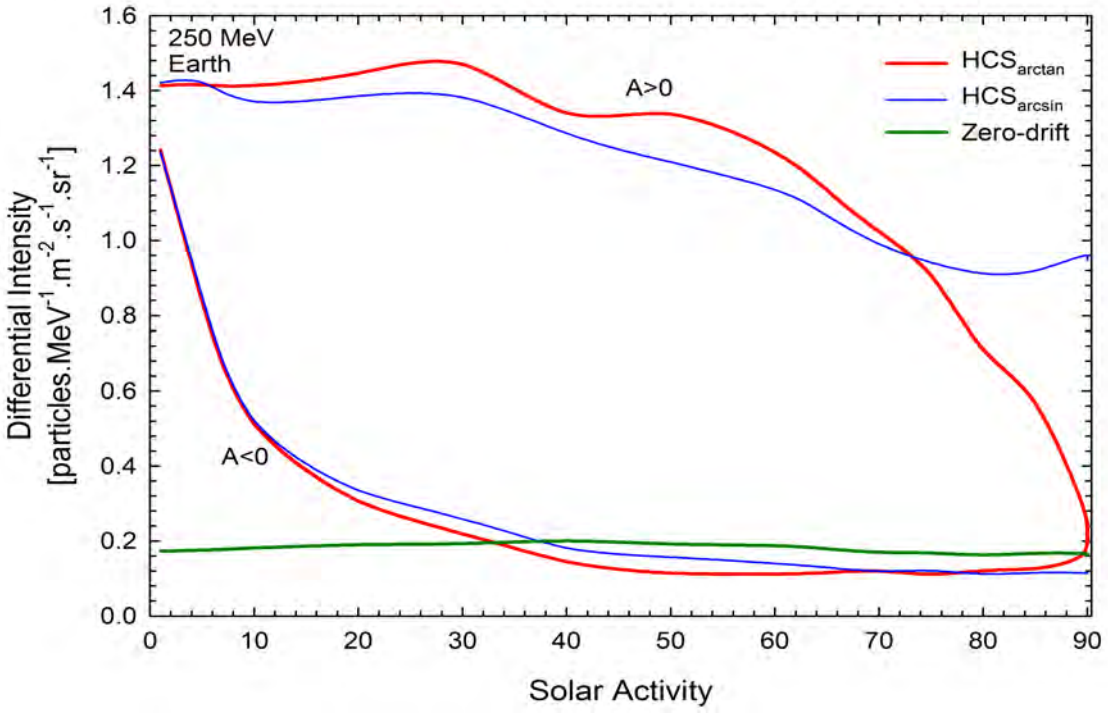


Figure 5.26: *Similar to Figures 5.20 and 5.25, but now for 250 MeV.*

overwhelming majority of $\sim 76\%$ have entered at other points further away from the poles. On the other hand, the bottom panel, presenting the case for $\text{HCS}_{\text{arcsin}}$ shows that a clear majority of $\sim 61\%$ of protons have entered in the near polar regions, while the remaining $\sim 39\%$ have come from the lower latitudes. This confirms the deductions first arrived at from consideration of Figure 5.21 and 5.22: protons will more easily cross the thin arms of the $\text{HCS}_{\text{arcsin}}$ than the thick arms of the $\text{HCS}_{\text{arctan}}$.

For the $A < 0$ solutions a similar process is followed to explain the observed behaviour. Figure 5.24 is similar to Figure 5.23, but for the $A < 0$ polarity cycle. The two vertical black dashed lines are drawn at $\theta = 60°$ and $\theta = 120°$, dividing $\theta \in [0°, 180°]$ into three equal intervals spanning 60° each. From the top panel it is evident that, in the case of $\text{HCS}_{\text{arctan}}$, protons arriving at Earth have entered at positions more or less uniformly between $\theta \in [0°, 180°]$. Only a slight decrease is seen towards the extreme near polar regions at $\theta \in \{0°, 180°\}$. For the $\text{HCS}_{\text{arcsin}}$ case (bottom panel), in comparison, it follows that about 60% of all protons to reach Earth have in fact entered within the interval $\theta \in [60°, 120°]$, i.e. within the first 30° above and below the equatorial plane. Furthermore, the distribution steadily drops off towards the poles so that it is clear that, in this case, the preferred entering positions of the protons are the equatorial regions. This accounts for the rise in the $A < 0$ intensity versus solar activity profile in the case of $\text{HCS}_{\text{arctan}}$ at large $\alpha_{\text{s}}$, while the corresponding profile in the case of $\text{HCS}_{\text{arcsin}}$ stays flat: in the latter case protons can still effectively drift out at the poles despite the large tilt angle, since the thin arms of the $\text{HCS}_{\text{arcsin}}$ cannot impede this motion, i.e. the effective tilt angle is smaller than the actual tilt angle $\alpha_{\text{e}} < \alpha$; in the former case, however, $\alpha_{\text{e}}$ is much larger and the thick arms of the $\text{HCS}_{\text{arctan}}$ inhibit the outward drift at the poles to such an extent that intensities show an increase.

To conclude the treatment of the scenario for what is considered realistically low diffusion, the energy dependencies of some of the effects described thus far are considered.

Table 5.2: Intensities at $\alpha_s = 90°$ expressed as fraction of those at $\alpha_s = 1°$ during the $A > 0$ and $A < 0$ polarity cycles of both the cases for $HCS_{arctan}$ and $HCS_{arcsin}$. These are indicated for each of the proton energies 1 GeV, 500 MeV, and 250 MeV.

| **Energy** | **HCS**$_{arctan}$ | | **HCS**$_{arcsin}$ | |
|---|---|---|---|---|
| | ***A>0*** | ***A<0*** | ***A>0*** | ***A<0*** |
| 1 GeV | 0.22 | 0.25 | 0.74 | 0.14 |
| 500 MeV | 0.17 | 0.20 | 0.71 | 0.10 |
| 250 MeV | 0.14 | 0.20 | 0.67 | 0.09 |

Figures 5.25 and 5.26 are analogous to Figure 5.20, but present the results for the two lower proton energies half and half again of 1 GeV, i.e. 500 MeV and 250 MeV respectively. Comparing these three figures it is clear that intensity profiles at these two lower energies behave in a largely similar fashion to that seen at 1 GeV. The distinctively different qualitative behaviour of the cases for $HCS_{arctan}$ and $HCS_{arcsin}$ at 1 GeV is again reflected at each energy.

Before looking at these results in more detail, it is noted that the extent of modulation, i.e. to what degree proton intensities are decreased over the entire range of solar activity $\alpha_s = 1°$ to $\alpha_s = 90°$, is evidently dependent on the energy of the protons. This is illustrated clearly in Figure 5.27, showing the normalised intensity profiles for each of the proton energies 1 GeV, 500 MeV, and 250 MeV; the first and second panels do so for the $A > 0$ polarity cycle for the cases of $HCS_{arctan}$ and $HCS_{arcsin}$ respectively, while the third and the fourth panels present the normalised $A < 0$ solutions for these two cases respectively. For each of these cases, Table 5.2 indicates the total decrease in intensity from $\alpha_s = 1°$ to $\alpha_s = 90°$ by expressing the intensity at $\alpha_s = 90°$ as a fraction of that at $\alpha_s = 1°$; From this table it is clear that modulation in all cases increases with a decrease in proton energy. For example, for the successively lower proton energies of 1 GeV, 500 MeV, and 250 MeV and in the case for $HCS_{arctan}$, the intensity levels at $\alpha_s = 90°$ during the $A > 0$ polarity cycle were respectively at 0.22, 0.17, and 0.14 of what it was at $\alpha_s = 1°$; intensities during the $A < 0$ polarity cycle also seem to follow this trend though the energy dependence is markedly weaker. In both the cases for $HCS_{arctan}$ and $HCS_{arcsin}$ and in both polarity cycles the energy dependence tends to become weaker as the energy is decreased.

Despite this largely similar behaviour exhibited by the cases for $HCS_{arctan}$ and $HCS_{arcsin}$ at the selected lower proton energies, there are a few features that prove insightful upon closer inspection. Towards this end, the following few paragraphs will in more detail look at: (1) a comparison of the energy dependent behaviour of intensity profiles in the respective cases for $HCS_{arctan}$ and $HCS_{arcsin}$ at lower values of solar activity where the geometries of the two cases are still more or less identical; (2) a corresponding comparison at higher levels of solar activity where the geometries are expected to become progressively different.

The $A > 0$ solutions of both the cases for $HCS_{arctan}$ and $HCS_{arcsin}$ over the first $\sim 60°$ do not respond strongly to increases in $\alpha_s$, but the decreases that do occur are still due to a combination of the first and the second processes. Consider the area between the $A > 0$ solutions for these two cases. This area grows larger as the energy is decreased and implies a difference in the energy dependence of the $A > 0$ solutions in each of the HCS cases. This can in principle come about in more than one way, but having a look at Figure 5.27 proposes an explanation: the first panel of this figure shows the normalised $A > 0$ solutions for the case of $HCS_{arctan}$ and it is clear that the development of these solutions over the first $\sim 60°$ is largely identical for each of the energies; the second panel

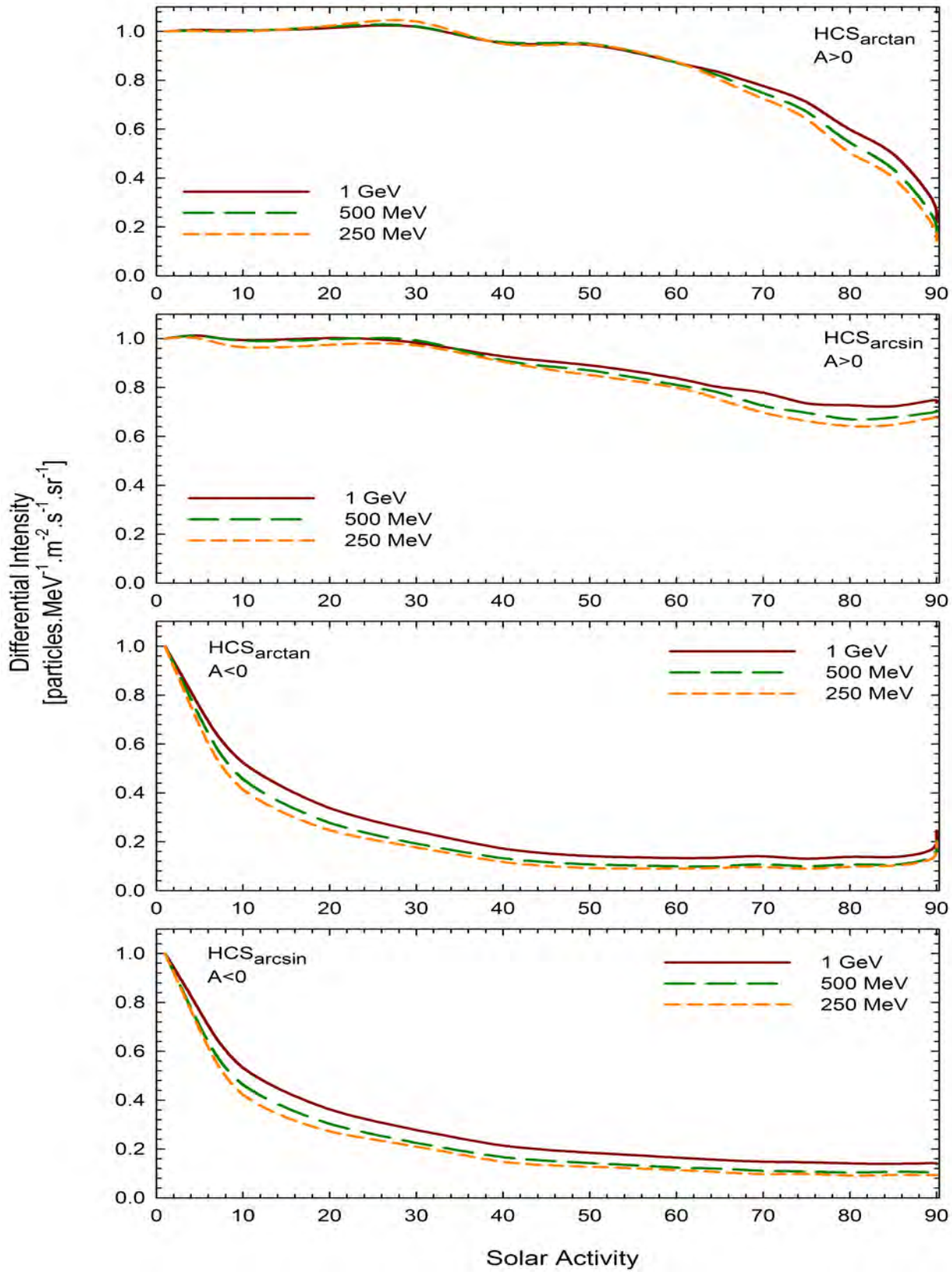


Figure 5.27: *The intensity versus solar activity for protons of energies 1 GeV (solid dark red lines), 500 MeV (dashed green lines), and 250 MeV (dash-dotted orange lines) plotted together for comparison. The first and second panels are for the $A > 0$ polarity cycle for the cases of $HCS_{\text{arcsin}}$ and $HCS_{\text{arctan}}$ respectively, while the third and fourth panels are for the $A < 0$ polarity cycles of these two cases respectively.*

of this figure indicates that the $A > 0$ solutions in the case of $\text{HCS}_{\text{arcsin}}$ decreases more strongly as the energy is lowered and this is necessarily the cause of the increasing area. Considering these results, the difference in the energy dependence of the $A > 0$ profiles of the cases for $\text{HCS}_{\text{arctan}}$ and $\text{HCS}_{\text{arcsin}}$ can be explained as follows. Using $\kappa_{||,0} = 7.0$, the case for $\text{HCS}_{\text{arctan}}$ is much closer to being drift dominated than the case for $\text{HCS}_{\text{arcsin}}$; in fact, the solution for 250 MeV is by definition still drift dominated. Therefore the energy dependencies of the two cases must differ, because in the case for $\text{HCS}_{\text{arctan}}$ the effect of large $\nabla j$ still plays a significant role and competes with the first and second processes, while in the case for $\text{HCS}_{\text{arcsin}}$ the first and second processes are far more important than the effect for large $\nabla j$. No corresponding change in the area between the $A < 0$ solutions for the two HCS cases are evident from Figure 5.27.

One final word on the $A < 0$ solutions at $\alpha_{\text{s}} < 60^{\circ}$ must be added. This regards the fact that $\alpha_{\text{s}}^{*}$ is shifted down to lower values as the proton energy is decreased; the difference of $\sim 6^{\circ}$ between the cases for $\text{HCS}_{\text{arctan}}$ and $\text{HCS}_{\text{arcsin}}$ is retained throughout. This means that as the energy is reduced, the value of $\alpha_{\text{s}}$ at which the HCS is no longer able to affect an increase in intensities via drift effects gets smaller or, put differently, occurs sooner. Keeping in mind that for $\kappa_{||} = 7.0$ modulation is still to a large extent determined by drift effects, this can be understood from pure drift considerations as follows. The combined drift velocity field, i.e. $\vec{v}_{\text{d}} = \vec{v}_{\text{gc}} + \vec{v}_{\text{ns}}$, is of such a nature or configuration as to bring about this result. The reason why intensities decrease with an increase in $\alpha_{\text{s}}$ is because of the expanding HCS making it more probable for a proton to leave the HCS and drift out and away. In the absence of diffusion, once a proton leaves the HCS its chances of returning or reaching the Earth are slim at best. If the HCS expands, i.e. if $\alpha_{\text{s}}$ gets larger, and the proton must still have the same probability of reaching Earth, it will have to increase the speed at which it drifts in along the HCS, i.e. its $v_{\text{ns}}$. Therefore, protons of larger speed or energy will have reasonable chances of reaching Earth up to larger values of $\alpha_{\text{s}}$ and thus the value of $\alpha_{\text{s}}^{*}$ is larger that for protons of lower energy.

Considering the energy dependent behaviour of the $A > 0$ solutions at higher $\alpha_{\text{s}}$, only those of the case for $\text{HCS}_{\text{arctan}}$ are discussed further since, in the case for $\text{HCS}_{\text{arcsin}}$, the situation was less clear. An approach is followed in which the intensities at $\alpha_{\text{s}} = 90^{\circ}$ are compared to intensities at $\alpha_{\text{s}} = 70^{\circ}$. From the top panel of Figure 5.27 it is evident that at $\alpha_{\text{s}} = 90^{\circ}$ intensities for protons of lower energies not only decrease to lower values in relation to the value at $\alpha_{\text{s}} = 70^{\circ}$, but it is also seen that the enhanced decrease in intensities that is associated with the HCS entering the near polar regions starts earlier for lower energies. At $\alpha_{\text{s}} > 70^{\circ}$, the geometrical interpretation presented earlier is sure to be valid. Table 5.3 shows the decreases in intensity from $\alpha_{\text{s}} = 70^{\circ}$ to $\alpha_{\text{s}} = 90^{\circ}$ by expressing the intensity at $\alpha_{\text{s}} = 90^{\circ}$ as a fraction of that at $\alpha_{\text{s}} = 70^{\circ}$. These values indicate that the decrease is successively larger for protons of lower energy: the value in the case of 1 GeV was at 0.28, while for 500 MeV and 250 MeV it was at successively lower values of 0.22 and 0.20 respectively. These results can therefore be interpreted as meaning that protons of higher energy will be less impaired by the HCS entering the polar regions and to a greater extent still be able to reach Earth. From this it is concluded that the effective tilt angle $\alpha_{\text{e}}$ defined earlier is dependent on the energy of the proton, i.e. $\alpha_{\text{e}} = \alpha_{\text{e}}(E)$, an effect that was first suggested by le Roux and Potgieter (1992).

Since, in the case for $\text{HCS}_{\text{arcsin}}$, no further modulation is seen when $\alpha_{\text{s}}$ approaches $90^{\circ}$, the discussion of the energy dependent behaviour of the $A < 0$ solutions at these high levels of solar activity is once again restricted to the case for $\text{HCS}_{\text{arctan}}$. From what was found for the $A > 0$ solutions of this case at large $\alpha_{\text{s}}$, i.e. the fact that $\alpha_{\text{e}} = \alpha_{\text{e}}(E)$, it is expected that the increases observed in the $A < 0$ solutions should be successively higher as proton energies decrease, since the lower the energy the more the HCS will be able

Table 5.3: Intensities at $\alpha_s = 90°$ expressed as fraction of those at $\alpha_s = 70°$ during the $A > 0$ and $A < 0$ polarity cycles for the case of $HCS_{arctan}$. These are indicated for each of the proton energies 1 GeV, 500 MeV, and 250 MeV.

| **Energy** | ***A>0*** | ***A<0*** |
|---|---|---|
| 1 GeV | 0.28 | 1.75 |
| 500 MeV | 0.22 | 1.91 |
| 250 MeV | 0.20 | 2.08 |

to prevent outflow at the poles. This is indeed depicted in Table 5.3: at $\alpha_s = 90°$, the $A < 0$ intensities in each of the cases for 1 GeV, 500 MeV, and 250 MeV have respectively increased to 1.75, 1.91, and 2.08 of that at $\alpha_s = 70°$. The value of $\alpha_s$ at which this increase starts also shifts to lower values as the energy is decreased, dropping from $\sim 86°$ for 1 GeV and 500 MeV to $\sim 78°$ at 250 MeV; a proton of lower energy is expected to become obstructed sooner than a proton of higher energy.

This concludes the relatively extensive illustration of the capabilities of the SDE-based model. The results presented and conclusions reached in Section 5.6 are, of course, open to further investigation and much of what was left to speculation only can easily be cleared up by further and more extensive application of the model, since the model evidently provides what is necessary for such an investigation.

## 5.7 Future Improvements of the Model

This model, while already an improvement of the pre-established model, still leaves room for improvement and expansion in future. Some specifics to be targeted for such improvement include matters on the SW, the TS, and the heliosheath.

The SW radial profile assumed in this study is simple and uncomplicated, illustrated in Chapter 2. It is assumed that the SW accelerates and becomes a steady radial flow over the first 0.3 AU and the matter is only complicated by the decrease over the simulated termination shock at $r = r_{TS}$. In future, this simple radial dependence may be replaced by a more realistic profile, making provision for effects such as mass-loading, i.e. a decrease in the SW speed due to the pickup of interstellar neutrals. Richardson and Stone (2009) have found that the SW is, on average, constant out to about 30 AU before it starts a slow decrease due to mass-loading; this effect then reduces the SW speed by about 20% before the TS is encountered.

In section 5.5.1 there was mention of the 'simulated' TS employed in this work. The shock was simulated by affecting $V_{sw}$ to drop from supersonic to subsonic levels at the position of the TS. The model does not account for the TS or its effects in any other way − no shock acceleration occurs at the shock. These effects, however, only become increasingly important in studies involving the anomalous component of CRs. Since the focus of this study is on GCRs, these complications are avoided. The drop at $r = r_{TS}$ is also not the most realistic way to treat the $V_{sw}$ profile near the TS. Voyager 2 measurements have shown a slowdown in the SW velocity commencing 80 days (or 0.7 AU) before the TS crossing. See Richardson and Stone (2009) for a detailed discussion of Voyager measurements near the TS. See also and Richardson and Burlaga (2011). For a review on more of these matters relevant to CR modulation, see Potgieter (2013).

The current model also employs a highly simplified approach to the simulation of the inner heliosheath, or the region between the TS and the heliopause (HP). After crossing the TS and nearing the HP, Voyager 1 non-plasma observations have indicated that the

SW speed had basically decreased to zero (Krimigis et al., 2011). The plasma detector on Voyager 2, still in working condition, has been observing heliosheath plasma since August 2007 and has indicated how it evolved across the inner heliosheath. The radial speed slowly decreased as the plasma flow turned tailwards, but remained above 100 km.s$^{-1}$, indicating that Voyager 2 was still a substantial distance from the HP in 2012; its approach towards the HP was also developing differently from a SW point of view, indicating that the heliosheath is clearly a highly variable region.

It is concluded, therefore, that ample scope exists in this regard for further expansion and development of the current model.

## 5.8 Summary and Conclusions

In Section 5.2 the reader was reminded of the credibility of the numerical model that was properly established in Chapter 4, explaining that the model is based on the extensively benchmarked model of Strauss et al. (2011b, c, 2012). This section also pointed out some basic advantages of utilising numerical modulation models based on the solution of the appropriate set of stochastic differential equations (SDEs), as compared to other numerical models. SDE-type modulation models allow for the calculation of relevant quantities such as particle travel time and particle energy losses in the heliosphere. Furthermore, this type of model encourages a physical and intuitive understanding of cosmic ray (CR) modulation in the heliosphere.

Section 5.3 was allocated to a discussion of the accuracy and convergence of solutions obtained when utilising this model. The margin of error was indicated to be determined by statistical considerations, solutions typically showing less variation with the use of an increasing number of pseudo-particles in any one simulation. It was shown that, for purposes of this study, the use of $N = 1 \times 10^3$ pseudo-particles was sufficient for the simulation of spectra solutions at Earth. The convergence of solutions obtained by the model was also clearly illustrated. The issues pertaining to the boundary conditions implemented in the model were discussed in the next section, where the model was shown to react in a logical and coherent manner to any changes in these conditions.

In Section 5.5 the effects of each of the Smith-Bieber (SBM) and Jokipii-Kóta (JKM) modifications on the unmodified Parker heliospheric magnetic field (PHMF) profile were shown, together with the eventual effect on the heliospheric modulation of galactic CR protons. Important conclusions from this section include the observation that, although the effects of the JKM may be locally greater than those of the SBM, the effects of the SBM are exercised over a greater part of modulation space and hence its overall effect on CR intensities is greater than that of the JKM. The PHMF was shown to be especially conducive to drift dominated modulation, while the JKM and SBM were shown to induce successively greater contributions from diffusive processes.

Section 5.6, divided into three subsections, was devoted to matters related to the neutral heliospheric current sheet (HCS) and constituted the core of Chapter 5. In the first of these subsections the role of the HCS tilt angle $\alpha$ as a proxy for solar activity was explained. Section 5.6.2 returned to the two different expressions for the HCS profile that were first presented in Chapter 2. These two profiles, referred to as the cases for $\text{HCS}_{\text{arctan}}$ and $\text{HCS}_{\text{arcsin}}$ respectively, were considered in much more detail. It was concluded that, while at small tilt angles there is no difference between the geometries of these two profiles, there is a remarkable difference at larger tilt angles, $\alpha \gtrsim 65°$. The HCS drift velocity associated with the case of $\text{HCS}_{\text{arctan}}$, corresponding to Eq. (2.15), was formally derived and compared with that for the case of $\text{HCS}_{\text{arcsin}}$, corresponding to Eq. (2.14). The final subsection of Section 5.6.3 presented comparative CR proton modulation results

for the two HCS profiles, employing the SBM throughout. In the first of two scenarios, modulation under drift dominated conditions was investigated. In the second scenario diffusion was set to values that could be considered realistically low and the insights obtained from the investigation of the drift dominated scenario were extensively employed to explain these results.

Discussion of the results for both scenarios proceeded after distinction was made between two roughly separate but connected processes of modulation, referred to as the first and second processes respectively throughout this work. The first process involves the expansion of the HCS (waviness) with an increase in solar activity, i.e. an expansion of the drift velocity field $\vec{v}_{\rm ns}$. The second process is established by the presence of the tilt angle $\alpha$ in the expression for the solar wind (SW) profile $V_{\rm sw}$ affecting this profile to change as a function of solar activity, in accordance with observations from Ulysses. The treatment of the drift dominated scenario allowed for the identification of an effect called the effect of large gradients $\nabla j$. This effect is associated with the second process and was seen to be the cause of the rather peculiar result of proton intensities actually increasing as function of solar activity for the drift dominated scenario.

At lower levels of solar activity, the first process was found to be more effective in the case for $\rm HCS_{arcsin}$ than in the case for $\rm HCS_{arctan}$. The drift velocity field $\vec{v}_{\rm ns}$ associated with $\rm HCS_{arcsin}$ was found to more effectively drift CR protons out and away from Earth along the HCS during $A > 0$ polarity cycles; during $A < 0$ polarity cycles, it was found to be more effective in drifting these protons in and towards Earth along the HCS. An important conclusion drawn from this, was that the drift velocity fields $\vec{v}_{\rm ns}$ associated with the $\rm HCS_{arctan}$ and $\rm HCS_{arcsin}$ profiles respectively are significantly different, i.e. it leads to significantly different modulation, even at such low levels of solar activity where no difference in the respective HCS geometries is yet in evidence.

At the highest levels of solar activity, the first process was found to be more effective in the case for $\rm HCS_{arctan}$ and an explanation of this result was presented from a geometrical perspective, indicating that the thick arms of the $\rm HCS_{arctan}$ profile would exert greater influence on protons than the thin arms of the $\rm HCS_{arcsin}$ profile. The $\rm HCS_{arctan}$ was more effective to such an extent as to cause the solutions for the $A > 0$ and $A < 0$ polarity cycles to close up at the highest level of solar activity to form a closed loop. This is a result that has not been achieved before without setting the drift coefficient to zero during extreme solar maximum activity, as was done by Ndiitwani et al. (2005). Furthermore, by extensively utilising the SDE-based model, it was possible to explain and motivate this result to satisfaction. This research showed that the use of $\rm HCS_{arctan}$ was the preferred approach for modulation studies extended to high levels of solar activity.

The concept of an effective tilt angle $\alpha_{\rm e}$ was defined, and it was indicated that at such high levels of solar activity where the differences between the geometries of the cases for $\rm HCS_{arctan}$ and $\rm HCS_{arcsin}$ were clear, this value was greater in the former case than in the latter. Furthermore, it was indicated to be energy dependent, i.e. $\alpha_{\rm e} = \alpha_{\rm e}(E)$, supporting the work of le Roux and Potgieter (1992). In general, the effect on modulation measured from the lowest to the highest levels of solar activity was found to increase with a decrease in proton energy, as expected.

Section 5.7 pointed out the scope for expansion and further development of this model. This included such topics as the SW, the termination shock, and the heliosheath.

# Chapter 6

# Application of the SDE-based Modulation Model: Modeling the PAMELA Proton Spectra

## 6.1 Introduction

This chapter presents an application of the numerical modulation model discussed in Chapters 4 and 5, i.e. the model based on the solution of the set of stochastic differential equations (SDEs) corresponding to the Parker transport equation (TPE). The model is applied to reproduce galactic proton spectra measured at Earth by the PAMELA instrument during the peculiar minimum of solar cycle 23/24. This solar minimum period, spanning 2006 to 2009, has widely been recognised as being atypical compared to other solar minima. Preliminary galactic cosmic ray (GCR) proton observations from PAMELA during this period enabled an in depth study and analysis of this minimum (e.g. Vos, 2011; Potgieter et al., 2014). In this chapter, the results and conclusions of these authors are revisited and the SDE-based numerical model of this study is utilised with the same purpose, making use of the final proton data from PAMELA published by Adriani et al. (2013). The results are also briefly compared with the work of other authors.

The aim in this chapter is not only to show that the model is able to reproduce these spectra, but also to independently test the qualitative results obtained by Vos (2011), who employed a numerical modulation model based on the finite difference approach of the alternating direction implicit (ADI) method. As will be explained, the SDE-based model is different from the ADI-based model and this application will therefore also illustrate the impact of these differences. This application is by no means a full account of the applicability of the SDE-based model, since yearly averaged tilt angles only go up to 15.7°, whereas Chapter 5 illustrated conclusively that the model was well suited for studying modulation up to the highest levels of solar activity. However, no sufficient data are available for such conditions, since modulation during solar maximum is markedly complicated by e.g. solar particle events and strong transient phenomena.

## 6.2 The Local Interstellar Proton Spectrum

The proton local interstellar spectrum (LIS) is the spectrum in the local interstellar medium (LISM) before it starts undergoing modulation upon entering the heliosphere assumingly at the heliopause (HP). Modulation in the heliosphere then alters this spectrum to eventually yield a spectrum at a required position in the heliosphere. The LIS

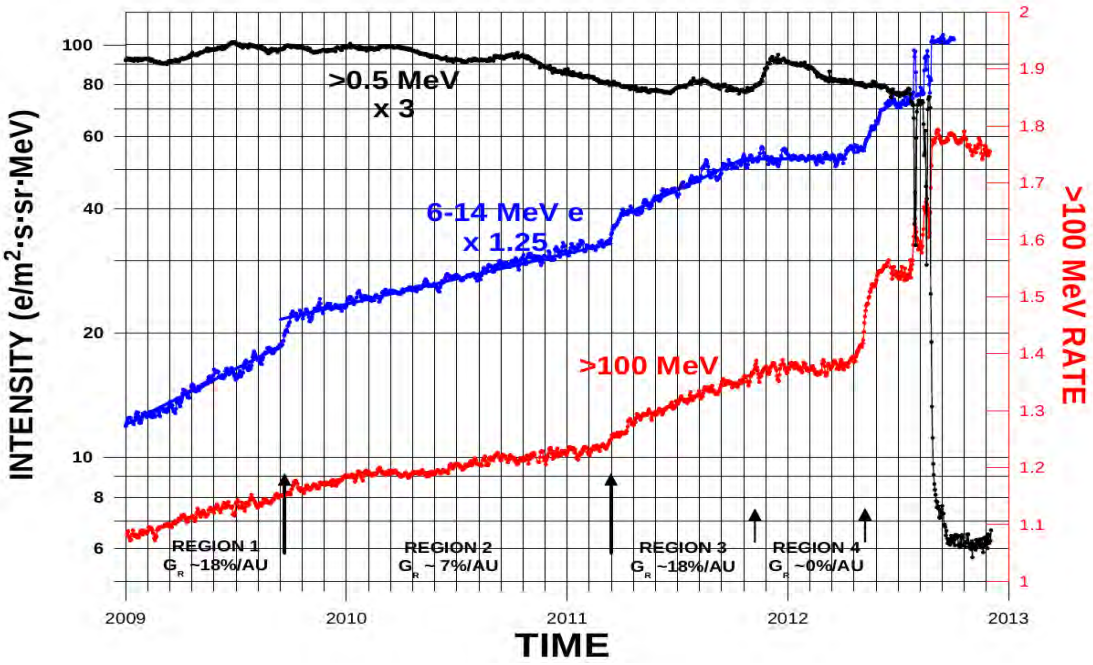


Figure 6.1: *Five day running average intensities of >0.5 MeV ACR protons (represented in black), and of 6 MeV - 14 MeV GCR electrons (blue) and >100 MeV protons (red) from 2009 to the end of the data observed at the time of writing. At the bottom of the figure, the radial gradients are indicated percentage wise by $G_R$ and the arrows indicate possible zones in the outer heliosphere. The scale on the right axis of the figure (indicated in red) corresponds to the >100 MeV proton counting rates. This figure was taken from Webber et al. (2012).*

serves as the primary input spectrum in numerical modulation models and, consequently, a proper knowledge of the exact shape of the proton energy spectrum in the LISM is of particular importance for the study of proton modulation in the heliosphere. See also Potgieter (2014).

In the past, the task of determining such an LIS had proven itself to be quite formidable. At energies relevant to modulation studies, neither the absolute flux nor the spectral shape of the proton LIS could be determined to adequate precision (Menn et al., 2000). The task may have been formidable, yet it was not hopeless and there was enough research that could be carried out to improve on this state of affairs. Many measurements of CR proton intensities, as is the case with the PAMELA experiment (Picozza et al., 2007), include observations at higher energies at which the effect of heliospheric modulation is negligible (see also Strauss and Potgieter, 2014a). Measurements at these energies enabled confinement of the proton LIS above 30 GeV within a region indicative of its true value. However, at energies below 30 GeV, the task was much more complicated, since adiabatic energy losses experienced by CR protons, together with the other modulation mechanisms, become increasingly important, exerting an ever increasing influence. For this reason, due to the fact that no *in situ* measurements were available, the low energy proton LIS remained significantly uncertain.

Fortunately, this might not be the prevailing case any longer. On July 28th, 2012, at about 121 AU, came the first indication of a possible encounter with the HP when Voyager 1 detected an abrupt decrease in the intensities of termination shock particles (TSPs) and anomalous cosmic rays (ACRs), coincided with an increase in the GCR intensities (Webber et al., 2012; Webber and McDonald, 2013; Krimigis et al., 2013). These observations are depicted in Figure 6.1, taken from Webber et al. (2012). If this signaled the crossing

of the HP, it would mean that Voyager 1 had at that time begun direct measurement of the LIS. During a $\sim$ 1 month period after these first indications of a HP crossing, there were five more 'crossings' of similar nature. During this time ACRs decreased to nearly undetectable levels. Because TSPs and ACRs are the dominant energetic charged particles in the heliosheath (Stone et al., 2005; Decker et al., 2005), the decrease in their intensities is consistent with a crossing of the HP, as is the increase in GCR intensities. A study of electron plasma oscillation observations by Voyager 1 (Gurnett et al., 2013) presented further strong indication that the HP crossing had occurred on or about August 25, 2012.

Though it is generally accepted by now that Voyager 1 had indeed crossed the HP in August of 2012, some doubts remain. The main reason for these doubts is that no significant change in the direction of the magnetic field has been observed over the supposed HP crossing (Burlaga et al., 2013). The magnetic field in the interstellar plasma is not expected to be in the same direction as the magnetic field within the heliosheath. Though the mentioned plasma density observations are considered by many scientists associated with Voyager to be the more significant in determining whether the HP crossing had occurred or not, authors like Fisk and Gloecker (2014) contend that the evidence is still inconclusive; they present an analytical model in which the higher plasma densities are simply due to compressed solar wind (SW), and show that the HP crossing of Voyager 1 is still years away. These disputes will probably only be settled after Voyager 2 crosses the HP.

However, as mentioned earlier, the main stream of authors are in favor of the HP crossing having occurred in August of 2012 and as such many explanations for the problem concerning the direction of the magnetic field across the HP have been proposed. Making use of a simple draping model, Grygorczuk et al. (2014) show that the magnetic field observations can be explained in a natural way if the heliographic latitude of Voyager 1 happens to be the same as that of the undisturbed interstellar magnetic field which they assume to be given by the Interstellar Boundary Explorer (IBEX) ribbon center; this ribbon is the band of increased intensity of energetic neutral atoms at 1 keV in the outer heliosphere. However, according to Opher and Drake (2014), the idea that the interstellar magnetic field is aligned with the IBEX ribbon is in need of revision. These authors present simulations that reveal that strong rotations in the direction of the magnetic field across the HP at the location of Voyager 1 is not expected, since the solar magnetic field plays a crucial role in the draping of the interstellar magnetic field outside the HP; regardless of the orientation of the interstellar magnetic field, the magnetic field just outside of the HP twists to a Parker-like orientation. Borovikov and Pogorelov (2014) could not confirm this, but have shown that the solar cycle creates conditions favorable for HP instabilities and deep penetration of the LISM plasma into the inner heliosheath, accounting for the early interaction of Voyager 1 with the LISM; this is considered "early", since no realistic steady-state model of the SW interaction with the LISM predicts an inner heliosheath width as narrow as $\sim$ 30 AU.

The issue of the magnetic field direction not changing sufficiently over the HP has still not been explained to satisfaction and has led to the proposition of a transition layer at the HP that would allow for enhanced exchange of energetic particles with the interstellar medium while still conserving interstellar magnetic field characteristics typical of the heliosheath (McComas and Schwadron, 2012; Fisk and Gloecker, 2013; Schwadron and McComas, 2013; Stone et al., 2013). Strauss et al. (2013a) used a hybrid GCR modulation model, where the resulting heliospheric geometry and plasma flow fields from a 3D magneto-hydrodynamic (MHD) model were coupled to an SDE-based model, to study the modulation of GCRs beyond the HP; they showed that GCR modulation continues

beyond the HP so that Voyager 1 will continue to measure a small but positive gradient well into the outer heliosheath before eventually beginning to measure the pristine LIS. See also Scherer et al. (2011) and Strauss et al. (2013b). Kóta and Jokipii (2014), on the other hand, have shown by theoretical arguments and simple spherical and non-spherical model simulations that GCR modulation beyond the HP must be small if parallel diffusion in the outer heliosheath and interstellar medium is as expected from observations of the composition of GCRs.

Whether the HP crossing has indeed occurred or not and whether or not Voyager 1 has begin sampling the LIS, this work assumes that new lower boundaries for the proton LIS have indeed been established. The proton LIS assumed in this study has its origin in that of Langner and Potgieter (2004a), based on the computations of Moskalenko et al. (2002). Vos (2011) and Potgieter et al. (2014) improved on this LIS by taking into account PAMELA measurements at energies between 30 and 50 GeV. At the time of the work of Vos (2011), Voyager 1 had not yet reached the HP. The LIS of Vos (2011) and Potgieter et al. (2014), denoted by $\mathrm{LIS_{Vos,2011}}$, was therefore modified to take into account these new Voyager 1 observations in the lower energy range; see Potgieter (2014) in this regard. The LIS resulting from these modifications, denoted by $\mathrm{LIS_{Vos,2013}}$ and expressed in units of particles.$\mathrm{MeV^{-1}.m^{-2}.s^{-1}.sr^{-1}}$, is employed in this work and can be specified by the expressions

$$j_{\mathrm{Vos,2013}} = 0.6978 \exp\left\{4.64 - 0.023(\ln E)^2 - 2.91E^{-0.5}\right\}$$

for energies less that 1.4 GeV, and

$$j_{\mathrm{Vos,2013}} = 0.6847 \exp\left\{3.22 - 2.78(\ln E) - 1.5E^{-1}\right\} \tag{6.1}$$

for energies above this value.

In Figure 6.2 the $\mathrm{LIS_{Vos,2013}}$ (solid black line) and $\mathrm{LIS_{Vos,2011}}$ (dashed black line) are plotted together for comparison. The modulated spectra calculated at Earth while using the same modulation parameters and assuming each of the $\mathrm{LIS_{Vos,2013}}$ and $\mathrm{LIS_{Vos,2011}}$ in turn, are also indicated (solid and dashed red lines respectively). The Voyager 1 data (taken from Stone et al., 2013), used to modify the LIS at the lower end of the energy spectrum, are indicated by the blue triangles. At energies above $\sim$ 200 MeV the $\mathrm{LIS_{Vos,2013}}$ is below the $\mathrm{LIS_{Vos,2011}}$, while at energies below this value and toward the lower end of the energy spectrum the $\mathrm{LIS_{Vos,2013}}$ is progressively higher than the $\mathrm{LIS_{Vos,2011}}$. Owing to the effect of adiabatic cooling, the Earth spectrum assuming the $\mathrm{LIS_{Vos,2011}}$ is higher than the spectrum assuming $\mathrm{LIS_{Vos,2013}}$ not only at energies above the mentioned $\sim$ 200 MeV, but down to energies of $\sim$ 100 MeV. At this point, the two spectra become about equal, both bent into the characteristic $\sim E^{1.0}$ shape which is ascribed to the dominating effects of adiabatic cooling at these low energies.

## 6.3 The PAMELA Proton Spectra

The PAMELA instrument, discussed in detail in Chapter 2, entered into orbit in the final stages of solar cycle 23, from mid-2006, during which time conditions in the heliosphere calmed down for the onset of solar minimum. Cosmic ray intensities measured at this time made it possible to study the minimum of solar cycle 23/24 to a greater degree of accuracy than was previously possible. The study of Vos (2011) made use of the first set of preliminary data from PAMELA, whereafter Potgieter et al. (2014) made use of the final published data (Adriani et al., 2013); this final set of data is also employed in this study.

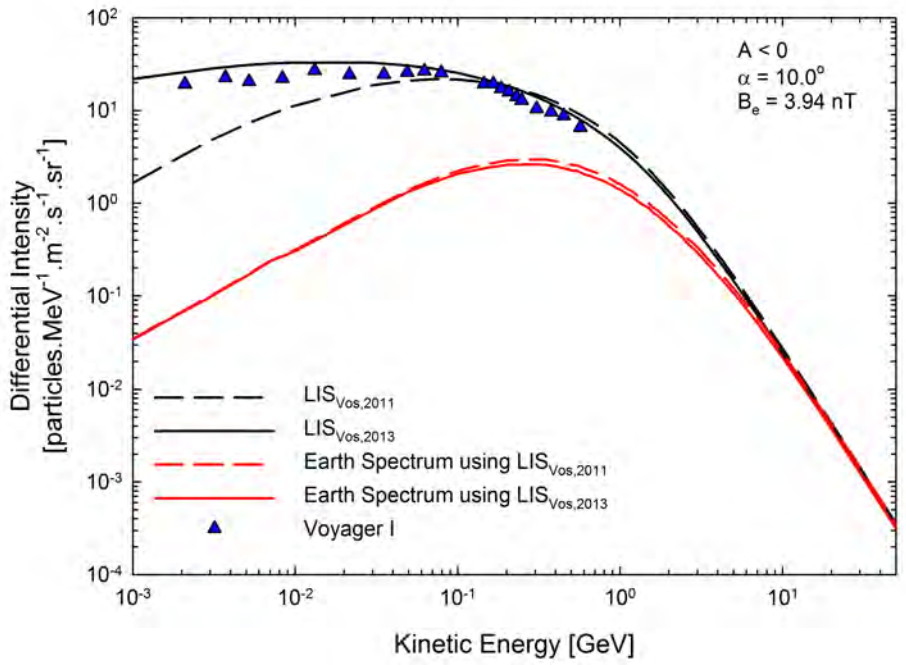


Figure 6.2: *The proton LIS used in this study is denoted by* $LIS_{\mathrm{Vos,2013}}$ *and is indicated by the solid black line. The Voyager 1 data used to establish this LIS is presented by the blue triangles (Stone et al., 2013). The solid red line presents the calculated spectrum at Earth using the* $LIS_{\mathrm{Vos,2013}}$ *as input. The dashed black line represents the LIS used by Vos (2011) and Potgieter et al. (2014), and is denoted by* $LIS_{\mathrm{Vos,2011}}$*. The dashed red line the computed modulated spectrum at Earth using this LIS as input. These computed results represent solar minimum conditions during 2009, as is explained in the text.*

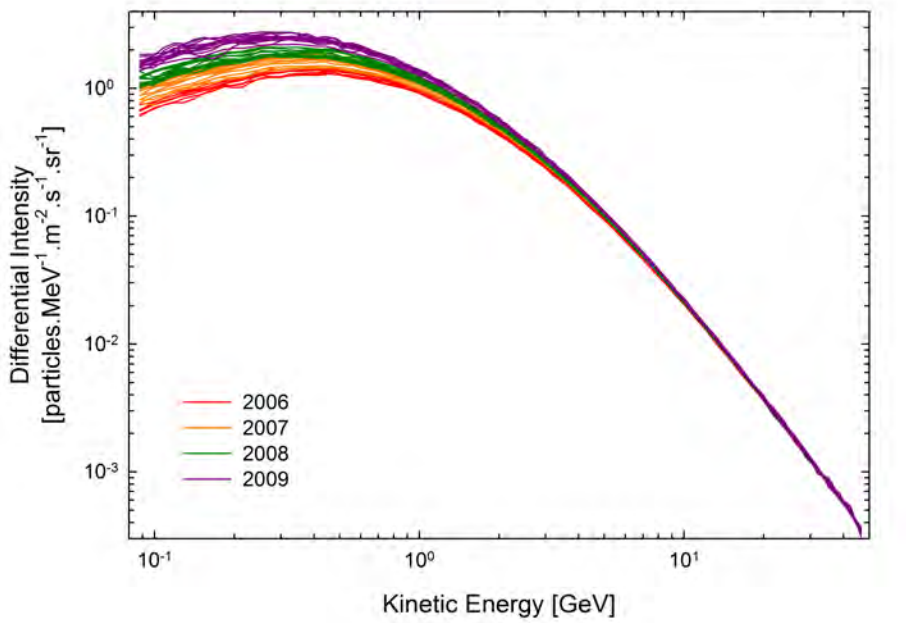


Figure 6.3: *The PAMELA proton data for 2006, 2007, 2008, and 2009 are presented in red, orange, green, and purple, respectively; these spectra were averaged over one Carrington rotation. The data are as published by Adriani et al. (2013) and Potgieter et al. (2014).*

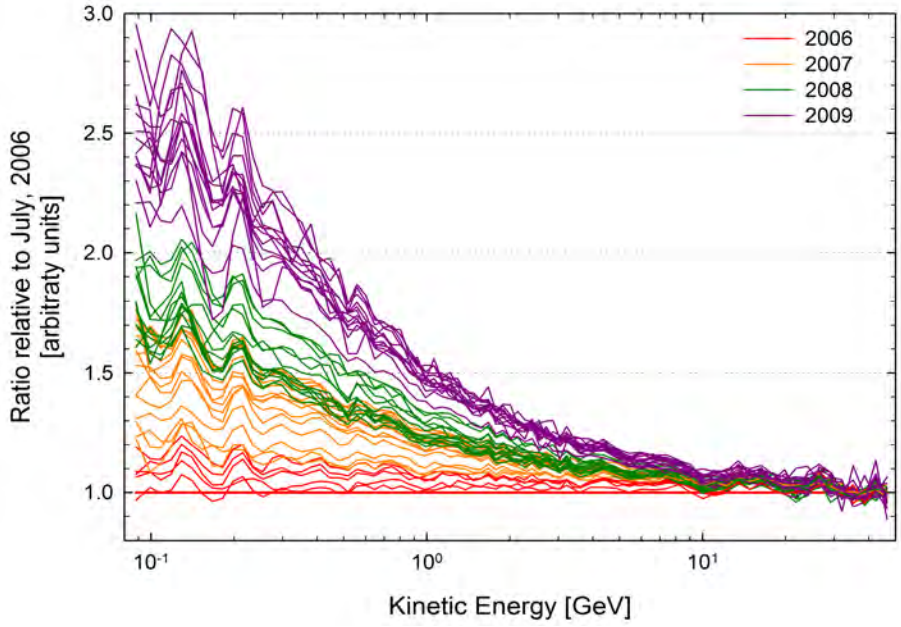


Figure 6.4: *The ratios of consecutive PAMELA proton spectra with respect to July 2006; these spectra were averaged over a period of one Carrington rotation. Different colours are used to present the ratios for each of 2006, 2007, 2008, and 2009, as specified in Figure 6.3. Note how the spectra became progressively softer over these years.*

Spanning July 2006 to December 2009, Figure 6.3 shows a plot of this final set of data and different colours are used to indicate the averaged proton spectra measured during 2006, 2007, 2008 and 2009 respectively; these spectra have been averaged over a period of one Carrington rotation or $\sim$ 27 days. The most apparent feature is the progress in the overall intensities from lower to higher levels from 2006 to 2009. In fact, in 2009, the highest proton spectrum at Earth since the beginning of the space age was recorded (e.g. Heber et al., 2009; Strauss and Potgieter, 2014b; Zhao et al., 2014). A closer inspection of the figure reveals that intensities in the energy range between about 80 MeV and 2 GeV have experienced the greatest increase. With a maximum intensity of $\sim$ 1.3 particles.MeV$^{-1}$.m$^{-2}$.s$^{-1}$.sr$^{-1}$ in July 2006, at around 440 MeV, the peak in the energy spectra has shifted to about 210 MeV in 2009 with an intensity of $\sim$ 2.8 particles.MeV$^{-1}$.m$^{-2}$.s$^{-1}$.sr$^{-1}$, representing an increase by a factor of about 2.2.

Figure 6.4 gives the ratios of the consecutive averaged spectra relative to July 2006. From this figure it is clear that the largest increase in intensity occurred at the lower end of the energy spectrum, where it increased by close to a factor of 3.0 from July 2006 to December 2009. In the energy region around 130 MeV, proton intensities increased by a factor $\sim$ 1.3 over the 12 months from December 2006 to December 2007, with a smaller fractional increase of $\sim$ 1.2 from December 2007 to December 2008. From 2008 to 2009 these intensities increased by a factor of about 1.4. Evidently, the spectra became increasingly softer towards 2009 and reached maximum intensities at the end of 2009, thereby marking the climax of the solar cycle 23/24 minimum.

## 6.4 The Minimum of Solar Cycle 23/24

As mentioned earlier, the minimum of solar cycle 23/24 was highly atypical, a fact well identified by various authors (Heber et al., 2009; McDonald et al., 2010; Mewaldt et al., 2010; Russell et al., 2010; Potgieter et al., 2014). This solar minimum has been unlike any other over the past half century in that it has shown an extended period of very low solar activity from 2006 to December 2009 (McDonald et al., 2010), with the sunspot number (SN) and every other indicator of solar activity continuing to drop for at least two years after the ontake of the new solar cycle was expected (Russell et al., 2010). As such, it is necessary to take a closer look at the heliospheric conditions that led to such a solar minimum. See also Vos (2011) and Zhao et al. (2014).

The Sun-heliosphere connection was explained in Chapter 2, where it was established that the level of solar activity over time also determines the time evolution of conditions in the heliosphere. These conditions then, of course, have direct influence on the modulation of CR particles in the heliosphere. Figure 6.5 was taken from Potgieter et al. (2014) and gives an outline of the heliospheric conditions from 2000 to mid-2011. The SN is presented in the first panel, along with CR neutron monitor data, measurements of the heliospheric current sheet (HCS) tilt angle $\alpha$, and averaged heliospheric magnetic field (HMF) magnitudes at Earth from the second to the fourth panels respectively. See also Vos (2011).

As a proxy for solar activity, the SN is a good place to start in such an investigation into the heliospheric conditions that had led to this unprecedented solar minimum. The solar minimum of cycle 23/24 has been marked by a prolonged and continuing period of very low solar activity that began in 2006. In January 2008, the first sunspots of cycle 24 appeared, but vanished after just a few days, continuing the quiet period. Since that time there have been several periods of moderate activity which did not persist for more than a single solar rotation until mid-December 2009. During this minimum, the number of spotless days, which is a parameter specifically designed to gauge solar minimum conditions, has attained the highest value for the past 96 years or since the solar cycles 14/15 (McDonald et al., 2010).

The extended minimum of cycle 23/24 created heliospheric conditions that were very different from those present over previous minima in the 'modern era' and McDonald et al. (2010) identified the two most significant features as (1) the slower approach and higher value of the tilt angle at the end of the 23/24 minimum compared to the minimum of cycles 20 to 22, and (2) the weaker HMF as compared to cycles 19 to 22. Wang et al. (2009) pointed out that these two features appear to be related − the weaker polar fields resulted in the apparent refusal of the HCS to flatten closer to the equator.

Concerning the first of these features, for the minimum of solar cycle 23/24, HCS tilt angles have remained higher than usual with values between $\sim 15^\circ$ and $\sim 5^\circ$ (according to the radial tilt angle model) between 2007 and 2009. Looking back at previous solar minima, the lowest annual tilt calculated since the beginning of observation at the Wilcox solar Observatory, was $\sim 3^\circ$.

Concerning the latter of the two features mentioned above, the development of the average HMF magnitude at Earth is shown in the fourth panel of Figure 6.5. During the minimum of solar cycle 23/24, the HMF magnitude dropped to values as low as 3.5 nT in May 2009, 30 % less than the 5.0 nT of the previous four minima (see e.g. Smith and Balogh, 2008). This value is also about 24 % less than the 'floor value' determined by Svalgaard and Cliver (2007), which acts as a baseline to which the magnitude of the HMF falls during solar minimum conditions. Furthermore, Wang et al. (2009) reported polar fields about 40 % weaker during that time, compared to previous sunspot minima.

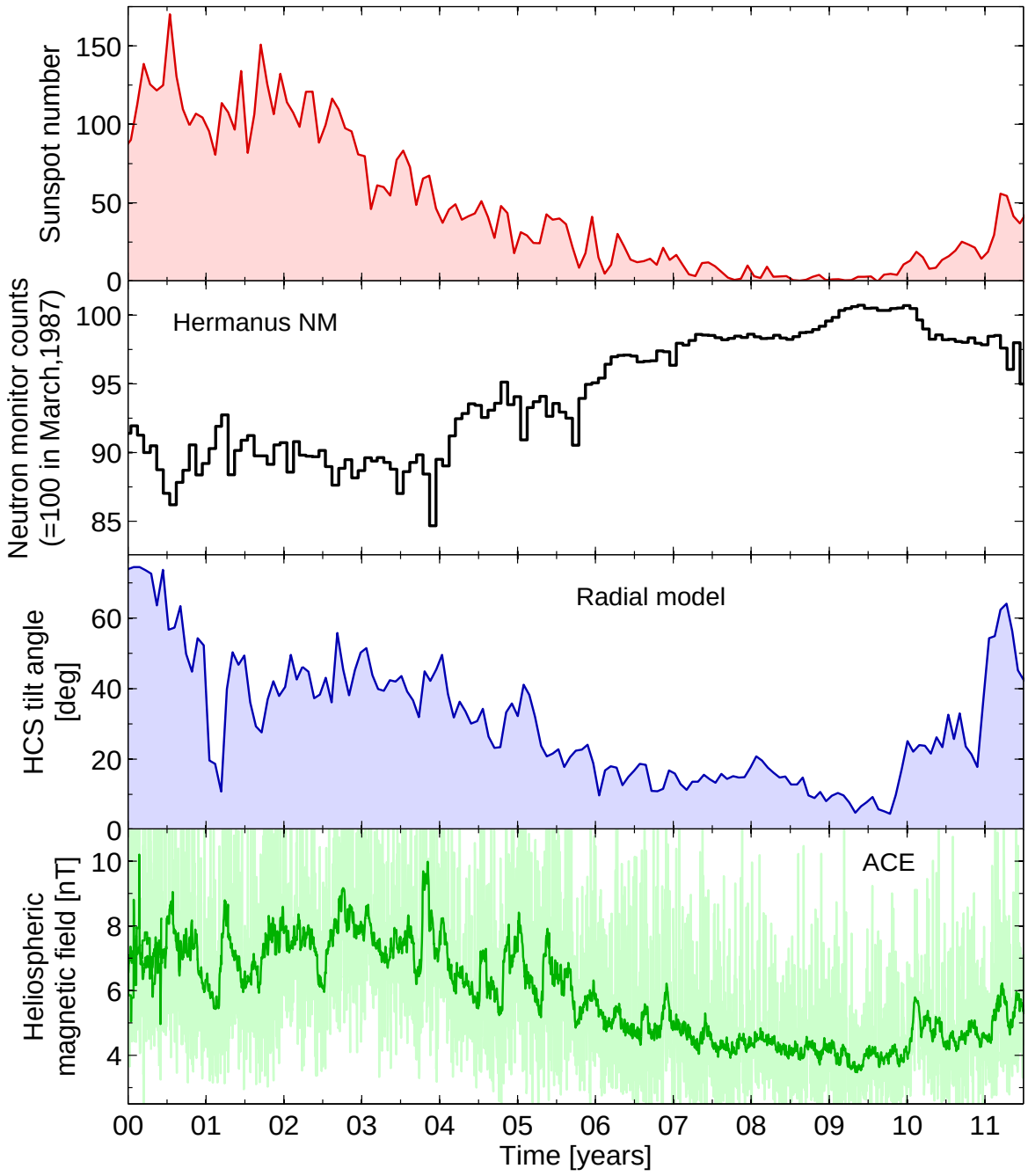


Figure 6.5: *An illustration of heliospheric modulation conditions from the year 2000 (indicated by 00) to solar minimum activity in 2009, and up to mid-2011. The top panel shows the SN. The second panel gives the count rate of the Hermanus neutron monitor, normalised to 100 % in March, 1987. The third panel shows the HCS tilt angle as calculated according to the radial model. The fourth panel gives the monthly (green) and daily (light green) averaged HMF magnitudes observed close to Earth by the Advanced Composition Explorer (ACE). This figure was taken from Vos (2011) and Potgieter et al. (2014).*

McDonald et al. (2010) reported a response time of $\sim$ 4 solar rotations between changes in the tilt angle and the onset of CR decreases. Even though both the HCS tilt angle and the averaged HMF magnitude decreased sufficiently as solar cycle 23 reached its minimum, the increase in CR intensities, as seen in the second panel of Figure 6.5, was not as steep as expected (Heber et al., 2009).

Looking at the SW during this time, Ulysses observations showed that the SW pressure had decreased by $\sim$ 20 % compared to solar cycle 22 and, furthermore, that SW density measurements have reached the lowest values ever measured (McComas et al., 2008). These were all indications that the heliosphere had reached exceptionally quiet modulation conditions during the minimum of solar cycle 23/24.

According to Russell et al. (2010), this lull in solar activity presents advantages for solar activity related studies in the mere sense that there are less complications and confusion − the studies may be easier and more accurate conclusions may be drawn. Except for the fact that these conditions provide ample opportunity to study heliospheric modulation parameters and their properties under solar quiescent conditions, there are numerous other reasons why the heliospheric conditions that give rise to such solar minima are studied. CR modulation studies aim to predict future modulation and, in looking back to the Dalton minimum (solar cycles 5 and 6), may be suggesting that a similar period of low solar activity is approaching (Russel et al., 2010). These solar quiet conditions also hold advantages to cosmoclimatological studies in that it provides the ideal situations in which to separate the effects of the Sun from other factors influencing global climate change. This, however, is not a topic of this work and the reader is referred to Russell et al. (2010).

## 6.5 Modeling the PAMELA Proton Spectra

This section is divided into three subsections. Section 6.5.1 gives a brief overview of the ADI-based modeling of the PAMELA proton spectra performed by Vos (2011) and Potgieter et al. (2014). Only the basic and most relevant results and conclusions that are needed for a comparison with the SDE-based modeling performed in this work are presented. Section 6.5.2 presents the results of the SDE-based modeling and, in Section 6.5.3, the results and conclusions drawn from the previous two sections are laid out for comparison. The results are also briefly compared with those of a few other authors.

### 6.5.1 ADI-based Modeling

The ADI-based model employed by Vos (2011) and Potgieter et al. (2014) was a three-dimensional (3D) and time-stationary model. After an analysis of the heliospheric conditions during the minimum of solar cycle 23/24, this model was utilised to reproduce intermittent proton energy spectra, measured at Earth by the PAMELA instrument, during the extended solar minimum period of 2006 to 2009. Four monthly averaged sampled spectra were chosen for this purpose. The first of these was for November 2006 and the others were for December of 2007, 2008 and 2009 respectively. The reason as to why the November spectrum was used in 2006, is the occurrence of increased solar activity during mid-December which resulted in transient increases in intensities in the 80 MeV to 3 GeV range (Adriani et al., 2011). Out of these four sampled spectra, the spectrum of December 2009 displayed the highest measurements and marked the peak of proton intensities for this solar minimum. See also Potgieter et al. (2014).

In order to reproduce modulation conditions that would coincide with the sampled monthly spectra, Vos (2011) calculated average representative values for the SW speed

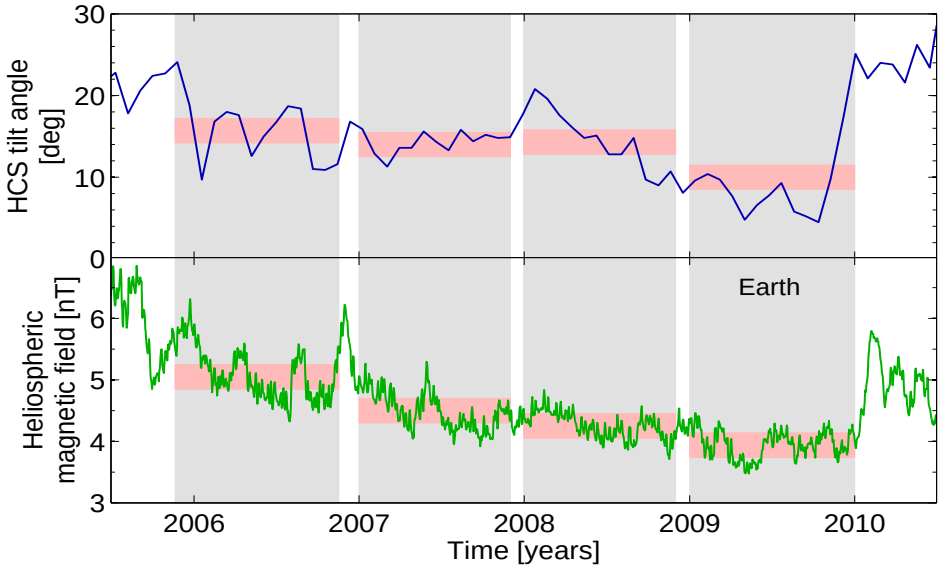


Figure 6.6: *Yearly average values are calculated for the HCS tilt angle $\alpha$ and HMF magnitude at Earth as an attempt to estimate modulation conditions in the heliosphere throughout the prior year. The light-grey regions of interest correspond to the time frames over which averages are calculated, while the red highlighted bands give an indication of the calculated averages (along with some margin of error). The first panel shows the radial tilt angle model for the HCS tilt angle, with the monthly averaged values for the HMF magnitude at Earth measured by ACE in the bottom panel. This figure was taken from Vos (2011).*

$V_{\rm sw}$, the HCS tilt angle $\alpha$, and the HMF magnitude at Earth over the preceding months in the case of each of the sampled spectra; these values reflected the actual preceding and at that time prevalent heliospheric conditions. Furthermore, because of the dynamic structure of the heliosphere, the position of the termination shock (TS) was expected to change with time. This was accounted for by assuming the TS to be located at heliocentric distances of 88 AU, 86 AU, 84 AU, and 80 AU during 2006, 2007, 2008 and 2009, respectively (Webber and Intriligator, 2011). These values together with the sets of averaged values were then used to adjust the ADI-based numerical model for each sampled spectrum, so as to simulate the modulation of protons under conditions that closely resembled those of the actual heliosphere. The Jokipii-Kóta modified heliospheric magnetic field (JKM) was selected for the HMF profile, as discussed in Chapter 2; see Eq. (2.10). The $\rm HCS_{arcsin}$ profile, i.e. Eq. (2.14), was chosen for the treatment of the HCS and its associated drift velocity field $\vec{v}_{\rm ns}$. The $\rm LIS_{Vos,2011}$ was used as primary input at the HP. The results of the study by Vos (2011) are summarised in Table 6.1, with all quantities as defined in Chapters 2 and 3.

Note that the averages for the HCS tilt angle $\alpha$ and HMF magnitude at Earth were calculated over timescales of approximately one year, since it was argued that, during typical solar minimum conditions, it takes about a year for changes in the HCS tilt angle and solar magnetic field to be transported via the SW to the outermost regions of the heliosphere. This averaging process is illustrated in Figure 6.6, taken from Vos (2011). The fact that $V_{\rm sw}$ essentially remains steady throughout solar minimum conditions allowed for the use of a single average $V_{\rm sw}$ profile for all four the sampled spectra.

From Table 6.1, looking at the consecutive values of $\kappa_{||,0}$ (in units of $6 \times 10^{20}$ $\rm cm^2.s^{-1}$) from 2006 to 2009, it is clear that the overall diffusion had increased over this time. The value of $\kappa_{||,0}$ was required to change from 11.57 in 2006 to 12.70, 13.57, and 15.85 in 2007, 2008, and 2009 respectively. Additionally, from the value of $a$ in Table 6.1, it is evident

Table 6.1: Summary of parameters used in the ADI-based study of Vos (2011) to reproduce the 2006 to 2009 PAMELA proton spectra. The quantities in the first column of this table are as defined in Chapters 2 and 3.

| **Parameter** | **2006** | **2007** | **2008** | **2009** |
|---|---|---|---|---|
| $\alpha$ [deg] | 15.7 | 14.0 | 14.3 | 10.0 |
| $B_{\rm e}$ [nT] | 5.05 | 4.50 | 4.25 | 3.94 |
| $r_{\rm TS}$ | 88.0 | 86.0 | 84.0 | 80.0 |
| $\kappa_{\parallel,0}$ [$6 \times 10^{20}$ cm$^2$.s$^{-1}$] | 11.57 | 12.70 | 13.57 | 15.85 |
| $\kappa^0_{\perp r}$, $\kappa^0_{\perp\theta}$ | 0.02 | 0.02 | 0.02 | 0.02 |
| $\kappa_{\rm D,0}$ | 1.0 | 1.0 | 1.0 | 1.0 |
| $a$ | 0.56 | 0.48 | 0.39 | 0.28 |
| $b$ | 1.95 | 1.95 | 1.95 | 1.95 |
| $c$ | 3.0 | 3.0 | 3.0 | 3.0 |
| $d$ | 3.0 | 3.0 | 3.0 | 3.0 |
| $P_0$ [GV] | $1/\sqrt{10}$ | $1/\sqrt{10}$ | $1/\sqrt{10}$ | $1/\sqrt{40}$ |
| $P_{\rm k}$ [GV] | 4.0 | 4.0 | 4.0 | 4.2 |

that the rigidity dependence of the diffusion coefficients had also changed with time. The slope of $\kappa_{||}$ at rigidities below $\sim 2$ GV had to be adjusted from $P^{0.56}$ in 2006 to $P^{0.48}$, $P^{0.39}$, and $P^{0.28}$ in 2007, 2008, and 2009 respectively. This time dependent change in the rigidity dependence of the diffusion coefficients was one of the main conclusions of the work done by Vos (2011) and Potgieter et al. (2014) and, as such, one of the main results this study set out to test qualitatively via application of the SDE-based modulation model.

### 6.5.2 SDE-based Modeling

This section employs the SDE-based modulation model discussed in detail in Chapters 4 and 5, aiming to test for the results of the previous section. The set of data used is the final set from Adriani et al. (2013), and the model employs the Smith-Bieber modified heliospheric magnetic field (SBM), as discussed in Chapter 2; see Eq. (2.12). The $\rm HCS_{arctan}$ profile, i.e. Eq. (2.15), is selected for the treatment of the HCS and its associated drift velocity field $\vec{v}_{\rm ns}$, as explained in Chapter 5. The $\rm LIS_{Vos,2013}$ expressed by Eq. (6.1) is selected as primary input at the HP. The model is expected to yield the same qualitative results, the only differences being of a quantitative nature. The factors that would cause such quantitative differences are discussed in the next section.

Four sampled monthly averaged proton spectra are selected from the PAMELA data. These sampled spectra are shown in Figure 6.7 and are, again, for November, 2006 (red circles) and for December of 2007 (orange circles), 2008 (green circles), and 2009 (purple circles), respectively. The SDE-based model was then used to reproduce the four sampled spectra by adjusting the diffusion coefficients after assuming the values for $\alpha$, $B_{\rm e}$, $r_{\rm TS}$ and the drift coefficient set out in Table 6.1.

The first of the four sampled spectra, taken during November 2006 is shown in Figure 6.8 and is overlaid by the modulated spectrum at Earth that was computed by the SDE-based model for an $A < 0$ cycle, after adjusting the diffusion coefficients. Also shown in this figure are SDE-computed spectra, still using the same parameters, but at heliocentric distances of 30 AU, 60 AU, and 90 AU, in the equatorial plane. Note from Table 6.1 that the HCS had an average tilt of 15.7° and the HMF at Earth had an average magnitude of 5.05 nT.

As mentioned before, heliospheric modulation only becomes noticeable below kinetic

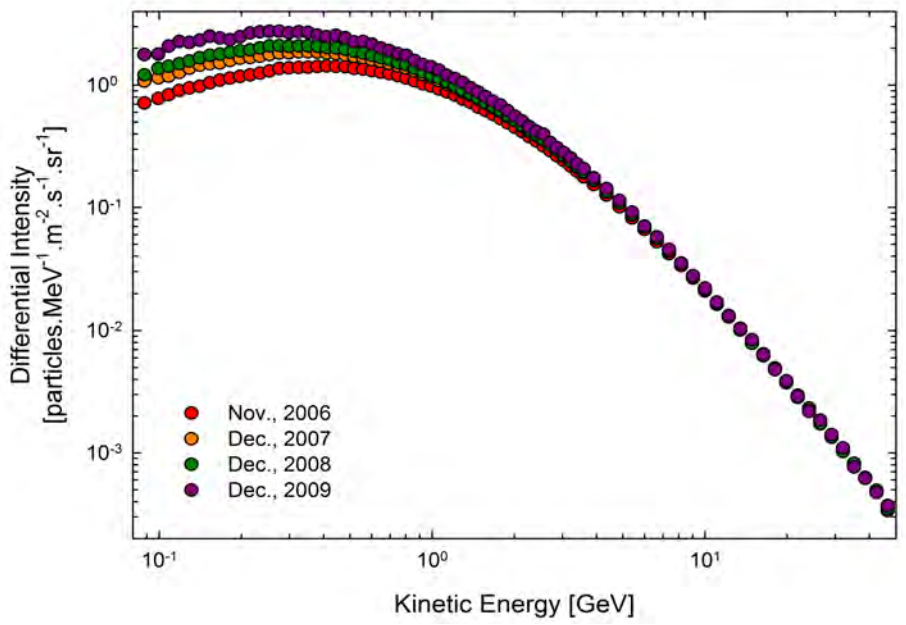


Figure 6.7: *The four monthly averaged proton spectra selected from the PAMELA data. The spectrum for November 2006 is indicated by the red circles and the spectra for December of 2007, 2008, and 2009 are indicated by the orange, green, and purple circles, respectively. The data are as published by Adriani et al. (2013) and Potgieter et al. (2014).*

energies of $\sim$ 30 GeV, at which point the observed intensities drop below the intensities specified by the LIS. This fact is well evident at the higher end of the spectrum in Figure 6.8 and the SDE-based model is thus seen to accurately imitate this behaviour. Furthermore, the computed spectrum represents the PAMELA observations well over all energies. The peak of this spectrum is observed to occur at $\sim$ 450 MeV, where particle intensities rise to a value of 1.44 particles.MeV$^{-1}$.m$^{-2}$.s$^{-1}$.sr$^{-1}$.

Still following Table 6.1, going from 2006 to 2007, both the average HCS tilt angle and HMF magnitude at Earth have decreased by $\sim$ 11 % from 15.7° to 14.0° and from 5.05 nT to 4.50 nT, respectively. Figure 6.9 shows the proton intensities measured by PAMELA for December 2007 and, again, it is overlaid by the SDE-computed spectrum at Earth computed for an $A < 0$ cycle. The peak in the intensities has shifted to $\sim$ 350 MeV and at this energy the intensity has increased to 1.90 particles.MeV$^{-1}$.m$^{-2}$.s$^{-1}$.sr$^{-1}$ in 2007. This represents an increase by a factor of $\sim$ 1.32 compared to 2006. Lower down the spectrum in the energy region where changes in intensities are greatest, the intensity at 100 MeV has increased by a factor of $\sim$ 1.43 from 2006 to 2007. According to the computed solutions, at heliocentric distances of 30 AU, 60 AU, and 90 AU the 2007 intensities at 100 MeV have respectively increased by factors of $\sim$ 1.43, $\sim$ 1.32, and $\sim$ 1.21, relative to those in 2006.

The values in Table 6.1 for 2008 show the average HCS tilt angle at 14.3°. This higher value in the average tilt is the result of the transient increase in the HCS tilt angle at the beginning of 2008, clearly visible in Figure 6.6. The average HMF magnitude at Earth has decreased by another $\sim$ 6 % from 4.50 nT to 4.25 nT. This is about half the decrease of $\sim$ 11 % from 2006 to 2007. This smaller decrease, together with the larger HCS tilt angle explains why the spectrum of 2008 is located so close to the spectrum of 2007, as seen from Figure 6.7. It is, therefore, a logical conclusion that the apparent change

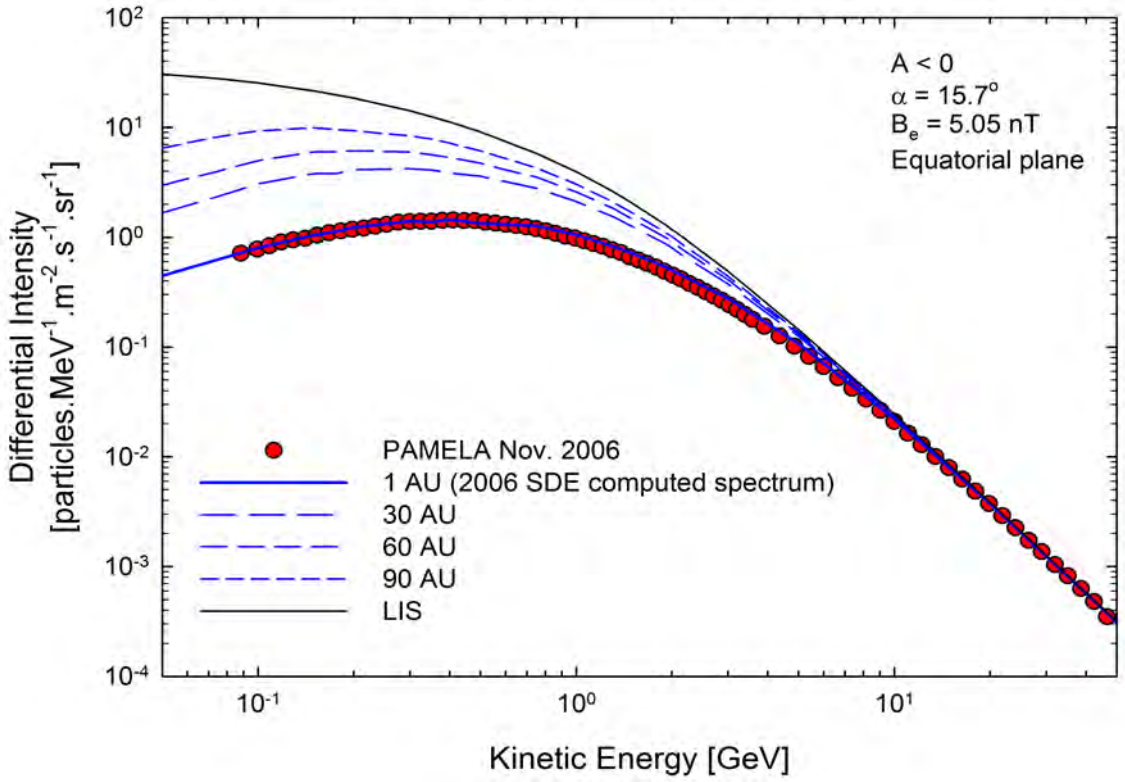


Figure 6.8: *The November 2006 PAMELA proton intensities with the SDE-computed spectrum (solid blue line) at Earth overlaid. The long, medium, and short dashed blue lines correspond to the computed modulated intensities in the equatorial plane at 30 AU, 60 AU, and 90 AU respectively. The LIS at 120 AU is represented by the solid black line. The modeled spectra are for an $A < 0$ cycle, with $\alpha = 15.7°$ and $B_e = 5.05$ nT and were calculated assuming an SBM modified HMF, as discussed in Chapter 2.*

in proton intensities during 2008, as compared to 2007, is related to the changes in the average HMF magnitude (Vos, 2011). This, of course, includes the modulation processes (in particular drifts) dependent on the magnitude of the HMF.

Figure 6.10 shows the proton intensities measured by PAMELA for December 2008, overlaid by the SDE-computed spectrum at Earth for an A $< 0$ cycle. The peak in intensities is seen to have shifted to $\sim$ 350 MeV and the corresponding intensity has increased to 2.05 particles.MeV$^{-1}$.m$^{-2}$.s$^{-1}$.sr$^{-1}$, an increase by a factor of $\sim$ 1.08 from 2007 to 2008. Lower down the spectrum, at 100 MeV, the intensity has increased by a factor of $\sim$ 1.18 from 2007 to 2008, as compared to the $\sim$ 1.43 going from 2006 to 2007. According to the computed 2008 spectra at heliocentric distances of 30 AU, 60 AU, and 90 AU, the 2008 intensities have respectively increased by $\sim$ 1.11, $\sim$ 1.05, and $\sim$ 1.04, relative to 2007. These increases are much lower than the corresponding increases going from 2006 to 2007.

Figure 6.11 shows the final sampled spectrum, that measured during December 2009, overlaid by the SDE-computed modulated spectrum at Earth for an $A < 0$ cycle. The average HCS tilt angle for this period has decreased by $\sim$ 30 % and would have been even lower, had it not been for the fact that tilt angles abruptly began to increase from October, 2009 onward, marking the onset of the new solar activity cycle 24. The average HMF magnitude at Earth during 2009 was less than the value during 2008 by about 7 %.

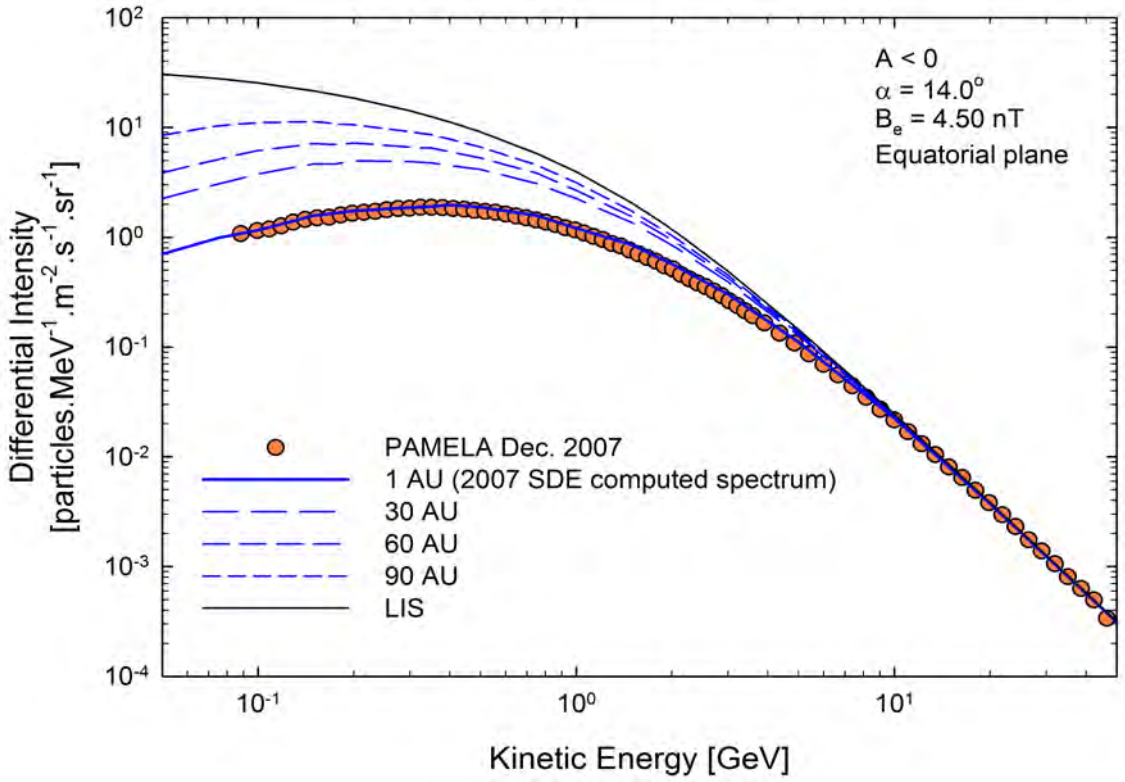


Figure 6.9: *Similar to Figure 6.8, but for December 2007. The yearly averaged values of the tilt angle and HMF magnitude at Earth were at* $\alpha = 14.0°$ *and* $B_e = 4.50$ *nT respectively.*

It is evident from Figures 6.7 and 6.11 that the data for the 2009 spectrum exhibit more variation in absolute value as compared to the previous three sampled spectra. These variations are ascribed to systematic errors and are only prominent at energies below $\sim$ 200 MeV and above $\sim$ 20 GeV. The data set used in this study contains significantly less variation than the set used by Vos (2011), and consequently the SDE-based reproduction of the data is of sufficient accuracy over all energies. The set used by Vos (2011) made for less accurate fits at energies below $\sim$ 200 MeV and complicated the comparison of the 2009 spectrum with those of the previous three years. In this study, the measurements and numerical solutions are still sufficiently consistent at energies below $\sim$ 200 MeV and it was possible to carry on the comparison for 2008 to 2009 in the same way as was done for e.g. 2006 to 2007 or 2007 to 2008.

The peak of the 2009 spectrum has remained at $\sim$ 350 MeV and intensities at this energy have risen to 2.63 particles.MeV$^{-1}$.m$^{-2}$.s$^{-1}$.sr$^{-1}$, representing an increase by a factor of $\sim$ 1.28 from the intensity level of 2008. Considering energies lower down the spectrum again, at $\sim$ 100 MeV, the intensity has increased by a factor of $\sim$ 1.48 from 2008 to 2009. This is consistent with what is observed in the PAMELA data presented in Figure 6.7: intensities have increased significantly from 2006 to 2007 (factor of $\sim$ 1.43 at 100 MeV), increased to a lesser extent from 2007 to 2008 (factor of $\sim$ 1.18 at 100 MeV), and then again greatly increased from 2008 to 2009. This is also reflected in the computed 100 MeV intensities at the heliocentric distances of 30 AU, 60 AU, and 90 AU, which in 2009 respectively showed fractional increases of $\sim$ 1.40, $\sim$ 1.32, and $\sim$ 1.21 as compared to 2008 intensity levels.

The results of the SDE-based modeling are summarised in Table 6.2. The overall

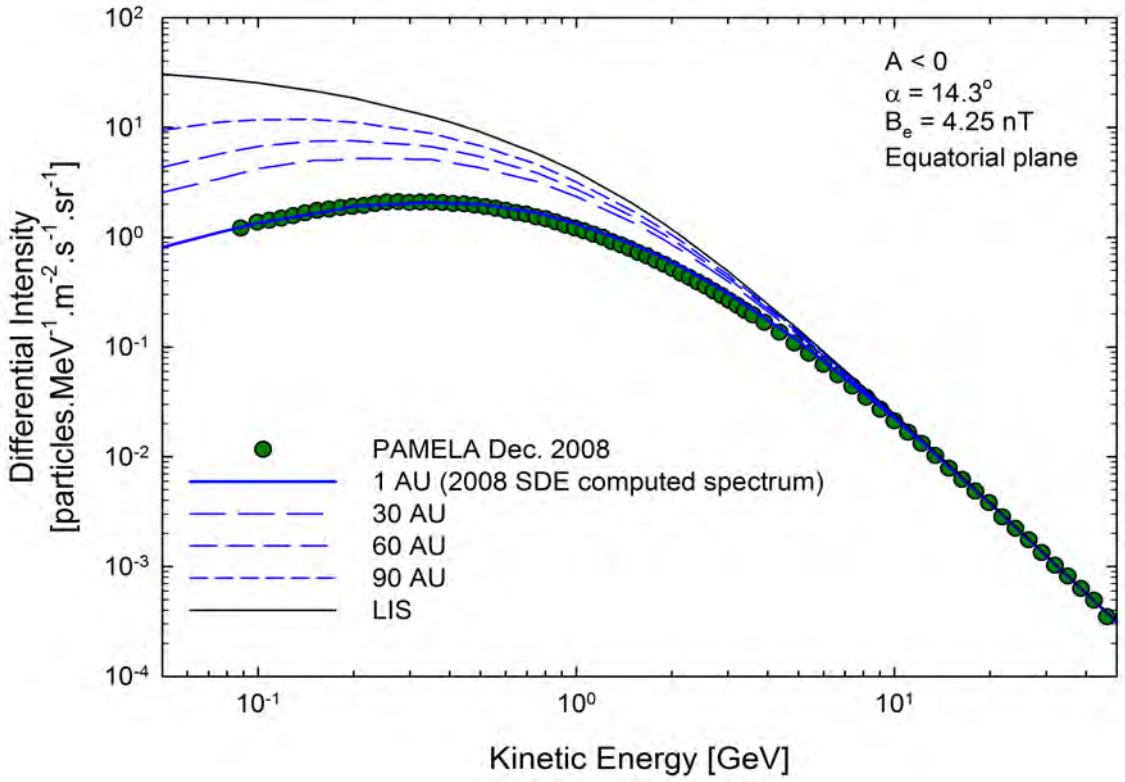


Figure 6.10: *Similar to Figures 6.8 and 6.9, but for December 2008. The yearly averaged values of the tilt angle and HMF magnitude at Earth were at* $\alpha = 14.3°$ *and* $B_e = 4.25$ *nT respectively.*

diffusion was required to consistently increase from 2006 to 2009 with the value of $\kappa_{||,0}$, in units of $6 \times 10^{20}$ cm$^2$.s$^{-1}$, changing from 16.0 in 2006 to 17.1, 17.5, and 19.4 in 2007, 2008, and 2009 respectively. The greatest increase occurred from 2008 to 2009. Furthermore, the rigidity dependence of the diffusion coefficients was required to change from 2008 to 2009, the slope below $\sim 3$ GeV changing from $P^{0.85}$ in 2006 to $P^{0.81}$, $P^{0.78}$ and $P^{0.73}$ in 2007, 2008 and 2009 respectively.

### 6.5.3 Comparison of the Results from the SDE- and ADI-based Modeling

Figure 6.12 presents a comparison of the results summarised in Tables 6.1 and 6.2 and shows the parallel mean free paths $\lambda_{||}$, which is related to $\kappa_{||}$ through Eq. (3.29), for 2006, 2007, 2008 and 2009 as a function of rigidity. From this figure it is clear that the results found by means of the SDE-based modeling of this work are qualitatively similar to that found in the ADI-based study of Vos (2011). In both cases $\kappa_{||}$ was found to have consistently increased over the course of 2006 to 2009; the SDE-based results show the largest increase in intensities to have occurred from 2008 to 2009. Both studies also required the rigidity dependence of $\kappa_{||}$ to change over this period. The reader is reminded of the fact that a change in $\kappa_{||}$ produces corresponding changes in all the diffusion coefficients according to Eqs. (3.32) and (3.33). These results are also in qualitative agreement with the results found by Potgieter et al. (2014).

As mentioned in before, there are various factors contributing to the quantitative differences between the SDE-based results of this study and the ADI-based results of Vos

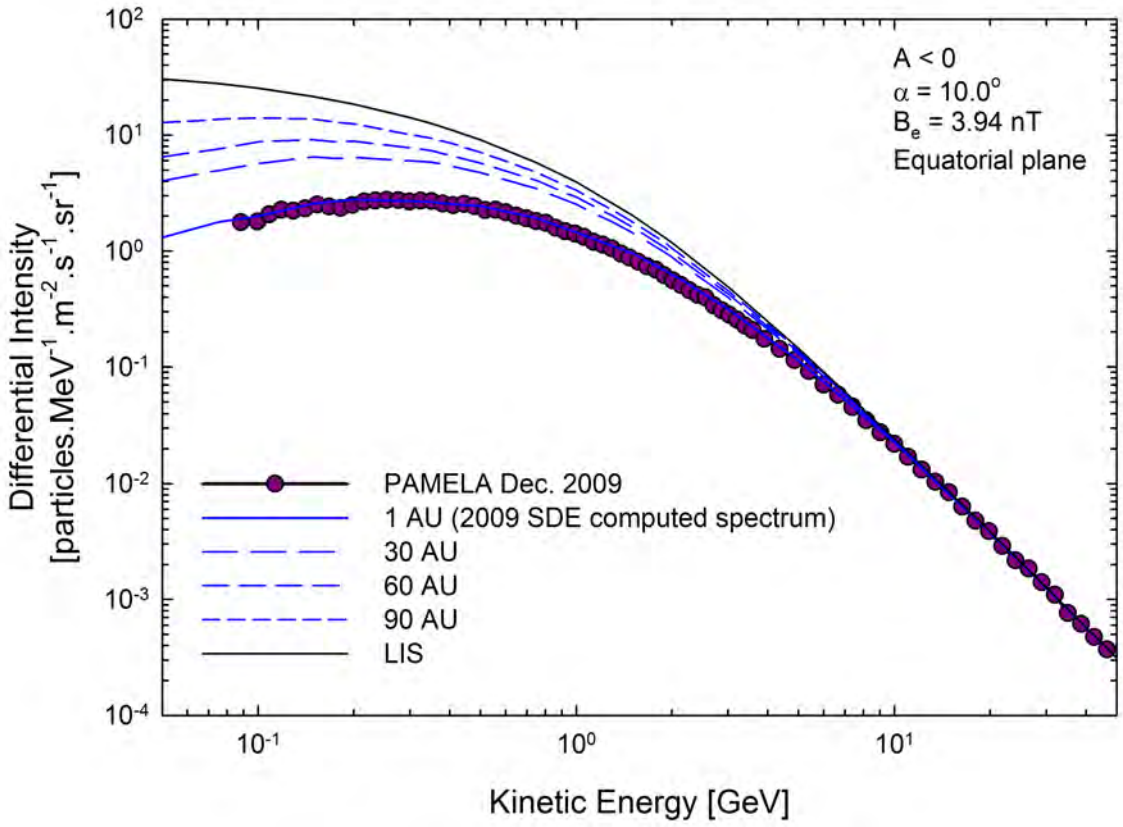


Figure 6.11: *Similar to Figures 6.8, 6.9 and 6.10, but for December 2009. The yearly averaged values of the tilt angle and HMF magnitude at Earth were at* $\alpha = 10.0°$ *and* $B_e = 3.94$ *nT respectively.*

(2011). The most important of these factors can be summarised as (1) the choice of HMF profile was not the same; (2) the sets of data used were not identical; (3) the approaches in handling the HCS and its associated drift velocity field $\vec{v}_{ns}$ were different; (4) the choice of LIS was different in each case.

The fact that the SDE-based modeling of this study assumed an SBM, while the ADI-based modeling of Vos (2011) had employed the JKM, is expected to cause significant differences in the modulation results. The effects of each of the SBM and JKM on modulated spectra at Earth were illustrated in Chapter 5 and it was clear that, using the same set of modulation parameters, the SBM-spectrum was comfortably below that of the JKM. This implies that, in order to achieve the same intensities at Earth, the diffusion coefficients in the case of the SBM must be greater than those for the JKM. The use of the different HMF profiles is therefore identified as a sure factor contributing to the quantitative differences.

The fact that the data from PAMELA used in this study were different from that used by Vos (2011) is another sure factor to cause quantitative differences in the results, though on a smaller scale than the first factor. The reason why the set of data analysed in this study differs from that of Vos (2011) was explained before.

The treatment of the HCS and $\vec{v}_{ns}$ was different in three ways: (1) this work assumed Eq. (2.15) or $\text{HCS}_{\text{arctan}}$ for the latitudinal extent of the HCS, while the ADI-based modeling had assumed Eq. (2.14) or $\text{HCS}_{\text{arcsin}}$; (2) in this study, $\vec{v}_{ns}$ was adapted according to the work of Burger (2012), while this not being the case in the ADI-based study; (3) the SDE-based model of this work assumed the $V_{sw}$ that occurs explicitly in

Table 6.2: Summary of parameters used in this SDE-based study to reproduce the 2006 to 2009 PAMELA proton spectra. The quantities in the first column of this table are as defined in Chapters 2 and 3.

| **Parameter** | **2006** | **2007** | **2008** | **2009** |
|---|---|---|---|---|
| $\alpha$ [deg] | 15.7 | 14.0 | 14.3 | 10.0 |
| $B_{\rm e}$ [nT] | 5.05 | 4.50 | 4.25 | 3.94 |
| $r_{\rm TS}$ | 88.0 | 86.0 | 84.0 | 80.0 |
| $\kappa_{\parallel,0}$ [$6 \times 10^{20}$ cm$^2$.s$^{-1}$] | 16.0 | 17.1 | 17.5 | 19.4 |
| $\kappa^0_{\perp r}$, $\kappa^0_{\perp\theta}$ | 0.02 | 0.02 | 0.02 | 0.02 |
| $\kappa_{\rm D,0}$ | 1.0 | 1.0 | 1.0 | 1.0 |
| $a$ | 0.85 | 0.81 | 0.78 | 0.73 |
| $b$ | 1.95 | 1.95 | 1.95 | 1.95 |
| $c$ | 3.0 | 3.0 | 3.0 | 3.0 |
| $d$ | 3.0 | 3.0 | 3.0 | 3.0 |
| $P_0$ [GV] | $1/\sqrt{10}$ | $1/\sqrt{10}$ | $1/\sqrt{10}$ | $1/\sqrt{40}$ |
| $P_{\rm k}$ [GV] | 4.0 | 4.0 | 4.0 | 4.2 |

the expression for the HCS latitudinal extent to retain its radial dependence expressed by Eqs. (2.4) and (2.5), while the ADI-based model had assumed this value to be constant $V_{\rm sw} = 400$ km.s$^{-1}$, i.e. the SDE-based model featured an HCS that was compressed in the heliosheath, while the ADI-based model had left the HCS unchanged beyond the TS. The first of these differences was looked at in detail in Chapter 5 and it was indicated that the difference in modulation at such small tilt angles should not be significant − at least not on the scale of the differences due to the use of the SBM instead of the JKM. The second of these differences is not expected to lead to modulation results that can be considered significant, since Burger (2012) had concluded that the effects of this more realistic approach − and, once again, especially at these small values of $\alpha$ − were very small: as an example, it was found that, at $\alpha = 10°$, the intensity of 1.6 GeV protons at Earth in the $A < 0$ cycle differed by only $\sim 3\%$ from modeling results neglecting this more realistic approach. Since the statistical nature of the SDE-based model in this study already implies a $\sim 3\%$ uncertainty in spectra solutions (see Chapter 5), this effect is rightfully deemed negligible. The third of the differences listed above, i.e. the compression of the HCS in the heliosheath, may be expected to cause some changes in modulation, but has not been investigated in this work.

Considering modulation at Earth, the effect of using a different LIS was illustrated in Section 6.2 to be limited to energies above $\sim 100$ MeV; at energies below this value there was no significant difference, owing to the dominance of adiabatic cooling effects at these lower energies. The effect may well be significant over a larger range of energies at radial distances closer to the HP.

Another possible effect, not mentioned in the above compilation of most important factors, is the extent of the intrinsic differences that may exist between the ADI- and SDE-based models. The extent of such differences has not yet been determined, but the effect is not expected to rival the differences due to e.g. the effect of using a different HMF profile. This, however, constitutes a topic deserving of further study in the future.

The main result of Section 6.5 is the qualitative confirmation of the results found by Vos (2011) and Potgieter et al. (2014). These results have also been confirmed qualitatively by Ndiitwani et al. (2013), using a time dependent ADI-based model to reproduce the PAMELA proton spectra from 2006 to 2009. Bazilevskaya et al. (2012) also concluded that the CR spectrum has indeed become softer between 2008 and 2009; these

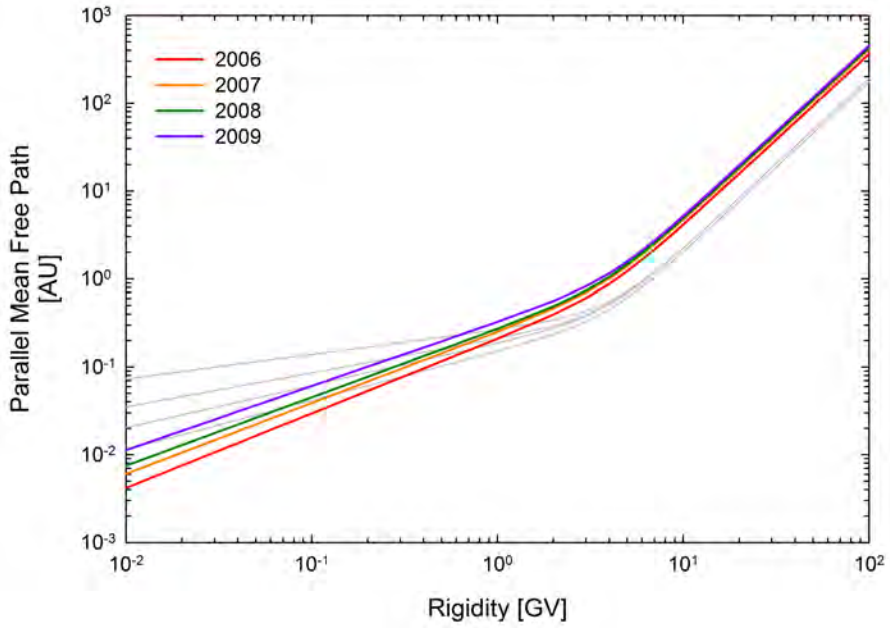


Figure 6.12: *The parallel mean free paths $\lambda_{||}$ for 2006, 2007, 2008, and 2009 obtained from the SDE-based modeling are represented by the red, orange, green, and purple lines respectively. For comparison, the corresponding parallel mean free paths resulting from the ADI-based modeling (Vos, 2011; Potgieter et al., 2014) are included and represented by the grey lines.*

results were obtained by comparing the values of CR fluxes in 2009 as observed by balloon flights to previous years and as observed by the Moscow neutron monitor, i.e. as observed in different energy ranges.

## 6.6 Summary and Conclusions

The numerical modulation model based on the solution of the set of stochastic differential equations (SDEs) corresponding to the Parker transport equation (TPE), i.e. the SDE-based model, was applied in this chapter. In the introduction to this chapter, presented in Section 6.1, the context in which this application is to be interpreted was explained: the aim was not only to show that the model is able to reproduce the 2006 to 2009 PAMELA proton spectra at Earth, but to independently test the results of Vos (2011) and Potgieter et al. (2014); it was stressed that this application was by no means a full account of the applicability of the model, since the yearly averaged heliospheric current sheet (HCS) tilt angles associated with the 2006 to 2009 PAMELA proton spectra only went as high as 15.7°, whereas Chapter 5 had conclusively illustrated that the model is well suited for modulation studies up to extreme solar maximum conditions.

In Section 6.2 the importance of selecting a sufficiently good estimation for the local interstellar spectrum (LIS) in modulation studies was emphasised. The difficulty behind obtaining a sound estimation was pointed out and it was illustrated how the supposed encounters of Voyager 1 with the heliopause (HP) since about August 2012 have alleviated this problem and enabled far more accurate estimations for the LIS. The proton LIS selected for use in this study was defined in the context of that used by Vos (2011) and Potgieter et al. (2014), at the same time illustrating it to be a suitable choice.

Section 6.3 presented and discussed the final proton observations from the PAMELA

instrument for the period July, 2006 to December, 2009. It was confirmed that proton intensities peaked in December, 2009, reaching considerably high levels especially at the lower end of the energy spectrum. This period marked the climax of the solar cycle 23/24 minimum.

The next section looked at solar cycle 23 in more detail, discussing the causes to the observations from PAMELA. It was pointed out that the minimum of solar cycle 23/24 was marked by: unusually low SNs and a noticeable drop in the averaged heliospheric magnetic field (HMF) magnitude to values less than 4.0 nT at Earth; an HCS tilt angle remaining at values above usual for a longer period and only at a late stage reaching the kind of minimum values expected when compared to previous solar minima.

The four sampled PAMELA spectra, from 2006 to 2009, selected to be used in this study, were specified and illustrated in Section 6.5. The yearly averaged HCS tilt angle and HMF magnitudes at Earth calculated by Vos (2011) were tabulated in Table 6.1. The section then continued with a detailed discussion and graphs of the computed energy spectra produced by the SDE-based numerical model used in this study, whereafter the results were tabulated in Table 6.2. The yearly computed energy spectra, along with the PAMELA observations, were depicted in Figures 6.8 to 6.11.

Section 6.5.3 ended off this chapter by concluding that the results of the SDE-based modeling performed in this work presented a qualitative confirmation of the results obtained by Vos (2011) and Potgieter et al. (2014). It was further pointed out that these results have have also been confirmed by other authors such as Ndiitwani et al. (2013), reinforcing the established qualitative result. The quantitative differences between the two sets of results were indicated to be primarily due to the employment of the two different HMF profiles; other discrepancies arising due to the different way in which the HCS and HCS drifts were handled were indicated to be negligible, owing to the fact that only relatively small tilt angles were considered. The fact that the sets of data analysed by the two studies respectively were not identical, as well as the use of a different LIS, was also shown to cause differences in the proton spectra at Earth.

# Chapter 7

# Summary and Conclusions

This chapter serves to summarise the most important aspects of this work, with emphasis on the most significant conclusions. References in this chapter are limited to only those most relevant or necessary.

Where once the field of cosmic ray modulation in the heliosphere was dominated by numerical models based on the finite different approach of the alternating direction implicit (ADI) method, models based on stochastic differential equations (SDEs) have become increasingly popular in recent times. In this study, such a spatially 3D and time independent SDE-based model was refined and utilised to investigate a number of phenomena. The nature of this study was distinctly comparative, with comparisons made between SDE- and ADI-based numerical models, as well as between the modulation results obtained by utilising these models respectively. The comparative nature of this study was also extended to other topics such as the neutral heliospheric current sheet (HCS) and heliospheric magnetic field (HMF) profiles.

The relevant background pertinent to cosmic ray modulation studies and the wider field of heliospheric physics was discussed in Chapter 2. The dynamic magnetic nature of the Sun was explained, establishing the concept of the solar activity cycle. The concept of the solar wind was introduced and its role in the formation and structuring of the heliosphere was explained. It was also explained how the solar wind carries the solar magnetic field with it out into the heliosphere to form the heliospheric magnetic field. The Parker heliospheric magnetic field (PHMF) model was discussed together with the two prominent modifications to this model, these being the Jokipii-Kóta modification (Jokipii and Kóta, 1989) and the Smith-Bieber modification (Smith and Bieber, 1991), respectively referred to in this work as the JKM and SBM. The JKM was criticised, while the SBM was reserved for further application and investigation in later chapters. The neutral heliospheric current sheet was introduced as a major co-rotating structure in the heliosphere and two different expressions for its latitudinal extent were introduced; the HCS tilt angle was introduced as proxy for solar activity. This was followed by a discussion of cosmic rays, classifying them according to origin and illustrating their modulation in the heliosphere as a function of the solar activity cycle. Chapter 2 concluded with a discussion of the spacecraft missions most relevant to this study: the PAMELA space mission, important in this work for its measurement of the 2006 to 2009 proton spectra; and the Voyager 1 and Voyager 2 space missions, Voyager 1 being of particular interest in the calculation of the proton local interstellar spectrum (LIS).

Chapter 3 presented a mathematical description of the relevant theory behind the transport of cosmic rays in the heliosphere. The Parker transport equation (TPE) was introduced and it was indicated that this equation accounts for all the relevant physical modulation processes. The processes of drift and diffusion were discussed in particular.

A simplified approach was followed for the proton diffusion coefficient, the spatial dependence of both the parallel diffusion coefficient ($\kappa_{||}$) and perpendicular diffusion coefficients in the radial and polar directions ($\kappa_{\perp r}$ and $\kappa_{\perp \theta}$ respectively) scaling as $B^{-1}$, with $B$ the HMF magnitude; the rigidity dependence of these coefficients was assumed to be a combination of two power laws. Both $\kappa_{\perp r}$ and $\kappa_{\perp \theta}$ were scaled by 2% of $\kappa_{||}$, with $\kappa_{\perp \theta}$ also scaled as a function of the polar angle. Particle drifts were assumed to be at a maximum, i.e. full drift. The TPE was finally converted to spherical coordinates in order to be incorporated into a numerical modulation model.

The numerical modulation model employed in this study was introduced in Chapter 4; the model was derived by arriving at the appropriate set of stochastic differential equations (SDEs) corresponding to the TPE. This was done after a general introduction to SDEs and an illustration of how these equations are utilised to solve real life physical problems. The concepts of pseudo-particles and pseudo-particle trajectories were defined clearly. Chapter 4 also sketched the relevant context establishing background regarding CR modulation models by presenting a chronological description of the modeling done by the Potchefstroom modulation group; this was done for SDE-based models as well as for models based on the alternating differential implicit (ADI) method. Furthermore, the advantages and disadvantages of SDE-based models and those of ADI-based models were compared and it was concluded that, in addition to their superior numerical stability and compatibility for implementation on multiple processors, SDE-based models also allow for significant new insights into the physical processes of CR modulation in the heliosphere. It was also indicated that SDE-based models allow for the calculation of two additional and especially useful quantities, namely particle propagation times and energy losses. The chapter concluded with an overview of the benchmarking of the SDE-based model carried out by Strauss et al. (2011b, c, 2012); from this benchmarking, it was concluded that the SDE-based numerical model was able to accurately and reliably describe the modulation of actual CRs in the heliosphere, despite the fact that SDE-models make use of pseudo-particles in obtaining any solution.

Chapter 5 constituted the core of this study, illustrating the properties and features of the SDE-based numerical modulation model featured in this work. The accuracy and convergence of the solutions obtained upon utilisation of this model were discussed, illustrating these solutions to converge with the use of an increasing number of pseudo-particles and the estimated error on these solutions to decrease accordingly; it was concluded that, for spectra solutions, sufficient convergence was obtained when employing $N = 1 \times 10^3$ pseudo-particles, while this number was increased to $N = 1 \times 10^4$ when studying modulation as function of solar activity. Issues pertaining to the boundary conditions were discussed and it was illustrated that the model behaves in a logical and coherent manner when adjusting the positions of the inner and outer modulation boundaries; it was concluded that, for the purposes of this this study, spectra solutions at Earth were not significantly affected by choosing either a reflecting or an absorbing inner modulation boundary; furthermore, it was indicated that throughout this study a reflective inner modulation boundary would be assumed.

In the next section of Chapter 5 the SBM and JKM modifications to the PHMF were implemented in the numerical model and the radial and latitudinal profiles for each of these were compared. The impact on the drift and diffusion coefficients and the ultimate effect on modulation were also illustrated. It was concluded that, although the effects of the JKM may locally be greater than those of the SBM, the effects of the SBM are exercised over a greater part of the modulation space and hence its overall effect on CR intensities is greater than that of the JKM. The PHMF was shown to be especially conducive to drift dominated modulation, while the JKM and SBM were shown to induce

successively greater contributions from diffusive processes, consequently reducing extreme drift effects on CR modulation that may otherwise occur, as in the modeling of Jokipii and Kopriva (1979). Attention was again directed to the respective definitions of the concepts of pseudo-particles and particles, emphasising the fact that these two concepts are not identical. It was indicated that, although SDE-based models make use of pseudo-particles, the results obtained throughout this study were primarily interpreted in terms of what it suggests about the behavior of actual CR particles (protons), i.e. what it says about the processes of modulation.

The next section of Chapter 5 was devoted to matters related to the HCS. After an explanation of just how the HCS tilt angle $\alpha$ was employed as a proxy for solar activity, the two expressions for the latitudinal extent of the HCS given in Chapter 2 were discussed and investigated in detail. These two HCS profiles were referred to as the cases for $\text{HCS}_{\text{arcsin}}$ and $\text{HCS}_{\text{arctan}}$ respectively and it was concluded that the geometries of these two cases differed remarkably at tilt angles larger than about 65°. The HCS drift velocity field associated with the case for $\text{HCS}_{\text{arctan}}$ was formally derived and compared with that of the case for $\text{HCS}_{\text{arcsin}}$. This was done in more detail in the next section, where CR proton modulation results for these two cases were compared; the SBM was employed throughout. Two scenarios in particular were investigated: a drift dominated scenario, and a scenario in which the diffusion coefficients were still low, but not to such an extent that the situation was entirely drift dominated.

Before discussing the results of each of these scenarios, distinction was made between two roughly separate but connected processes; these processes were referred to as the first and second processes respectively. The first process accounts for the expansion of the HCS (waviness), i.e. the expansion of the extent of the HCS drift velocity field $\vec{v}_{\text{ns}}$. The second process is established by the presence of the HCS tilt angle $\alpha$ in the expression for the solar wind velocity which causes it to change as a function of solar activity, in accordance with observations by the Ulysses spacecraft. Furthermore, the treatment of the drift dominated scenario led to the identification of an effect referred to in this work as the effect of large gradients in CR intensities $\nabla j$, which proved essential to explain the peculiar result of CR intensities actually increasing with an increase in solar activity; this effect was associated with the second process. The first process was found to be more effective in the case for $\text{HCS}_{\text{arcsin}}$ at lower levels of solar activity, i.e. the drift velocity field $\vec{v}_{\text{ns}}$ associated with $\text{HCS}_{\text{arcsin}}$ was found to more effectively drift CR protons out and away from Earth during $A > 0$ polarity cycles, while during $A < 0$ polarity cycles it was found to more effectively drift these particles in and towards Earth along the HCS. These results led to an important conclusion: even at such low levels of solar activity where there are as yet no differences observable in the geometries of the respective HCS profiles, the drift velocity fields $\vec{v}_{\text{ns}}$ of the two cases for $\text{HCS}_{\text{arctan}}$ and $\text{HCS}_{\text{arcsin}}$ are significantly different, i.e. in the sense that it leads to significantly different modulation.

At the highest levels of solar activity, the first process was seen to be more effective in the case for $\text{HCS}_{\text{arctan}}$. An explanation for this was presented from geometrical considerations, since at such large tilt angles the geometries of the cases for $\text{HCS}_{\text{arctan}}$ and $\text{HCS}_{\text{arcsin}}$ are markedly different: the peaks or arms of the $\text{HCS}_{\text{arctan}}$ geometry are more extended or "thicker" than those of the $\text{HCS}_{\text{arcsin}}$ and it was shown that these thick arms exert a greater influence on CR protons that does the thin arms of the $\text{HCS}_{\text{arcsin}}$. It was shown that when $\alpha$ becomes large enough so that the arms of the $\text{HCS}_{\text{arctan}}$ profile enters deep enough into the polar regions, it significantly reduces the inward drift of protons along the poles and $A > 0$ intensity profiles plummet to levels in the order of the zero-drift solution; $A < 0$ intensity profiles are seen to increase towards the level of the zero-drift solution due to the arms of the $\text{HCS}_{\text{arctan}}$ geometry now inhibiting outward drift along

the poles. The first process in the case for $\text{HCS}_{\text{arctan}}$ was thus more effective to such an extent that the $A > 0$ and $A < 0$ solutions were seen to coincide at the highest levels of solar activity to form a closed loop. This is a result that has never been reported before without setting the drift coefficient to zero at the highest levels of solar activity, as was done by e.g. Ndiitwani et al. (2005). By utilising the SDE-based model, these results were motivated to satisfaction and it was concluded that the $\text{HCS}_{\text{arctan}}$ was the preferred HCS profile at the highest levels of solar activity, since it leads to realistic modulation even at these values.

The results from Chapter 5 allowed for one final conclusion regarding a concept known as the effective tilt angle $\alpha_{\text{e}}$, defined as the tilt angle effectively 'experienced' by a particle. It was indicated that at levels of solar activity high enough such that the geometric differences between the cases for $\text{HCS}_{\text{arctan}}$ and $\text{HCS}_{\text{arcsin}}$ were clear, this value was greater in the former case, as can be expected considering the respective geometries. Furthermore, this value was indicated to be energy dependent, supporting the work of le Roux and Potgieter (1992). In general, the effect on modulation measured from the lowest to the highest levels of solar activity was found to increase with a decrease in proton energy, as expected.

In Chapter 6, the SDE-based numerical modulation model was applied to reproduce four observed galactic proton spectra which were selected from measurements by the PAMELA instrument. These measurements were taken during the atypical minimum of solar cycle 23/24 and the four spectra corresponded to each of the four years spanning this minimum, i.e. 2006 to 2009. A brief discussion of this atypical solar minimum was also included, and it was indicated that the 2009 proton spectrum was the highest such spectrum measured since the beginning of the space age. The SDE-based reproductions of these spectra were compared to that obtained by the ADI-based modeling of Vos (2011) and it was concluded that these results were largely similar: in order to reproduce these spectra, the diffusion had to be increased consistently from 2006 to 2009 and the rigidity dependence of the diffusion coefficients below about 3 GV had to be decreased over this time, resulting in the proton spectrum becoming increasingly softer from 2006 to 2009. It was also pointed out that these same qualitative results have been obtained by other authors such as Ndiitwani et al. (2013). The quantitative differences in the results obtained in this study and those obtained by Vos (2011) were indicated to be primarily due to the employment of the SBM in this study, while the former study had employed the JKM. This chapter has illustrated that the numerical modulation model of this study can be applied to reproduce observations. A new proton LIS was used in this study and was accordingly discussed and motivated; this LIS was normalised according to PAMELA data above 50 GeV by Vos (2011) and at lower energies according to Voyager 1 data. The recent crossing of the HP by Voyager 1 was also discussed and some of the latest research relevant to this topic and the question of when Voyager 1 will actually start measuring the pristine LIS was summarised.

Further development of the numerical model of this study and avenues of research include:

- The radial profile of the solar wind velocity before the TS is encountered is to be adapted to account for the effect of mass loading from the pick-up of interstellar neutrals, thus decreasing steadily even before the TS is encountered (e.g. Richardson and Stone, 2009).

- The radial profile of the solar wind velocity in the inner heliosheath is to be adjusted so that it will decrease according to Voyager 1 non-plasma observations which have

indicated it to decrease to close to zero when nearing the HP (Krimigis et al., 2011). Equally important is that the solar wind profile should be adjusted to include polar and azimuthal components in the heliosheath according to Voyager 2 observations. This has already been done by coupling the results of hydrodynamic (HD) and magneto-hydrodynamic (MHD) models with modulation models e.g. Scherer and Ferreira (2005), Strauss et al. (2013a) and Luo et al. (2013a).

- The nature of the drop in the solar wind velocity over the position of the TS is also to be reviewed, since Voyager 2 measurements have indicated that the solar wind showed a slowdown already commencing 80 days before the TS was encountered (e.g. Richardson and Stone, 2009).

- The TS employed in this work was described as a "simulated" shock, since it was implemented entirely by means of the solar wind velocity dropping over the position of the TS and in the process producing a well-defined heliosheath but not accounting for the actual shock acceleration of CRs. Such effects should be incorporated into the model, which will make it suitable for studies of the acceleration of the anomalous component and the re-acceleration of galactic CRs at the TS. Such attempts have already been reported by e.g. Luo et al. (2013a).

- The HCS was modified in the inner heliosheath also solely by means of the drop in the solar wind velocity over the TS, which caused the HCS to compress. An even more realistic HCS in the heliosheath will be established once the solar wind profile in this region has been modified, including concepts such as magnetic reconnection.

- The current model produces steady-state CR modulation and should be extended to include time-varying modulation parameters such as were recently reported by Luo et al. (2011, 2013b).

- Since it was shown in Chapter 5 that this model was suitable to be used up to the highest levels of solar activity by producing realistic results, this model can now be applied to such studies.

- The SDE-based numerical modulation model is of such numerical prowess and stability that the HMF can be adapted to incorporate the Fisk field, which is considered too complicated to be implemented in ADI-based models, so that various alternative and more simple HMF profiles were used (e.g. Sternal et al., 2011).

# Bibliography


Adriani, O., et al., Observations of the 2006 December 13 and 14 solar particle events in the 80 MeV $n^{-1}$ - 3 GeV $n^{-1}$ range from space with the PAMELA detector, Astrophys. J., 742, 102 - 112, 2011.

Adriani, O., et al., Time dependence of the proton flux measured by PAMELA during the 2006 July - 2009 December solar minimum, Astrophys. J., 765, 91 - 98 , 2013.

Adriani, O. et al., The PAMELA mission: Heralding a new era in precision cosmic ray physics, Phys. Rep., 544, 323 - 370, 2014.

Alanko-Huotari, K., I.G. Usoskin, K. Mursula, G.A. Kovaltsov, Stochastic simulation of cosmic ray modulation including a wavy heliospheric current sheet, J. Geophys. Res., 112, A08101, 1 - 10, 2007.

Bazilevskaya, G.A., M.B. Krainev, V.S. Makhmutov, Yu.I. Stozhkov, A.K. Svirzhevskaya, N.S. Svirzhevsky, Change in the rigidity dependence of the galctic cosmic ray modulation in 2008 - 2009, Adv. Space Res., 49, 4, 784 - 790, 2012.

Bieber, J.W., W.H. Matthaeus, Cosmic ray pitch angle scattering in dynamical magnetic turbulence, Int. Cosmic Ray Conf. Proc., 3, 248 - 251, 1991.

Bieber, J.W., W.H. Matthaeus, C.W. Smith, W. Wanner, M.-B. Kallenrode, G. Wibberenz, Proton and electron mean free paths: the Palmer consensus revisited, Astrophys. J., 420, 294 - 306, 1994.

Bieber, J.W., W.H. Matthaeus, A. Shalchi, G. Qin, Nonlinear guiding center theory of perpendicular diffusion: general properties and comparison with observation, Geophys. Res. Lett., 31, 1 - 4, 2004.

Biermann, L., The solar wind and the interplanetary media, *Space Astrophysics*, edited by W. Liller, McGraw-Hill, New York, 1961.

Bobik, P., et al., Systematic investigation of solar modulation of galactic protons for solar cycle 23 using a monte carlo approach with particle drift effects and latitudinal dependence, Astrophys. J., 745, 986 - 996, 2012.

Borovikov, S.N., N.V. Pogorelov, Voyager 1 near the heliopause, Astrophys. J. Lett., 783, L16 - L21, 2014.

Burger, R.A., On the theory and application of drift motion of charged particles in inhomogeneous magnetic fields, Ph.D. thesis, Potchefstroom University for CHE, South Africa, 1987.

Burger, R.A., Cosmic ray modulation and the heliospheric magnetic field, Adv. Space Res., 35, 4, 636 - 642, 2005.

Burger, R.A., Modelling drift along the heliospheric wavy neutral current sheet, Astrophys. J., 760, 60 - 64, 2012.

Burger, R.A., M.S. Potgieter, The calculation of neutral sheet drift in two-dimensional cosmic-ray modulation models, Astrophys. J., 339, 501 - 511, 1989.

Burger, R.A., M. Hattingh, Effect of Fisk-type heliospheric magnetic fields on the latitudinal transport of cosmic rays, Int. Cosmic Ray Conf. Proc., 9, 3698 - 3701, 2001.

Burger, R.A., M. Hitge, The effect of a Fisk-type heliospheric magnetic field on cosmic-ray modulation, Astrophys. J. Lett., 617, L73 - L76, 2004.

Burger, R.A., H. Moraal, G.M. Webb, Drift theory of charged paticles in electric and magnetic fields, Astrophys. Space Sci., 116, 107 - 129, 1985.

Burger, R.A., M.S. Potgieter, B. Heber, Rigidity dependence of cosmic ray proton latitudinal gradients measured by the Ulysses spacecraft: implications for the diffusion tensor, J. Geophys. Res., 105, A12, 27447 - 27456, 2000.

Burger, R.A., T.P.J. Krüger, M. Hitge, N.E. Engelbrecht, A Fisk-Parker hybrid heliospheric magnetic field with a solar-cycle dependence, Astrophys. J., 674, 511 - 519, 2008.

Burlaga, L.F., N.F. Ness, Large-scale distant heliospheric magnetic field: Voyager 1 and 2 observations from 1986 through 1989, J. Geophys. Res., 98, A10, 17451 - 17460, 1993.

Burlaga, L.F., N.F. Ness, M.H. Acuña, R.P. Lepping, J.E.P. Connerney, J.D. Richardson, Magnetic fields at the solar wind termination shock, Nature, 454, 75 - 77, 2008.

Burlaga, L.F., N.F. Ness, E.C. Stone, Magnetic field observations as Voyager 1 entered the heliosheath depletion region, Sci., 341, 147 - 150, 2013.

Caballero-Lopez, R.A., H. Moraal, The numerical description of neutral sheet drift effects, Int. Cosmic Ray Conf. Proc., 7, 3871 - 3874, 2003.

Calder, N., *The Manic Sun, weather theories confounded*, Pilkington Press Ltd., Northamptonshire, 1997.

Carlson, P., A century of cosmic rays, Phys. Today, 65, 30 - 36, 2012.

Casolino, M., et al., The PAMELA experiment: A space-borne observatory for heliospheric phenomena, Adv. Space Res., 41, 12, 2043 - 2049, 2008.

Chenette, D.L., T.F. Conlon, J.A. Simpson, Burst of relativistic electrons from Jupiter observed in interplanetary space with the time variation of the planetary rotation period, J. Geophys. Res., 79, 25, 3551 - 3558, 1974.

Choudhuri, A.R., *The physics of fluids and plasmas: an introduction for astrophysicists*, Cambridge University Press, UK, 1998.

Cliver, E.W., Solar energetic particles: Acceleration and transport, Int. Cosmic Ray Conf. Proc., 516, 103 - 119, 2000.

Decker, R.B., S.M. Krimigis, E.C. Roelof, M.E. Hill, T.P. Armstrong, G. Gloeckler, D.C. Hamilton, L.J. Lanzerotti, Voyager 1 in the foreshock, termination shock, and heliosheath, Sci., 309, 2020 - 2024, 2005.

Dröge, W., Y.Y. Kartavykh, B. Klecker, G.A. Kovaltsov, Anisotropic three-dimensional focused transport of solar energetic particles in the inner heliosphere, Astrophys. J., 709, 912 - 919, 2010.

Earl, J.A., The diffusive idealization of charged-particle transport in random magnetic fields, Astrophys. J., 193, 231 - 242, 1974.

Engelbrecht, N.E., On the heliospheric diffusion tensor and its effect on the 26-day recurrent cosmic ray variations, M. Sc dissertation, North-West University, South Africa, 2008.

Engelbrecht, N.E., On the development and applications of a three-dimensional *ab inito* cosmic-ray modulation model, Ph.D. thesis, North-West University, South Africa, 2012.

Fahr, H.J., T. Kausch, K. Scherer, A 5-fluid hydrodynamic approach to model the solar system-interstellar medium interaction, Astron. Astrophys., 357, 268 - 282, 2000.

Ferreira, S.E.S., A study of the modulation of cosmic ray electrons in the heliosphere, M.Sc. dissertation, Potchefstroom University for CHE, South Africa, 1998.

Ferreira, S.E.S., The heliospheric transport of galactic cosmic rays and jovian electrons, Ph.D. thesis, Potchefstroom University for CHE, South Africa, 2002.

Ferreira, S.E.S., M.S. Potgieter, Long-term cosmic-ray modulation in the heliosphere, Astrophys. J., 603, 744 - 752, 2004.

Ferreira, S.E.S., M.S. Potgieter, R.A. Burger, B. Heber, Modulation effects of anisotropic perpendicular diffusion on cosmic ray electron intensities in the heliosphere, J. Geophys. Res., 105, A8, 18305 - 18314, 2000.

Ferreira, S.E.S., M.S. Potgieter, R.A. Burger, B. Heber, and H. Fichtner, Modulation of jovian and galactic electrons in the heliosphere 1. Latitudinal transport of a few MeV electrons, J. Geophys. Res., 106, A11, 24979 - 24988, 2001a.

Ferreira, S.E.S., M.S. Potgieter, B. Heber, H. Fichtner, R.A. Burger, P. Ferrando, A study of the compatibility between observations and model simulations for Jovian and galactic electrons, Adv. Space Res., 27, 3, 553 - 558, 2001b.

Ferreira, S.E.S., M.S. Potgieter, B. Heber, H. Fichtner, G. Wibberenz, J. , Latitudinal transport effects on the modulation of a few-MeV cosmic ray electrons from solar minimum to solar maximum, J. Geophys. Res., 109, A02115, 1 -10, 2004.

Fichtner, H., Anomalous Cosmic Rays: Messengers from the outer heliosphere, Space Sci. Rev., 95, 639 - 754, 2001.

Fichtner, H., K. Scherer, The Heliosphere: A Brief Overview, *The Outer Heliosphere: Beyond the Planets*, edited by K. Scherer, H. Fichtner, and E. Marsch, Copernicus Gesellschaft, Katlenburg-Lindau, 2000.

Fichtner, H., J.A. le Roux, U. Mall, D. Rucinski, On the transport of pick-up ions in the heliosphere, Astron. Astrophys., 314, 650 - 662, 1996.

Fichtner, H., M.S. Potgieter, S.E.S. Ferreira, R.A. Burger, On the propagation of Jovian elctrons in the heliosphere: transport modelling in 4-D phase space, Geophys. Res. Lett., 27, 1611 - 1614, 2000.

Fichtner, H., M.S. Potgieter, S.E.S. Ferreira, B. Heber, Time-dependent 3D modelling of the heliospheric propagation of few-MeV electrons, Int. Cosmic Ray Conf. Proc., 8, 3666 - 3669, 2001.

Fisk, L.A., Solar modulation of galactic cosmic rays, 2, J. Geophys. Res., 76, 1, 221 - 226, 1971.

Fisk, L.A., Modulation of solar cosmic rays, NASA Special Publication, 342, 418, 1973.

Fisk, L.A., Motion of the footprints of heliospheric magnetic field lines at the Sun: Implications for recurrent energetic particle events at high heliographic latitudes, J. Geophys. Res., 101, A7, 15547 - 15554, 1996.

Fisk, L.A., An overview of the transport of galactic and anomalous cosmic rays in the heliosphere: theory, Adv. Space Res., 23, 3, 415 - 423, 1999.

Fisk, L.A., G. Gloeckler, The global configuration of the heliosheath inferred from recent Voyager 1 observations, Astrophys. J., 776, 79 - 88, 2013.

Fisk, L.A., G. Gloeckler, On whether or not Voyager 1 has crossed the heliopause, Astrophys. J., 789, 41 - 49, 2014.

Florinski, V., On the transport of cosmic rays in the distant heliosheath, Adv. Space Res., 48, 2, 308 - 313, 2011.

Florinski, V., N.V. Pogorelov, Four-dimensional transport of galactic cosmic rays in the outer heliosphere and heliosheath, Astrophys. J., 701, 642 - 659, 2009.

Forbush, S.E., Three unusual cosmic-ray increases possibly due to charged particles from the Sun, Phys. Rev., 70, 771 - 772, 1946.

Forsyth, R.J., A. Balogh, E.J. Smith, G. Erdös, D.J. McComas, The underlying Parker spiral structure in the Ulysses magnetic field observations, 1990 - 1994, J. Geophys. Res., 101, A1, 395 - 404, 1996.

Fujii, Z., F.B. McDonald, Study of the properties of the step decreases in galactic and anomalous cosmic rays over solar cycle 21, J. Geophys. Res., 100, A9, 17043 - 17052, 1995.

Gardiner, C.W., *Handbook of Stochastic Methods*, Springer, Berlin, 1983.

Giacalone, J., J.R. Jokipii, The transport of cosmic rays across a turbulent magnetic field, Astrophys. J., 520, 204 - 214, 1999.

Gil, A., M.V. Alania, 27-day variations of cosmic rays for the minimum epochs of solar activity: Experimental and 3-D drift modelling results, Int. Cosmic Ray Conf. Proc., 9, 3725 - 3728, 2001.

Ginzburg, V.L., S.I. Syrovatskii, *The origin of cosmic rays*, Gordon and Breach, New York, 1969.

Gleeson, L.J., W.I. Axford, Cosmic rays in the interplanetary medium, Astrophys. J. Lett., 149, L115 - L118, 1967.

Gleeson, L.J., W.I. Axford, The Compton-getting effect, Astrophys. Space Sci., 2, 431 - 437, 1968.

Grygorczuk, J., A. Czechowski, S. Grzedzielski, Why are the magnetic field directions measured by Voyager 1 on both sides of the heliopause so similar?, Astrophys. J. Lett., 789, L43 - L46, 2014.

Gurnett, D.A., W.S. Kurth, L.F. Burlaga, N.F. Ness, In situ observations of interstellar plasma with Voyager 1, Sci., 341, 1489 - 1492, 2013.

Haasbroek, L.J., Modulation of cosmic rays in the heliosphere: a model study for the Ulysses spacecraft (in Afrikaans), M.Sc. dissertation, Potchefstroom University for CHE, South Africa, 1993.

Haasbroek, L.J., The transport and acceleration of charged particles in the heliosphere, Ph.D. thesis, Potchefstroom University for CHE, South Africa, 1997.

Haasbroek, L.J., M.S. Potgieter, The modulation of cosmic rays in the high latitude heliosphere: A computer simulation, Space Sci. Rev., 72, 385 - 390, 1995.

Haasbroek, L.J., M.S. Potgieter, J.A. le Roux, The time-dependent recovery after the large cosmic-ray decrease in 1991, Int. Cosmic Ray Conf. Proc., 4, 710 - 713, 1995.

Hale, G.E., On the probable existence of a magnetic field in sun-spots, Astrophys. J., 28, 315 - 343, 1908.

Hattingh, M., Drift of cosmic rays at a wavy neutral sheet in the heliosphere (in Afrikaans), M.Sc. dissertation, Potchefstroom University for CHE, South Africa, 1993.

Hattingh, M., The modulation of galactic cosmic rays in a three-dimensional heliosphere, Ph.D. thesis, Potchefstroom University for CHE, South Africa, 1998.

Hattingh, M., R.A. Burger, A new simulated wavy neutral sheet drift model, Adv. Space Res., 16, 9, 213 - 216, 1995a.

Hattingh, M., R.A. Burger, Some properties of a fully three-dimensional drift model for the modulation of galactic cosmic rays, Int. Cosmic Ray Conf. Proc., 4, 337 - 340, 1995b.

Heber, B., M.S. Potgieter, Cosmic rays at high heliolatitudes, Space Sci. Rev., 127, 117 - 194, 2006.

Heber, B., A. Kopp, J. Gieseler, R. Müller-Mellin, H. Fichtner, K. Scherer, M.S. Potgieter, S.E.S. Ferreira, Modulation of galactic cosmic ray protons and electrons during an unusual solar minimum, Astrophys. J., 699, 1956 - 1963, 2009.

Hess, V.F., Über Beobachtungen der durchdringenden Strahlung bei sieben Freiballonfahrten, Physikalische Zeits., 13, 1084 - 1091, 1912.

Hey, N., *Solar System*, Weidenfeld and Nicholson, UK, 2002.

Hoeksema, J.T., Large-scale structure of the heliospheric magnetic field − 1976 - 1991, *Solar Wind Seven Colloquium*, edited by E. Marsch and R. Schwenn, 1992.

Johnson, L.W., R.D. Riess, J.T. Arnold, *Introduction to linear algebra* 5$^{th}$ *ed.*, Addison Wesley, USA, 2002.

Jokipii, J.R., Cosmic-ray propagation. I. Charged particles in a random magnetic field, Astrophys. J., 146, 480 - 487, 1966.

Jokipii, J.R., Particle acceleration at a termination shock. I - Application to the solar wind and the anomalous component, J. Geophys. Res., 91, 2929 - 2932, 1986.

Jokipii, J.R., Latitudinal heliospheric magnetic field: stochastic and causal components, J. Geophys. Res., 106, A8, 15841 - 15848, 2001.

Jokipii, J.R., E.N. Parker, On the convection, diffusion, and adiabatic deceleration of cosmic rays in the solar wind, Astrophys. J., 160, 735 - 744, 1970.

Jokipii, J.R., D.A. Kopriva, Effects of particle drift on the transport of cosmic rays III. Numerical models of galactic cosmic ray modulation, Astrophys. J., 234, 384 - 392, 1979.

Jokipii, J.R., B. Thomas, Effects of drift on the transport of cosmic rays. IV − Modulation by a wavy interplanetary current sheet, Astrophys. J., 243, 1115 - 1122, 1981.

Jokipii, J.R., J. Kóta, The polar heliospheric magnetic field, Geophys. Res. Lett., 16, 1 - 4, 1989.

Jokipii, J.R., E.H. Levy, W.B. Hubbard, Effects of particle drift on cosmic-ray transport. I - General properties, application to solar modulation, Astrophys. J., 213, 861 - 868, 1977.

Jokipii, J.R., J. Kóta, J. Giacalone, T.S. Horbury, E.J. Smith, Interpretation and consequences of large-scale magnetic variances observed at high heliospheric latitude, Geophys. Res. Lett., 22, 3385 - 3388, 1995.

Kallenrode, M., *Space Physics: An introduction to plasmas and particles in the heliosphere and magnetospheres*, Springer, Germany, 2001.

Kloeden, P.E., E. Platen, H. Schurz, *Numerical Solution of SDE Through Computer Experiments*, Springer, Berlin, 1994.

Kloeden, P.E., E. Platen, *Numerical solutions of stochastic differential equations*, Springer, Berlin, 1999.

Kopp, A., I. Büsching, R.D. Strauss, M.S. Potgieter, A stochastic differential equation code for multidimensional Fokker-Planck type problems, Comp. Phys. Comm., 183, 530 - 542, 2012.

Kóta, J., 3-D simulations of heliospheric transport: A comparison of models, Int. Cosmic Ray Conf. Proc., 2, 25 - 28, 1997.

Kóta, J., Cosmic-ray modulation and the structure of the heliosperic magnetic field, Int. Cosmic Ray Conf. Proc., 7, 9 - 12, 1999.

Kóta, J., J.R. Jokipii, Effects of drifts on the transport of cosmic rays, VI − A three-dimensional model including diffusion, Astrophys. J., 265, 573 - 581, 1983.

Kóta, J., J.R., Jokipii, 3-D distribution of cosmic rays in the outer heliosphere, Int. Cosmic Ray Conf. Proc., 4, 680 - 683, 1995.

Kóta, J., J.R. Jokipii, Are cosmic rays modulated beyond the heliopause?, Astrophys. J., 782, 24 - 29, 2014.

Koyama, K., R. Petre, E.V. Gotthelf, U. Hwang, M. Matsuura, M. Ozati, S.S. Holt, Evidence for shock acceleration of high-energy electrons in the supernova remnant SN1006, Nature, 378, 255 - 258, 1995.

Krieger, A.S., A.F. Timothy, E.C. Roelof, A coronal hole and its identification as the source of a high velocity solar wind stream, Solar Phys., 29, 505 - 525, 1973.

Krimigis, S.M., E.C. Roelof, R.B. Decker, M.E. Hill, Zero outflow velocity for a plasma in a heliosheath transition layer, Nature, 474, 359 - 361, 2011.

Krimigis, S.M., Decker, R.B., Roelof, E.C., et al., Search for the exit: Voyager 1 at heliosphere's border with galaxy, Sci., 341, 144 - 147, 2013.

Krüger, T.P.J., The effect of a Fisk-Parker hybrid magnetic field on cosmic rays in the heliosphere, M. Sc. dissertation, North-West University, South Africa, 2005.

Krülls, W.M., A. Achterberg, Computation of cosmic-ray acceleration by Itō's stochastic differential equations, Astron. Astrophys., 286, 314 - 327, 1994.

Langner, U.W., Effects of different local inerstellar spectra on the heliospheric modulation of cosmic rays, M.Sc. dissertation, Potchefstroom University for CHE, South Africa, 2000.

Langner, U.W., Effects of termination shock acceleration on cosmic rays in the heliosphere, Ph.D. thesis, Potchefstroom University for CHE, South Africa, 2004.

Langner, U.W., M.S. Potgieter, Solar wind termination shock and heliosheath effects on the modulation of protons and antiprotons, J. Geophys. Res., 109, A01103, 1 - 12, 2004a.

Langner, U.W., M.S. Potgieter, Effects of the solar wind termination shock and heliosheath on the heliospheric modulation of galactic and anomalous Helium, Ann. Geophys., 22, 8, 3063 - 3072, 2004b.

Langner, U.W., M.S. Potgieter, Modulation of galactic protons in an asymmetrical heliosphere, Astrophys. J., 630, 1114 - 1124, 2005.

Langner, U.W., M.S. Potgieter, Possible explanations of anomalous spectra observed with Voyager I crossing the solar wind termination shock, AIP Conf. Proc., 858, 233 - 238, 2006.

le Roux, J.A., The solar modulation of galactic cosmic rays as described by a time-dependent drift model, Ph.D. thesis, Potchefstroom University for CHE, South Africa, 1990.

le Roux, J.A., M.S. Potgieter, The simulation of Forbush decreases with time-dependent cosmic ray modulation models of varying comlexity, Astron. Astrophys., 234, 531 - 545, 1991.

le Roux, J.A., M.S. Potgieter, The simulated features of heliospheric cosmic-ray modulation with a time dependent drift model. IV. The role of heliospheric neutral sheet deformation, Astrophys. J., 397, 686 - 693, 1992.

le Roux, J.A., M.S. Potgieter, The simulation of complete 11 and 22 year modulation cycles for cosmic rays in the heliosphere using a drift model with global merged interaction regions, Astrophys. J., 442, 847 - 851, 1995.

le Roux, J.A., M.S. Potgieter, V.S. Ptuskin, A transport model for the diffusive acceleration and modulation of anomalous cosmic rays in the heliosphere, J. Geophys. Res., 101, A3, 4791 - 4804, 1996.

Li, H., C. Wang, J.D. Richardson, Properties of the termination shock observed by Voyager 2, Geophys. Res. Lett., 351, 1 - 4, 2008.

Longair, M.S., Cosmic rays and Galactic radio background emission, *Low Frequency Astrophysics from Space*, Springer-Verlag, 1990.

Luo, X., M. Zhang, H.K. Rassoul, N.V. Pogorelov, Cosmic-ray modulation by the global merged interaction region in the heliosheath, Astrophys. J., 730, 13 - 22, 2011.

Luo, X., M. Zhang, H.K. Rassoul, N.V. Pogorelov, J. Heerikhuisen, Galactic cosmic-ray modulation in a realistic global magnetohydrodynamic heliosphere, Astrophys. J., 764, 85 - 100, 2013a.

Luo, X., M. Zhang, X. Feng, J.E. Mendoza-Torres, Investigation of the transient cosmic ray decreases observed by voyagers in 2007: A numerical approach, J. Geophys. Res., 118, 12, 7517 - 7524, 2013b.

Magidimisha, E., A study of the time-dependent modulation of cosmic rays in the inner heliosphere, M.Sc. dissertation, North-West University, Potchefstroom, South Africa, 2010.

Manuel, R., Time-dependent modulation of cosmic rays in the outer heliosphere, Ph.D. thesis, North-West University, Potchefstroom, South Africa, 2013.

Manuel, R., S.E.S. Ferreira, M.S. Potgieter, R.D. Strauss, N.E. Engelbrecht, Time-dependent cosmic ray modulation, Adv. Space Res., 47, 9, 1529 - 1537, 2011a.

Manuel, R., S.E.S. Ferreira, M.S. Potgieter, Cosmic ray modulation in the outer heliosphere: prediction for cosmic ray intensities up to the heliopause along Voyager I and Voyager II trajectories, Adv. Space Res., 48, 5, 874 - 883, 2011b.

Manuel, R., S.E.S. Ferreira, M.S. Potgieter, Time-dependent cosmic ray modulation in the outer heliosphere: Signatures of a heliospheric asymmetry and model predictions along Voyager 1 and Voyager 2 trajectories, eprints ArXiv, 1310.5522, 2013.

Manuel, R., S.E.S. Ferreira, M.S. Potgieter, Time-dependent modulation of cosmic rays in the heliosphere, Solar Phys. 289, 2207 - 2231, 2014.

Marsch, E., Kinetic physics of the solar wind plasma, *Physics of the Inner Heliosphere II*, edited by R. Schwenn and E. Marsch, Springer-Verlag, Berlin, 1991.

Marsch, E., W.I. Axford, J.F. McKenzie, Solar Wind, *Dynamic Sun*, edited by B.N. Dwivedi, Cambridge University Press, 2003.

Maruyama, G., Continuous Markov processes and stochastic equations, Rend. Circ. Mat. Palermo, 4, 48 - 90, 1955.

Matthaeus, W.H., G. Qin, J.W. Bieber, G.P. Zank, Nonlinear collisionless perpendicular diffusion of charged particles, Astrophys. J. Lett., 590, L53 - L56, 2003.

McComas, D.J., N.A. Schwadron, Disconnection from the termination shock: The end of the voyager paradox, Astrophys. J., 758, 19 - 20, 2012.

McComas, D.J., R.W. Ebert, H.A. Elliott, B.E. Goldstein, J.T. Gosling, N.A. Schwadron, R.M. Skoug, Weaker solar wind from the polar coronal holes and the whole Sun, Geophys. Res. Lett., 35, 1 - 5, 2008.

McComas, D.J., et al., The heliosphere's interstellar interaction: Now bow shock, Sci., 336, 1291 - 1293, 2012.

McDonald, F.B., W.R. Webber, D.V. Reames, Unusual time histories of galactic and anomalous cosmic rays at 1 AU over the deep solar minimum of cycle 23/24, Geophys. Res. Lett., 37, 1 - 5, 2010.

Menn, W., et al., The absolute flux of protons and helium at the top of the atmosphere using IMAX, Astrophys. J., 533, 281 - 297, 2000.

Mewaldt, R.A., et al., Record-setting cosmic-ray intensities in 2009 and 2010, Astrophys. J. Lett., 723, L1 - L6, 2010.

Minnie, J., Observational constraints on the heliospheric diffusion tensor for galactic cosmic rays, M.Sc. dissertation, Potchefstroom University for CHE, South Africa, 2002.

Minnie, J., An ab initio approach to the heliospheric modulation of galactic cosmic rays, Ph.D. thesis, North-West University, Potchefstroom, South Africa, 2006.

Minnie, J., J.W. Bieber, W.H. Matthaeus, R.A. Burger, Suppression of particle drifts by turbulence, Astrophys. J., 670, 1149 - 1158, 2007.

Moeketsi, D.M., Modelling of galactic and Jovian electrons in the heliosphere, M.Sc. dissertation, North-West University, Potchefstroom, South Africa, 2004.

Moeketsi, D.M., M.S. Potgieter, S.E.S. Ferreira, B. Heber, H. Fichtner, V.K. Henize, The heliospheric modulation of 3 - 10 MeV electrons: Modeling of changes in the solar wind speed in relation to perpendicular polar diffusion, Adv. Space Res., 35, 4, 597 - 604, 2005.

Moraal, H., Proton modulation during solar minimum periods in consecutive solar cycles, Int. Cosmic Ray Conf. Proc., 6, 140 - 143, 1990.

Moraal, H., L.J. Gleeson, Three-dimensional models of the galactic cosmic-ray modulation, Int. Cosmic Ray Conf. Proc., 12, 4189 - 4194, 1975.

Moraal, H., L.J. Gleeson, G.M. Webb, Effects of charged particle drifts on the modulation of the intensity of galactic cosmic rays, Int. Cosmic Ray Conf. Proc., 3, 1 - 6, 1979.

Moses, D., Jovian electrons at 1 AU — 1978 - 1984, Astrophys. J., 313, 471 - 486, 1987.

Moskalenko, I.V., A.W. Strong, J.F. Ormes, M.S. Potgieter, Secondary antiprotons and propagation of cosmic rays in the Galaxy and heliosphere, Astrophys. J., 565, 280 - 296, 2002.

Ndiitwani, D.C., A study of the time-dependent modulation of galactic cosmic rays in the heliosphere, M.Sc. dissertation, North-West University, Potchefstroom, South Africa, 2005.

Ndiitwani, D.C., S.E.S. Ferreira, M.S. Potgieter, B. Heber, Modelling cosmic ray intensities along Ulysses trajectory, Ann. Geophys., 23, 3, 1061 - 1070, 2005.

Ndiitwani, D.C., M.S. Potgieter, R. Manuel, S.E.S. Ferreira, The time-dependent modulation of cosmic ray protons in the inner heliosphere from 2006 to 2009, Int. Cosmic Ray Conf. Proc., icrc2013-0187, 2013.

Ngobeni, M.D., Aspects of the modulation of cosmic rays in the outer heliosphere, M.Sc. dissertation, North-West University, Potchefstroom, South Africa, 2006.

Ngobeni, M.D., M.S. Potgieter, Cosmic ray anisotropies in the outer heliosphere, Adv. Space Res., 41, 2, 373 - 380, 2008.

Ngobeni, M.D., M.S. Potgieter, The heliospheric modulation of cosmic rays: Effects of a lititude dependent solar wind termination shock, Adv. Space Res., 46, 4, 391 - 401, 2010.

Ngobeni, M.D., M.S. Potgieter, Modulation of galactic cosmic rays in a north-south asymmetrical heliosphere, Adv. Space Res., 48, 2, 300 - 307, 2011.

Ngobeni, M.D., M.S. Potgieter, Modelling of galactic Carbon in an asymmetrical heliosphere: Effects of asymmetrical modulation conditions, Adv. Space Res., 49, 12, 1660 - 1669, 2012.

Nkosi, G.S., A study of cosmic ray anisotropies in the heliosphere, M.Sc. dissertation, North-West University, Potchefstroom, South Africa, 2006.

Nkosi, G.S., M.S. Potgieter, S.E.S. Ferreira, Electron anisotropies in the inner heliosphere, Int. Cosmic Ray Conf. Proc., 1, 429 - 432, 2008.

Nkosi, G.S., M.S. Potgieter, B. Webber, Modelling of low-energy galactic electrons in the heliosheath, Adv. Space Res., 48, 9, 1480 - 1489, 2011.

Nndanganeni, R.R., Modeling of galactic cosmic ray electrons in the heliosphere, M.Sc. dissertation, North-West University, Potchefstroom, South Africa, 2012.

O'Gallagher, J.J., A time-dependent diffusion-convection model for the long-term modulation of cosmic rays, Astrophys. J., 197, 495 - 507, 1975.

Øksendal, B., *Stochastic Differential Equations: An Introduction with Applications*, Springer, Berlin, 2003.

Opher, M., J.F. Drake, On the rotation of the magnetic field across the heliopause, Astrophys. J. Lett., 778, L26 - L31, 2013.

Palmer, I.D., Transport coefficients of low-energy cosmic rays in interplanetary space, Rev. Geophys. and Space Phys., 20, 335 - 351, 1982.

Parker, E.N., The formation of sunspots from the solar toroidal field, Astrophys. J., 121, 491 - 507, 1955.

Parker, E.N., Dynamics of the interplanetary gas and magnetic fields, Astrophys. J., 128, 664 - 676, 1958.

Parker, E.N., The stellar-wind regions, Astrophys. J., 134, 20 - 27, 1961.

Parker, E.N., *Interplanetary Dynamical Processes*, Interscience Publishers, New York, 1963.

Parker, E.N., The passage of energetic charged particles through interplanetary space, Planet Space Sci., 13, 9 - 49, 1965.

Parker, E.N., A history of early work on the heliospheric magnetic field, J. Geophys. Res., 106, A8, 15797 - 15802, 2001.

Pauls, H.L., G.P. Zank, L.L. Williams, Interaction of the solar wind with the local interstellar medium, J. Geophys. Res., 100, A11, 21595 - 21604, 1995.

Pei, C., J.W Bieber, R.A. Burger, J. Clem, A general time-dependent stochastic method for solving Parker's transport equation in spherical coordinates, J. Geophys. Res., 115, A12107, 1 - 12, 2010.

Pei, C., J.W. Bieber, R.A. Burger, Three-dimensional wavy current sheet drifts, Astrophys. J., 744, 170 - 174, 2012.

Perko, J.S., L.A. Fisk, Solar modulation of galactic cosmic rays. V - time-dependent modulation, J. Geophys. Res., 88, 9033-9036, 1983.

Pesses, M.E., D. Eichler, J.R. Jokipii, Cosmic ray drift, shock wave acceleration, and the anomalous component of cosmic rays, Astrophys. J. Lett., 246, L85 - L88, 1981.

Phillips, J.L., et al., Ulysses solar wind plasma observations from pole to pole, Geophys. Res. Lett., 22, 3301 - 3304, 1995.

Picozza et al., PAMELA: A payload for antimatter matter exploration and light-nuclei astrophysics, Astroparticle Phys., 27, 296-315, 2007.

Pogorelov, N.V., J. Heerikhuisen, G.P. Zank, Probing heliospheric asymmetries with and MHD-kinetic model, Astrophys. J. Lett., 675, L41 - L44, 2008.

Pogorelov, N.V., J. Heerikhuisen, G.P. Zank, S.N. Borovikov, Influence of the interstellar magnetic field and neutrals on the shape of the outer heliosphere, Space Sci. Rev., 143, 31 - 42, 2009.

Potgieter, M.S., The modulation of galactic cosmic rays as described by a three-dimensional drift model, Ph.D. thesis, Potchefstroom University for CHE, South Africa, 1984.

Potgieter, M.S., Heliospheric termination shock acceleration and modulation of the anomalous cosmic-ray component, Adv. Space Res., 9, 12, 21 - 24, 1989.

Potgieter, M.S., Time-dependent cosmic-ray modulation: Role of drifts and interaction regions, Adv. Space Res., 13, 6, 239 - 249, 1993.

Potgieter, M.S., Heliospheric modulation of galactic electrons: consequences of new calculations for the mean free path of electrons between 1 MeV and ∼10 GeV, J. Geophys. Res., 101, A11, 24411 - 24422, 1996.

Potgieter, M.S., The heliospheric modulation of galactic cosmic rays at solar minimum, Adv. Space Res., 19, 6, 883 - 892, 1997.

Potgieter, M.S., The modulation of galactic cosmic rays in the heliosphere: theory and models, Space Sci. Rev., 83, 147 - 158, 1998.

Potgieter, M.S., Heliospheric modulation of cosmic ray protons: Role of enhanced perpendicular diffusion during periods of minimum solar modulation, J. Geophys. Res., 105, A8, 18295 - 18304, 2000.

Potgieter, M.S., Cosmic rays in the inner heliosphere: insights from observations, theory and models, Space Sci. Rev., 176, 165 - 176, 2011.

Potgieter, M.S., Solar Modulation of Cosmic Rays, Living Rev. Solar Phys., 10, 3, 1 - 66, 2013.

Potgieter, M.S., Very local interstellar spectra for galactic electrons, protons and helium, Braz. J. Phys., 44, 581 - 588, 2014.

Potgieter, M.S., H. Moraal, A drift model for the modulation of galactic cosmic rays, Astrophys. J., 294, 425 - 440, 1985.

Potgieter, M.S., H. Moraal, Acceleration of cosmic rays in the solar wind termination shock. I - A steady state technique in a sperically symmetric model, Astrophys. J., 330, 445 - 455, 1988.

Potgieter, M.S., R.A. Burger, The modulation of cosmic-ray electrons, positrons and helium nuclei as predicted by a drift model with a simulated wavy neutral sheet, Astron. Astrophys., 233, 598 - 604, 1990.

Potgieter, M.S., L.J. Haasbroek, The simulation of base-line cosmic-ray modulation for the Ulysses trajectory, Int. Cosmic Ray Conf. Proc., 3, 457 - 460, 1993.

Potgieter, M.S., J.A. le Roux, The long-term heliospheric modulation of galactic cosmic rays according to a time-dependent drift model with merged interaction regions, Astrophys. J., 423, 817 - 827, 1994.

Potgieter, M.S., S.E.S. Ferreira, The importance of perpendicular diffusion in the heliospheric modulation of cosmic ray electrons, Adv. Space Res., 23, 3, 463 - 466, 1999.

Potgieter, M.S., S.E.S. Ferreira, Modulation of cosmic rays in the heliosphere: theory and models, Highlight papers of Int. Cosmic Ray Conf., 217 - 225, 2001.

Potgieter, M.S., S.E.S. Ferreira, Effects of the solar wind termination shock on the modulation of Jovian and galactic electrons in the heliosphere, J. Geophys. Res., 107, A7, SSH 1 - 9, 2002.

Potgieter, M.S., U.W. Langner, Heliospheric modulation of cosmic ray positrons and electrons: effects of the heliosheath and the solar wind termination shock, Astrophys. J., 602, 993 - 1001, 2004a.

Potgieter, M.S., U.W. Langner, The heliospheric modulation of cosmic ray boron and carbon, Ann. Geophys., 22, 10, 3729 - 3740, 2004b.

Potgieter, M.S., R.R. Nndanganeni, The solar modulation of electrons in the heliosphere, Astrophys. Space Sci., 345, 33-40, 2013.

Potgieter, M.S., J.A. le Roux, R.A. Burger, Interplanetary cosmic ray radial gradients with steady state modulation models, J. Geophys. Res., 94, 2323 - 2332, 1989.

Potgieter, M.S., S.E.S. Ferreira, R.A. Burger, Modulation of cosmic rays in the heliosphere from solar minimum to solar maximum: a theoretical perspective, Space Sci. Rev., 97, 295 - 307, 2001.

Potgieter, M.S., E.E. Vos, M. Boezio, N. De Simone, V. Di Felice, V. Formato, Modulation of galactic protons in the heliosphere during the unusual solar minimum of 2006 to 2009, Solar Phys., 289, 1, 391 - 406, 2014.

Ptuskin, V.S., Origin of galactic cosmic rays: sources, acceleration and propagation, Int. Cosmic Ray Conf. Proc., 10, 317 - 328, 2005.

Reames, D.V., The two sources of solar energetic particles, Space Sci. Rev., 75, 53 - 92, 2013.

Richardson, J.D., E.C. Stone, The solar wind in the outer heliosphere, Space Sci. Rev., 143, 7 - 20, 2009.

Richardson, J.D., L.F. Burlaga, The solar wind in the outer heliosphere and heliosheath, Space Sci. Rev., 176, 217 - 235, 2011.

Roberts, D.A., J. Giacalone, J.R. Jokipii, M.L. Goldstein, T.D. Zepp, Spectra of polar heliospheric magnetic fields and implications for field structure, J. Geophys. Res., 112, A08103, 1 - 6, 2007.

Russell, C.T., J.G. Luhmann, L.K. Jian, How unprecedented a solar minimum?, Rev. Geophys., 48, 2, 1 - 16, 2010.

Shalchi, A., *Nonlinear cosmic ray diffusion theories*, Springer-Verlag, Berlin, 2009.

Shalchi, A., R. Schlickeiser, The parallel mean free path of heliospheric cosmic rays in composite slab/two-dimensional geometry. I. The damping model of dynamical turbulence, Astrophys. J., 604, 861 - 873, 2004.

Sheeley, N.R., Jr., et al., Measurements of flow speeds in the corona between 2 and 30 $R_{\rm sun}$, Astrophys. J., 484, 472 - 478, 1997.

Scherer, K., S.E.S. Ferreira, A heliospheric hybrid model: Hydrodynamic plasma flow and kinetic cosmic ray transport, ASTRA, 1, 17 - 27, 2005.

Scherer, K., H. Fichtner, The return of the bow shock, Astrophys. J., 782, 25 - 29, 2014.

Scherer, K., H. Fichtner, B. Heber, U. Mall (Eds.), *Space weather: The physics behind a slogan*, Springer, Germany, 2005.

Scherer, K., S.E.S. Ferreira, M.S. Potgieter, H. Fichtner, Time and latitude-dependence of the compression ratio and the injection efficiency at the heliospheric termination shock, AIP Conf. Proc., 858, 20 - 26, 2006a.

Scherer, K., et al., Interstellar-terrestrial relations: Variable cosmic ray environments, the dynamic heliosphere, and their imprints on terrestrial archives and climate, Space Sci. Rev., 127, 327 - 465, 2006b.

Scherer, K., H. Fichtner, R.D. Strauss, S.E.S. Ferreira, M.S. Potgieter, H.-J. Fahr, On cosmic ray modulation beyond the heliopause: Where is the modulation boundary?, Astrophys. J., 735, 1 - 5, 2011.

Schlickeiser, R., On the interplanetary transport of solar cosmic rays, J. Geophys. Res., 93, A4, 2725 - 2729, 1988.

Schlickeiser, R., *Cosmic ray astrophysics*, Springer, Berlin, 2002.

Schwadron, N.A., D.J. McComas, Is Voyager 1 inside an interstellar flux transfer event?, Astrophys. J. Lett., 778, L33 - L37, 2013.

Schwenn, R., The average solar wind in the inner heliosphere: Structures and slow variations, Proc. of the NASA Conference Publication, 2280, 489 - 507, 1983.

Simpson, J.A., Cosmic radiation: Particle astrophysics in the heliosphere, *Frontiers in Cosmic Physics: Symposium in memory of Serge Korff*, edited by R.B. Mendell, and A.J. Mincer, New York Academy of Sciences, New York, 1992.

Simpson, J.A., The cosmic radiation: Reviewing the present and future, Inter. Cosmic Ray Conf. Proc., Invited, Rapporteur and Highlighted Papers, 4 - 8, 1998.

Simpson, J.A., D. Hamilton, G. Lentz, R.B. McKibben, A. Mogro Campero, M. Perkins, K.R. Pyle, A.J. Tuzzolino, J.J. O'Gallagher, Protons and electrons in Jupiter's magnetic field: Results form the University of Chicago Experiment on Pioneer 10, Sci., 183, 306 - 309, 1974.

Smith, C.W., J.W. Bieber, Solar cycle variation of the interplanetary magnetic field spiral, Astrophys. J., 370, 435 - 441, 1991.

Smith, E.J., Interplanetary magnetic field over two solar cycles and out to 20 AU, Advances in Space Research, 9, 4, 159 - 169, 1989.

Smith, E.J., The Sun, solar wind, and magnetic field. I., *Proceedings of the International School of Physics "Enrico Fermi" Cource CXLII*, edited by B. Coppi, A. Ferrari, and E. Sindoni, 2000.

Smith, E.J., The heliospheric current sheet, J. Geophys. Res., 106, 15819 - 15832, 2001.

Smith, E.J., The global heliospheric magnetic field, *The heliosphere through the solar activity cycle*, edited by A. Balogh, L.J. Lanzerotti, and S.T. Suess, 2008.

Smith, E.J., A. Balogh, Decrease in heliospheric magnetic flux in this solar minimum: recent Ulysses magnetic field observations, Geophys. Res. Lett., 35, 1 - 4, 2008.

Snodgrass, H.B., Magnetic rotation of the solar photosphere, Astrophys. J., 270, 288 - 299, 1983.

Soon, W.W., S.H. Yaskell, *The Maunder minimum and the variable Sun-Earth connection*, World Scientific Publishing, Singapore, 2003.

Steenberg, C.D., Modelling of anomalous and galactic cosmic ray modulation in the outer heliosphere, Ph.D. thesis, Potchefstroom University for CHE, South Africa, 1998.

Steenberg, C.D., H. Moraal, An Acceleration/Modulation Model for Anomalous Cosmic-Ray Hydrogen in the Heliosphere, Astrophys. J., 463, 776 - 783, 1996.

Steenkamp, R., Shock acceleration as source of the anomalous component of cosmic rays in the heliosphere, Ph.D. thesis, Potchefstroom University for CHE, South Africa, 1995.

Steenkamp, R., H. Moraal, Acceleration and modulation of anomalous helium and oxygen in 1977 and 1987, Int. Cosmic Ray Conf. Proc., 3, 539 - 542, 1993.

Sternal, O., N.E. Engelbrecht, R.A. Burger, S.E.S. Ferreira, H. Fichtner, B. Heber, A. Kopp, M.S. Potgieter, K. Scherer, Possible evidence for a Fisk-type heliospheric magnetic field. I. Analyzing Ulysses / KET electron observations, Astrophys. J., 741, 1 - 12, 2011.

Stone, E.C., A.C. Cummings, F.B. McDonald, B.C. Heikkila, N. Lal, W.R. Webber, Voyager 1 explores the termination shock region and the heliosheath beyond, Sci., 309, 2017 - 2020, 2005.

Stone, E.C., A.C. Cummings, F.B. McDonald, B.C. Heikkila, N. Lal, W.R. Webber, An asymmetric solar wind termination shock, Nature, 454, 71 - 74, 2008.

Stone, E.C., A.C. Cummings, F.B. McDonald, Voyager 1 observes low-energy galctic cosmic rays in a region depleted of heliospheric ions, Sci., 341, 150 - 153, 2013.

Strauss, R.D., Modelling of anomalous cosmic rays, M.Sc. dissertation, North-West University, Potchefstroom, South Africa, 2010.

Strauss, R.D., Modelling of cosmic rays in the heliosphere by stochastic processes, Ph.D. thesis, North-West University, Potchefstroom, South Africa, 2013.

Strauss R.D., M.S. Potgieter, Where does the heliospheric modulation of galactic cosmic rays start?, Adv. Space. Res., 53, 7, 1015 - 1023, 2014a.

Strauss, R.D., M.S. Potgieter, Is the highest cosmic-ray flux yet to come?, Solar Phys., 289, 8, 3197 - 3205, 2014b.

Strauss, R.D., M.S. Potgieter, S.E.S. Ferreira, The heliospheric transport and modulation of multiple charged anomalous oxygen revisited, Astron. Astrophys., 513, 1 - 6, 2010.

Strauss, R.D., M.S. Potgieter, S.E.S. Ferreira, Modelling the acceleration and modulation of anomalous cosmic ray oxygen, Adv. Space Res., 48, 1, 65 - 75, 2011a.

Strauss, R.D., M.S. Potgieter, I. Büsching, A. Kopp, Modeling the modulation of galactic and Jovian electrons by stochastic processes, Astrophys. J., 735, 83 - 95, 2011b.

Strauss, R.D., M.S. Potgieter, I. Büsching, A. Kopp, On the propagation times and energy losses of cosmic rays in the heliosphere, J. Geophys. Res., 116, A12105, 1 - 13, 2011c.

Strauss, R.D., M.S. Potgieter, I. Büsching, A. Kopp, Modeling heliospheric current sheet drift in stochastic cosmic ray transport models, Astrophys. Space Sci., 339, 223 - 236, 2012.

Strauss, R.D., M.S. Potgieter, S.E.S. Ferreira, H. Fichtner, K. Scherer, Cosmic ray modulation beyond the heliopause: a hybrid modeling approach, Astrophys. J. Lett., 765, L18 - L23, 2013a.

Strauss, R.D., M.S. Potgieter, S.E.S. Ferreira, H. Fichtner, K. Scherer, Galactic cosmic ray modulation beyond the heliopause: When will Voyager I measure the LIS?, Int. Cosmic Ray Conf. Proc., 2013-0154, 2013b.

Svalgaard, L., E.W. Cliver, A floor in the solar wind magnetic field, Astrophys. J., 661, L203 - L206, 2007.

Svensmark, H., N. Calder, *The chilling stars, a new theory of climate change*, Icon Books Ltd., UK, 2007.

Tanimori, T., et al., Discovery of TeV gamma rays from SN1006: Further evidence for the supernova remnant region of cosmic rays, Astrophys. J. Lett., 497, L25 - L28, 1998.

Teufel, A., R. Schlickeiser, Analytic calculation of the parallel mean free path of heliospheric cosmic rays. II. Dynamical magnetic slab turbulence and random sweeping slab turbulence with finite wave power at small wavenumbers, Astron. Astrophys., 397, 15 - 25, 2003.

Usoskin, I.G., A history of solar activity over millennia, Living Rev. Solar Phys., 10, 1, 1 - 94, 2013.

Visser, D.J., The effect of turbulence-modified drift on the modulation of cosmic rays in the heliosphere, M.Sc. dissertation, North-West University, South Africa, 2009.

von Steiger, R., et al., Composition of quasi-stationary solar wind flows from Ulysses / Solar Wind Ion Composition Spectrometer, J. Geophys. Res., 105, A12, 27217 - 27238, 2000.

Vos, E.E., Cosmic ray modulation processes in the heliosphere, M.Sc dissertation, North-West University, Potchefstroom, South Africa, 2011.

Vos, E.E., M.S. Potgieter, M. Boezio, N. De Simone, V. Di Felice, V. Formato, Modulation mechanism for galactic protons during the unusual solar minimum of 2009, Int. Cosmic Ray Conf. Proc., 2013-0273, 2013a.

Vos, E.E., M.S. Potgieter, M. Boezio, V. Di Felice, N. De Simone, V. Formato, R. Munini, Modulation of galactic electrons during the unusual solar minimum of 2009, Int. Cosmic Ray Conf. Proc., 2013-0276, 2013b.

Wang, Y.-M., E. Robbrecht, N.R. Sheeley, Jr., On the weakening of the polar magnetic fields during solar cycle 23, Astrophys. J., 707, 1372 - 1386, 2009.

Webb, G.M., L.J. Gleeson, Green's theorem and Green's function for the steady-state cosmic-ray equation of transport, Astrophys. Space Sci., 50, 205 - 223, 1977.

Webber, W.R., Intriligator, D.S., Voyagers 1 and 2 in a shrunken and squashed heliosphere, Journal of Geophys Research, 116, A06105, 1-8, 2011.

Webber, W.R., F.B. McDonald, Recent Voyager 1 data indicate that on August 25, 2012 at a distance of 121.7 AU from the Sun, sudden and unprecedented intensity changes were observed in anomalous and galactic cosmic rays, Geophys. Res. Lett., 40, 1665 - 1668, 2013.

Webber, W.R., M.S. Potgieter, R.A. Burger, A comparison of predictions of a wavy neutral sheet drift model with cosmic-ray data over a whole modulation cycle − 1976 - 1987, Astrophys. J., 349, 634 - 640, 1990.

Webber, W.R., F.B. McDonald, A.C. Cummings, E.C. Stone, B. Heikkila, N. Lal, At Voyager 1 starting on about August 25, 2012 at a distance of 121.7 AU from the Sun, a sudden disappearance of anomalous cosmic rays and an unusuallly large sudden increase of galactic cosmic ray H and He nuclei and electron occurred, eprints ArXiv, 1212.0883, 2012.

Williams, T., The influence of the wavy heliospheric neutral current sheet on the modulation of cosmic rays (in Afrikaans), M.Sc. dissertation, Potchefstroom University for CHE, South Africa, 1990.

Yamada, Y., S. Yanagita, T. Yoshida, A stochastic view of the solar modulation phenomena of cosmic rays, Geophys. Res. Lett., 25, 2353 - 2356, 1998.

Zhang, M., A Markov stochastic process theory of cosmic-ray modulation, Astrophys. J., 513, 409 - 420, 1999.

Zhao, L.-L., G. Qin, M. Zhang, B. Heber, Modulation of galactic cosmic rays during the unusual solar minimum between cycles 23 and 24, J. Geophys. Res., 119, 3, 1493 - 1506, 2014.

Zurbuchen, T.H., N.A. Schwadron, L.A. Fisk, Direct observational evidence for a heliospheric magnetic field with large excursions in latitude, J. Geophys. Res., 102, A11, 24175 - 24182, 1997.

# Acknowledgements


- Prof. M.S. Potgieter, my supervisor, for the essential guidance, assistance and support which enabled me to complete this dissertation. In addition, I would like to thank Prof. Potgieter for his support on a personal level, thereby being a mentor to me in more than just one sense of the word.
- Dr. R.D. Strauss, my co-supervisor, for much needed assistance on various occasions.
- Dr. A. Kopp, for discussions related to the SDE-based modulation model.
- Mr. E.E. Vos, for discussions related to the PAMELA data and providing results obtained via the ADI-based modulation model.
- Mrs. M.P. Sieberhagen, for assistance with financial and other administrative matters.
- Mrs. E. van Rooyen and Mrs. L. van Wyk for handling various administrative issues.
- Mr. M. Holleran, for his help with computer related problems.
- My parents, family and friends for their love and support throughout the term of this study.
- The National Research Foundation, the South African National Space Agency and the Centre for Space Research at the North-West University for financial support throughout this study.



Jan Louis Raath
*Centre for Space Research, North-West University*

*November 2014*